Doctoral theses at NTNU, 2020:148

Kara Kamen Poon

Development of Piezoelectric BCZT Ceramics as Electroactive Bone Implant Materials

Doctoral thesis

Kara Kamen Poon

ISBN 978-82-326-4644-9 (printed ver.)
ISBN 978-82-326-4645-6 (electronic ver.)
ISSN 1503-8181

NTNU
Norwegian University of
Science and Technology

NTNU
Norwegian University of Science and Technology
Thesis for the Degree of
Philosophiae Doctor
Faculty of Natural Sciences
Department of Materials Science and Engineering

Doctoral theses at NTNU, 2020:148

NTNU
Norwegian University of
Science and Technology

Kara Kamen Poon

Development of Piezoelectric BCZT Ceramics as Electroactive Bone Implant Materials

Thesis for the Degree of Philosophiae Doctor

Trondheim, May 2020

Norwegian University of Science and Technology
Faculty of Natural Sciences
Department of Materials Science and Engineering

NTNU
Norwegian University of
Science and Technology

NTNU
Norwegian University of Science and Technology

Thesis for the Degree of Philosophiae Doctor

Faculty of Natural Sciences
Department of Materials Science and Engineering

ISBN 978-82-326-4644-9 (printed ver.)
ISBN 978-82-326-4645-6 (electronic ver.)
ISSN 1503-8181

Doctoral theses at NTNU, 2020:148

Printed by NTNU Grafisk senter

This thesis has been submitted to the

Department of Materials Science and Engineering

Norwegian University of Science and Technology (NTNU)

in partial fulfilment of the requirements for

the academic degree

Philosophiae Doctor

February 2020

Preface

The doctoral studies described in this thesis were mainly performed in the Functional Materials and Materials Chemistry Research Group (FACET) at the Department of Materials Science and Engineering (IMA), NTNU (Trondheim), from August 2016 to January 2020, under the supervision and guidance of Associate Professor Julia Glaum (main supervisor) and Professor Mari-Ann Einarsrud (co-supervisor). The research work was funded by the Norwegian Research Council (FRINATEK 250098) and by Horizon 2020 Marie Skłodowska-Curie Actions (H2020 MSCA 655866).

The majority of the work was performed by the author, including the design of experiments, preparation and performance of measurements, post-processing, analyses and discussion of the results. Cell proliferation and viability were performed in collaboration with Dr. Matthias C. Wurm and Dr. Rainer Lutz (Department of Oral and Maxillofacial Surgery, Friedrich-Alexander-Universität Erlangen-Nürnberg, Erlangen, Germany), whom provided advice on the design of experiments, and performed the cell studies and statistical analyses. Dr. Donald M. Evans (IMA, NTNU) conducted the surface roughness measurements using the scanning probe technique. The inductively coupled plasma mass spectroscopy (ICP-MS) analyses were performed by Senior Engineer Syverin Lierhagen (Department of Chemistry (IKJ), NTNU). The dielectric impedance spectroscopy measurements, mechanical testing, and measurement of piezoelectric properties throughout the mechanical testing process were carried out by Louis Guinamard (École Nationale Supérieure des Ingénieurs en Arts Chimiques et Technologiques, INP-ENSIACET, Toulouse, France). Senior Engineer Morten Peder Raanes (IMA, NTNU) performed the electron probe microanalyses (EPMA).

Parts of this thesis were published in a scientific journal (p. 173).

K. K. Poon, M. C. Wurm, D. M. Evans, M.-A. Einarsrud, R. Lutz, J. Glaum, "Biocompatibility of (Ba,Ca)(Zr,Ti)O_3 piezoelectric ceramics for bone replacement materials," *Journal of Biomedical Materials Research Part B: Applied Biomaterials,* vol. 108, pp. 1295–1303, 2020, doi: 10.1002/jbm.b.34477

Trondheim, February 2020

Kara Kamen Poon

Acknowledgements

First and foremost, I would like to express my deepest gratitude to my supervisor, Associate Professor Julia Glaum, for the opportunity to work on this interesting topic for the last three and a half years. Her guidance, expertise, immense support, and kind spirit have been invaluable, and it has been a privilege to have had the freedom to explore this topic with her encouragement. I am sincerely grateful also to my co-supervisor, Professor Mari-Ann Einarsrud, for her expertise, advice, and motivating encouragement. It has been an invaluable experience working with them both, and I am wholeheartedly grateful for their persistent enthusiasm and our stimulating discussions.

Immense gratitude and appreciation go to all of the people whose assistance aided the completion of this work: To Dr. Rainer Lutz and Dr. Matthias C. Wurm for their eagerness, input and experimental work on the biological cell studies, to Dr. Donald M. Evans for his input on the surface roughness measurements, to Syverin Lierhagen for his assistance with the ICP-MS measurements, to Louis Guinamard for his immeasurable contribution to the mechanical loading experiments, to Morten Peder Raanes for his assistance with the EPMA measurements, to Assistant Professor Stefan Schafföner for his invaluable expertise and advice on metal/ceramic interfaces, and to the technicians at IMA – Anita, Eli, Elin, Eva, Johannes, Julie, Kristin, Magnus BF, Magnus R, Mikko, Morten, Pål, Pei Na, Sergey, Silje, Solveig, Torild, Trygve, and Yingda – for their kindness and assistance with trainings, experimental procedures and set-ups.

I am indebted to the members of IMA, and especially to the those in the FACET group including the academic staff, Post Docs, PhDs and Master students. I could not have asked for a better working environment – open, warm, friendly, supportive, and keenly willing to help one another. I will forever try to emulate these qualities I have experienced here. To the guys in the office – Nikolai, Mikalai and Magnus R – thank you for all the chats and laughs over the years! My warmest thanks go to Magnus BF, Emily, and Kevin for your love, (virtual and real) shoulders to lean on, and words of encouragement.

Finally, to mum, dad, and Jon – thank you for always supporting me in all that I do, even when it means moving to the other side of the world! My achievements are a tribute to you and your loving support. I love you!

Abstract

The repair of load-bearing bone with metal implant materials and the application of external electrical stimuli for accelerated healing are common procedures in clinical practice. However, these procedures involve extended recuperation periods, the risk of implant instabilities that necessitate corrective revision surgeries due to poor bone-implant bonding, and the inefficient application of electrical stimuli via external wired devices. Functionalisation of current metal implant materials with piezoelectric ceramics offers a novel opportunity for promoting tissue healing *in vivo* via independent electrical stimulation. Piezoelectric materials have the inherent ability to generate electric surface charges under mechanical loading just like bone tissue, thereby offering the potential to accelerate patient recuperation, enhance bone-implant interface stability, and reduce the necessity for revision surgeries and external devices. Calcium- and zirconium-doped barium titanate (BCZT) is a lead-free piezoelectric material with a perovskite structure exhibiting exceptional piezoelectric responses. However, it has yet to be implemented as a biomedical implant material. Therefore, several aspects of the functionality of BCZT must be assessed to transfer this material into the biomedical field. Aspects include the piezoelectric response relative to crystallographic phase composition, the compatibility with human cells and interaction with liquid environments, the resistance to mechanical depolarisation, and the process for integrating these piezoelectric ceramics with existing implant materials.

In the first part of this thesis, the influence of crystallographic phase fractions on piezoelectric response was investigated through assessment of four bulk BCZT materials prepared via solid-state synthesis. Their piezoelectric and dielectric properties showed a clear influence of the proportions of the contained tetragonal, orthorhombic, and rhombohedral phases.

The compatibility of BCZT with human osteoblast and endothelial cells was evaluated over a 10-day period. Cell proliferation and viability studies showed BCZT to be not cytotoxic. In addition, the behaviour of BCZT in liquid environments was assessed by soaking and ion release tests in deionised water and 0.154 M NaCl solution. Incongruent ion dissolution was observed, such that initial A-site release was followed by the

formation of a stable B-site terminated surface. This indicates the potential for developing a pre-conditioning treatment for BCZT prior to implantation to minimise the exposure of the implant site tissue to high concentrations of released ions.

Mechanical depolarisation resistance was assessed by static compressive mechanical loading over a 60 min period of four BCZT materials of different crystallographic phase compositions, and four BCZT materials of varying average grain sizes. Distinct relationships between resistance to mechanical depolarisation and phase composition and grain size were observed, highlighting potential methods for tailoring the piezoelectric response of these ceramics without the need for toxic elemental dopants.

Finally, BCZT ceramic coatings were spray-deposited onto common metal implant materials including stainless steel 316L and Ti-alloy Ti6Al4V. Several processing parameters were modified in the process of preparing mechanically robust ceramic coatings. However, the formation of an unstable hygroscopic reaction region during heat-treatment revealed that further monitoring and optimisation of the deposition process is required.

The work in this thesis demonstrates the potential of BCZT ceramics as bone repair materials. Good piezoelectric responses and mechanical depolarisation resistance were observed, and promising alternative routes to chemical dopants for optimising the piezoelectric response were revealed through modifications of crystallographic phase composition and grain size. BCZT ceramics were also shown to be compatible with human cells, and a feasible pre-conditioning treatment for these materials was proposed. Although the integration of BCZT piezoelectric ceramics to metal implant materials proved challenging, good attachment is foreseeable in the future with the implementation of several optimised synthesis parameters of the spray-deposition process.

Table of Contents

List of Figures

List of Tables

List of Acronyms

BCZT	$(Ba_{1-x}Ca_x)(Zr_yTi_{1-y})O_3$
BCT	$(Ba_{1-x}Ca_x)TiO_3$
BT	$BaTiO_3$
BZT	$Ba(Zr_yTi_{1-y})O_3$
EDS	electron dispersive spectroscopy
EPMA	electron probe micro analysis
FWHM	full width at half maximum
ICP-MS	inductively coupled plasma mass spectroscopy
MPB	morphotropic phase boundary
PDF	powder diffraction file
PPT	polymorphic phase transition
PZT	$Pb(Zr_xTi_{1-x})O_3$
RPM	rotations per min
SEM	scanning electron microscopy
SPM	scanning probe microscopy
TCP	tricritical point
Ti6Al4V	grade 5 titanium
WDS	wavelength dispersive spectroscopy
WTS	water-soluble tetrazolium salts
XRD	X-ray diffraction
YTZ	yttria-stabilised zirconia

List of Symbols

Sign	Unit	Description
$\boldsymbol{diam}$	nm	diameter
$\boldsymbol{d_{33}}$	pC/N	remanent piezoelectric coefficient
$\boldsymbol{P_r}$	μC/cm^2	remanent polarisation
$\boldsymbol{R_a}$	μm	average surface roughness
$\boldsymbol{r_{core}}$	nm	core radius
$\boldsymbol{r_0}$	nm	initial radius
$\boldsymbol{S_{max.}}$	%	maximum strain
$\boldsymbol{S_{min.}}$	%	minimum strain
$\boldsymbol{SSA}$	m^2/g	specific surface area
$\boldsymbol{TEC}$	K^{-1}	thermal expansion coefficient
$\boldsymbol{T_c}$	°C	Curie temperature
$\boldsymbol{T_{R-O}}$	°C	rhombohedral-orthorhombic phase transition temperature
$\boldsymbol{T_{O-T}}$	°C	orthorhombic-tetragonal phase transition temperature
$\boldsymbol{T_{R-T}}$	°C	rhombohedral-tetragonal phase transition temperature
$\boldsymbol{T_{T-C}}$	°C	tetragonal-cubic phase transition temperature
$\boldsymbol{X}$	moles	amount of ions
$\boldsymbol{X_t}$	moles	amount of ions after soaking time, *t*
$\boldsymbol{\rho}$	g/cm^3	density
$\boldsymbol{\varepsilon_r}$	–	remanent relative permittivity
$(\ldots)_{\boldsymbol{pc}}$	–	pseudo-cubic reflection

Chapter 1

Background and Aims

1.1. Background

The surgical implantation of synthetic materials acting as supports or scaffolds to aid bone healing is a routine procedure in the treatment of diseased and critically damaged bone tissue. These materials repair, stabilise, replace, and eventually restore function to the affected tissue area, and are typically selected for their physical characteristics that mimic the biological environment. For instance, metals are selected to replace load-bearing bone due to their high strength and fracture toughness, whilst ceramics such as zirconia and alumina are chosen for their lower cytotoxicity [1]–[3]. These well-established implant materials are in themselves inert, having the advantage that they are not rejected by the body. However, as they do not interact with the host tissue in a positive manner either, and are rather at risk to be encapsulated within scar tissue, they do not integrate well with bone tissue [4]. In the specific case of load-bearing implants, loosening is a common issue induced by poor stress distributions and local micromotions of the implant relative to the tissue [5]. This may cause clinical failure of the implant, inevitably necessitating corrective revision surgeries that are substantial and stressful procedures to the patient. In Norway alone, revision surgeries have accounted for approximately 15 % of the ~100 000 total hip replacement procedures performed in the last decade [6]. With the primary age group for bone tissue implants from 60–79 [6], and the growing ageing population, demand for technical advancements in bone repair materials to improve the bonding between synthetic biomaterials and the host tissue to facilitate stable, long-lasting fixation, that can withstand physiological loads is obvious.

Novel biomaterial design today focuses on the intrinsic properties of biomaterials to encourage cell interactions by mimicry of natural stimulatory processes, such as the provision of biophysical or biochemical cues [7]–[12]. The generation of electric surface charge potentials under application of mechanical load, or piezoelectric behaviour, has

been known to be exhibited by bone tissue since the 1950s, and potentials of up to 0.7 pC/N have been recorded [13], [14]. Although the specific mechanism underlying electrically-stimulated bone formation is debated, *in vitro* application of electrical stimuli to bone-forming cells (osteoblasts) encourages cell responses such as proliferation, differentiation, and apatite mineral formation (bioactivity) [15]–[17]. Moreover, electrical stimulation is utilised to accelerate bone fracture healing in current clinical practice via external therapies [16], [18]–[20]. Replicating the piezoelectric behaviour displayed by bone and introducing it as a functionality to a load-bearing implant could therefore be beneficial for bone regeneration, as localised electric potentials could be generated *in vivo* directly at the implant site.

The unique behaviour of piezoelectric materials to inherently form electric surface charges under a mechanical load is in most cases based on their non-centrosymmetric crystallographic structures [21]. Both organic and inorganic piezoelectric materials can be suitable *in vivo* sources of electrical stimuli, with inorganic systems commonly exhibiting the higher piezoelectric response [22]. *In vitro* studies on charged surfaces indicate enhanced bioactivity and cell responses, supporting the approach to utilise piezoelectric materials as electric functionalisation for bone implants [8], [23]–[25].

While most commercially used piezoelectric materials contain high amounts of lead and are for toxicity reasons not suitable as tissue replacement materials, the intense search for lead-free alternatives over the past decades has brought forward several promising systems. Among these, compositions based on barium titanate ($BaTiO_3$) (BT) exhibit the most competitive piezoelectric response compared to lead-based standards [26]. In particular, the Ca- and Zr-doped derivative of this material class $(Ba_{100-x}Ca_x)(Zr_yTi_{100-y})O_3$ (BCZT) shows exceptional piezoelectric responses ($d_{33} \approx 620$ pC/N) for the morphotropic phase boundary composition [27]. *In vitro* studies on the parent material system, BT, indicate good biocompatibility and bioactivity, and positive effects of piezoelectricity on osteoblasts, making this system highly attractive for the autonomous generation of electric charge in load-bearing implants [28]–[30]. Studies on the applicability of BCZT as a biomaterial, however, are limited. Although some concern surrounds the toxicity of Ba ions, early *in vitro* studies on BCZT show that it is biocompatible [31]–[35]. As such, BCZT can be envisioned as an electroactive bone

replacement material for load-bearing applications such as in joints and dental implants, where a material is mechanically loaded in a cyclic manner.

1.2. Aims

BCZT piezoelectric ceramics are currently not utilised in bone implant devices, nor is there significant research into their compatibility with the biological environment. This thesis therefore aims to address fundamental questions related to the implementation of BCZT ceramics as suitable electroactive implant materials.

The magnitude of electrical stimuli applied *in vivo* will need to be tailored to the local bone tissue environment for optimal cell response. As such, it is critical to understand how the piezoelectric properties of BCZT can be modified without the use of toxic elemental additives. Crystallographic phase composition was investigated as a suitable alternative via piezoelectric and dielectric measurements of four BCZT materials containing various proportions of tetragonal, orthorhombic, and rhombohedral phases.

As a load-bearing bone replacement material, BCZT will be subject to mechanical loads. It is therefore necessary to investigate how the piezoelectric response changes relative to applied physiological loads to assess the material's functional lifetime as an electroactive biomaterial. Particular attention is focused on the influence of crystallographic phase composition and grain size.

BCZT materials are not typically used in liquid environments, let alone with biological cells. Therefore, the compatibility of BCZT with human osteoblast and endothelial cells will be investigated via *in vitro* cell viability and proliferation testing. Ion release can be detrimental to the success of a biomaterial. As such, the behaviour of BCZT materials in liquid environments and the release of ions will be monitored.

Finally, the potential of integrating BCZT as a functional coating on commonly used load-bearing metal implants will be investigated via the development of a deposition process for BCZT ceramic coatings on metal substrates including stainless steel 316L and Ti-alloy Ti6Al4V.

Chapter 2

Introduction

This chapter begins with fundamental physical concepts on dielectric materials, piezoelectricity, and ferroelectricity as an introduction to piezoelectric ceramics such as lead zirconate titanate, and lead-free alternatives: barium titanate, and Ca- and Zr-doped barium titanate. A description of bone repair and the current implant materials used in the biomedical field are provided, followed by a range of topics related to the potential of piezoelectric ceramics as electrically stimulative bone repair materials.

2.1. Fundamental Physical Concepts

2.1.1. Dielectric Materials

A dielectric material is an electrical insulator that displays an electric dipole moment upon application of an external electric field, such that the centres of two equal and opposite point charges are displaced from their equilibrium positions. The dipole moment, $\vec{p}$, is defined by [36]:

$$\vec{p} = q\vec{d} \tag{1}$$

where q is the electric charge in Coulombs (C), and $\vec{d}$ is the displacement vector between the opposite charges in metres (m). The dipole moment is directed from the negative to positive charge.

Polarisation, $\vec{P}$, is the total dipole moment per unit volume of dielectric material [37]:

$$\vec{P} = \frac{\vec{p}}{V} \tag{2}$$

where $\vec{p}$ is the dipole moment (Cm), and V is the volume of material (m^3).

There are several types of polarisation, including electronic, ionic (or atomic), space charge, and orientation (dipolar) polarisation [36], [37]. These are visually described in Figure 2.1. Electronic polarisation is a property of all dielectric materials, where an

external electric field causes the distortion of an electron cloud surrounding a nucleus. Ionic (or atomic) polarisation is the displacement of ions within a crystal structure when an electric field is applied. Space charge polarisation involves the displacement of mobile charge carriers to structural interfaces under an applied electric field. Orientation (dipolar) polarisation involves the alignment of asymmetric molecules that have a permanent dipole moment, e.g. H_2O, under an applied electric field.

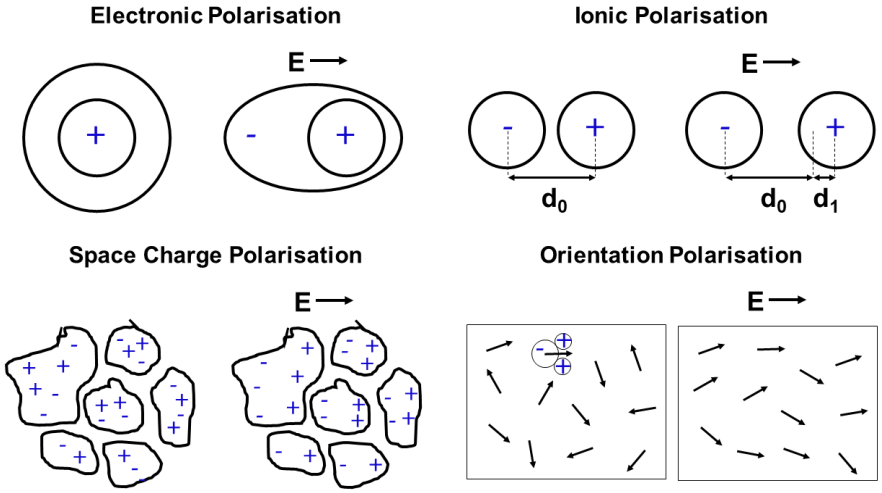

Figure 2.1: Types of polarisation mechanisms. Adapted from [38]*, with the permission of Taylor and Francis Group LLC, Copyright © 2006. Adapted from* [39]*, with the permission of John Wiley & Sons, Copyright © 2003.*

A figure of merit of dielectric materials is the relative permittivity or dielectric coefficient, ε_r, which describes the degree of polarisability of a material, or its ability to store charge. It is defined as:

$$\varepsilon_r = \frac{\varepsilon}{\varepsilon_0} \tag{3}$$

where ε is the absolute permittivity of a material, and ε_0 is the vacuum permittivity (8.5×10^{-12} F/m).

2.1.2. Piezoelectricity

Piezoelectricity, derived from the Greek word (*piezin*) for pressure, is an electromechanical coupling effect that is displayed by a sub-set of dielectric materials. Specifically, it is a property that applies to 21 non-centrosymmetric crystal classes, except the cubic class 432 due to symmetry [40].

When a compressive or tensile mechanical stress is applied to a piezoelectric material, electric surface charges are generated in response. This is known as the direct piezoelectric effect (Figure 2.2 (a)). In reverse, the application of an electric field generates a mechanical strain by the indirect (converse) piezoelectric effect (Figure 2.2 (b)).

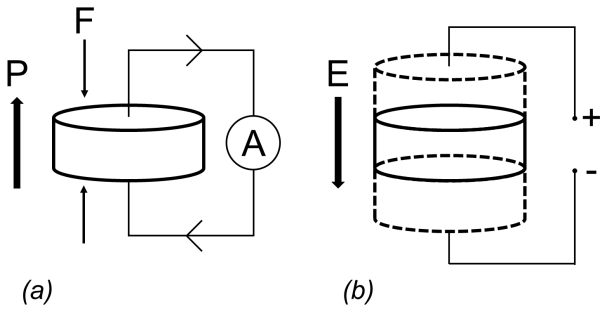

Figure 2.2: The (a) direct and (b) indirect piezoelectric effects. The dotted lines indicate the original dimensions. Adapted from [39]*, with the permission of John Wiley & Sons, Copyright © 2003.*

The direct and indirect piezoelectric effects are described as follows [39]:

$$D = dX + \varepsilon^X E \tag{4}$$

$$S = s^E X + dE \tag{5}$$

where D is the dielectric displacement or the generated charge density, S is the mechanical strain, X is mechanical stress, ε^X is the permittivity measured at constant stress, s^E is the elastic compliance, E is the electric field [39]. The piezoelectric coefficient, d, is a third rank tensor that quantifies the direct and indirect effects as the dielectric displacement generated per unit stress (C/N), and the strain induced per unit voltage (m/V), respectively [40]. It is thermodynamically equivalent in the direct and indirect effects, where $d_{direct} = d_{indirect}$ [40].

Different piezoelectric coefficients can be obtained depending on the applied field direction compared to the direction of the polar axis. As such, the tensor nature of d can be considered with respect to an orthogonal coordinate system using a reduced tensor notation, as d_{xy}, where x denotes the direction of applied field or generated electric displacement, and y the direction of generated strain or applied stress. Values of 1, 2, or 3

describe the orthogonal axes, while values of 4, 5, or 6 indicate the respective perpendicular planes (Figure 2.3).

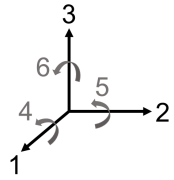

Figure 2.3: Reference axes for poling piezoceramics.

The direct piezoelectric coefficient can be expressed as a matrix as follows [40]:

$$\begin{bmatrix} d_{11} & d_{12} & d_{13} & d_{14} & d_{15} & d_{16} \\ d_{21} & d_{22} & d_{23} & d_{24} & d_{25} & d_{26} \\ d_{31} & d_{32} & d_{33} & d_{34} & d_{35} & d_{36} \end{bmatrix} \quad (6)$$

Of these, the longitudinal piezoelectric coefficient, d_{33}, is the most commonly reported coefficient [40]. It is defined as the piezoelectric coefficient when the applied electric field and generated strain are parallel to the direction of polarisation.

2.1.3. Pyroelectricity

Pyroelectricity is a property exhibited by some piezoelectrics. In these materials, a spontaneous electric polarisation arises below a certain critical temperature known as the Curie temperature, T_c. Above this temperature, materials display paraelectric behaviour due to the absence of dipoles and the dielectric coefficient obeys the Curie-Weiss Law, expressed as [37], [40]:

$$\varepsilon_r - 1 = \frac{C}{T - T_c} \quad (7)$$

where ε_r is the dielectric coefficient, C is a material-specific Curie constant, T is the absolute temperature (K), and T_c is the Curie temperature (K).

Of the already mentioned non-centrosymmetric crystal classes that display the piezoelectric effect, ten of these have a unique polar axis and show a temperature dependence of the electric polarisation, exhibiting the pyroelectric effect [40].

2.1.4. Ferroelectricity

Ferroelectric materials are a sub-set of pyroelectrics that display a spontaneous polarisation below the T_c that can be switched by the application of an electric field [39].

The spontaneous polarisation can originate from different mechanisms [21]. The first is displacive ferroelectricity, where the ferroelectric behaviour emerges from electron-lattice coupling between empty transition metal *d*-states and O 2*p*-states [21]. This is commonly seen in d^0 transition metal perovskite materials such as $BaTiO_3$, where the effect occurs from interactions between Ti 3*d*-states and O [40]. In the lone-pair mechanism, the free valence electrons are anisotropically distributed around a host ion creating a local dipole, e.g. $BiFeO_3$ [21]. Through geometric ferroelectricity, entire sublattices can shift with respect to each other and cause ionic shifts. The effect is in response to steric effects or packing optimisation of different-sized atoms and is observed in hexagonal manganites [21]. Charge ordering is another mechanism through which ferroelectricity can be exhibited, where valence electrons are non-uniformly distributed about a host ion in a crystal lattice forming a periodic superlattice. This effect is seen in materials like $LuFe_2O_4$ [21]. Finally, spin-driven ferroelectricity is induced by breaking inversion symmetry by magnetic order [21].

2.1.4.1. The Perovskite Structure

Many ferroelectric materials crystallise in the perovskite crystal structure, signified by the general chemical formula ABO_3 (Figure 2.4). With consideration to the ideal cubic structure, the large cations (A) are located at the corner sites with 12-fold coordination, the small cations (B) are located at the body-centre with 6-fold coordination, and the face-centred anions (O) form octahedra surrounding the small cations (B).

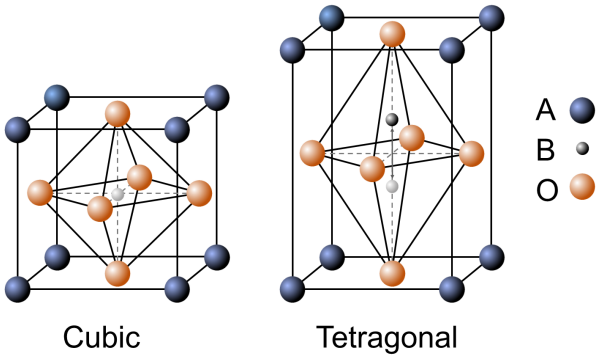

Figure 2.4: Unit cell schematic for the cubic and tetragonal perovskite structures. Adapted from [40]*, with the permission of Taylor & Francis, Copyright © Reports on Progress in Physics 1998.*

Upon cooling from the T_c, a perovskite undergoes successive phase transitions from the paraelectric cubic ($Pm\bar{3}m$) structure into ferroelectric non-centrosymmetric structures [40]. Each of the ferroelectric structures display small distortions from the cubic symmetry. Taking barium titanate ceramics as an example, where the A-site cations are Ba^{2+} and B-site cations are Ti^{4+}, the structure first transitions from a paraelectric cubic structure into a ferroelectric tetragonal ($P4mm$) phase upon cooling through the T_c (T_{T-C} ≈ 120 °C), followed by the orthorhombic ($Amm2$) (T_{O-T} ≈ 5 °C), and rhombohedral ($R3m$) structures (T_{R-O} ≈ -90 °C) [41]. The ferroelectric structures involve a change of the cubic structure, such that there is an elongation along an edge [001] in the tetragonal structure, along a face diagonal [110] for the orthorhombic phase, and along a body diagonal [111] in the rhombohedral phase. These distortions create a net displacement of the B-site cations with respect to the oxygen octahedra, giving rise to a dipole and a spontaneous polarisation in the ferroelectric phases [42], [43]. In addition, the displacement of the B-site cations is directed in specific equivalent polarisation directions dictated by the structure. For instance, the tetragonal, orthorhombic, and rhombohedral structures have six <100>, twelve <110>, and eight <111> polarisation directions, respectively. These are visualised in Figure 2.5.

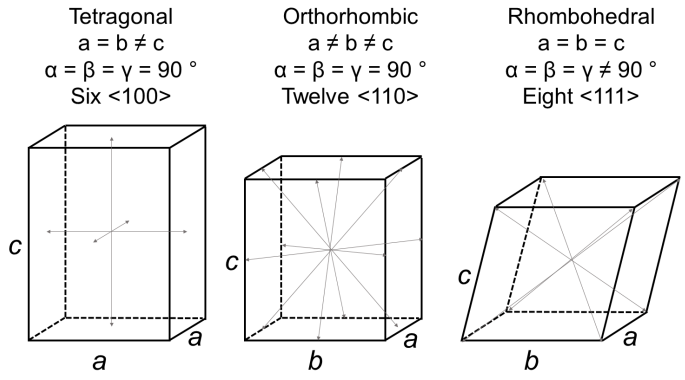

Figure 2.5: The tetragonal, orthorhombic, and rhombohedral crystal structures. The letters a,b,c and α,β,γ denote the length of each edge and the size of the internal angles, respectively. The grey lines indicate the polarisation directions. Adapted from [44]*, with the permission of Taylor & Francis, Copyright © Philosophical Magazine B 2001.*

2.1.4.2. Domain Structures

A ferroelectric ceramic contains homogeneous regions of electric dipoles that have the same spontaneous polarisation orientation [40]. These regions are defined as domains and

are separated from neighbouring domains of differing polarisation orientation by domain walls. Domains form to reduce the electric and elastic energy of a system, particularly as a material transitions to lower symmetry ferroelectric phases upon cooling from the T_c [40]. Certain types of domain walls are possible based on the crystal structure and its spontaneous polarisation directions. For instance, in the cubic ($Pm\bar{3}m$) structure, no spontaneous polarisation exists and therefore it does not contain domains. In the tetragonal ($P4mm$) structure, there are 6 <100> equivalent crystallographic directions in which the spontaneous polarisation can point, and two possible domain walls: 90° and 180° (Figure 2.6). For orthorhombic ($Amm2$) structures, there are four domain wall types: 60°, 90°, 120°, and 180°, and for the rhombohedral ($R3m$) system, there are three domain wall orientations: 71°, 109°, and 180° [40]. The piezoelectric and dielectric response of ferroelectric materials is affected by intrinsic and extrinsic contributions [40], [45]. Intrinsic contributions are associated with lattice properties, or the atomic displacements within individual unit cells, while extrinsic contributions arise mainly from domain wall movement driven by the application of an external electric field or mechanical stress of sufficient magnitude [40], [46].

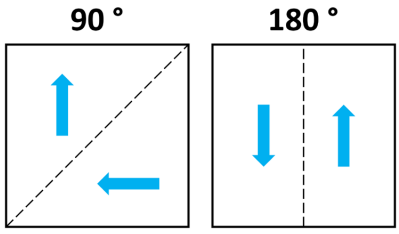

Figure 2.6: Schematic of domain walls (---) separating regions in which the polarisation orientation is perpendicular (90°) and anti-parallel (180°).

Considerable internal stresses induced on a polycrystalline ceramic material by the application of mechanical stress or an electric field (force) can be relieved by a mechanism known as domain twinning, which is the formation of specific domain structures depending on grain size. In the case of a tetragonal, unconstrained cube-shaped grain, the application of a force will cause the grain to deform as shown in Figure 2.7 (a). If the cube-shaped grain is instead clamped by surrounding grains as in a polycrystalline material, the application of a force will cause homogenous shear stresses to form within the grain, as well as longitudinal stresses at the grain boundaries that maintain the cubic

structure. At a critical grain size, g_{crit1}, dependent on the domain size ($d \approx g^{0.5}$), the stress energy acting on the system can be considerably lowered via 90° domain twinning. The homogeneous stresses within the system are replaced by inhomogeneous stresses (labelled T) at the grain boundaries that keep the grain cube-shaped (Figure 2.7 (b)). To remove the inhomogeneous stresses at the grain boundaries, grains that are larger than g_{crit2} will form banded domain structures, as shown in Figure 2.7 (c). In this form, the stress energy is relieved in three-dimensions. In barium titanate, the critical grain size, g_{crit2}, below which the simple lamellar structure can be observed is ≈ 10 µm, as shown in Figure 2.7 (b) [47].

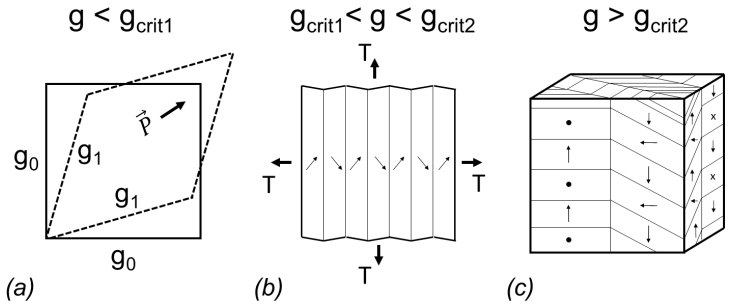

Figure 2.7: (a) The deformation of a free cube-shaped grain, (b) domain twinning in a clamped grain, and (c) the banded domain structure in three-dimensions. 'g' describes the grain size. Adapted from [47]*, with the permission of Springer Nature, Kluwer Academic Publishers, Copyright © Journal of Materials Science 1990.*

2.1.4.3. Domain Polarisation and Switching

When cooled through the T_c, a ferroelectric material will develop a spontaneous polarisation due to the formation of dipoles. However, the dipoles are spatially oriented in a random fashion and therefore cancel out the macroscopic piezoelectric response. When an electric field (or mechanical stress) of sufficient magnitude is applied, the dipoles become aligned into domains that can enlarge or rotate in the direction of the applied field such that a macroscopic piezoelectric response can be measured [48]. This process is known as poling. A visual representation of the polarisation process is given in Figure 2.8, with reference to both the polarisation- and strain-electric field (P-E and S-E) hysteresis loops.

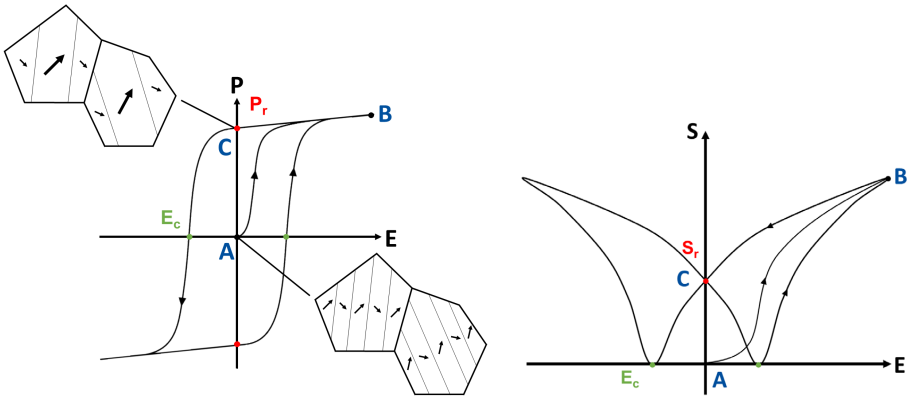

Figure 2.8: Ideal polarisation- and strain-electric field (P-E and S-E) hysteresis loops of a ferroelectric material. Adapted from [48]*, with the permission of John Wiley & Sons, Copyright © The American Ceramic Society 2013.*

At point A ($E = 0, P = 0, S = 0$), a ferroelectric material is unpoled and the domains are randomly oriented causing a net zero polarisation, and no strain effect. Upon application of an electric field, domain walls move about their equilibrium positions, giving a linear increase in the polarisation as the field is not strong enough to cause domain switching. At the coercive field, E_c, an abrupt non-linear increase in the polarisation and strain is observed as the domains orient themselves in the direction of the applied field. The coercive field indicates whether a piezoelectric material is soft or hard. In simple terms, soft materials are characterised by large electromechanical coefficients, a large hysteresis and nonlinearity, low T_c, and are easier to polarise such that a low applied field is required to initiate domain reorientation [49]. Hard piezoelectrics display the opposite. Approaching point B, the number of remaining non-oriented domains decreases. At point B ($E > 0, P = P_s, S = S_s$), saturation polarisation and strain states are reached. Domain switching processes are complete and the domains are aligned. Further application of field causes the unit cells to elongate. As the electric field is reduced, some domains move out of alignment (back-switch), but the material does not return to its original state. Upon complete removal of the electric field, the material maintains a remanent alignment of the domains at point C ($E = 0, P = P_r, S = S_r$), such that a remanent polarisation and strain are maintained. When the electric field is applied in the negative direction, the polarisation is zero and the strain reaches a minimum value near the E_c. Upon further application of an electric field, the domains are reoriented and cause the material to develop a polarity in the reverse direction and exhibit a strain response.

Relative permittivity-electric field (ε-E) hysteresis loops can be used to characterise the domain switching processes and subsequently, the crystallographic phase of a material [50], [51]. Polarisation switching of 180° and non-180° domains require the application of different coercive fields that appear as distinct peaks in the ε-E loop. Figure 2.9 displays a sketch of a typical ε-E loop of a tetragonal material having 180° and 90° domains. Two maxima (B & C) are observed under increasing positive field and the same features are observed with the application of negative fields (E & F). Peaks B and E correspond mostly to 180° domain switching, while peaks C and F are related to 90° switching [50]. As an electric field is applied from point A to D, the material experiences a reversal in the 180° domains at point B, which in turn reduces the internal electric field allowing the first rotation of 90° domains. At point C, the next 90° domain rotation occurs, but is not in conjunction with a 180° domain reversal and hence, the observed peak is lower in value. Similar peaks at point E and F are observed with the application of the reverse electric field from point D to A. For materials with a higher number of domain types, the shape of the ε-E loop appears to have only distinct but broad 180° peaks. This is because the internal field of the ordered domains facilitates the rotation of other domains. For instance, a rhombohedral material has three domain types. Initially, the 180° domains switch upon application of an electric field and reduce the internal electric field, enabling the rotation of 109° domains, and subsequently 71° domains. Hence, the switching processes appear to occur at lower and more similar coercive fields with less distinct differences in the relative permittivity.

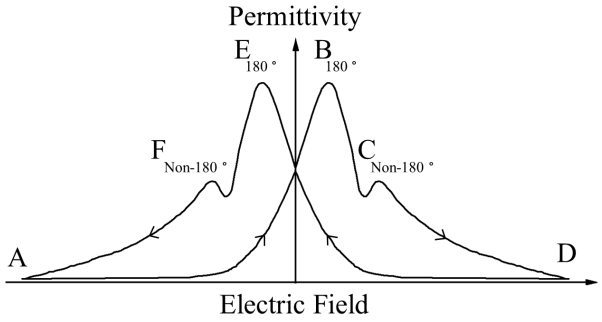

Figure 2.9: Sketch of permittivity maxima. The contributions from 180° and non-180° domain switching are indicated at points B, C, E, and F. Adapted from [50]*, with the permission of AIP Publishing, Copyright © Journal of Applied Physics 1974.*

2.1.4.4. Variations in the Piezoelectric and Dielectric Properties

Ideally, the polarisation, strain, relative permittivity and piezoelectric coefficient hysteresis loops are symmetric. However, factors such as the presence of charged defects (e.g. oxygen vacancies, defect dipoles) and grain size can affect the shape and symmetric nature of the loops of real ceramics [40]. Internal bias fields can be formed in oxide ferroelectrics as a result of defect dipoles that originate from acceptor or donor doping, impurities during synthesis, or oxygen vacancy formation during ageing. The internal bias fields can pin domain wall motion and restrict domain switching during polarisation, resulting in poor domain alignment [48], [52]. The effect is obvious for materials that are sensitive to applied fields, i.e. soft piezoelectric materials. Coarse- and fine-grained piezoelectric ceramics exhibit different behaviours upon electric field application. Stresses induced from neighbouring grains constrain grain shape such that a clamping effect occurs under an applied electric field, inhibiting domain switching. The effect is more pronounced for fine- than coarse-grained ceramics, and is observable in polarisation hysteresis loops (Figure 2.10) [53]. Domain switching is relatively unrestricted in coarse-grained ceramics, allowing polarisation reversal to occur within a narrow electric field range, unlike in fine-grained ceramics (sloped hysteresis) [47], [48], [54], [55].

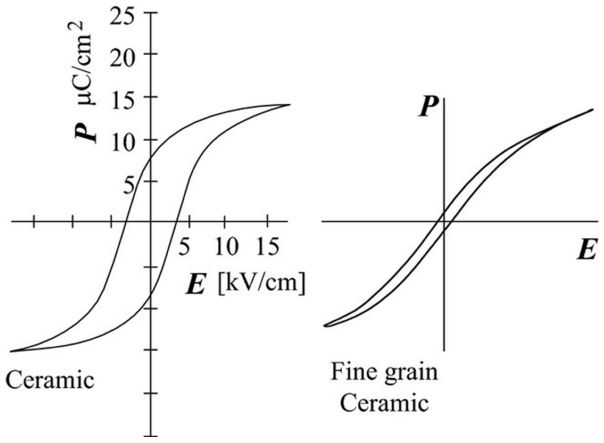

Figure 2.10: Grain size effect on domain switching and the polarisation hysteresis loop for ferroelectric materials. Reprinted from [48]*, with the permission of John Wiley & Sons, Copyright © The American Ceramic Society 2013.*

Grain size also influences dielectric behaviour. For example, maximum relative permittivity is observed for barium titanate ceramics with an average grain size of ≈ 1 μm

(Figure 2.11) [47], [53]. This is attributed to 90° domain wall mobility, and more significantly, the number of domain walls per volume (domain wall density). Below grain sizes of 1 µm, clamping effects from surrounding grains, lower domain densities, and distortion of the unit cell into a more paraelectric cubic structure cause the reduction of the measured permittivity [47], [56], [57]. The effect of grain size on the piezoelectric coefficient of barium titanate is debated. Maximal values are reported for average grain sizes ≈ 1 and ≈ 10 µm, attributed to domain size for the former [58], [59] and on enhanced domain alignment and reduced clamping effects for the latter grain size [55], [60].

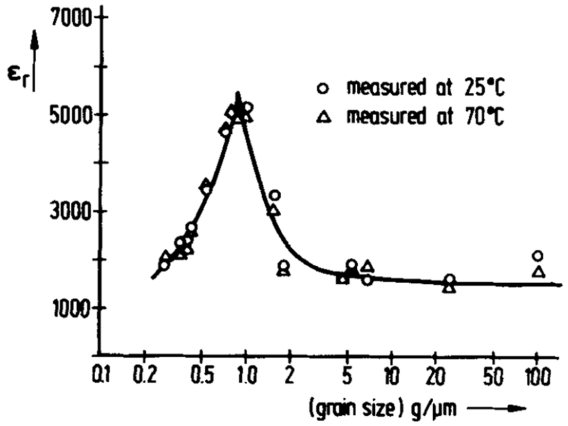

Figure 2.11: Relative permittivity dependence on grain size in barium titanate ceramics Reprinted from [47]*, with the permission of Springer Nature, Kluwer Academic Publishers, Copyright © Journal of Materials Science 1990.*

2.2. Piezoelectric Ceramics

Piezoelectric ceramics are used in a variety of applications, such as transducers, sensors, and actuators. Currently, the most widely used piezoelectric ceramic is lead zirconate titanate owing to its exceptional piezoelectric properties. However, concerns regarding the environmental impacts and health hazards of lead have culminated in the implementation of governmental directives such as the Restriction of Hazardous Substances (RoHS) and Waste Electrical and Electronic Equipment (WEE). These directives aim to limit the use of lead-based materials in electronics, and to subsequently drive the development of lead-free alternatives [61]–[63]. Today, the most competitive lead-free options that have been implemented into the electronics industry are based on the barium titanate system. However, these have yet to be utilised in the field of

biomedical engineering despite growing interest for the development of an electrically stimulative material to encourage cell growth. This section presents an introduction to lead zirconate titanate, and two lead-free alternatives: barium titanate, and Ca- and Zr-doped barium titanate.

2.2.1. Lead Zirconate Titanate (PZT)

Lead zirconate titanate ($Pb(Zr_xTi_{1-x})O_3$) piezoelectric ceramics exhibit a perovskite structure with Pb at the A-site, and Zr and Ti at the B-site. The system demonstrates an exceptional piezoelectric response at the morphotropic phase boundary (MPB) that is attributed to enhanced domain reorientation during poling due to the coexistence of ferroelectric tetragonal and rhombohedral phases (Figure 2.12). In addition, the MPB is nearly independent of temperature (morphotropic), such that the phase is relatively unaffected by changes in temperature [26]. At room temperature, the MPB composition occurs where the Ti to Zr ratio is 0.48:0.52.

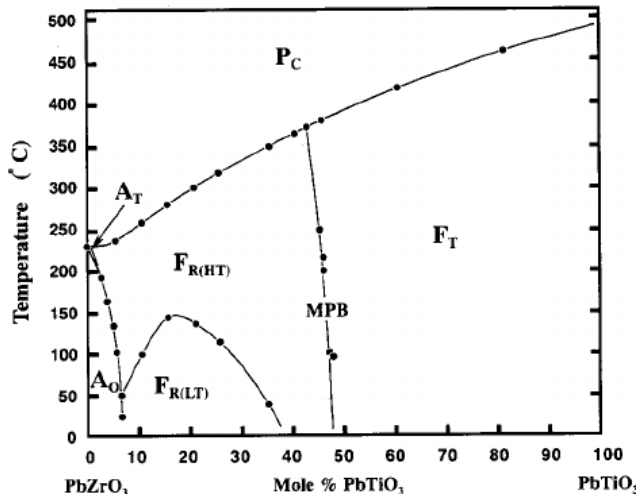

Figure 2.12: The phase diagram of lead zirconate titanate (PZT). Reprinted from [64]*, with the permission of Elsevier, Copyright © 1971.*

Compositional engineering can be used to alter the piezoelectric properties for specific applications. PZT can be doped with isovalent, donor, or acceptor dopants [65]. Isovalent dopants are either divalent or tetravalent cations that substitute onto the A- and B-sites of equal valency, respectively. Donor doping involves the substitution of cations with cations of a higher valency, and acceptor doping is the substitution of cations with a lower

valency. In PZT, donor doping forms soft piezoelectrics with high relative permittivities and piezoelectric coefficients that tend to be used for actuating applications, where the maximum piezoelectric displacement at a given voltage is of interest. Acceptor doping creates hard piezoelectrics that have lower relative permittivities, higher coercive fields, and better stability against high voltage due to the formation of oxygen vacancies that migrate to and pin domain walls [66].

2.2.2. Barium Titanate (BT)

Barium titanate ($BaTiO_3$) was discovered in the 1940s and is considered as the archetypal ferroelectric ceramic having a perovskite crystal structure. It has been widely studied since its discovery and is typically used for its high dielectric properties [39]. However, its low piezoelectric coefficient ($d_{33} \approx 190$ pC/N) in its room temperature-stable tetragonal phase, combined with its low Curie temperature ($T_c \approx 115$ °C) limit its use [67], [68].

2.2.3. Barium Calcium Zirconium Titanate (BCZT)

One derivative of BT-based ceramics is barium calcium zirconium titanate, a solid solution of barium zirconium titanate (BZT) and barium calcium titanate (BCT), with a perovskite crystal structure, where Ca^{2+} and Zr^{4+} are doped on the A- and B-sites, respectively. The system is represented as $(Ba_{100-x}Ca_x)(Zr_yTi_{100-y})O_3$ and hereafter denoted by the simplified notation BC_xZ_yT. It was first discovered in 1954 by McQuarrie and Behnke and was primarily studied for its exceptional dielectric properties and ferroelectric relaxor behaviour [69]. It was not until 2009 that this material system attracted considerable interest due to the reports by Liu and Ren of its high piezoelectric coefficient ($d_{33} \approx 620$ pC/N) [27], [69]. Given its good piezoelectric response, it is considered as one of the most promising lead-free alternatives for low temperature applications ($T_c \approx 60$–100 °C) (Figure 2.13) [26], [62].

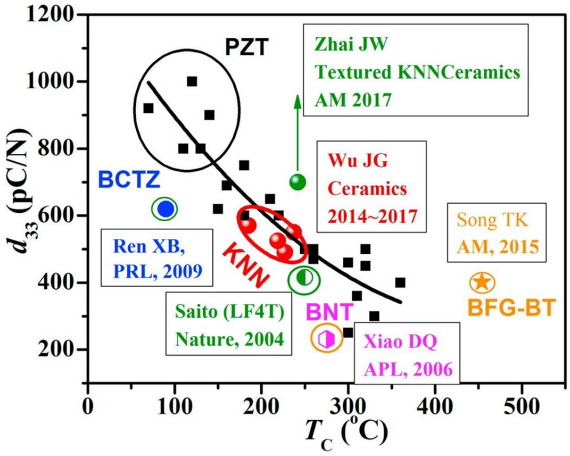

Figure 2.13: A comparison of the reported piezoelectric coefficients for PZT and lead-free piezoelectric ceramics. Reprinted from [26]*, with the permission of Elsevier, Copyright © Elsevier Ltd. 2018.*

The phase diagram of the BCZT system was first proposed in the 1950s and although it has undergone successive revisions, it remains controversial particularly with respect to the MPB region. Here, the most significant features of the phase diagram proposed within the last 10 years are described.

The diagram proposed by Liu and Ren describes a solid solution of BZT and BCT with a tilted MPB separating rhombohedral and tetragonal phases (Figure 2.14). Unlike PZT, a single chemical composition is significantly affected by changes in temperature such that it can display different crystal structures upon increasing temperature. Therefore, it is more correct to notate the delineation of the ferroelectric phases as a polymorphic phase transition (PPT). However, the region is often referred to as an MPB in literature and will hereafter be denoted in the same manner in this work. The exceptional piezoelectric response of the MPB composition is attributed to its proximity to the tricritical point (TCP) between the paraelectric cubic (C) phase and ferroelectric rhombohedral (R) and tetragonal (T) phases, where polarisation anisotropy almost vanishes enabling polarisation rotation between the T and R states [27].

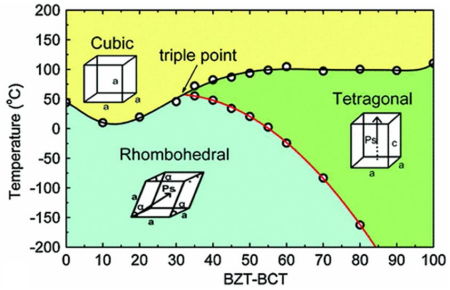

Figure 2.14: The BZT-BCT phase diagram proposed by Liu and Ren. Reprinted from [27]*, with the permission of the American Physical Society, Copyright © 2009.*

More recent work on the BCZT system, however, proposes that there is a bridging orthorhombic (O) phase between the rhombohedral and tetragonal phases (Figure 2.15) [70], [71]. In a model proposed by Keeble et al. based on high-resolution powder diffraction experiments and dielectric data, a phase sequence identical to the BT parent system is described: C-T-O-R (upon cooling) [71]. In contrast to Liu and Ren, Keeble et al. relate the high piezoelectric properties to a phase convergence region rather than proximity to a TCP, based on the observation of dielectric anomalies in this area. In this region, structural instabilities increase the degrees of freedom in the system and reduce the free energy landscape to facilitate polarisation [71].

Other reports contest the existence of the orthorhombic phase. These instead describe a diffuse phase transition region with coexisting nanodomains of tetragonal and rhombohedral phases [72], [73].

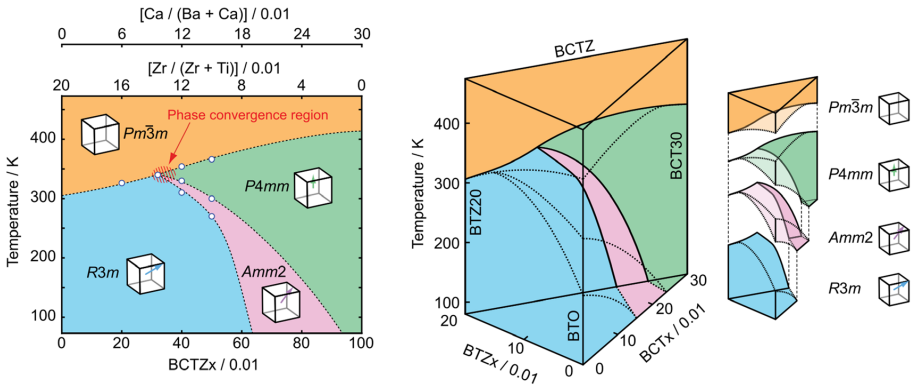

Figure 2.15: The BCZT phase diagram proposed by Keeble et al. Reprinted from [71]*, with the permission of AIP Publishing, Copyright © American Institute of Physics 2013.*

2.3. Bone Implant Materials

In this section, an overview of the anatomy, remodelling process, and electromechanical behaviour of bone are presented. Additionally, an overview of common materials used for the repair and regeneration of hard tissues such as bone is provided, as an introduction to the development of electroactive implant materials.

2.3.1. Bone Anatomy

The adult human skeleton consists of 206 bones in the form of long, short, flat, and irregular shapes. Bones serve several functions including structural support, locomotion, protection of internal organs, maintenance of mineral homeostasis (particularly calcium and phosphate), sensing and secretion of hormones, and haematopoiesis [11].

Chemically, bone is a composite tissue consisting of inorganic and organic components. The inorganic phase of carbonated apatite (hydroxyapatite) is exceptionally hard and resistant to compression, whilst the organic phase is composed mostly of proteoglycans, glycoproteins and collagen fibres, the latter of which contributes to the elasticity and toughness of bone [11], [74].

The anatomical structure of bone is complex and hierarchical, as visualised in Figure 2.16. Macroscopically, it consists mainly of dense cortical (compact) bone that provides protection, support, strength, and resistance to bending and torsion. A smaller fraction is composed of trabecular (spongy) bone, which has a porous, open lattice structure facilitating weight reduction, load transfer, and the protection of bone marrow. Microscopically, cortical tissue consists of a set of repeating structural units of osteons, or tubes of lamellae surrounding canals of nerves and blood vessels. On the nanoscale, both the cortical tissue and the trabecular struts comprise of collagen fibres that are infiltrated and surrounded by inorganic minerals [11].

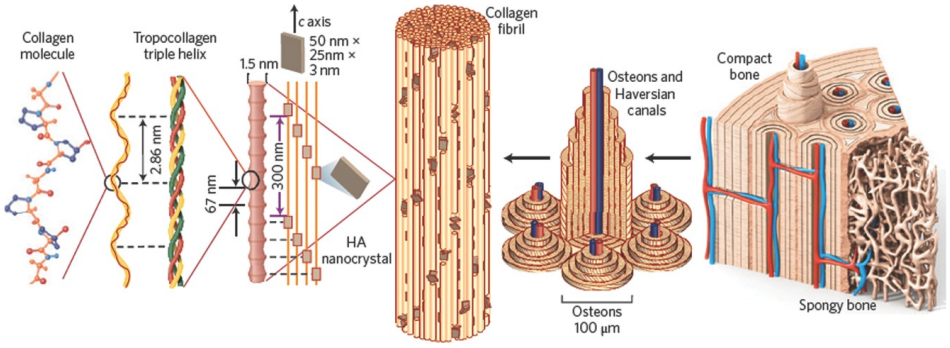

Figure 2.16: Schematic of the hierarchical organisation of bone from the macro- to nanoscale. Reprinted from [75]*, with the permission of Springer Nature, Copyright © 2014.*

2.3.2. Remodelling and Healing of Bone

2.3.2.1. Bone Remodelling

Bone is a metabolically active tissue that undergoes a continuous process of remodelling, or the removal (resorption) and deposition of bone, to maintain the integrity of the tissue. The bone mineral matrix is populated by four types of bone cells including bone lining cells, osteoblasts, osteocytes, and osteoclasts that each have specific roles in the remodelling process [11]. Osteoblasts are responsible for the deposition of bone, osteocytes (mature osteoblasts) maintain the bone matrix, and osteoclasts resorb bone tissue. Additionally, osteocytes act as the primary mechanosensors in bone and detect perturbations in the bone fluid or cell membrane from tissue deformations [76].

The remodelling cycle involves three main phases: resorption, reversal, and formation [74]. In the initial phase lasting approximately 2 weeks, mineralised bone matrix is resorbed by osteoclasts. The reversal phase follows and involves the appearance of mononuclear cells on the bone surface to signal osteoblast differentiation and migration. The duration of this phase is 4–5 weeks. During the final formation phase (up to 4 weeks), osteoblasts deposit new bone until all the old tissue is replaced. Generally, the rates of bone deposition and resorption are equal, however, remodelling is not uniform over the entire skeleton.

In bone tissue, the application of mechanical stimuli affects the bone remodelling process, such that optimal bone structures develop on the local and systemic scales to withstand

the applied stresses and strains [77]. This relationship is categorised under the broader term of mechanotransduction, the mechanism by which specific cellular responses are induced by the conversion of mechanical stimuli into electrical or chemical activity. The behaviour is described by Wolff's Law: "every change in the form and function of bone … is followed by certain definite changes in their internal architecture, and … in their external conformation, in accordance with mathematical laws" [78].

The influence of mechanical loading on bone is further defined by Frost's Mechanostat Theory. It suggests that bone formation and resorption are influenced by local mechanical deformations of the tissue and furthermore, that bone acts as feedback loop, such that it will remodel and gain mass at higher applied mechanical loads [78]. The Theory is visualised in Figure 2.17 and the effect is observed for instance by the increase in bone size of the serving arm of a tennis player, or the overall loss in bone mass of an astronaut as a result of zero gravity.

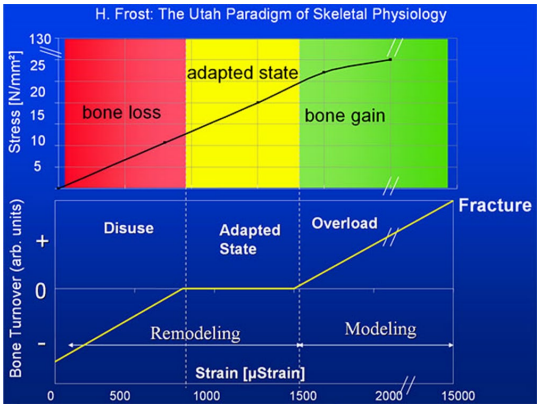

Figure 2.17: Mechanostat theory of modelling and remodelling thresholds [78].

2.3.2.2. Fracture Healing

Bone fracture healing involves the restoration of mechanical stability of an affected area through the replacement of fragile provisional tissues with more stable tissues until vascular ingrowth and mineralisation occur. It can occur via two bone formation (ossification) pathways: indirect endochondral or direct intramembranous. The former involves the formation of an intermediate cartilage, while the latter involves ossification on the surfaces of existing bone [79]. Fracture healing generally proceeds via three

primary steps: inflammation, callus formation, and remodelling [80]. Initially, a haematoma forms on the injury site, which is closely followed by acute inflammation caused by the infiltration of neutrophils and macrophages that remove necrotic tissue. After several days, a soft fibrocartilaginous callus of fibrotic tissues and cartilage develops to span and stabilise the fracture area. Finally, woven bone encases the callus, enhancing the mechanical stability of the area. The healing process is completed by remodelling of the healed fracture site.

2.3.2.3. Healing Around Implanted Materials

The bone is well-adept at repairing itself, however, intervention with biotherapies such as implantable supports and scaffolds may be required to repair large defects that do not heal spontaneously. In these cases, healing proceeds via a foreign body reaction (FBR) and osseointegration (bone in-growth) (Figure 2.18) [80]. The FBR involves the adsorption of proteins onto the surface of the implant to initialise a biological interaction between the implant and surrounding bone tissue, where cells such as macrophages, osteoclasts and osteoblasts are recruited. During the osseointegration stage, the mechanical stability of the affected area is increased by the integration of bone tissue around and into the implant. Once the implant is integrated, it should remain stable within the body. However, if micromotions occur or if the implant releases corrosion products, osteolysis (cell death) around the implanted material can occur and destabilise the implant [80].

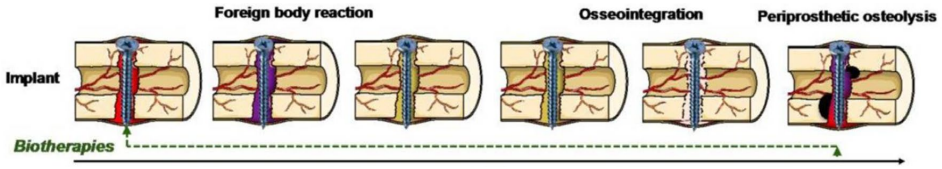

Figure 2.18: The process of healing after implantation of a bioregenerative therapy. Reprinted from [80]*, with the permission of Elsevier, Copyright © 2016.*

2.3.3. 'Piezoelectricity' in Bone

The formation of electric charges under the application of a mechanical load has been observed in a variety of biological tissues, first in the 1940s in a bundle of wool wrapped in shellac, and later in dry and wet bone in the 1950s [13]. The 'piezoelectric effect' is

somewhat loosely applied to bone, given that it does not have the prototypical crystallographic structure of oxide ferroelectric materials. Nevertheless, the term exists due to the generation of surface charge potentials (up to 0.7 pC/N) under an applied load that is reminiscent of the behaviour of piezoelectric materials [14]. The origin is highly debated and attributed for example to endogenous fields, streaming potentials, the helical structure and inherent polarisation of collagen fibrils (Figure 2.19), or the piezoelectricity of hydroxyapatite crystals [25], [81].

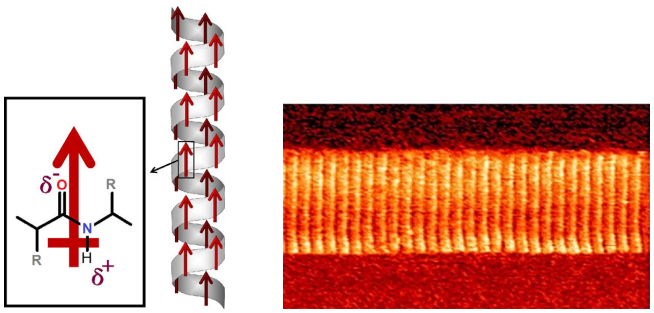

(a) *(b)*

Figure 2.19: (a) Schematic illustration of a helical structure, and (b) topography of a single collagen fibril imaged by atomic force microscopy. Both are theorised as contributors to the 'piezoelectric effect' in bone. Reprinted from [81]*, with the permission of Elsevier, Copyright © Acta Materialia Inc. 2015.*

2.3.4. Biomaterials for Hard Tissue Repair

Bone has a high regenerative capacity with the ability to heal itself without scar formation. However, in cases of critical trauma, disease, or poor loading situations, bone regenerative therapies are required to support healing. This involves the surgical modification of an affected tissue area and the implantation of a support or scaffold to aid healing. The implanted components are biomaterials: "any substance… that can be used as a system or part of a system that treats, augments, or replaces any tissue, organ, or function of the body" [82]. The pursuit of the ideal biomaterial for bone repair has an extensive history dating to 2000 BC, as revealed by archaeological discoveries in Peru, Armenia, and Egypt of gold and animal bone for the repair of skull defects, and iron knee joint prostheses [11]. Since then, significant advances in the development of biomaterials have been aided by improved understanding of bone regeneration and material-host tissue interactions. In particular, focus has shifted towards the development of biocompatible

biomaterials that “perform with an appropriate host response in a specific application” within acceptable levels of toxicity, sensitisation, irritation and reactivity [82].

The physicality of today’s ageing population, combined with the need to design implantable components with extended functional lifetimes and stabilities within the physiological environment, have driven the progress of novel bone repair biomaterials. The clinical gold standard for bone repair are autologous bone grafts (tissue grafts derived from a donor site from a patient) [83]. These are most effective at interacting with the host tissue as they encourage ossification (osteogenesis), provide a scaffold for the attachment and ingrowth of cells (osteoconduction), and provide a material surface that locally promotes the proliferation and differentiation of stem cells into bone cells (osteoinduction). However, there are several disadvantages associated with autologous bone grafts, including donor site morbidity, the requirement of an additional surgery to procure the bone tissue graft, and limited bone tissue supply from the patient. Alternatives include allografts (tissue grafts derived from another patient) or xenografts (tissue grafts derived from another species). However, these pose the risk of bacterial and viral infection transmission. Furthermore, treating allo- and xenografts to remove antigenicity and viable cells also eliminates their ability to interact with the host tissue in a similar manner as autografts.

The alternative to biological biomaterials is synthetic biomaterials. Depending on the application, these can be polymers, glasses, metals, and ceramics, or any composite of these components. The design of synthetic bone repair implants has evolved over four distinct functional generations [3], [84]. First generation biomaterials are inert, such that they “achieve a suitable combination of physical properties to match those of the replaced tissue with a minimal toxic response in the host” [84]. They generally have very high purity to eliminate the risk of releasing toxic by-products, for example gold, ivory, stainless steel, and Ti-alloys. However, the inert nature of these biomaterials can be detrimental to their stability and lifetime in the physiological environment, as they tend to be encapsulated within a fibrous capsule of scar tissue. Second generation biomaterials are designed to be resorbable, such that there is a controlled chemical breakdown of the biomaterial until it is ultimately replaced by regenerating tissue. Examples include bioactive glasses, hydroxyapatite (HA) thick films, and resorbable supports. Third generation biomaterials are typically associated with the field of tissue engineering. These

materials are for instance pre-seeded or loaded with growth factors prior to implantation to promote active regeneration of the tissue via the release of biochemical stimuli for improved cell attachment and proliferation. The fourth generation of biomaterials rely on the intrinsic properties of the implanted material to encourage cell interactions, such as the ability to generate electrical stimuli. In the present work, piezoelectric BCZT is investigated as a fourth generation biomaterial, given its ability to generate electric surface charge potentials under a mechanical load similar to the intrinsic property of bone.

The surface properties of biomaterials including roughness, wettability, and porosity significantly influence cell and tissue interactions and are therefore an important factor considered in implant design. Nano- and microstructural scale roughness can guide cell attachment and encourage cell proliferation [7], while enhanced surface wettability improves cell spreading and adhesion [8]. Cell migration, vascularisation, and nutrient supply can be facilitated by porous features (~300 μm), enabling porous biomaterials to be osseointegrated with the host tissue [9].

For the repair of load-bearing joints in the body, such as hip and knee joints, the main prosthesis component is typically formed from metal due to its toughness [3]. However, one of the primary disadvantages of metal joint prostheses is the elastic modulus (E) mismatch between the implanted material (high E) and bone tissue (low E). When a load is applied to the prosthesis, stress is poorly transferred from the implant to the surrounding bone tissue. This is known as stress shielding. It creates a poor loading situation, and leads to the loss of healthy bone tissue around the implant and eventual failure of the bone-implant bond (aseptic loosening) [85]. To alleviate the modulus mismatch between the implant and surrounding bone, materials with similar properties to bone can be selected, or ceramic coatings with more similar moduli to cortical bone can be applied to metal implants (Figure 2.20).

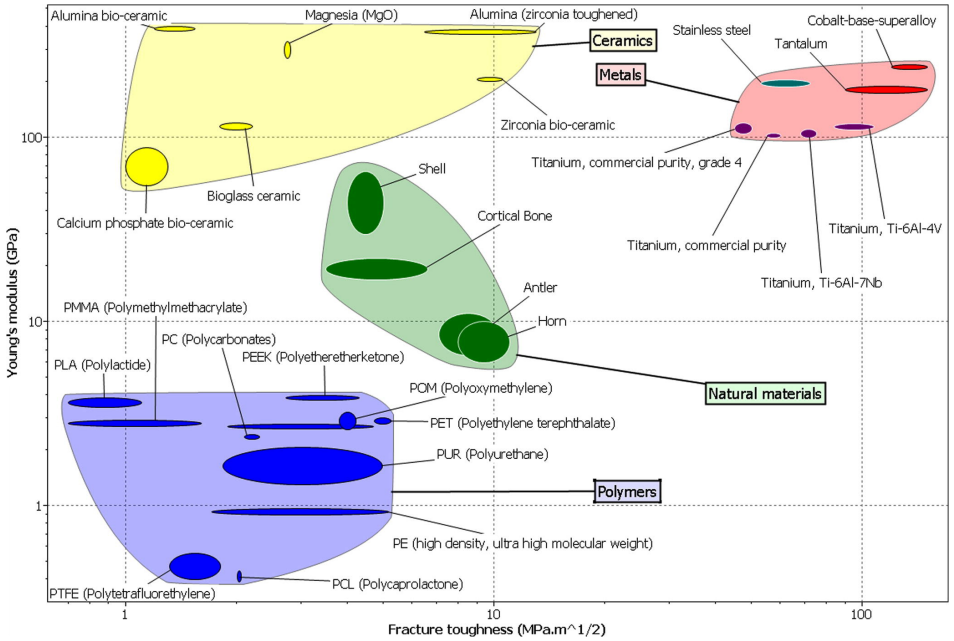

Figure 2.20: Young's modulus and fracture toughness of common implant materials, and organic materials including bone. Reprinted from [2]*, with the permission of Elsevier, Copyright © Acta Materialia Inc. 2010.*

A comparison of the mechanical properties of cortical bone, common metal implant materials (stainless steel 316L and Ti-alloy Ti6Al4V), as well as BT and BCZT piezoelectric ceramics are presented in Table 2.1. In addition, a comparison of their piezoelectric coefficients is provided.

Table 2.1: The Young's modulus, fracture toughness, and piezoelectric coefficients of BT and BCZT ceramics, cortical bone, and common metal implant materials.

Material	E **(GPa)**		K_{IC} **(MPa.m$^{0.5}$)**		d_{33} **(pC/N)**	
BT	70–110	[86]	0.6–0.8	[87]	190	[68]
BCZT	105–263	[88]–[90]	0.67	[89]	280–620	[27]
Cortical bone	20–30	[91]	3–6	[92]	0.7	[93]
Stainless steel	190–205	[94]	112–278	[94]	–	
Ti6Al4V	110–119	[95]	84–107	[95]	–	

2.4. BT-Based Ceramics as Biomaterials

2.4.1. The Effect of Piezoelectric Ceramics on the Body

2.4.1.1. Electrical Stimulation and Piezoelectricity Effect on Cells

Electrical stimulation is currently used as a therapy for non-union fractures via inductive coupling, direct current, and capacitive coupling procedures [18]–[20]. The application of direct current electrical stimulation to an implant site is shown to improve the osseointegration of an implant during initial-stage healing, as well as the interfacial strength and bone formation [96]–[98].

Although the use of electrical stimulation is used in the clinic today, these treatments typically rely on wired devices that make the procedures cumbersome as they restrict a patient's range of motion. In addition, patients are required to attach the external devices to themselves, making the nature of the electrical stimulation application infrequent and dependent on the motivation of the patient. It is therefore of importance to develop new materials and devices that can autonomously generate electric charges in a constant and power source independent fashion.

Since it has been observed that piezoelectricity can be generated within bone, the effect of piezoelectricity on cells has also been explored. *In vitro* cell studies on piezoelectric materials indicate that negatively-charged surfaces enhance the attachment of cells, encouraging cell proliferation and osseoinduction [8], [25].

2.4.1.2. Biocompatibility and Biological Interactions

The potential of piezoelectric BT ceramics for biomedical applications was first explored in the late 1970s to the early 1980s, through the investigation of their behaviour in *in vitro* and *in vivo* environments. Initial assessment of the compressive strength stability after soaking in liquid environments or subcutaneous implantation for up to 28 weeks showed losses of ≈ 50 % [99]. In addition, studies on the effect of polarised and non-polarised BT in the femora of dogs proved inconclusive due to poor loading interactions between the implants and the surrounding bone tissue [100]. From then to the early 2000s, work on BT ceramics for biological applications has been sparse.

BT ceramics as nanoparticles, thin films and composites with hydroxyapatite for biomedical use have been explored in recent years [28]–[30]. However, research into the potential of BCZT ceramics as implant materials has been minimal. To date, only BCZT nanocrystal composites with hydroxyapatite or Bioglass, BCZT thin films, and unpoled BCZT ceramics have been considered for their biocompatibility in initial attempts to characterise the ceramics for the promotion of bone growth [32]–[35]. As such, the application of BCZT ceramics as medical implant materials is a young field of study.

2.4.1.3. Toxicity of Barium

Barium compounds can be toxic to humans depending on their solubility due to the release of Ba^{2+} [101]. Barium compounds that display some degree of solubility in water and are toxic to humans include compounds of chlorides, nitrates, hydroxides and carbonates. Ba^{2+} can interfere with the body's interaction with potassium, causing gastrointestinal issues, hypokalaemia, muscle weakness, and paralysis in chronic amounts. However, insoluble compounds such as barium sulphates are non-toxic and are used as contrast agents for radiographic procedures [101].

2.4.2. The Effect of the Body on Piezoelectric Ceramics

BT-based piezoelectric ceramics tend to be used for electrical applications in ambient conditions. The implementation of these materials in the physiological environment is drastically different to its conventional applications, and therefore, the effect of its interaction with body fluids or simulated fluids, and mechanical loads must be considered.

2.4.2.1. Water Adsorption on Piezoelectric Surfaces

Water adsorption to piezoelectric material surfaces can influence the piezoelectric response, particularly within the top few atomic layers of the structure. Water can adsorb onto BaO- or TiO_2-terminated surfaces of BT thin films, however, due to the tendency of BT materials to release Ba^{2+} in solution, only the TiO_2-terminated structure will be considered here. DFT calculations reveal that bare TiO_2-terminated surfaces are chemically unstable [102]. Increased stability and reduced surface energy can be achieved through water adsorption in either molecular or dissociated (hydroxylated) states, where the former is slightly more stable [102]. However, chemisorption energies favour the

dissociation of adsorbed water. On TiO_2 terminations, water dissociates into H^+ and OH^-, where the H^+ binds to the surface O and OH^- binds to the surface Ti (Figure 2.21).

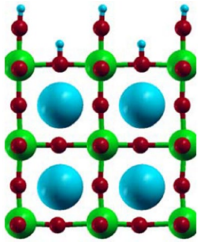

Figure 2.21: Schematic of TiO_2-terminated BT with hydroxylated H_2O adsorbed on the surface. Atom colours: red (O), large blue (Ba), green (Ti), small blue (H). Adapted from [102]*, with the permission of the American Physical Society, Copyright © 2009.*

DFT calculations show that polarisation at the material surface is pinned by the orientation of the attached OH^- groups, but the pinning effect only exists within the first three unit cells of the material. In a comparison of water-treated BT with a hydroxylated surface and a non-treated surface containing oxygen vacancies, non-treated samples showed asymmetric hysteresis behaviour (an imprint effect) due to the presence of oxygen vacancies acting as domain wall pinning centres (Figure 2.22 (a,b)).

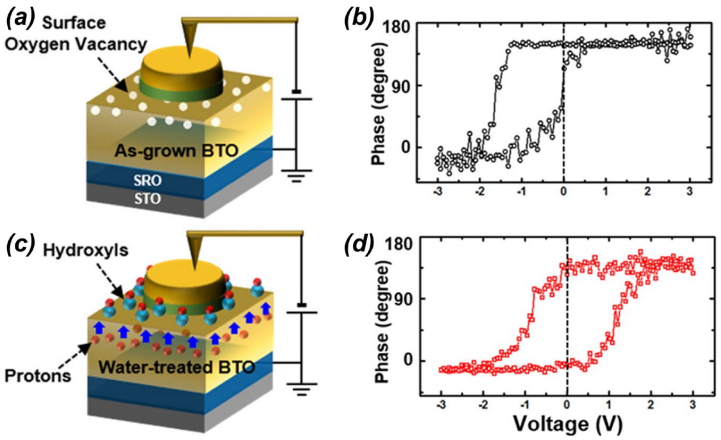

Figure 2.22: Schematic showing a ferroelectric tunnel junction based on a BT thin film. (a) As-grown film containing surface O vacancies (b) displays an imprint effect. (c) Water-treated film with a chemically induced surface polarisation in the top passive layer (d) does not display the imprint effect. Adapted from [103]*, with the permission of the American Chemical Society, Copyright © 2016.*

By treating the sample with water to hydroxylate the surface to induce polarisation pinning via the OH^- groups, the imprint effect could be removed from the bulk piezoelectric response (Figure 2.22 (c,d)) [103]. Although an effect of water adsorption on the piezoelectric response of thin films has been observed, it is unlikely that it influences thick films or bulk samples, since the effect appears to be limited to a few layers at the surface.

2.4.2.2. Mechanical Loading and Depolarisation

Due to the coupling between the electrical and mechanical interactions of a piezoelectric material, applying a mechanical stress beyond a certain threshold stress can cause the material to depolarise. The effect is illustrated in Figure 2.23.

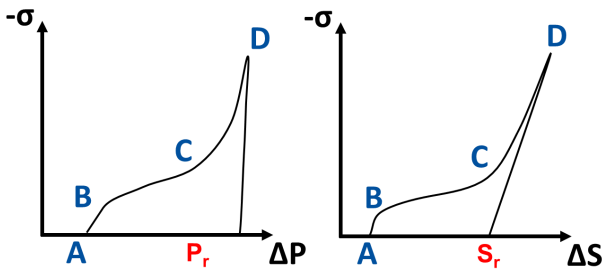

Figure 2.23: The effect of compressive stress, -σ, on a polarised piezoelectric ceramic with respect to changes in polarisation and strain. Adapted from [104]*, with permission of Elsevier, Copyright © Elsevier Ltd. 1996.*

At point A, the ceramic is poled and has a remanent polarisation and strain, and domains are aligned to the poling direction. With the application of small compressive uniaxial stresses to point B, the piezoelectric material exhibits a linear direct piezoelectric effect and no domain switching occurs. Upon applying larger compressive loads close to the coercive stress at point B, ferroelastic switching begins to occur, and mechanical depolarisation begins. At this point, the unit cell is compressed into a cubic-like structure and the *c*-axis is reoriented to a position orthogonal to the applied load. Here, the domains become reoriented out of alignment and a loss in the polarisation is observed. At point C, the domain switching processes are almost complete and the stress-strain behaviour becomes linear elastic until point D. When the compressive stress is completely removed, the piezoelectric ceramic maintains its depolarised state [104].

The mechanical depolarisation resistance of a piezoelectric ceramic is related to the electrical softness. As mentioned in Section 2.2.3, the piezoelectric response of BCZT materials is significantly enhanced for the MPB composition, due to the softness of the material afforded by the high number of polarisation direction variants facilitating domain reorientation [105]. Contrarily, this property adversely affects the mechanical depolarisation resistance because of the low coercive field strength [105]. As shown by Ehmke et al., MPB compositions of BCZT are least resistant to mechanical depolarisation, followed by rhombohedral and tetragonal crystallographic phases (Figure 2.24) [105]. In addition to phase composition, the mechanical depolarisation resistance can be enhanced through domain wall pinning by defect dipoles or internal bias fields.

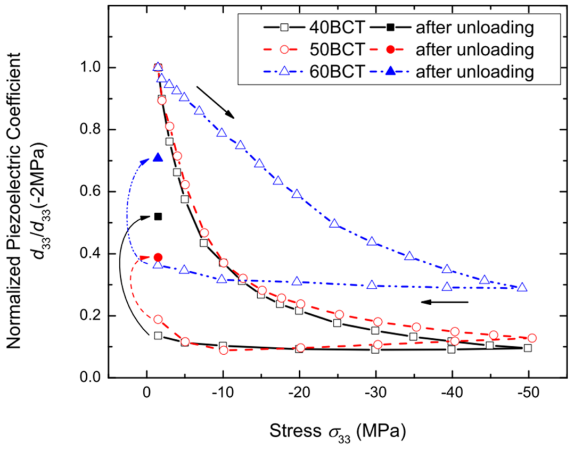

Figure 2.24: Normalised piezoelectric coefficients for tetragonal (blue), rhombohedral (black), and MPB (red) compositions of BCZT during and after mechanical loading. Open symbols: initial mechanical loading cycle. Solid symbols: the d_{33} after complete unloading and reloading to a pre-stress value. Reprinted from [105]*, with the permission of AIP Publishing, Copyright © American Institute of Physics 2012.*

2.4.3. Integration of BCZT Ceramics into the Body

As mentioned in Section 2.3.4, metal implants used in load-bearing applications are typically coated with a ceramic material to alleviate the elastic modulus mismatch between the surrounding bone tissue and the metal. The deposition of BCZT ceramic coatings on metal substrates is a niche field of study, however, thick film electroceramics between sub-micron to 200 µm in thickness are often synthesised for use as fuel cells, sensors and ferroelectric memory technologies [39]. One of the common techniques for

solid-phase fabrication of dense coatings is spray-deposition. It involves the spraying of low solid content suspensions in water or ethanol through a constricted nozzle onto a substrate, with controlled drying between each layer deposition, and a final firing step of the coated substrate. The line-of-sight technique is used in industrial processes for the application of thermal barrier coatings and requires tailoring of the thermal expansivities of both the deposited and substrate material to prevent cracking caused by tensile stresses [39].

Stainless steel 316L and Ti-alloy Ti6Al4V are common metal implant materials utilised for prosthetic components and dental implants, respectively [1]. In comparison, BT-based ceramics have quite dissimilar thermal expansion coefficients (TEC) (Table 2.2). Ideally, a coating should have a similar but slightly lower TEC than the substrate, such that the coating is under compressive stress and constrains crack formation. As such, interlayer materials can be utilised to mediate the thermal expansion mismatch. For example, $CaZrO_3$ and $CaTiO_3$ perovskites have potential as interlayer materials due to their intermediate TEC between BT-based ceramics and Ti6Al4V metals (Table 2.2).

Table 2.2: Thermal expansion coefficients of stainless steel 316L, Ti6Al4V, BT-based ceramics, $CaZrO_3$, and $CaTiO_3$.

Material	$\boldsymbol{TEC}$ **(K^{-1})**	**Temperature Range (°C)**	
Stainless Steel 316L	20.5 x 10^{-6}	600–1000	[106]
Ti6Al4V	10.3 x 10^{-6}	600–1000	[106]
BT-based	17.5 x 10^{-6}	350–1050	[107]
$CaZrO_3$	10.5 x 10^{-6}	25–1000	[108]
$CaTiO_3$	12.2 x 10^{-6}	30–700	[109]

Chapter 3

Materials and Methods

This chapter presents the materials and methods used in the preparation of BCZT ceramics, characterisation techniques, and the experimental methods followed for Chapters 4–7.

3.1. Materials

BCZT ceramics were prepared following the solid-state synthesis route from oxide and carbonate precursor powders, as detailed in Table 3.1. Four compositions of BC_xZ_yT were prepared, where x is the mol. % of Ca on the A-site, and y is the mol. % of Zr on the B-site. These include the MPB composition ($BC_{15}Z_{10}T$), and three primarily rhombohedral compositions ($BC_{14}Z_{10}T$, $BC_{12}Z_{10}T$, and $BC_{10}Z_{10}T$). The ceramics were utilised in various forms including bulk, powder, and ceramic slurries for coatings in Chapters 4–7, as outlined in Table 3.2. The synthesis batches of each BCZT material is indicated by the letters (A–E, H–K).

Table 3.1: Precursor powders used for the synthesis of BCZT ceramics.

Material	Chemical Formula	Purity (%)	Supplier & Identification No.
Barium carbonate	$BaCO_3$	≥ 99.000 ≥ 99.980	Sigma Aldrich (Series 1) 237108 (Series 2) 329436
Calcium carbonate	$CaCO_3$	≥ 99.000	Sigma Aldrich C6763
Zirconium (IV) oxide	ZrO_2	≥ 99.978	Alfa Aesar Puratronic 11141
Titanium (IV) oxide, anatase	TiO_2	≥ 99.800	Sigma Aldrich 23203

In general, the BCZT materials were prepared from the same precursor powders. However, bulk ceramics prepared for Chapter 5 were produced using two different $BaCO_3$ precursor powders of purity level ≥ 99.00 and ≥ 99.98 %. The synthesis batches are classified into Series 1 (C1 & C2) and Series 2 (C3–C6), respectively. All other BCZT materials were produced using $BaCO_3$ precursor powders of purity level ≥ 99.98 %.

Table 3.2: Overview of BCZT materials used for each experiment in Chapters 4–7, including the form i.e. bulk, powder, slurry, and the synthesis batch indicated by letters A–E, H–K.

	Experiment (incl. form and synthesis batch identification label)				
Material	**Composition Dependence of Piezoelectric Performance (Ch. 4)**	**Biological Cell Testing – Cell Proliferation & Viability (Ch. 5)**	**Biological Cell Testing – Soaking & Ion Release (Ch. 5)**	**Piezoelectric Stability After Static Mechanical Loading (Ch. 6)**	**Piezoelectric Coatings on Metal Implant Substrates (Ch. 7)**
$BC_{15}Z_{10}T$	Bulk (A)	Bulk (Series 1: C1&C2 Series 2: C3–C6)	Powder (H)	Bulk (H)	
$BC_{14}Z_{10}T$	Bulk (B)			Bulk (I)	
$BC_{12}Z_{10}T$	Bulk (D)			Bulk (J)	
$BC_{10}Z_{10}T$	Bulk (E)			Bulk (K)	Slurry (E)

3.2. Processing

3.2.1. Powder Synthesis

Precursor powders of barium carbonate ($BaCO_3$), calcium carbonate ($CaCO_3$), zirconium dioxide (ZrO_2), and titanium dioxide (TiO_2) were initially dried overnight at ≈ 100 °C (Termaks AS, Bergen, Norway) to remove physically bonded water. In preparation for wet ball-milling, a wide-mouth 250 mL high-density polyethylene (HDPE) milling bottle with a screw top lid (Nalgene Thermo Fisher Scientific Inc., Rochester, USA) was

half-filled with cleaned and dried yttria-stabilised zirconia (YTZ) milling balls (5 mm diameter, 6.0 g/cm^3 density, Tosoh Europe BV, Amsterdam, The Netherlands). Stoichiometric amounts of dried precursor powders were weighed and gently washed from the weighing boat into the milling bottle, using a wash bottle containing 96 % ethanol to ensure complete transfer and minimal flying of the powders. By filling the bottle first with milling balls, sticking of the powders to the walls of the bottle was largely prevented. The milling bottle was subsequently topped up with 96 % ethanol until it was two-thirds full, closed, sealed with paraffin film to prevent leakage, and shaken to prevent formation of large agglomerates. Ball-milling was performed on a rolling bench at 205 rpm for 24 h to ensure homogeneous mixing of the precursor powders.

After ball-milling, the ethanol was evaporated from the powder suspension using a rotary evaporator (Rotavapor, Büchi Labortechnik AG, Flawil, Switzerland). The suspension was strained into a Rotavapor beaker, while the milling balls were transferred to a separate clean beaker, covered with 96 % ethanol and placed in an ultrasonic bath for 5 min. The sonicated suspension was strained into the Rotavapor beaker. The sonication and straining steps were repeated until the sonicated suspension was relatively clear, ensuring that most of the powders were removed from the surface of the milling balls. After rotary evaporation at 60 °C and 175 mbar, the dried powders were lightly grinded with an agate mortar and pestle and sieved using a 250 µm mesh to remove larger agglomerates.

The powders were formed into pellets (3 g, 25 mm diameter) using a uniaxial press (hydraulic C-press, -4 MPa pressure), and stainless steel dies (I Holland Ltd., Nottingham, UK) that were lubricated with steric acid to prevent the formation of pressing defects and abrasion of the dies. The pellets were stacked within a Pt crucible, with sacrificial powders of the same mixed powders below, above, and in between the pellets. The crucible was covered with an alumina lid, leaving a 1–2 mm opening. Calcination was performed in a muffle furnace (Entech Chamber Furnace with Super Kanthal Elements, Entech Energiteknik AB, Engelholm, Sweden) at 1300 °C for 2 h, with heating and cooling rates of 350 and 400 °C/h, respectively.

After calcination, the pellets were grinded using an agate mortar and pestle, sieved using a 250 µm mesh, and wet ball-milled in ethanol for 24 h at 205 rpm. Ethanol was

subsequently removed with a rotary evaporator (60 °C, 175 mbar) and the dried powders were grinded and sieved according to the same procedure as described earlier.

3.2.2. Bulk Ceramic Processing

Sintering curves (Appendix 1) were recorded for all four BCZT compositions via dilatometry (Netzsch DIL402C, Netzsch-Gerätebau GmbH, Selb, Germany) to determine the most suitable sintering temperature. Prepared calcined BCZT powders were uniaxially pressed into green body pellets of 0.5 g, with green densities ≈ 50 % of the theoretical density, and diameter and length of 5 and 5–10 mm, respectively. Heat-treatment was performed at 1450 °C for 3 h, with heating and cooling rates of 350 and 400 °C/h, respectively. A temperature exceeding the maximum sintering rate was chosen as an appropriate sintering temperature to ensure densification and coarsening for the synthesis of dense bulk BCZT ceramics.

Dense bulk BCZT pellets were synthesised via sintering of green body pellets of calcined powders. The pellets were prepared for sintering by uniaxial pressing (-10 MPa). Samples were prepared to different dimensions for each of the experiments presented in Chapters 4–6 (Table 3.3).

Table 3.3: Green body pressing parameters for sintered samples in Chapters 4–6.

Ch.	Experiment	Mass of Calcined Powder (g)	Diameter of Pressing Die (mm)
4	Composition Dependence of Piezoelectric Performance	0.5	10
5	Biological Cell Testing: Cell Proliferation & Viability	0.5	15
5	Biological Cell Testing: Soaking & Ion Release	3.0	10
6	Piezoelectric Stability After Static Mechanical Loading	0.3	10

The green body pellets were stacked with sacrificial powder below, between, and on top of the pellets within a Pt crucible and covered with an alumina lid, leaving a 1–2 mm

opening. For bulk samples utilised in Chapters 4–6, heat-treatment was performed at 1450 °C for 3 h for $BC_{15}Z_{10}T$ and $BC_{14}Z_{10}T$, and at 1400 °C for 3 h for $BC_{12}Z_{10}T$ and $BC_{10}Z_{10}T$ compositions (Figure 3.1 (a)). The heating and cooling rates were 350 and 400 °C/h, respectively. Sintered $BC_{10}Z_{10}T$ bulk ceramics of various grain sizes were obtained for Chapter 6 by sintering at 1100 and 1400 °C for 1 or 3 h (Figure 3.1 (b)).

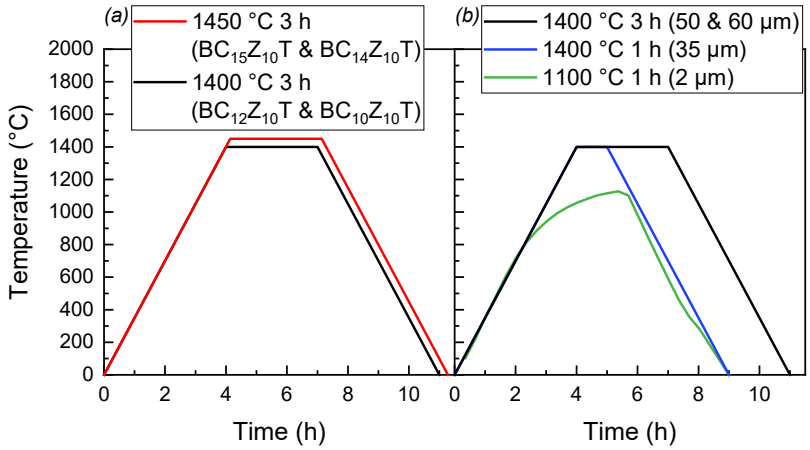

Figure 3.1: Sintering programs for the syntheses of bulk BCZT ceramics. (a) $BC_{15}Z_{10}T$, $BC_{14}Z_{10}T$, $BC_{12}Z_{10}T$, and $BC_{10}Z_{10}T$ samples utilised in Chapters 4–6, and (b) $BC_{10}Z_{10}T$ samples of various grain sizes utilised in Chapter 6.

3.2.3. Milling of Bulk Ceramics into Powders

Sintered bulk $BC_{15}Z_{10}T$ ceramics were milled into fine powders for Chapter 5 Soaking and Ion Release experiments. The ceramics were broken with impaction before planetary milling (Retsch PM 100, Retsch GmbH, Haan, Germany) for 30 min at 300 rpm in isopropanol in a 125 mL zirconia milling jar with 2 cm diameter YTZ milling balls. The slurry was transferred to a 250 mL HDPE milling bottle and wet ball-milled in isopropanol with 5 mm diameter YTZ milling balls for 24 h at 250 rpm. After milling, the isopropanol was evaporated using a rotary evaporator (60 °C, 175 mbar) and the powders were sieved using a 250 µm mesh.

3.2.4. Ceramic Coating Processing

Ceramic coatings were produced for Chapter 7 by spray-deposition of ceramic slurries onto metal substrates. Slurries were prepared by ultrasonicating suspensions of calcined

$BC_{10}Z_{10}T$ and $CaZrO_3$, and as-received $CaTiO_3$ powders ($CaZrO_3$ and $CaTiO_3$ details provided in Appendix 2 & Appendix 3) in 96 % ethanol (0.05 g/mL) using an ultrasonic needle (15 min, 30 % amplitude, Branson Ultrasonics Corp., Danbury, USA).

Metal substrates of stainless steel 316L, pure Ti and Ti6Al4V (ANKURO Int. GmbH, Rostock, Germany) of 10 x 10 x 1 mm^3 size were prepared by grinding with 1200 grit SiC paper and 96 % ethanol. Substrates were degreased and cleaned in an ultrasonic bath in ethanol for at least 5 min, rinsed with ethanol, and dried using lint-free paper. The substrates were placed on a paper towel in a heating cabinet at 100 °C.

Ceramic layers were spray-coated on pre-warmed metal substrates using an Aztek spray-coating gun (Testors, Vernon Hills, USA) with a 0.7 µm nozzle size and pressurised air (0.5 bar). Spray-coating was performed not more than 1 h after substrate preparation. After each layer was deposited, substrates were transferred to the heating cabinet (Termaks AS, Bergen, Norway) at 100 °C for 20 s before the next layer was applied. This maintained the heat within the metal substrate and allowed for instant drying of the deposited ceramic layers.

Coated substrates were heat-treated in a tube furnace (Entech Horizontal Tube Furnace with Super Kanthal Elements, Entech Energiteknik AB, Engelholm, Sweden) under Ar atmosphere. Samples were placed into zirconia crucible boats, partially covered with alumina disc lids (30 mm diameter) (Figure 3.2) and centred within the tube furnace. Prior to heat-treatment, the furnace was evacuated to ≈ 0 mbar and purged at least three times with Ar gas. Gas flow was adjusted to ensure the bubble rate was approximately 13 bubbles/10 sec. Heat-treatment was conducted at temperatures between 900–1350 °C, with heating and cooling rates of 200 °C/h. Bi-layered coatings were heat-treated in one- or two-step procedures. For the one-step procedure, $CaTiO_3$ was spray-deposited onto a prepared Ti6Al4V substrate. Immediately afterwards, a BCZT coating was deposited on top, and the sample was heat-treated at 900 °C for 1 h. For the two-step procedure, $CaTiO_3$ was initially deposited onto a prepared Ti6Al4V substrate and heat-treated at 900 °C for 1 h. Subsequently, a BCZT ceramic coating was deposited onto the heat-treated $CaTiO_3$ coating, and heat-treated at 900, 950, 970 or 1000 °C for 1 h.

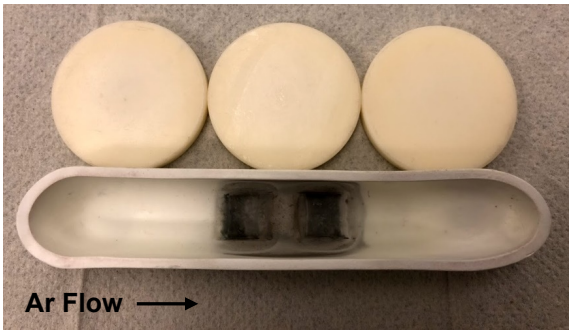

Figure 3.2: Zirconia crucible boat and alumina disc lids used during the heat-treatment of ceramic coatings on metal substrates.

The coating process was optimised by varying parameters including: surface preparation and treatment (Table 3.4), direct deposition of BCZT onto metal substrates (Table 3.5) and the use of ceramic interlayer materials, $CaZrO_3$ and $CaTiO_3$, to enhance adhesion of BCZT to the metal substrates (Table 3.6). Further investigation on $CaTiO_3$ and BCZT on Ti6Al4V was focused on the effect of heat-treatment temperatures, one- vs. two-step heat-treatment, argon gas flow, and ceramic coating thickness (Table 3.7). An overview of all samples is visualised in flowcharts presented in Appendix 4–Appendix 21.

Table 3.4: Overview of heat-treatment of uncoated stainless steel 316L and Ti6Al4V substrates in Ar and air atmospheres.

Plain Substrates 316L and Ti6Al4V			
Substrate	**Temperature (°C)**	**Time (h)**	**Atmosphere**
316L	900	1	Ar
	1000	1	
	1100	1	
	1200	1	
	1300	1	
Ti6Al4V	900	1	Ar
	1000	1	
	1100	1	
	1200	1	
	1300	1	
Ti6Al4V	900	1	Air

Table 3.5: Overview of BCZT-coated stainless steel 316L and Ti6Al4V substrates heat-treated from 900–1100 °C for 1 h in Ar atmosphere.

BCZT on 316L and Ti6Al4V			
Substrate	**Coating**	**Layers**	**Temperature (°C)**
316L	$BC_{10}Z_{10}T$	5 or 10	900 1000 1100
Ti6Al4V	$BC_{10}Z_{10}T$	5 or 10	900 1000 1100

Table 3.6: Overview of $CaZrO_3$- and $CaTiO_3$-coated pure Ti and Ti6Al4V substrates heat-treated from 900–1200 °C for 1 h in Ar atmosphere. As-received $CaTiO_3$ powders from 2017 and 2018 are distinguished due to the variation in their purity as determined from X-ray diffraction (Appendix 2 & Appendix 3). The 2017 powders were heat-treated at 900 °C for 1 h in air to improve purity. To enhance the contact between the spray-deposited $CaTiO_3$ powders and the Ti6Al4V substrates, a compressive uniaxial pressure of -10 MPa was applied.

$CaZrO_3$ and $CaTiO_3$ on Pure Ti and Ti6Al4V				
Substrate	**Coating**	**Layers**	**Powder Treatment**	**Temperature (°C)**
Ti6Al4V	$CaZrO_3$	29 or 78	–	1000 1100 1200
Pure Ti	$CaTiO_3$	93	–	900
Ti6Al4V (Grinded/ As-Received)	$CaTiO_3$ (2017)	38–95	As-Received/ Heat-Treated	900 1100
Ti6Al4V	$CaTiO_3$ (2017)	Powder	Uniaxially pressed	900
Ti6Al4V	$CaTiO_3$ (2018)	15–59	Uniaxially pressed	900

Table 3.7: Overview of $CaTiO_3$- and BCZT-coated Ti6Al4V substrates heat-treated in Ar atmosphere for 1 h. Ceramic coating thicknesses were varied, as were heat-treatment temperatures and procedures (one- vs. two-step), and Ar gas flow adjusted using alumina disc lids during heat-treatment. Some ceramic coatings were uniaxially pressed with -10 MPa to enhance contact between the powders and the substrate prior to heat-treatment, and some were scraped gently to reduce the ceramic coating thickness after heat-treatment.

$CaTiO_3$ and BCZT on Ti6Al4V				
Coating	**Layers**	**Powder Treatment**	**Temperature (°C)**	**Heat-Treatment Procedure**
$CaTiO_3$ (2017) E:$BC_{10}Z_{10}T$	68 & 76 33 & 40	–	900	One-step
$CaTiO_3$ (2018) E:$BC_{10}Z_{10}T$	15 & 15	Both coatings uniaxially pressed only	900 950 1000	Two-step
$CaTiO_3$ (2018) E:$BC_{10}Z_{10}T$	15 & 15	Both coatings uniaxially pressed & only $CaTiO_3$ coatings scraped or Both coatings uniaxially pressed only	900 950 1000	Two-step
$CaTiO_3$ (2018) E:$BC_{10}Z_{10}T$	8 & 15	–	900 950 970	Two-step
$CaTiO_3$ (2018) E:$BC_{10}Z_{10}T$	8 & 15	No lids & reoxidation after final heat-treatment	900	Two-step
$CaTiO_3$ (2018) E:$BC_{10}Z_{10}T$	20 & 20 40 & 40 20 & 40 40 & 20	No lids	900	One-step

3.3. Characterisation

3.3.1. Composition

Composition of Calcined and Sintered Powders

X-ray diffraction (XRD) measurements were performed on powder samples of calcined and sintered samples to determine phase purity. Sintered pellets were grinded using an agate mortar and pestle. A Bruker D8 A25 DaVinci X-ray diffractometer (Bruker Corp., Massachusetts, USA) with accelerating Cu Kα radiation of 1.54 Å was used. Phase purity analysis was performed with respect to PDF 00-065-0109. Crystal structure was determined by visual analysis of peak splitting behaviour of pseudo-cubic (200), (220), and (222) reflections compared to PDF 00-065-0109 (tetragonal), PDF 04-019-9415 (orthorhombic), and PDF 00-063-0612 (rhombohedral).

Composition of Ceramic Coatings on Metallic Implants

The elemental composition of BCZT coatings on metallic substrates was determined via scanning electron microscopy energy dispersive X-ray spectroscopy (SEM EDS) using a Zeiss Ultra 55 (Carl Zeiss AG, Oberkochen, Germany) and Quantax EDS system (Bruker, USA). In addition, electron probe microscopy wavelength dispersive spectroscopy (EPMA WDS) (JEOL JXA-8500F, JEOL Ltd., Tokyo, Japan) was performed on one sample to compare with elemental analyses obtained through SEM EDS. EDS analysis was performed using the Esprit 1.9 Software (Bruker, USA) and primary characteristic energies presented in Table 3.8.

Table 3.8: Characteristic energies selected for the analysis of SEM EDS data.

Element	keV	Series
Ti	4.512	K
Al	1.486	K
V	4.953	K
Ca	3.692	K
O	0.525	K
Ba	4.466	L
Zr	2.044	L

For SEM imaging, coating samples were cold mounted in epoxy (EpoFix Hardener & Resin, Struers) for at least 12 h. Grinding and polishing were performed (Tegramin-20, Struers Inc., Cleveland, USA) until a mirror-like finish was obtained of the cross-sectional area (Table 3.9). A mixture of colloidal silica (OP-S, Struers) and hydrogen peroxide (H_2O_2) was used for the final polishing step as the H_2O_2 reacts with titanium, while colloidal silica removes the reaction product from the surface during polishing. Samples were cleaned in an ultrasonic bath in ethanol for at least 5 min between grinding steps, and a final cleaning step of 15 min in the ultrasonic bath ensured removal of particles that may have smeared and embedded in the surface of the sample.

Table 3.9: Grinding and polishing steps for preparation of ceramic coatings on metal substrates for SEM imaging.

Grinding Surface	Grain Size (µm)	Force (N)	Time (min)	Plate Rotation (rpm)	Holder Rotation (rpm)	Lubricant/ Suspension
SiC Foil #320	46	10	2	300 ↻	150 ↺	Water
SiC Foil #500	30	10	2	300 ↻	150 ↺	Water
SiC Foil #1200	15	10	5	300 ↻	150 ↺	Water
MD Chem	0.25	10	5	150 ↻	150 ↻	OP-S + H_2O_2 (vol. ratio 4:1)

3.3.2. Microstructure

Density

The bulk density of sintered BCZT ceramic samples was determined from mass and geometric measurements obtained with a digital calliper. The theoretical crystallographic density (TD) was determined from XRD patterns of sintered samples of each synthesis batch and used to calculate the relative densities.

Grain and Particle Size

Bulk BCZT samples were imaged using a Zeiss Supra 55 and Ultra 55 SEM to determine grain size. To expose the grain boundaries, the samples were hand-polished to a 3 µm

finish, with ultrasound cleaning in ethanol for approximately 2 min between polishing steps. The polishing steps are outlined in Table 3.10.

Table 3.10: Grinding and polishing steps for preparation of bulk BCZT ceramics for SEM imaging.

Grinding Surface	Grain Size (µm)	Lubricant/Suspension
SiC Foil #1200	15	Water
SiC Foil #2400	8	Water
SiC Foil #4000	5	Water
Struers MD Dur	3	DiaPro Dur 3 (Struers)

The polished pellets were chemically etched with 37 % HCl and deionised water (1:1 vol. ratio) for 30 s (≈ 6.1 M). Pellets were subsequently thermally etched 100 °C below the sintering temperature for 5 min, with heating and cooling rates of 600 °C/h. Thermal etching was performed in a muffle furnace in a Pt crucible partially covered with an alumina lid, leaving a 1–2 mm opening. Sacrificial powders were not used. Samples were carbon coated prior to SEM imaging (208 carbon High Vacuum Carbon Coated, Cressington Scientific Instruments Ltd., Watford, UK).

Grain size measurements were performed using Lince software (Lince 2.31, Ceramics Group, TU Darmstadt, Germany), following the linear intercept method. At least 50 intersections were measured on a representative sample from each BCZT synthesis batch.

Particle size measurements were performed following the linear intercept method on at least 50 intersections (Lince software) on SEM micrographs of $BC_{10}Z_{10}T$ calcined powders in Chapter 6.

3.3.3. Surface Properties

Surface Area

Nitrogen adsorption (TriStar 3000, Micromeritics, Norcross, USA) was used to determine the specific surface area of powder samples prepared for Chapter 5 Soaking and Ion Release experiments.

Surface Roughness

Surface roughness of bulk BCZT and polystyrene samples for Chapter 5 Cell Proliferation and Viability were determined using a NT-MDT Ntegra Prima Scanning Probe Microscope (SPM) (NT-MDT Spectrum Instruments Ltd., Moscow, Russia) using HQ:NSC35/Pt tips in contact mode. Scan size area was 85 x 85 µm. BCZT samples were grinded using 1200 grit SiC paper, and polystyrene samples were measured as-received.

Contact Angle and Wettability

Static contact angles of 1 µL sessile drops of deionised water on bulk BCZT and polystyrene samples, used for Chapter 5 Cell Proliferation and Viability, were measured using the Krüss Drop Shape Analyser DSA100 (Krüss GmbH, Hamburg, Germany). BCZT samples were grinded with 1200 grit SiC paper prior to measurement, and polystyrene samples were measured as-received. Deionised water drops were deposited at a speed of 40 mm/min and allowed to relax on the sample surface for 30 s before the measurement. Ten independent contact angle measurements were obtained at 37 °C. The contact angles were determined using the Young Laplace fitting method and are presented as mean and standard deviation. An example of the contact angle measurement is shown in Figure 3.3.

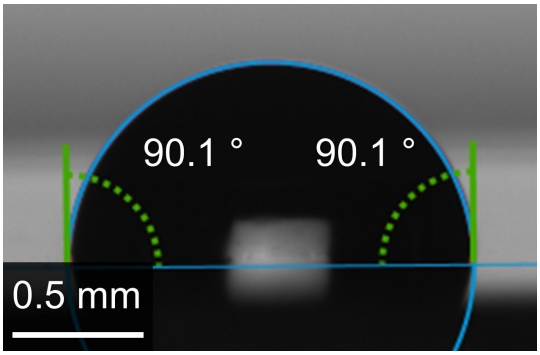

Figure 3.3: Representative image of the contact angle measurement performed on a polystyrene sample for the determination of wettability.

3.3.4. Piezoelectric and Dielectric Properties

In preparation for piezoelectric property measurements, bulk BCZT ceramic samples were grinded with 1200 grit SiC paper to obtain flat, parallel surfaces. The samples were

cleaned in an ultrasonic bath in ethanol for 10 min and gold electrodes were applied by sputter deposition (Edwards Sputter Coater S150B, Edwards, Burgess Hill, UK). Polarisation, strain, piezoelectric coefficient, and permittivity measurements were performed using the TF Analyser 2000 (aixACCT, Aachen, Germany). The specific measurement parameters utilised in Chapters 4–6 are presented below.

Composition Dependence of Piezoelectric Performance

In Chapter 4, $BC_{15}Z_{10}T$, $BC_{14}Z_{10}T$, $BC_{12}Z_{10}T$, and $BC_{10}Z_{10}T$ samples were heat-treated at 200 °C for at least 24 h to de-pole and de-age. The freshly heat-treated samples were quenched in water and immediately tested using the TF Analyser 2000. The average time between quenching and measurements was 5–10 min. Samples were poled from 100 V/mm up to 500 V/mm (50 V increments) in air, using a triangular waveform with a frequency of 1 Hz. Polarisation and strain loops were acquired from the second measurement at 500 V/mm. Two measurements were then performed using a frequency and amplitude of 1 kHz and 20 V to obtain piezoelectric coefficient and permittivity loops. A staircase mode was applied with a long integration time of 200 data points. The remanent polarisation, coercive field, and remanent piezoelectric coefficient are presented as the average of positive and negative polarity values.

Low voltage impedance measurements were performed on unpoled bulk BCZT samples using a dielectric analyser (Novocontrol Technologies GmbH & Co. KG, Montabaur, Germany) to investigate the dielectric behaviour of the ceramics with respect to composition. Measurements were performed at 1 V/mm, from room temperature to 100 °C at 1 K/min, and at frequencies from 1 to 100 000 Hz.

Biological Cell Testing

In Chapter 5 Cell Proliferation and Viability, bulk $BC_{15}Z_{10}T$ samples were heat-treated at 200 °C for 12 h, quenched in water and immediately measured using the TF Analyser 2000. Four polarisation and strain measurements at 800 V/mm were obtained using a triangular waveform with a frequency of 1 Hz. Subsequently, two measurements at 800 V/mm were performed using a staircase mode with a frequency and amplitude of 1 kHz and 20 V, and a long integration time of 200 data points to acquire piezoelectric coefficient and permittivity loops.

Piezoelectric Stability After Static Mechanical Loading

The degradation of piezoelectric performance after static mechanical loading was investigated with respect to BCZT composition ($BC_{15}Z_{10}T$, $BC_{14}Z_{10}T$, $BC_{12}Z_{10}T$, and $BC_{10}Z_{10}T$) and average grain size (2, 35, 50, and 60 µm) in Chapter 6.

The piezoelectric performance of the BCZT pellets were determined before, during, and after mechanical loading, as illustrated in Figure 3.4. Before the first electrical measurements were performed, all samples were heat-treated at 200 °C to de-pole and de-age. Initially, the coercive field for each BCZT composition was determined by piezoelectric measurements conducted using a TF Analyser 2000 on an unpoled sample. BCZT samples were then poled at five times the coercive field (5 x E_c) for their composition. Five polarisation and strain measurements were conducted per sample using a triangular waveform with a frequency of 1 Hz. The initial piezoelectric coefficient was measured twice per sample using a frequency and amplitude of 1 kHz and 1 V. A staircase mode was applied with a long integration time of 200 data points. The second measured hysteresis loop was plotted as the initial curve.

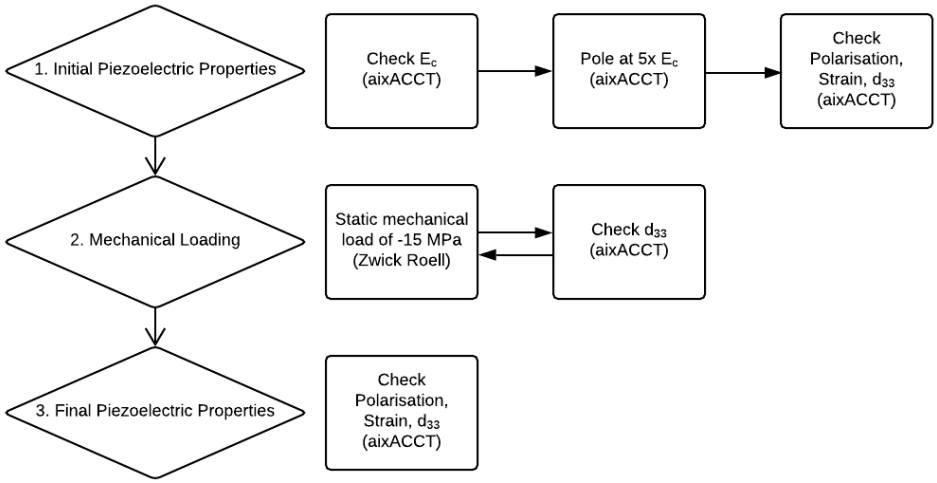

Figure 3.4: Procedure for piezoelectric testing and static compressive mechanical loading of bulk BCZT ceramics.

After poling, static mechanical loading was performed using a Zwick Roell Materials Testing Machine Z2.5 (ZwickRoell, Ulm, Germany). Samples were wrapped in aluminium foil to short-circuit the material during loading. A uniaxial compressive

pressure of -15 MPa was applied to samples for 1, 4, 5, 10, 20, and 30 min to achieve accumulative 1, 5, 10, 20, 30, and 60 min mechanical loading. The pre-load and loading speed were 5 N and 10 N/s, respectively. After loading at each of the time frames, the piezoelectric coefficient was determined from electric measurements at 0 V bias with the TF Analyser. Measurements were recorded on two ceramic samples per composition, and for both positive and negative polarities. The piezoelectric coefficient values are expressed as an average of the polarities. After the mechanical loading time frames were completed, the polarisation, strain, and piezoelectric coefficient were again measured using the TF Analyser and the same measurement parameters as were applied during the initial characterisation.

3.3.5. Biological Cell Testing

Cell Viability and Proliferation

The MPB composition, $BC_{15}Z_{10}T$, was chosen for Chapter 5 Cell Proliferation and Viability testing due to its good piezoelectric performance. In preparation for cell testing, sintered BCZT samples were grinded with 1200 grit SiC paper to form homogeneous surfaces. A control group of polystyrene discs (T175 Nunc™ EasYFlask™, Thermo Scientific, Waltham, USA) with 12 mm diameter were used as-received [110]. The ceramic BCZT samples were sterilised using high pressure saturated steam autoclaving at 120 °C, and the polystyrene samples were sterilised using plasma radiation.

Primary human umbilical vein endothelial cells and primary human osteoblasts (HUVEC & HOB, PromoCell GmbH, Heidelberg, Germany) were used for cell testing. Cells were cultured in flasks with cell growth areas of 25, 75, and 175 m^2 (Greiner Bio-One, Frickenhausen, Germany) with Endothelial Cell Growth Medium (ready-to-use) (PromoCell GmbH, Heidelberg, Germany) at 98 % humidity, 37 °C and 5 % CO_2 (Heracell 240i CO_2 Incubator, Thermo Scientific, Waltham, USA). Splitting was performed until passage three at 70–90 % confluency. The corresponding media was filled into a 24-well plate and 12 x 1 mm disc BCZT or polystyrene samples were inserted. Each sample was seeded with 1 x 10^4 cells. Incubation was performed at 37 °C and 5 % CO_2 for 30 min.

The morphology and cytotoxicity of the cells were analysed using FDA/PI dual staining (fluorescein diacetate: 10 µg/mL in phosphate buffered saline (PBS), propidium iodide: 50 µg/mL in PBS (Invitrogen GmbH, Karlsruhe, Germany)). After 24 h, media were removed from the samples. The samples were stained for 20 min, rinsed with PBS, and inspected with an inverse microscope (Axioscop, Carl Zeiss AH, Oberkochen, Germany).

Cell proliferation was determined by the number of live cells after 1, 3, 7, and 10 days using Scepter 2.0 Cell Counter (Merck KGaA, Darmstadt, Germany). At the specific time points, cells were detached with Accutase (Accutase Innovative Cell Technologies Inc., San Diego, USA), washed with PBS, and counted.

Cell viability was determined by mitochondrial dehydrogenase activity using a Water-Soluble Tetrazolium Salts colorimetric assay (WST-1 Cell Proliferation Assay, Roche Diagnostics GmbH, Mannheim, Germany).

Cell testing measurements were performed at least five times. Results are expressed as mean and standard deviation. Statistical analysis was performed using BiAs software (BiAs 11.08, epsilon-Verlag, Frankfurt, Germany). The statistical significance of the data was assessed using the Kruskal Wallis test, where probability values (p) of $p < 0.05$ were considered statistically significant [111]. The p-value indicates "the probability that a sample average will take on a value at least as extreme as the observed value when the null hypothesis H_0 is true" [112], i.e. the lower the p-value, the lower the probability a result is obtained by chance.

Soaking and Ion Release

Bulk $BC_{15}Z_{10}T$ ceramics were milled into fine powder samples and soaked in solutions of deionised water and NaCl (9 g/L or 0.154 M NaCl) to determine ion release over a 90-day period in Chapter 5. Centrifuge tubes (15 mL, HDPE) were filled with 0.5 g of BCZT powder and 5 mL solution. Blank control samples contained only 5 mL of solution. The tubes were sealed with paraffin film to prevent leakage, well-shaken to prevent the formation of large agglomerates, and loaded onto a Rocker 3D Digital Shaker (IKA-Werke GmbH & Co. KG, Staufen, Germany) within a heating chamber (BD 53, Binder GmbH, Tuttlingen, Germany) at 37 °C with a tumbling motion. After 1, 3, 7, 10, 20, 30, 60, and 90 days of soaking, samples were prepared for inductively coupled plasma

mass spectroscopy (ICP-MS) measurements (Agilent 8800 Triple Quadrupole ICP-QQQ-MS, Agilent Technologies Inc., Santa Clara, USA). For each time point, three ceramic and one blank control aliquot samples were removed from the tubes. Samples were centrifuged (10 000 rpm, 20 min), 2 mL of aliquot was removed using a micropipette, and diluted five times with deionised water. A micropipette was utilised to prevent the powders from mixing with the aliquot, which can affect the ICP-MS measurements. The diluted solutions were preserved with three drops of 0.1 M HNO_3.

Chapter 4

Composition Dependence of Piezoelectric Performance

When applied as an active electrical stimulation source within the body, it is important to understand how the piezoelectric performance of BCZT and subsequently, its ability to generate and supply charge to surrounding tissues for cell stimulation can be optimised. In this chapter, the dependence of piezoelectric performance on composition was investigated for $BC_{15}Z_{10}T$, $BC_{14}Z_{10}T$, $BC_{12}Z_{10}T$, and $BC_{10}Z_{10}T$. These compositions were chosen with the expectation that the room temperature MPB composition, $BC_{15}Z_{10}T$, should show an enhanced piezoelectric response, as compared to the primarily rhombohedral compositions, $BC_{14}Z_{10}T$, $BC_{12}Z_{10}T$, and $BC_{10}Z_{10}T$.

4.1. Results

4.1.1. Phase Purity and Composition

The XRD patterns of calcined and sintered $BC_{15}Z_{10}T$, $BC_{14}Z_{10}T$, $BC_{12}Z_{10}T$, and $BC_{10}Z_{10}T$ materials are displayed in Figure 4.1. Generally, the powders appear phase pure after calcination. After sintering, the crystallinity increased as shown by the smaller full width at half maximum (FWHM). Secondary phases are evident, as indicated by the asterisks (*). The secondary phases in the calcined powders may arise from off-stoichiometries or unreacted precursor powders. Those seen in the sintered samples may be from cation segregation facilitated by low temperature oxycarbonate formation, which have been observed in the wet chemical synthesis of BCZT thin films [113]. However, the secondary phases are in very small amounts and did not have an observable effect on the piezoelectric properties.

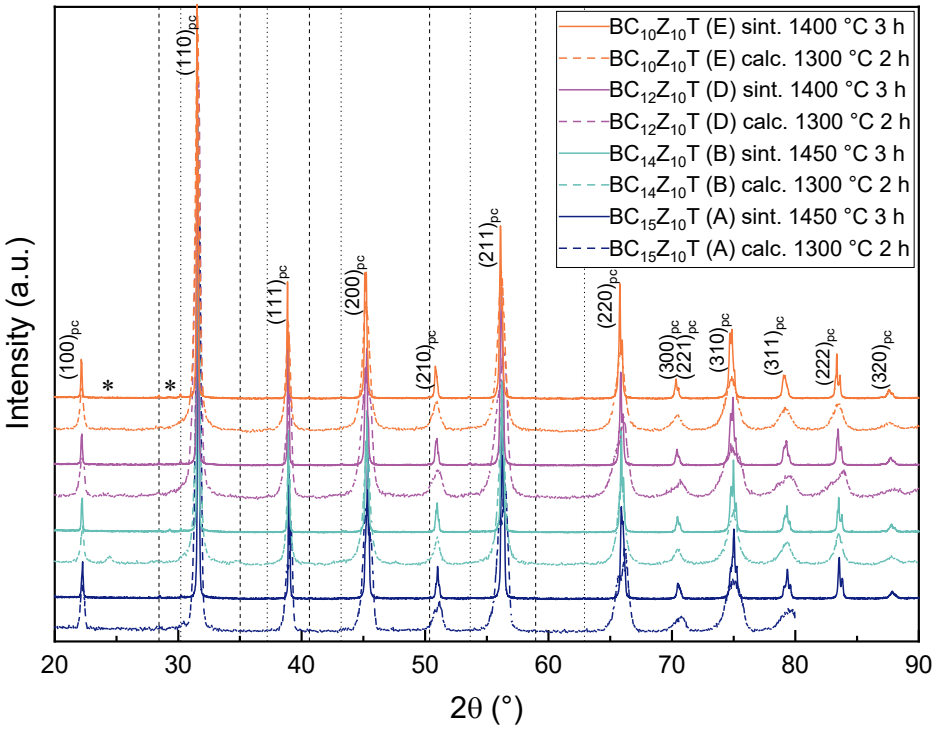

Figure 4.1: XRD patterns of calcined and sintered BCZT ceramics – $BC_{15}Z_{10}T$, $BC_{14}Z_{10}T$, $BC_{12}Z_{10}T$, and $BC_{10}Z_{10}T$. Letters (A,B,D,E) represent the synthesis batches. Dashed and dotted black lines: Cu $K\beta_1$ and W $L\alpha_1$ peaks, respectively. Asterisk (*): secondary phases.

Figure 4.2 shows the XRD patterns of the sintered BCZT materials – $BC_{15}Z_{10}T$, $BC_{14}Z_{10}T$, $BC_{12}Z_{10}T$, and $BC_{10}Z_{10}T$ for the 2Θ ranges 44.8–45.8°, 65.4–66.4°, and 82.5–84.5°. These ranges depict the pseudo-cubic (200), (220), and (222) reflections, respectively. A split in the $(200)_{pc}$ peak is evident for all compositions, with the width of the peak split increasing from the $BC_{10}Z_{10}T$ to $BC_{15}Z_{10}T$ materials. The opposite trend in peak splitting of the $(220)_{pc}$ and $(222)_{pc}$ peaks are observed, such that the width of the peak splits increase from the $BC_{15}Z_{10}T$ to $BC_{10}Z_{10}T$ samples. The appearance of splitting for all $(200)_{pc}$, $(220)_{pc}$, and $(222)_{pc}$ peaks indicate that the compositions lie within the MPB region with overlapping influences from tetragonal, orthorhombic and rhombohedral phases. A shift of the peak positions towards lower 2Θ values from $BC_{15}Z_{10}T$ to $BC_{10}Z_{10}T$ is indicative of the change in Ca dopant content on the A-site of the perovskite structure. As the composition progresses from $BC_{15}Z_{10}T$ to $BC_{10}Z_{10}T$, the unit cell increases in size as a result of the increasing content of barium, which has a larger

ionic radius (1.61 Å) than calcium (1.34 Å) [114]. This causes a shift of the XRD peak positions towards lower 2Θ values.

Inspection of the extent of the peak splitting indicates that the BCZT materials show a structural progression correlating with the reported MPB region [27], [71], [115]. For a tetragonal crystal structure, the $(200)_{pc}$ peak is split while the $(222)_{pc}$ reflection is not. The opposite is expected for a rhombohedral structure (single $(200)_{pc}$ and split $(222)_{pc}$ reflections). In Figure 4.2, $BC_{15}Z_{10}T$ shows a pronounced $(200)_{pc}$ peak split and a minimal $(222)_{pc}$ split, suggesting that it has a predominantly tetragonal crystal structure. A peak originating from an orthorhombic contribution lies between the two marked peaks in the $(200)_{pc}$ reflection and is intentionally indicated with an asterisk (*) as it overlaps with a Cu $K\alpha_2$ contribution. $BC_{10}Z_{10}T$ shows a slight splitting of the $(200)_{pc}$ peak and a more obvious $(222)_{pc}$ splitting, suggesting that it mainly has a rhombohedral crystal structure. $BC_{14}Z_{10}T$ and $BC_{12}Z_{10}T$ show obvious splitting for both the $(200)_{pc}$ and $(222)_{pc}$ reflections, indicating that a more even phase mixture between the tetragonal and rhombohedral structures exists. Observation of the $(220)_{pc}$ reflection splitting for all materials also suggests a potential contribution from an orthorhombic crystal structure.

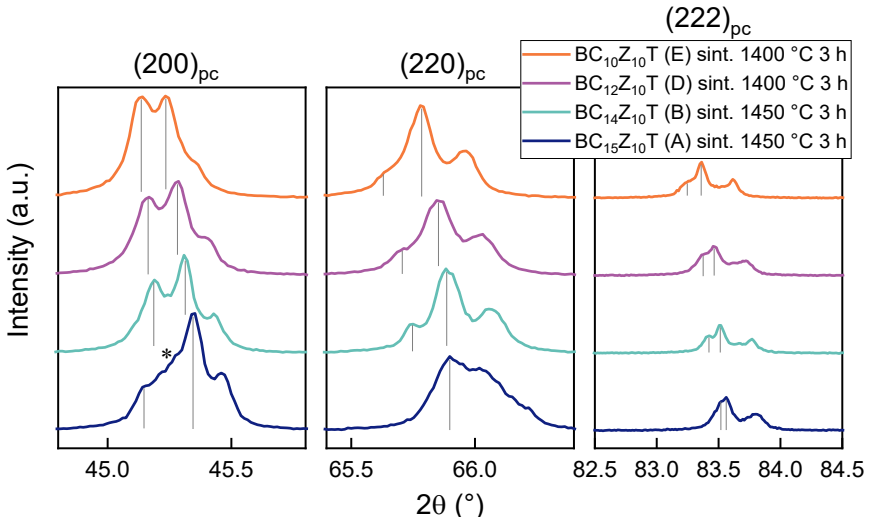

Figure 4.2: XRD patterns of sintered BCZT ceramics – $BC_{15}Z_{10}T$, $BC_{14}Z_{10}T$, $BC_{12}Z_{10}T$, and $BC_{10}Z_{10}T$. Ranges 44.8–45.8°, 65.4–66.4°, and 82.5–84.5° correlate with $(200)_{pc}$, $(220)_{pc}$, and $(222)_{pc}$ reflections, respectively. Grey lines: peak splitting. Unmarked peaks to the right of the grey lines: Cu $K\alpha_2$ contributions. Asterisk (*): overlap of a peak and Cu $K\alpha_2$ contribution.

4.1.2. Microstructure

The SEM micrographs of polished and etched bulk $BC_{15}Z_{10}T$, $BC_{14}Z_{10}T$, $BC_{12}Z_{10}T$, and $BC_{10}Z_{10}T$ are displayed in Figure 4.3. All materials show irregularly shaped grains with narrow grain size distributions. The ceramics are well-sintered, as evidenced by their high relative density (Table 4.1) and the presence of intergranular pores at triple points [116].

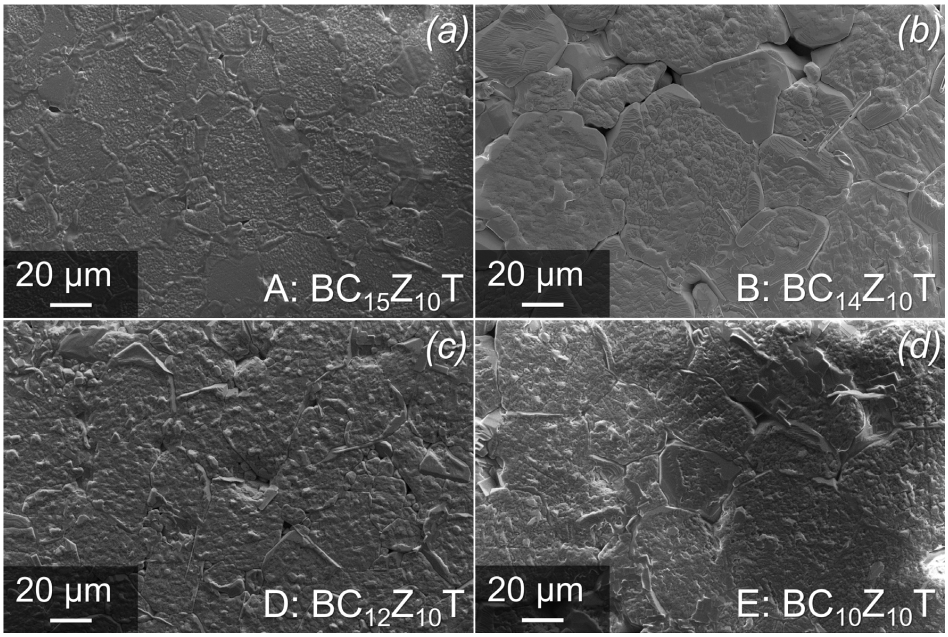

Figure 4.3: SEM micrographs of polished and etched (a) $BC_{15}Z_{10}T$, (b) $BC_{14}Z_{10}T$, (c) $BC_{12}Z_{10}T$, and (d) $BC_{10}Z_{10}T$ bulk sintered ceramics. Letters (A,B,D,E) represent the BCZT synthesis batches.

Table 4.1 displays the average grain size, density and relative density of each material measured from the SEM micrographs. $BC_{14}Z_{10}T$ has the largest average grain size followed by $BC_{10}Z_{10}T$, $BC_{12}Z_{10}T$, and $BC_{15}Z_{10}T$. The grain sizes are of the same order of magnitude and are not expected to dominate the piezoelectric response over compositional effects [55].

Table 4.1: Average grain sizes and densities of $BC_{15}Z_{10}T$, $BC_{14}Z_{10}T$, $BC_{12}Z_{10}T$, and $BC_{10}Z_{10}T$.

BCZT	Grain size (µm)	Density (g/cm^3)	Relative Density (%)
$BC_{15}Z_{10}T$	24 ± 5	5.8 ± (0.01)	99
$BC_{14}Z_{10}T$	61 ± 14	5.3 ± (0.01)	91
$BC_{12}Z_{10}T$	32 ± 6	5.6 ± (0.01)	95
$BC_{10}Z_{10}T$	58 ± 12	5.5 ± (0.01)	95

4.1.3. Piezoelectric and Dielectric Properties

The polarisation, strain, relative permittivity, and piezoelectric coefficient hysteresis loops of $BC_{15}Z_{10}T$, $BC_{14}Z_{10}T$, $BC_{12}Z_{10}T$, and $BC_{10}Z_{10}T$ are displayed in Figure 4.4 (a-d). The remanent polarisation, coercive field, minimum and maximum strain, remanent relative permittivity, and remanent piezoelectric coefficient values extracted from the hysteresis loops are displayed in Table 4.2.

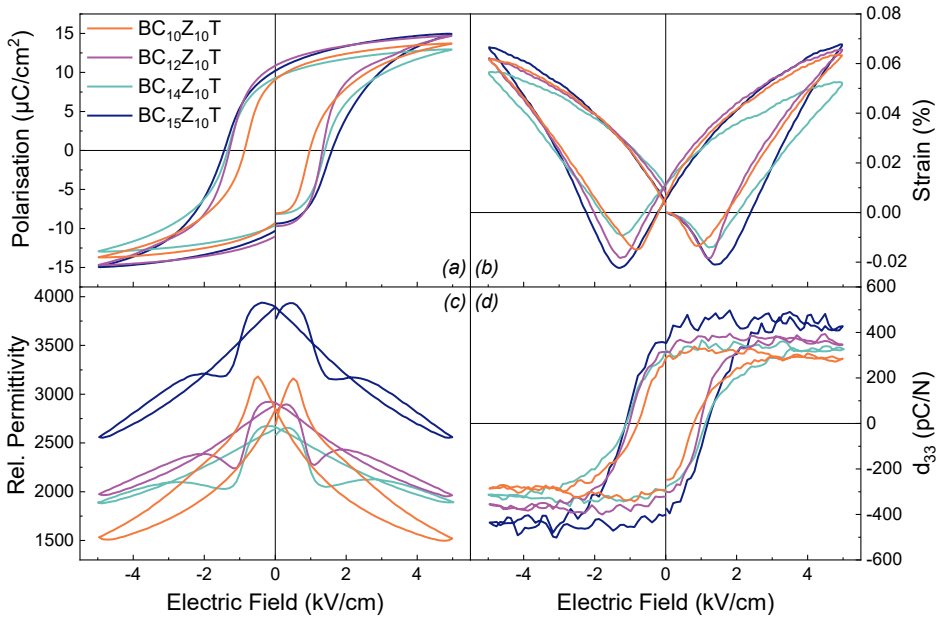

Figure 4.4: (a) Polarisation, (b) strain, (c) relative permittivity, and (d) piezoelectric coefficient hysteresis loops of $BC_{15}Z_{10}T$, $BC_{14}Z_{10}T$, $BC_{12}Z_{10}T$, and $BC_{10}Z_{10}T$.

Table 4.2: Remanent polarisation, coercive field, minimum and maximum strain, remanent relative permittivity, and remanent piezoelectric coefficient values for $BC_{15}Z_{10}T$, $BC_{14}Z_{10}T$, $BC_{12}Z_{10}T$, and $BC_{10}Z_{10}T$.

BCZT	Ave. P_r ($\mu C/cm^2$)	Ave. E_c (kV/cm)	$S_{min.}$ (%)	$S_{max.}$ (%)	ε_r	Ave. d_{33r} (pC/N)
$BC_{15}Z_{10}T$	10.28	1.52	-0.021	0.068	3896	377
$BC_{14}Z_{10}T$	9.46	1.37	-0.014	0.053	2642	312
$BC_{12}Z_{10}T$	10.96	1.32	-0.018	0.066	2889	318
$BC_{10}Z_{10}T$	9.21	0.92	-0.013	0.062	2847	291

All polarisation curves appear well-developed and symmetric, and display the classical ferroelectric hysteresis shape, in that a drastic change in the polarisation is observed in proximity to the coercive field (Figure 4.4 (a)) [48]. The polarisation loop near the coercive field is most perpendicular to the horizontal axis for $BC_{12}Z_{10}T$ and least perpendicular for $BC_{15}Z_{10}T$, showing that domain switching spans the broadest field for $BC_{15}Z_{10}T$. $BC_{12}Z_{10}T$ has the largest P_r value of 10.96 $\mu C/cm^2$, followed by $BC_{15}Z_{10}T$, $BC_{14}Z_{10}T$, and $BC_{10}Z_{10}T$, as given in Table 4.2. Additionally, inspection of the E_c shows that $BC_{15}Z_{10}T$ is the hardest piezoelectric ceramic because it requires the highest applied electric field for polarisation reversal. $BC_{10}Z_{10}T$ is the softest of the four compositions.

The strain loops presented in Figure 4.4 (b) have a butterfly shape, and are symmetric except for $BC_{14}Z_{10}T$, which is slightly asymmetric. The largest difference between the $S_{min.}$ and $S_{max.}$ values under positive electric field is 0.089 % for $BC_{15}Z_{10}T$.

The relative permittivity loops are displayed in Figure 4.4 (c). The highest and lowest ε_r are observed for $BC_{15}Z_{10}T$ and $BC_{14}Z_{10}T$, respectively. Furthermore, two maxima are observed under increasing positive field for $BC_{15}Z_{10}T$, $BC_{14}Z_{10}T$, and $BC_{12}Z_{10}T$, and only one maximum is seen under increasing positive field for $BC_{10}Z_{10}T$. Similar behaviour is observed under negative applied fields.

The d_{33r} is pertinent in this work as it indicates the amount of charge that BCZT would be able to retain and supply to stimulate surrounding cell tissue whilst used as an active bone repair material. The d_{33} hysteresis loops are displayed in Figure 4.4 (d). $BC_{15}Z_{10}T$ shows the highest d_{33r} at 377 pC/N, followed by $BC_{12}Z_{10}T$, $BC_{14}Z_{10}T$ and $BC_{10}Z_{10}T$.

The phase transition temperatures of the BCZT materials were investigated with impedance spectroscopy. Figure 4.5 displays the permittivity at a frequency of 1.56 Hz, over a temperature range of 20–100 °C.

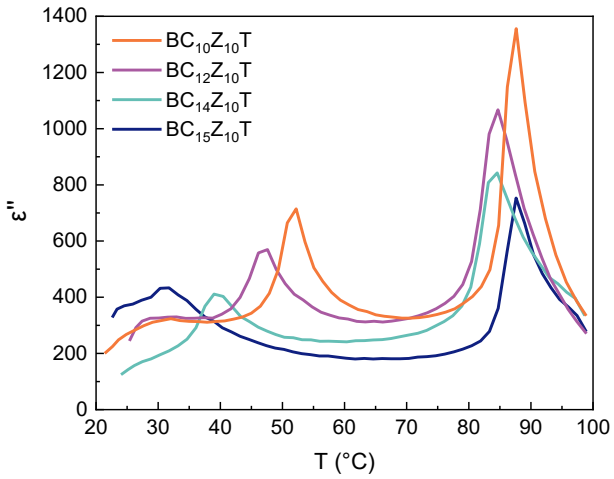

Figure 4.5: Impedance spectroscopy measurements of $BC_{15}Z_{10}T$, $BC_{14}Z_{10}T$, $BC_{12}Z_{10}T$, and $BC_{10}Z_{10}T$ performed over a temperature range of 20–100 °C.

The orthorhombic to tetragonal phase transition (T_{O-T}) is observed at 30–50 °C, increasing in temperature with decreasing Ca content from $BC_{15}Z_{10}T$ to $BC_{10}Z_{10}T$. The tetragonal to cubic phase transition (T_{T-C}) is observed at 80–90 °C. The transition temperatures for each composition are summarised in Table 4.3. The appearance of two transition temperatures indicates that all BCZT materials are multi-phase, with both tetragonal and orthorhombic structures at room temperature.

Table 4.3: Orthorhombic to tetragonal, and tetragonal to cubic transition temperatures of $BC_{15}Z_{10}T$, $BC_{14}Z_{10}T$, $BC_{12}Z_{10}T$, and $BC_{10}Z_{10}T$ determined from impedance spectroscopy.

BCZT	T_{O-T} **(°C)**	T_{T-C} **(°C)**
$BC_{15}Z_{10}T$	32	87
$BC_{14}Z_{10}T$	40	84
$BC_{12}Z_{10}T$	47	85
$BC_{10}Z_{10}T$	52	88

4.2. Discussion

The aim of this section of work was to investigate the effect of phase composition on piezoelectric performance, in order to understand how BCZT can be tailored for the biological environment without the need for toxic elemental additives.

4.2.1. Structural Transition

One of the recent models of the BCZT phase diagram by Liu and Ren describes a tilted MPB separating rhombohedral and tetragonal phases, as well as a TCP between cubic, tetragonal and rhombohedral phases [27]. Indeed, the XRD diffractograms of the $BC_{15}Z_{10}T$ composition in this work agree with Liu and Ren's description of the room temperature $BC_{15}Z_{10}T$ composition as an MPB composition of tetragonal and rhombohedral phases. However, their model describes the other three compositions as single-phase rhombohedral and omits the presence of an orthorhombic phase, which is not in agreement with the current XRD patterns (Figure 4.2). The revised BCZT phase diagram by Keeble et al. proposes an orthorhombic phase between the rhombohedral and tetragonal phases [70], [71], which is in accordance with the evident orthorhombic phase visible in the present XRD diffractograms. Furthermore, the present compositions follow the structural transition from tetragonal to rhombohedral structures with decreasing calcium content, as described by the phase diagram by Keeble et al. Other more recent reports dispute the presence of the orthorhombic phase and propose that the transition region arises instead from the coexistence of the tetragonal and rhombohedral phases only [72], [117]. The varying descriptions of the BCZT phase diagram, and the varied denotations of the transition region as a convergence region and diffuse phase transition, highlights the complexity of the system and the difficulties surrounding its characterisation. It also exposes the challenge to predict the piezoelectric and dielectric properties of specific BCZT compositions.

4.2.2. Influence of Phase Fractions on Piezo- and Dielectric Response

Distinct changes in the piezoelectric and dielectric properties were observed with a change in the calcium content of the different BCZT materials, showing that there is a correlation between the electromechanical behaviour and the specific proportion of tetragonal, orthorhombic, and rhombohedral phases.

XRD measurements and impedance spectroscopy confirm the presence of tetragonal and rhombohedral phases at room temperature (Figure 4.2 & Figure 4.5), and although the XRD patterns indicated that the BCZT materials contain an orthorhombic phase, the shapes of the relative permittivity loops suggest that it does not contribute significantly to the net electric properties (Figure 4.4 (c)). Any material having only an orthorhombic phase, or any mixture with the orthorhombic phase are expected to show one maximum under increasing electric field bias signifying one predominant domain switching event. This is because domain reorientations are facilitated at lower and more similar coercive fields by the lower energy landscape that is enabled by the high number of available polarisation directions. Not all of the BCZT curves show one maximum – hence, the orthorhombic phase does not contribute to a large extent to the net electric behaviour and therefore constitutes only a tiny fraction of the phase mixture.

The height difference between 180° and non-180° domain switching events reveal that there is an effect of the proportion of tetragonal and rhombohedral phases [50]. The relative permittivity curves from Figure 4.4 (c) are replotted in Figure 4.6, where the curves are shifted along the *y*-axis such that the ε_r values lie at the origin.

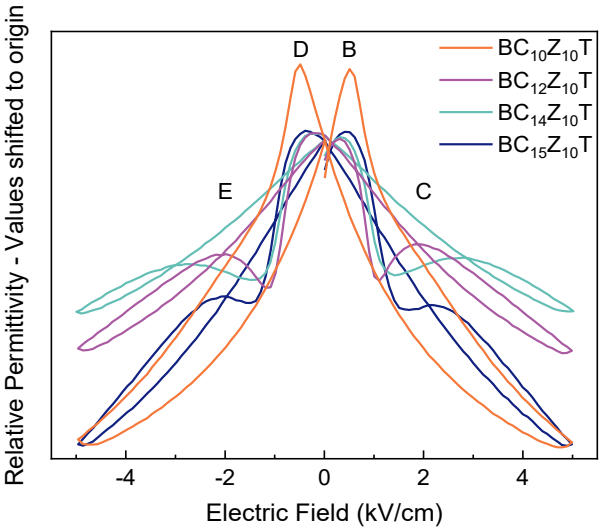

Figure 4.6: Relative permittivity hysteresis loops of $BC_{15}Z_{10}T$, $BC_{14}Z_{10}T$, $BC_{12}Z_{10}T$, and $BC_{10}Z_{10}T$ shifted along the y-axis such that the remanent relative permittivity values are located at the origin.

$BC_{10}Z_{10}T$ shows only one maximum (peak B) upon positive field application, showing that the majority of the phase mixture is rhombohedral. Of the other three materials, a comparison of the 180° and non-180° peaks (peaks B and C, respectively) shows that with increasing calcium content, the 180° and non-180° domain switching events occur with more dissimilar permittivity values (Table 4.4). From $BC_{12}Z_{10}T$ to $BC_{15}Z_{10}T$, the 180° reversals become more predominant over the non-180° switching processes, showing that the tetragonal phase increasingly contributes to the phase mixture. Hence, the relative permittivity data supports the XRD measurement that there is a structural transition from primarily tetragonal to primarily rhombohedral phase mixtures ($BC_{15}Z_{10}T$ to $BC_{10}Z_{10}T$).

Table 4.4: Measured peak heights for 180° (peak B) and non-180° (peak C) domain switching contributions, and the differences in peak heights for $BC_{15}Z_{10}T$, $BC_{14}Z_{10}T$, and $BC_{12}Z_{10}T$.

BCZT	**Max. Peak Height (B) (180°)**	**Max. Peak Height (C) (Non-180°)**	**Peak Height Difference**
$BC_{15}Z_{10}T$	3939	3211	728
$BC_{14}Z_{10}T$	2672	2098	574
$BC_{12}Z_{10}T$	2921	2388	533

The polarisation, strain, and piezoelectric coefficient hysteresis loops (Figure 4.4 (a,b,d)) confirm the phase mixture observed from XRD, relative permittivity and impedance spectroscopy measurements. As expected, the predominantly rhombohedral composition, $BC_{10}Z_{10}T$ shows the lowest coercive fields and exhibits the least strain during polarisation switching due to enhanced domain reorientation allowed by eight <111> polarisation directions (Figure 4.4 (a,b)) [40]. In addition, an enhanced piezoelectric response is expected and observed for $BC_{15}Z_{10}T$ as it shows the highest d_{33r}. This is attributed to its more even mixture of tetragonal and rhombohedral phases confirmed in the current work and as predicted from literature, as well as the associated better alignment of dipoles with the field direction [27], [118].

Impedance spectroscopy measurements showed two phase transition temperature ranges of 80–90 °C, and 30–50 °C (Figure 4.5). The temperature range of 80–90 °C is in accordance with reported tetragonal-cubic transition temperature values [71], [90], [117],

[119], [120]. However, the lower phase transition temperature range of 30–50 °C is reported in literature as either the orthorhombic-tetragonal, or rhombohedral-tetragonal transition for BCZT materials. Given the appearance of tetragonal, orthorhombic, and rhombohedral phases in the XRD measurements (Figure 4.2), the phase transition temperature range of 30–50 °C is assigned as T_{O-T} in the current work. Other literature studies state the T_{R-O} phase transition temperature as ≈ 5–10 °C, which is below the measurement range of this work [119]. Therefore, the rhombohedral phase is not confirmed in the current work via impedance spectroscopy. Of the four materials, it would be expected that $BC_{15}Z_{10}T$ should show the best piezoelectric response at room temperature, due to the proximity of the T_{O-T} to room temperature at which the measurements were performed. In the vicinity of the T_{O-T}, enhanced electromechanical responses are observed due to instabilities in the polarisation state facilitated by a relatively flat energy landscape, which eases the rotation of the domains [121], [122]. Indeed, $BC_{15}Z_{10}T$ displayed the best d_{33r} of the four materials. If implanted into the body however, it would be expected that $BC_{14}Z_{10}T$ would be most suitable as the T_{O-T} (40 °C) is more favourable at the human body temperature of 37 °C.

4.3. Summary

The BCZT material system is highly complex. This is highlighted by the varied literature descriptions of its phase diagram combined with the challenging nature of precise characterisation of the BCZT system. This complexity makes prediction of the piezoelectric and dielectric responses difficult. Nonetheless, the current work exemplifies that the electromechanical behaviour of these ceramics is significantly influenced by the structural phase, and the fraction of the phases in a mixed-phase material. Thus, the piezoelectric response of implantable BCZT ceramics in biological environments can be optimised through phase composition tailoring, eliminating the need for toxic chemical additives. Of the four BCZT materials studied, $BC_{15}Z_{10}T$ is the most suitable for application as an active bone replacement material. This is due to its high d_{33r}, which indicates the amount of charge the material could theoretically deliver as electrical stimuli to encourage the formation of bone cell tissue.

Chapter 5

Biological Cell Testing

To implement BCZT piezoelectric ceramics as novel electrically active implant materials for bone regeneration, it is imperative to understand its interaction with human cells and physiological media to assess its biocompatibility, and the potential release of ionic species that can be detrimental to the survival rate of an implant and the patient's health. In the first part of this chapter, unpoled bulk BCZT ceramics were investigated in an *in vitro* environment with human osteoblast and endothelial cells to determine their potential as implant materials. Further, poled BCZT samples were assessed for their piezoelectric response, microstructural adaption, and potential for storing and supplying charge. In the second part, the nature of ion release from BCZT ceramics in deionised water and 0.154 M NaCl solution was investigated to anticipate potentially adverse reactions and to enable the design of suitable pre-implantation material preparation procedures.

5.1. Results

5.1.1. Cell Proliferation and Viability

5.1.1.1. Phase Purity and Composition

The XRD patterns for the six synthesis batches of calcined and sintered $BC_{15}Z_{10}T$ are presented in Figure 5.1. The calcined powders appear phase pure. After sintering, the samples show increased crystallinity as evidenced by the smaller FWHM. No difference in the XRD patterns of Series 1 and 2 samples was observed (Series 1 $BaCO_3$ purity $\geq$ 99.00 %: C1,C2 & Series 2 $BaCO_3$ purity $\geq$ 99.98 %: C3–C6). A small amount of secondary phases are indicated by the asterisk (*) and were described in Chapter 4.

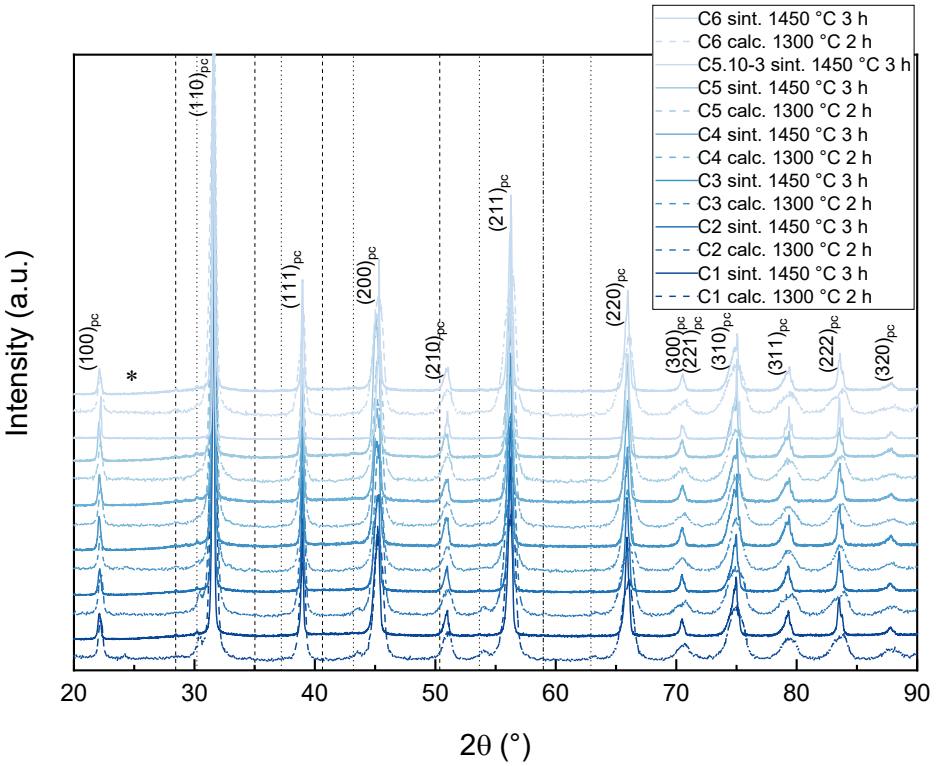

Figure 5.1: XRD patterns of calcined and sintered $BC_{15}Z_{10}T$ ceramics. Letters (C1–C6) represent the synthesis batches. Dashed and dotted black lines: Cu $K\beta_1$ and W $L\alpha_1$ peaks, respectively. Asterisk (*): secondary phases.

Figure 5.2 displays the pseudo-cubic (200), (220), and (222) reflections for a $BC_{15}Z_{10}T$ sample representative of the materials. Splitting is observed for all of the reflections, showing that the BCZT composition lies within the MPB region with influences from tetragonal, orthorhombic, and rhombohedral phases. The sintered material is primarily tetragonal, as shown by the significant splitting of the $(200)_{pc}$ peak and slight split of the $(222)_{pc}$ peak. An orthorhombic contribution is observed by the presence of a third peak between the two identified in the $(200)_{pc}$ reflection. This is intentionally marked with an asterisk (*) as it overlaps with a Cu $K\alpha_2$ peak.

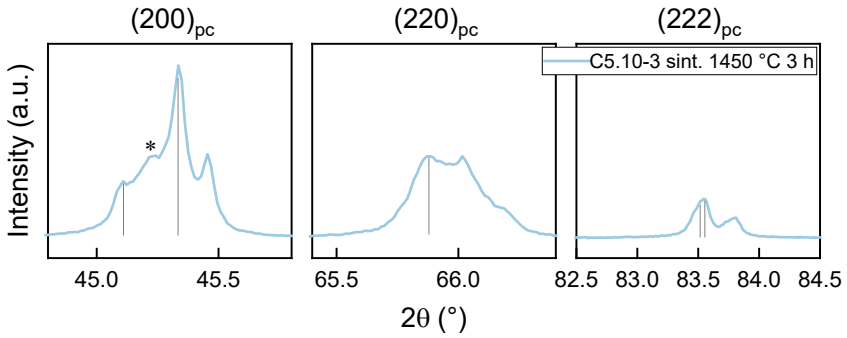

Figure 5.2: XRD pattern of sintered $BC_{15}Z_{10}T$. Ranges 44.8–45.8°, 65.4–66.4°, and 82.5–84.5° correlate with $(200)_{pc}$, $(220)_{pc}$, and $(222)_{pc}$ reflections, respectively. Grey lines: peak splitting. Unmarked peaks to the right of the grey lines: Cu $K\alpha_2$ contributions. Asterisk (*): overlap of a peak and Cu $K\alpha_2$ contribution.

5.1.1.2. Microstructure

Figure 5.3 shows representative SEM micrographs of BCZT ceramics from Series 1 and 2. Both microstructures show irregularly shaped grains, narrow grain size distributions, and intergranular porosity at grain triple points [116].

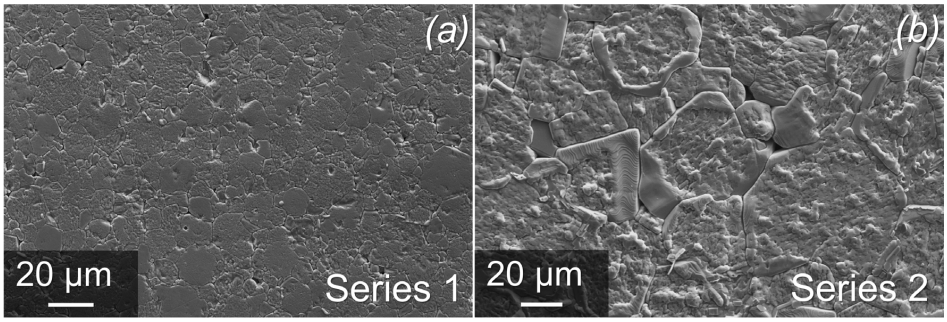

Figure 5.3: SEM micrographs micrographs of polished and etched $BC_{15}Z_{10}T$ (a) Series 1 and (b) Series 2 bulk sintered ceramics, synthesised using $BaCO_3$ precursor powders of purity level ≥ 99.00 and 99.98 %, respectively.

The average grain size, density and relative density of Series 1 and 2 are displayed in Table 5.1. Series 1 has a significantly smaller average grain size than Series 2, and a slightly higher average density. The relative density of all ceramic samples is ≈ 99 %.

Table 5.1: Average grain sizes and densities of $BC_{15}Z_{10}T$ Series 1 and 2, synthesised using $BaCO_3$ precursor powders of purity level ≥ 99.00 and 99.98 %, respectively.

BCZT Series	Ave. Grain Size (µm)	Ave. Density (g/cm^3)
1	10 ± 2	6.0 ± (0.33)
2	35 ± 8	5.6 ± (0.27)

5.1.1.3. Surface Properties

The surface morphologies of the BCZT and polystyrene control group samples as-prepared for cell testing are presented in Figure 5.4. The SEM micrographs show that the BCZT ceramic surface prepared with 1200 grit SiC paper is rougher than the as-received polystyrene surface. SPM measurements quantitatively confirm the surface roughness, R_a, of BCZT and polystyrene as 0.840 and < 0.001 µm, respectively.

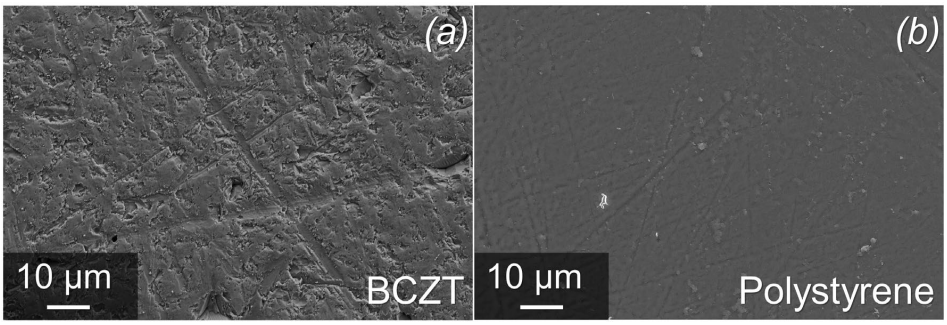

Figure 5.4: SEM micrographs of (a) $BC_{15}Z_{10}T$ surface grinded with 1200 grit SiC paper, and (b) polystyrene control group surface as-received. The surfaces reflect the surface roughness present during cell testing.

Deionised water contact angle measurements on BCZT and polystyrene were performed at 37 °C. An enhanced wettability was observed on BCZT surfaces (41.2 ± 3.9 °) as compared to the polystyrene surfaces (87.6 ± 1.6 °).

5.1.1.4. Piezoelectric Properties

The polarisation, strain, relative permittivity and piezoelectric coefficient hysteresis loops of Series 1 and 2 materials are displayed in Figure 5.5 (a-d). The remanent polarisation, coercive field, minimum and maximum strain, remanent relative permittivity, and remanent piezoelectric coefficient values are displayed in Table 5.2.

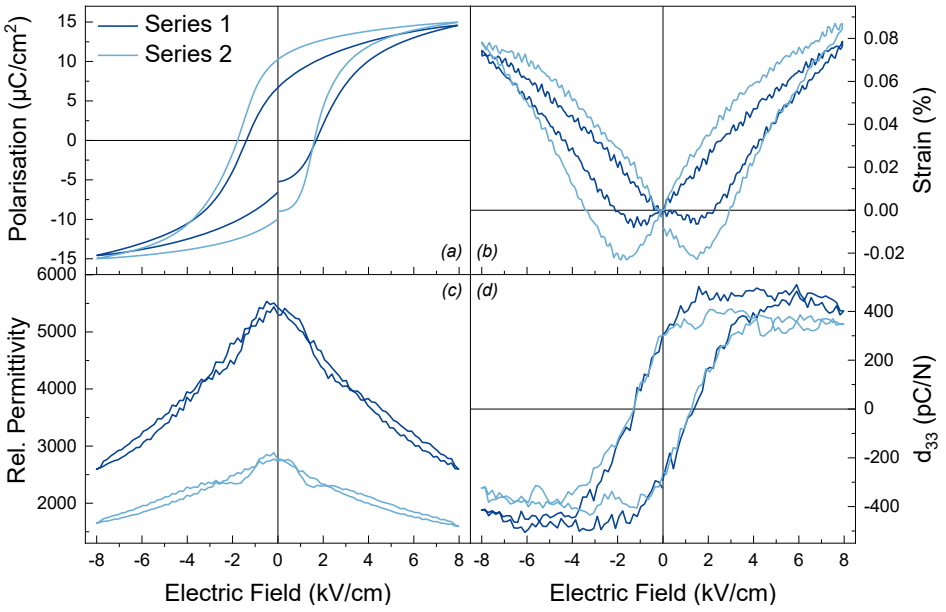

Figure 5.5: (a) Polarisation, (b) strain, (c) relative permittivity, and (d) piezoelectric coefficient hysteresis loops for $BC_{15}Z_{10}T$ Series 1 and 2.

The polarisation loops have a classical ferroelectric shape and are quite symmetric (Figure 5.5 (a)). Series 1 displays a lower P_r than Series 2, and a more slanted polarisation hysteresis loop near the coercive field indicative of its smaller grain size [47]. Series 2 is a slightly harder piezoelectric ceramic, as it requires a slightly higher polarisation field (E_c). The strain hysteresis loops are well-developed and symmetric (Figure 5.5 (b)), and Series 2 displays a larger overall strain magnitude than Series 1. Both permittivity hysteresis loops are quite symmetric and show two maxima on increasing positive field, which represent 180° and non-180° domain switching processes that typify primarily tetragonal structures (Figure 5.5 (c)) [50]. Series 1 shows a higher remanent relative permittivity than Series 2. Figure 5.5 (d) shows the piezoelectric coefficient hysteresis loops of ceramics from Series 1 and 2. Although Series 1 has a larger piezoelectric response while high electric fields are applied (d_{33s}), both Series 1 and 2 display similarly high remanent values, d_{33r}, of approximately 280 pC/N.

Table 5.2: Remanent polarisation, coercive field, minimum and maximum strain, remanent relative permittivity, and remanent piezoelectric coefficient values for $BC_{15}Z_{10}T$ Series 1 and 2.

BCZT Series	Ave. P_r (μC/cm^2)	Ave. E_c (kV/cm)	$S_{min.}$ (%)	$S_{max.}$ (%)	ε_r	Ave. d_{33r} (pC/N)
1	6.64	1.54	-0.006	0.079	5101	278
2	10.35	1.68	-0.023	0.087	2767	297

5.1.1.5. *In vitro* Interaction with HUVECs and HOBs

Cell viability of primary human osteoblasts (HOBs) and primary human umbilical vein endothelial cells (HUVECs) on BCZT and polystyrene were investigated via FDA/PI staining (Figure 5.6). The viable cells are stained green and dead cells are stained red. Well-spread filopodia are observed on vital and adjacent cells on both BCZT and polystyrene surfaces after 24 h in cell culture, with slightly more spreading observed on BCZT. Significantly more vital HOBs are observed on both BCZT and polystyrene surfaces than HUVECs, and more vital HOBs are seen on the BCZT surface than the polystyrene surface.

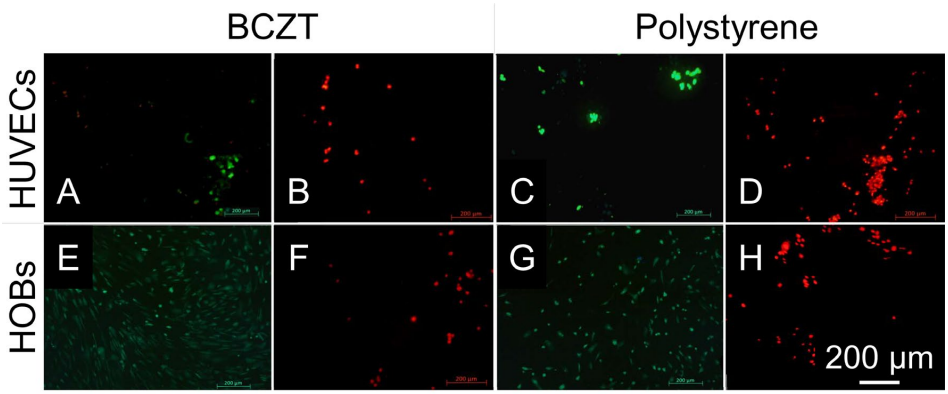

Figure 5.6: FDA/PI viability staining of HUVECs (A–D) and HOBs (E–H) on BCZT (A,B,E,F) and a polystyrene control group (C,D,G,H). Viable cells are stained green and dead cells are stained red.

Cell proliferation of HUVECs and HOBs were measured over a 10-day period on BCZT and polystyrene. The counted cell numbers are displayed Table 5.3, and illustrated in Figure 5.7 (a). A constant proliferation of both cell types on BCZT was observed from Days 1 to 7. The cell count on Day 10 decreased to 3.4 x 10^4 for HUVECs, and 3.8 x 10^4

for HOBs. Constant proliferation of HUVECs and HOBs was observed on the polystyrene control group during the entire testing period. The HUVECs cell culture notably showed significantly higher proliferation rates on BCZT than on polystyrene from Days 1 to 7. The HOBs cell culture showed statistically significant results on Days 7 and 10.

Table 5.3: Counted cell numbers at given time points. Asterisk (*): statistically significant results ($p < 0.05$).

Cell	Day	1	3	7	10
HUVECs	**BCZT**	9457 ± 423	20608 ± 6963	45620 ± 6254	34110 ± 9822
	Polystyrene	5126 ± 461	10175 ± 2659	30840 ± 7786	38270 ± 9771
	p	0.008*	0.016*	0.032*	0.690
HOBs	**BCZT**	6368 ± 3414	8582 ± 2538	45400 ± 18062	38120 ± 11179
	Polystyrene	5388 ± 2090	7138 ± 2203	8200 ± 2083	9072 ± 2605
	p	0.690	0.690	0.008*	0.008*

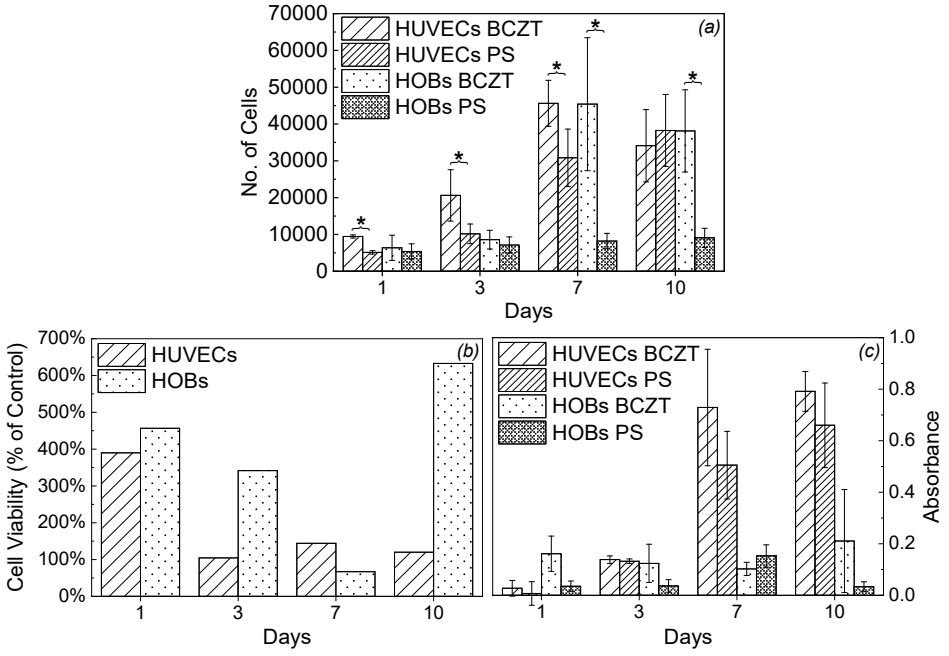

Figure 5.7: Comparison of HUVECs and HOBs cell activity over a 10-day period on BCZT and polystyrene (PS) surfaces: (a) cell proliferation, (b) number of viable cells observed on BCZT relative to PS, (c) cell viability shown by absorbance of mitochondrial dehydrogenase activity. Asterisk (*): statistically significant results ($p < 0.05$).

Cell viability of HUVECs and HOBs on BCZT and polystyrene was investigated using WST assays. The WST assay reveals that a higher number of living HUVECS and HOBs were detected on BCZT over the 10-day period compared to polystyrene, as displayed in Figure 5.7 (b), which shows the percentage of viable cells on the BCZT surface compared to the control group surface.

Figure 5.7 (c) presents a detailed progression of the cell viability during the testing period. A higher absorbance indicates a higher activity of mitochondrial dehydrogenase and therefore, the amount of viable, metabolically active cells. For all days, a higher activity of HUVECs was observed on BCZT than on polystyrene. Similarly, a higher proportion of viable HOBs were observed on BCZT than on polystyrene for all days except for Day 7, which is attributed to cell overcrowding that can limit growth.

5.1.2. Soaking and Ion Release

5.1.2.1. Phase Purity and Composition

The XRD patterns of calcined and sintered $BC_{15}Z_{10}T$ are presented in Figure 5.8. The BCZT powders appear to be phase pure after calcination, and more crystalline after sintering as shown by the reduced FWHM. Small amounts of a secondary phase (*) were observed, as described in Chapter 4. Sintered samples milled into fine powders were used for the soaking and ion release tests.

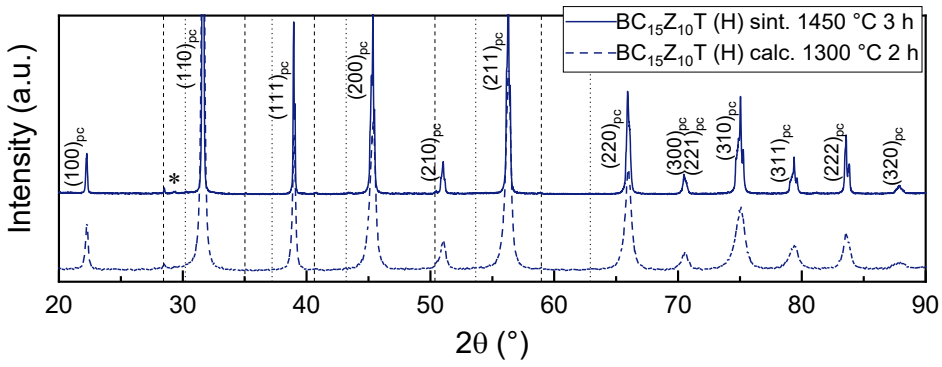

Figure 5.8: XRD patterns of calcined and sintered $BC_{15}Z_{10}T$ ceramics. Letter (H) represents the synthesis batch. Dashed and dotted black lines: Cu $K\beta_1$ and W $L\alpha_1$ peaks, respectively. Asterisk (*): secondary phases.

The XRD pattern of sintered $BC_{15}Z_{10}T$ is displayed in Figure 5.9 for the 2Θ ranges 44.8–45.8°, 65.4°–66.4°, and 82.5–84.5°, corresponding to the pseudo-cubic (200), (220), and (222) reflections. Splitting is observed for the $(200)_{pc}$, $(220)_{pc}$, and $(222)_{pc}$ reflections, showing that the BCZT material lies at the MPB region with tetragonal, orthorhombic, and rhombohedral phases. The exaggerated split of the $(200)_{pc}$ peak and less exaggerated split of the $(222)_{pc}$ peak shows that the composition is predominantly tetragonal. A third (*) peak is observed in the $(200)_{pc}$ reflection between the two marked peaks, which originates from orthorhombic contributions.

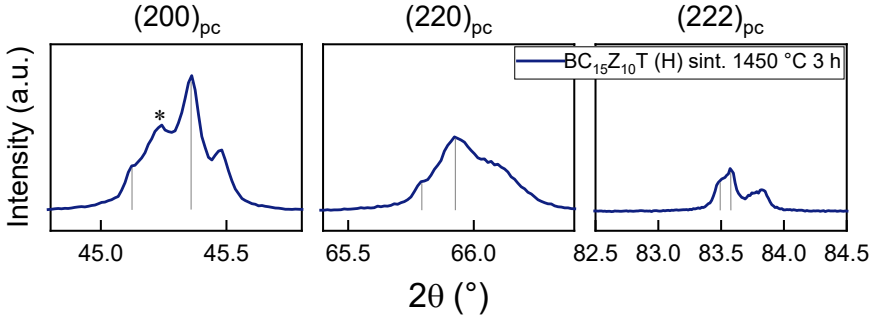

Figure 5.9: XRD pattern of sintered $BC_{15}Z_{10}T$. Ranges 44.8–45.8°, 65.4–66.4°, and 82.5–84.5° correlate with $(200)_{pc}$, $(220)_{pc}$, and $(222)_{pc}$ reflections, respectively. Grey lines: peak splitting. Unmarked peaks to the right of the grey lines: Cu Kα2 contributions. Asterisk (*): overlap of a peak and Cu Kα2 contribution.

5.1.2.2. Surface Area and Particle Size

The specific surface area (SSA) was determined to be 9.2 ± (0.07) m^2/g.

The average particle diameter, $diam$, was calculated to be ≈ 111 nm by the following equation assuming spherical particles, where ρ_{BCZT} is the crystallographic density of BCZT (g/cm^3).

$$diam = \frac{6000}{\rho_{BCZT} \times SSA} \tag{8}$$

A calculated crystallographic density of 5.827 g/cm^3 for $BC_{15}Z_{10}T$ was used.

5.1.2.3. Ion Release

Figure 5.10 displays the ICP-MS results of the Ba, Ca, Zr, and Ti ion release from $BC_{15}Z_{10}T$ powders in (a) 0.154 M NaCl solution and (b) deionised water at 37 °C, over a 90-day period. The values are presented in Table 5.4. The release of Ba ions throughout

the testing period was significantly higher than the release of Ca, Zr, and Ti ions in both 0.154 M NaCl solution and deionised water. Furthermore, the most substantial increase in the Ba ion release was observed within the first 10 days, after which it stabilised, and reduced after Day 30. A similar behaviour is seen in the Ca ion release however, the release remains stable until the end of the testing period. Both Zr and Ti ion concentrations were observed to slightly increase over the entire 90-day period. In 0.154 M NaCl solution, the average ion release over 90 days was the highest for Ba (7155 µg/g), followed by Ca (216 µg/g), Ti (33 µg/g), and Zr (3 µg/g). In deionised water, the same trend was observed in the average ion release values of Ba (6724 µg/g), Ca (201 µg/g), Ti (41 µg/g), and Zr (4 µg/g).

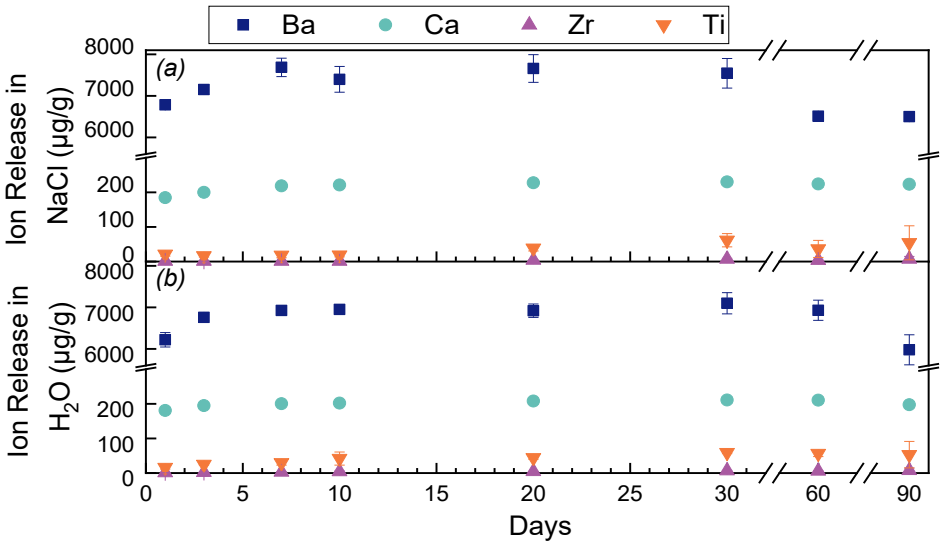

Figure 5.10: Ion release from $BC_{15}Z_{10}T$ powders in 0.154 M NaCl solution and deionised water at 37 °C a 90-day period. Values are in µg/g of BCZT powder.

Table 5.4: Release values of Ba, Ca, Zr, and Ti ions from $BC_{15}Z_{10}T$ powders in 0.154 M NaCl solution and deionised water over a 90-day period. Values are in µg/g of powder.

	Ion Release (µg/g)							
Day	**Ba**		**Ca**		**Zr**		**Ti**	
	NaCl	**H_2O**	**NaCl**	**H_2O**	**NaCl**	**H_2O**	**NaCl**	**H_2O**
1	6784 ± 89	6220 ± 174	185 ± 2	181 ± 9	1 ± 0	1 ± 0	21 ± 5	16 ± 5
3	7153 ± 107	6761 ± 74	200 ± 3	195 ± 3	1 ± 0	2 ± 0	16 ± 3	25 ± 1
7	7687 ± 220	6927 ± 99	219 ± 6	200 ± 3	1 ± 1	3 ± 1	18 ± 7	30 ± 7
10	7399 ± 311	6951 ± 106	221 ± 5	202 ± 3	1 ± 0	4 ± 2	19 ± 5	42 ± 19
20	7661 ± 333	6921 ± 160	227 ± 7	208 ± 7	4 ± 1	5 ± 0	39 ± 8	44 ± 4
30	7546 ± 356	7099 ± 256	230 ± 8	211 ± 8	7 ± 3	7 ± 1	62 ± 19	59 ± 3
60	6512 ± 94	6930 ± 243	225 ± 9	211 ± 9	4 ± 3	6 ± 1	36 ± 25	56 ± 8
90	6502 ± 77	5980 ± 362	224 ± 3	197 ± 8	7 ± 8	8 ± 7	54 ± 49	53 ± 38

The molar ratios Ba/Ca (0.85:0.15) and Zr/Ti (0.1:0.9) based on the nominal BCZT composition are presented in Table 5.5, as well as the maximum ion release ratios extracted from Day 30 concentration values. No significant difference in the ion release ratios were observed between the two different media, and the ratio of Zr/Ti loss fits well to the nominal values. Furthermore, significantly more Ba was released than Ca, which is expected as Ba constitutes a greater proportion of the composition ($BC_{15}Z_{10}T$). However, the concentration of Ba in both 0.154 M NaCl and deionised water is one order of magnitude higher than expected based on the Ba/Ca molar ratio.

Table 5.5: Molar ratios of Ba/Ca and Zr/Ti based on the nominal $BC_{15}Z_{10}T$ composition, and the observed ratios determined from the maximum ion release concentration values from Day 30.

Ions	**Molar Ratio**	**Observed Ion Release Ratio**	
		NaCl	**H_2O**
Ba/Ca	5.7	32.8	33.6
Zr/Ti	0.1	0.1	0.1

5.2. Discussion

BCZT ceramics are currently not implemented as implantable materials. Therefore, in this section of work it was critical to assess how BCZT ceramics affect human cells, and how a simulated physiological environment will interact with these ceramics.

5.2.1. Cell Proliferation and Viability

5.2.1.1. Piezoelectric Properties

Significantly different grain sizes for the two BCZT series were achieved by using two $BaCO_3$ precursor powders of differing purity levels. Series 1 produced using $BaCO_3$ of purity ≥ 99 % exhibits suppressed grain growth much like A-site deficient $PbTiO_3$ [39], [123], while Series 2 synthesised with $BaCO_3$ precursor powders of higher purity (≥ 99.98 %) displayed enhanced grain growth behaviour similar to B-site deficient $PbTiO_3$ [39], [123]. The minor cation non-stoichiometry introduced by different purity precursor powders affected the sintering behaviour and the resulting grain sizes.

The figure of merit for the application of piezoelectric ceramics as load-bearing bone implant materials is the d_{33r}, as it indicates the amount of electrical stimuli that can be provided. For Series 1 and 2 having the same BCZT composition ($BC_{15}Z_{10}T$) but dissimilar average grain sizes, similarly high d_{33r} values ≈ 280 pC/N were achieved. However, a grain size effect was observed under electric field application. This behaviour is attributed to the softness of the BCZT system. These materials display strong domain switching and high piezoelectric responses under electric field application, and strong relaxation of aligned domain structures as electric field is reduced [51], [52]. This is because of small lattice distortions, such that the energy barrier between different domain orientations is small and requires relatively little energy to overcome [52]. Although the influence of grain size on the piezoelectric response of BCZT is yet to be investigated in detail, there appears to be correlations to the BT system, where 90° domain wall motion associated with larger grains enhances piezoelectric performance [47], [54], [55]. In the current work, the effect of grain size does not dominate the electrical softness of the investigated composition. However, it can be assumed that the grain size would have a more prominent effect on single-phase compositions that are less affected by changes in the applied field. Therefore, it is probable that the piezoelectric response, and the effective

charge that can be used as cell stimulation, can be optimised through tailoring of the microstructure of BCZT ceramics. This offers a promising alternative optimisation route to using toxic chemical dopants.

5.2.1.2. Influence of Surface Properties on Cell Response

Optimisation of the design of implant surfaces revolves primarily on tailoring surface properties such as roughness, wettability, and surface energy, as these are properties known to have a great impact on cell interactions [7], [124], [125]. Nano-, micro-, and macro-roughness affect cell adhesion and spreading behaviour [10], [124]–[127]. In particular, surface roughness values of ≈ 1 µm enhance cell adhesion of osteoblasts, supporting the present observation of improved cell attachment and filopodia spreading on BCZT compared to polystyrene surfaces (Figure 5.4 & Figure 5.6) [7], [10], [125]. Surface wettability is another factor that influences cell adhesion and spreading. It has been reported that moderate contact angles of approximately 60 ° enhance osteoblast adhesion [7], [124]. An elevated number of HUVECs and HOBs were measured on the BCZT surfaces during the cell proliferation tests compared to the polystyrene surfaces, as displayed in Figure 5.7 (a). This could be the result of the better wettability of deionised water on BCZT than polystyrene, as evidenced by the contact angle values of ≈ 41 ° [128].

To maximise the stimulating effect of piezoelectric ceramic materials in bone replacement applications, the materials must be electrically poled. In bulk piezoelectric ceramics, each grain is oriented differently to the crystallographic axis with respect to the sample surface. In addition, the surface charge that develops under a mechanical load varies between grains, and between domains in a single grain. Variations between the grains occur on a length scale of 1–100 µm, and 10–500 nm on the domain scale [53]. Although the macroscopic remanent piezoelectric coefficient was found to be independent of the grain size between Series 1 and 2, it is likely that both grain size and domain size will electrically have a more dominating effect on local cell interactions. In addition, there is potential to tune the domain size since it scales with grain size ($d \approx g^{0.5}$) [47], [56]. Furthermore, atomic force microscopy studies on BT show that surface energies vary with domain type, and influence water adsorption such that preferential adsorption occurs on domains with higher electric potential [129]. It is likely that cells

would similarly be affected by the type and number of domains they interface with, and this could be a route for enhancing cell adhesion or guidance.

5.2.2. Soaking and Ion Release

5.2.2.1. Release of Ions

As a simple model, the preferential leaching of Ba compared to Ca ions can as a first approximation be attributed to the difference in ionic field strength, $Z/_{r^2}$, where Z is the valency of the ion and r is the ionic radius (Table 5.6) [130], [131]. Further, the smaller release of Zr^{4+} and Ti^{4+} compared to the A-site ions is related to their significantly higher ionic field strengths.

Table 5.6: Ionic radii and calculated ionic field strengths of Ba^{2+}, Ca^{2+}, Zr^{4+}, and Ti^{4+} [114], [130], [132].

Ion	Ionic Radius (Å)	Ionic Field Strength
Ba^{2+}	1.61	0.77
Ca^{2+}	1.34	1.11
Zr^{4+}	0.72	7.72
Ti^{4+}	0.605	10.9

Data for Zr^{4+} and Ti^{4+} fit the expected ion release molar ratios (Table 5.5) in both deionised water and 0.154 M NaCl. Although Ba^{2+} was expected to be released in greater proportions than Ca ions, it is one order of magnitude higher than expected. This may be due to solution pH, and dissolved CO_2 in solution or particle surface interactions with atmospheric CO_2.

The solution pH can influence the amount and rate of A- and B-site ion dissolution. In the current work, the pH of each aliquot was not measured to prevent contamination of the samples with foreign apparatus, as ICP-MS is a highly sensitive technique. The significant initial release of A-site ions, and the slight increase of B-site ion release later in the soaking period is similar to the observed behaviour reported by Ozmen et al. who studied the chemical stability of alkali niobates in aqueous media [131]. They argue that the trend is due to pH of the solution, such that A-site ion release is promoted by low pH (pH 4) and B-site ion release is encouraged by high pH (pH 10) [131]. A study on the

effect of solution pH on Ba ion leaching from BT powders in water showed significant ion loss from pH 2 to 7, more gradual loss from pH 7 to 8, and significantly less above pH 8 [133]. Although the pH was not measured in the current work, Pisitpipathsin et al. soaked BCZT Bioglass composites in simulated body fluid (SBF) for 7 days and showed that the pH of SBF increased throughout the soaking period from pH 7.45 to 7.75 [32]. Based on the similarity to the effect of pH on alkali niobates and BT, the BCZT here likely follows comparable behaviour to BT in acidic and basic environments, where the system initially consumes H^+ in an acidic environment and then produces OH^- when it is in neutral or basic environments following the equations [131], [133]:

$$BaTiO_3(s) + 2H^+(aq) \rightarrow Ba^{2+}(aq) + TiO_2(s) + H_2O(l) \quad (9)$$

$$BaTiO_3(s) + H_2O(l) \rightarrow Ba^{2+}(aq) + TiO_2(s) + 2OH^-(aq) \quad (10)$$

Although it is unlikely that BCZT will initially create an acidic environment when soaked in water, the increase in solution pH from pH 7 could still affect the Ba^{2+} release [133]. As such, it is deduced that BCZT undergoes an incongruent dissolution, such that the ionic species release at different rates from the surface. This results in an outer layer that has a different stoichiometry from the pristine inner core, and in this case, an inner BCZT core with a stable B-site terminated surface.

In addition to pH, surface interactions of BCZT with CO_2 can cause the formation of $BaCO_3$ and affect the observed Ba ion release due to the slightly more soluble nature of $BaCO_3$ to $BaTiO_3$ in water [133]. The solubility of Ba^{2+} from $BaCO_3$ in cold neutral water is 0.002 g/100 mL [134]. In the current work, the maximum Ba^{2+} release in deionised water from Day 30 is one order of magnitude higher (0.071 g/100 mL), indicating that there are indeed factors exacerbating the release of Ba ions from BCZT powders. It is possible that surface interactions of the BCZT powders with dissolved CO_2 in deionised water and 0.154 M NaCl solution, and with atmospheric CO_2 have caused the formation of a reactive $BaCO_3$ surface on the powders [133], hence contributing to the higher than expected release of Ba ions into the soaking media. A similar behaviour has been reported by Yoon et al. on BT powders in deionised water that were influenced by surface interactions with CO_2 [133].

From Day 30, the amount of released Ba ions decreases, suggesting that the solution becomes over-saturated and barium is precipitated out of the solution. Nesbitt et al.

observed similar behaviour during the dissolution of bulk BT ceramics in water over three weeks, where small crystals of alkaline earth hydroxides formed on the hydrated BT surfaces at extended dissolution periods [135].

5.2.2.2. Shrinking Core Model

It is apparent from the ICP-MS measurements that BCZT undergoes incongruent dissolution of A- and B-site ions. The incongruent dissolution can be considered in terms of the shrinking core model, whereby after dissolution of the ions, a reaction layer forms on the surface and acts as a diffusion barrier. BCZT has two possible surface terminations: BaO (A-site) or TiO_2 (B-site). Since Ba ions leach profusely from the BCZT surface, while Ti releases in very small and gradual amounts, it is apparent that once the A-site ions are lost from the surface, the structure forms a B-site terminated surface that is stable in aqueous solution [133]. Figure 5.11 shows a schematic of the BCZT particle as it undergoes dissolution, where r_0 is the radius of the original particle, r_{core} is the radius of the stoichiometric core after ion dissolution, and $t_{reaction\ layer}$ is the thickness of the B-site rich surface layer after ion dissolution.

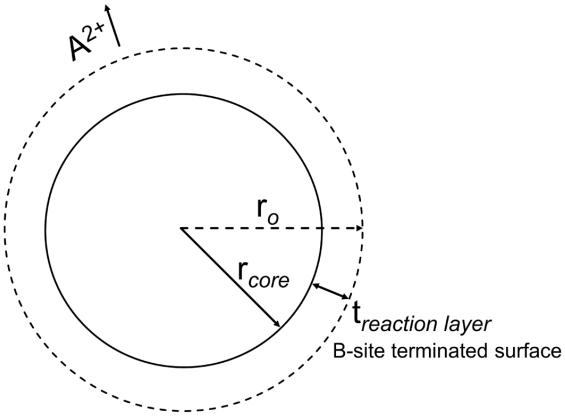

Figure 5.11: Schematic of the dissolution of a BCZT particle by the shrinking core model.

Based on the shrinking core model by Ring [116], applied by Kimel et al. and Ozmen et al. on YTZ and $K_{0.5}Na_{0.5}NbO_3$ (KNN), the approximate thickness of the reaction layer, $t_{reaction\ layer}$, can be determined through the parabolic rate function [131], [136]:

$$r_{core} = r_o * \left(\frac{X - X_t}{X}\right)^{1/3} \quad (11)$$

$$r_o - r_{core} = t_{reaction\ layer} \quad (12)$$

$$t_{reaction\ layer} = r_0 * (1 - \sqrt[3]{1-a}) \quad (13)$$

where X is the number of moles in 0.5 g of BCZT material, X_t is the amount of ions released after soaking time t in moles, and a is the fraction X_t/X. In the current work, X_t was taken as the amount of Ba ions released on Day 30 extracted from the ICP-MS data, and r_0 was calculated from the SSA (Section 5.1.2.2). Only Ba ion values were included in the calculation of the reaction layer thickness since they are leached in the highest proportion of all the ions. From the calculations, the reaction layer is approximately 0.22 nm and 0.23 nm in deionised water and 0.154 M NaCl, respectively. The approximate reaction layer thicknesses can be compared to the unit cell dimensions of tetragonal BCZT (c = 4 Å (PDF 00-065-0109)). It appears that only the first outer unit cell of the BCZT particle is affected by the soaking process since approximately half of the unit cell is removed. This correlates well with the theory that the removal of A-site ions during soaking alters the surface stoichiometry of the BCZT particle, such that it forms stable B-site terminations that prevent ongoing dissolution.

5.2.2.3. Toxicity

As the primary ion released in the current work, it is vital to compare the released Ba^{2+} values with the toxicity limit. Yamamoto et al. determined the cytotoxicity limit as 1.3 x 10^{-3} mol/L from viability testing of murine fibroblasts and osteoblasts with $BaCl_2$ salts [137]. In the current work, the maximum Ba ion release was observed on Day 7 in 0.154 M NaCl solution. The value is 5.5 x 10^{-3} mol/L when converted to the same units as used by Yamamoto et al. This value is higher than expected for an implanted bulk BCZT ceramic material due to the exceedingly high surface area of the particles used here. Nonetheless, the maximum Ba^{2+} release is almost 4.5 times higher than the determined cytotoxicity limit, which reveals the vulnerability of BCZT ceramics as implantable materials. However, based on the apparent removal of Ba^{2+} and the subsequent formation of a stable B-site surface layer on the BCZT material after soaking, a potential pre-implantation conditioning method can be proposed.

5.2.2.4. Pre-Conditioning of the Implant Material

The most significant loss of Ba^{2+} was observed within the first 10 days of soaking, followed by a stable period up to 30 days, at which the ion release values decreased due to precipitation of barium-species. Hence, a pre-conditioning route is proposed to remove the toxic Ba^{2+} from the BCZT bulk material prior to implantation. BCZT ceramics could feasibly be soaked for at least 10 days and adequately rinsed to remove mobile Ba^{2+} from the surface, leaving a stable B-site terminated surface that is insoluble in body fluids. Compounds of zirconium titanium oxides, particularly $ZrTiO_4$, are known to be biocompatible [138] and therefore, a B-rich BCZT surface would be a suitable non-cytotoxic interface with the surrounding cell tissue.

5.2.2.5. Effect of Surface Non-Stoichiometry on Piezoelectric Properties

Prior to implantation, BCZT ceramics should ideally be poled. However, when implanted, the ceramics will interact with adsorbed water from body fluids, which can affect their ferroelectric behaviour [102]. On B-site terminated BCZT surfaces, the hydroxyl groups will bond to the Zr^{4+} or Ti^{4+} on the surface [102]. DFT calculations by Geneste et al. on BT (001) surfaces have shown that surface hydroxylation causes polarisation pinning in the first unit cell by the orientation of OH^- groups [102]. This has been corroborated with empirical studies on BT thin films, where surface pinning creates a passive layer within three lattice constants in which ferroelectricity is lost and polarisation is not switchable [103]. Interestingly, the passive layer does not appear to adversely affect the bulk polarisation properties, but rather improves the symmetry of the bulk polarisation of materials that have polarisation imprint effects due to surface O vacancies [103], [139]. This indicates that although the polarisation is affected in the first 2–3 unit cells, the passive layer does not effectively screen the polarisation of the bulk material [103]. It is probable then, that the hydroxylation of BCZT surfaces will not alter the piezoelectric properties of the bulk material nor shall it screen the charge generated by the bulk material. Therefore, the effective charge that is determined through piezoelectric measurements is expected to be maintained even in an aqueous environment, ensuring that the high d_{33} measured will be transferred as electrical cell stimulation of similar magnitude.

Furthermore, it has been shown that compressive strain can reduce water chemisorption energy on TiO_2 terminations of BT (001) surfaces [102]. This indicates that when BCZT is applied as a compressive load-bearing material, the surface should be even less reactive to aqueous media, and therefore more stable against further hydroxylation during implantation [102]. However, it must be considered that a multitude of stresses, for example, compressive, tensile, and shear, will also be applied to the material while implanted as a result of cyclic mechanical loading, and may influence the chemical stability of the implant surface.

5.3. Summary

The BCZT MPB composition shows good piezoelectric response and compatibility with human osteoblast and endothelial cells. In particular, the enhanced cell proliferation observed on BCZT samples compared to the control group demonstrates the high potential of these ceramics as active bone replacement materials. Ion release studies on powder BCZT samples in deionised water and 0.154 M NaCl over a 90-day period show that incongruent dissolution of ions occurs. However, the release of A-site ions and the subsequent formation of a stable B-site terminated BCZT surface highlights a potential process for pre-conditioning BCZT prior to implantation.

Chapter 6

Piezoelectric Stability After Static Mechanical Loading

Mechanical loading can cause depolarisation of a piezoelectric material. BCZT ceramics will ideally be used in load-bearing applications for osteoblast stimulation. Therefore, it is important to understand how the piezoelectric response is affected by mechanical loading, and the influence of composition and grain size. Thereby, an avenue for tailoring the piezoelectric stability of BCZT and the length of its functional lifetime as a cell-stimulative material can be developed. In this chapter, the piezoelectric performance of bulk BCZT ceramics was investigated before and after the application of a compressive static mechanical load (-15 MPa) for up to 60 min. The following materials were investigated for dependence on composition – $BC_{15}Z_{10}T$, $BC_{14}Z_{10}T$, $BC_{12}Z_{10}T$, and $BC_{10}Z_{10}T$. For grain size dependency measurements, four grain size samples with average grain sizes of 60, 50, 35, and 2 μm were produced from $BC_{10}Z_{10}T$.

6.1. Results

6.1.1. Piezoelectric Stability as a Function of BCZT Composition

6.1.1.1. Phase Purity and Composition

XRD diffractograms of the calcined and sintered ceramics of $BC_{15}Z_{10}T$, $BC_{14}Z_{10}T$, $BC_{12}Z_{10}T$, and $BC_{10}Z_{10}T$ over the 2Θ range from 20–90° are displayed in Figure 6.1. The powders are phase pure after calcination and become more crystalline after sintering, as shown by the reduced FWHM. A small amount of secondary phases are observed and indicated by the asterisks (*), as described in Chapter 4.

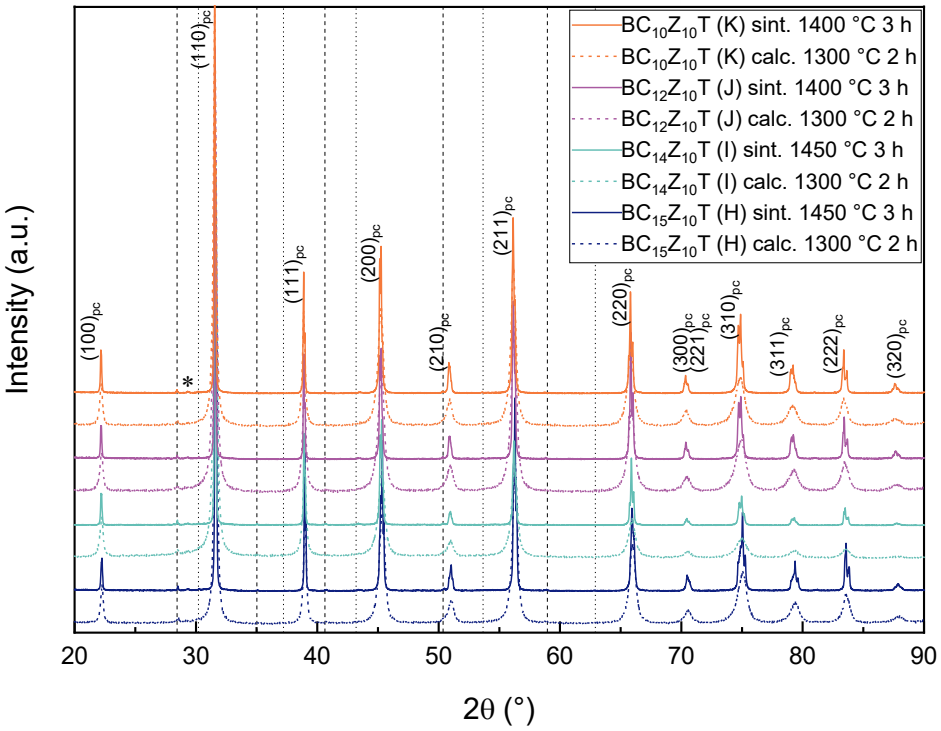

Figure 6.1: XRD patterns of calcined and sintered BCZT ceramics – $BC_{15}Z_{10}T$, $BC_{14}Z_{10}T$, $BC_{12}Z_{10}T$, and $BC_{10}Z_{10}T$. Letters (H,I,J,K) represent the synthesis batches. Dashed and dotted lines: Cu $K\beta_1$ and W $L\alpha_1$ peaks, respectively. Asterisk (*): secondary phases.

Figure 6.2 shows the XRD patterns of the BCZT materials – $BC_{15}Z_{10}T$, $BC_{14}Z_{10}T$, $BC_{12}Z_{10}T$, and $BC_{10}Z_{10}T$ for the 2Θ ranges 44.8–45.8°, 65.4–66.4°, 82.5–84.5°, corresponding to the pseudo-cubic $(200)_{pc}$, $(220)_{pc}$, and $(222)_{pc}$ reflections. The peak splitting of these reflections is similar to what was observed for the materials in Chapter 4. All samples are mixed-phase compositions with tetragonal, orthorhombic, and rhombohedral contributions and a structural transition is observed from primarily tetragonal ($BC_{15}Z_{10}T$) to primarily rhombohedral ($BC_{10}Z_{10}T$).

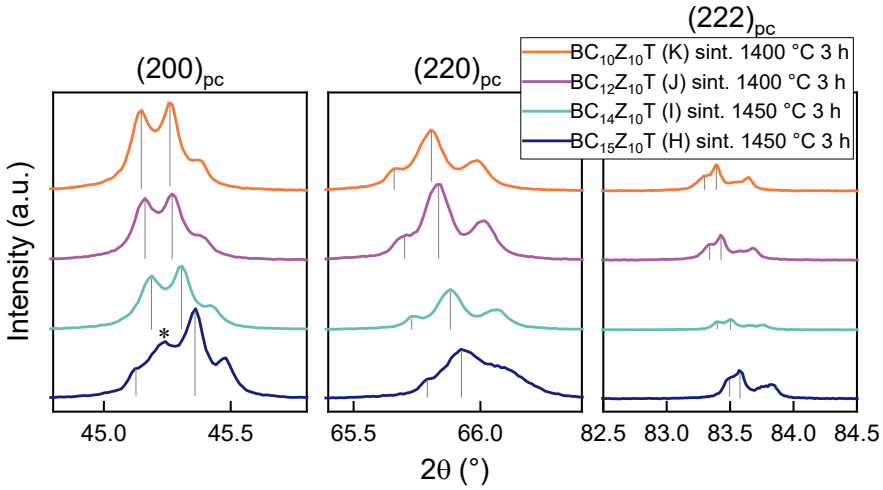

Figure 6.2: XRD patterns of sintered BCZT ceramics – $BC_{15}Z_{10}T$, $BC_{14}Z_{10}T$, $BC_{12}Z_{10}T$, and $BC_{10}Z_{10}T$. Ranges 44.8–45.8°, 65.4–66.4°, and 82.5–84.5° correlate with the $(200)_{pc}$, $(220)_{pc}$, and $(222)_{pc}$ reflections, respectively. Grey lines: peak splitting. Unmarked peaks to the right of the grey lines: Cu $K\alpha_2$ contributions. Asterisk (*): overlap of a peak and Cu $K\alpha_2$ contribution.

6.1.1.2. Microstructure

The average grain size, density, and SEM micrographs of the four materials are presented in Table 6.1 and Figure 6.3. $BC_{10}Z_{10}T$ has the largest average grain size, and all other compositions have similar average grain sizes of ≈ 40 µm. The four materials have a density above 89 %, with $BC_{10}Z_{10}T$ having the highest density of 97 %. The micrographs show that the grains are irregularly shaped with a narrow grain size distribution between 40–50 µm. Some intergranular porosity is observed at triple points [116].

Table 6.1: Average grain sizes and densities of $BC_{15}Z_{10}T$, $BC_{14}Z_{10}T$, $BC_{12}Z_{10}T$, and $BC_{10}Z_{10}T$.

BCZT	Ave. Grain Size (µm)	Ave. Density (g/cm³)	Relative Density (%)
$BC_{15}Z_{10}T$	44 ± 8	5.4 ± (0.10)	93
$BC_{14}Z_{10}T$	43 ± 9	5.3 ± (0.17)	91
$BC_{12}Z_{10}T$	40 ± 8	5.2 ± (0.11)	89
$BC_{10}Z_{10}T$	52 ± 11	5.6 ± (0.16)	97

Previous investigations have shown that optimised piezoelectric performances are observed for grain sizes greater than 10 µm [55]. Given this, and the similarity in the microstructural features of all materials, it is expected that the piezoelectric properties before and after mechanical poling should be independent of influences from microstructural differences.

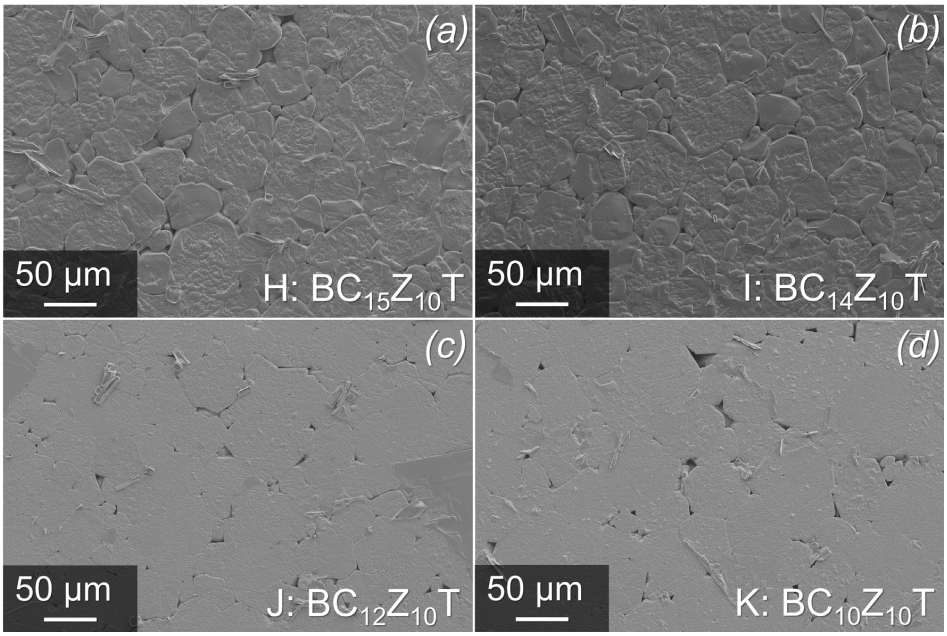

Figure 6.3: SEM micrographs of polished and etched (a) $BC_{15}Z_{10}T$, (b) $BC_{14}Z_{10}T$, (c) $BC_{12}Z_{10}T$, and (d) $BC_{10}Z_{10}T$ bulk sintered ceramics. Letters (H,I,J,K) represent the BCZT synthesis batches.

6.1.1.3. Piezoelectric Properties Before Mechanical Loading

Figure 6.4 displays the initial polarisation, strain, relative permittivity, and piezoelectric coefficient hysteresis loops of the four materials after poling. Samples were poled at five times the coercive field (5 x E_c) to ensure similar poling conditions for all materials prior to mechanical loading. The remanent polarisation, coercive field, minimum and maximum strain, remanent relative permittivity, and remanent piezoelectric coefficient values extracted from these loops are displayed in Table 6.2.

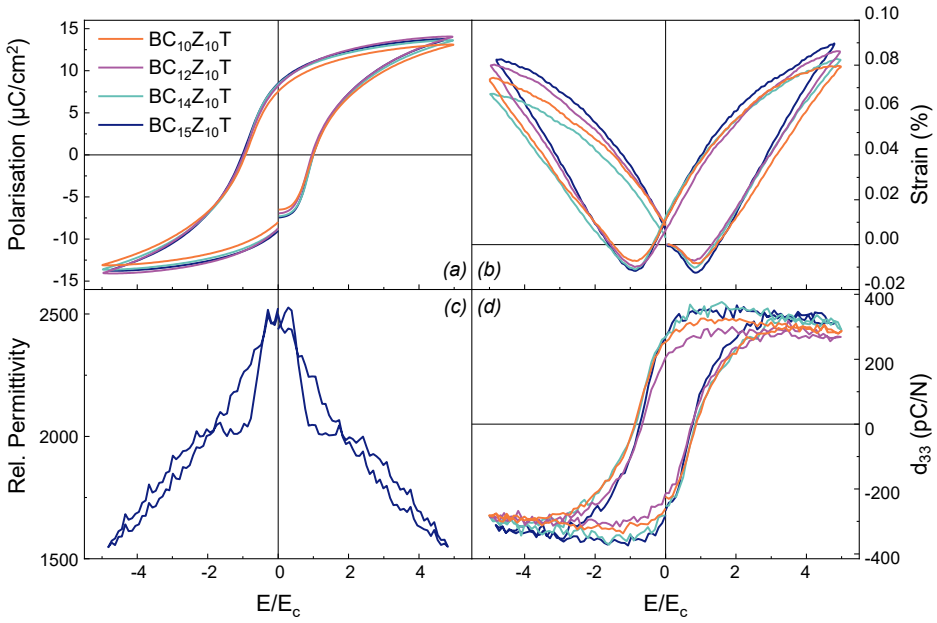

Figure 6.4: (a) Polarisation, (b) strain, (c) relative permittivity, and (d) piezoelectric coefficient hysteresis loops of $BC_{15}Z_{10}T$, $BC_{14}Z_{10}T$, $BC_{12}Z_{10}T$, and $BC_{10}Z_{10}T$. Only the relative permittivity loop of $BC_{15}Z_{10}T$ is displayed.

The polarisation hysteresis loops of $BC_{15}Z_{10}T$, $BC_{14}Z_{10}T$, $BC_{12}Z_{10}T$, and $BC_{10}Z_{10}T$ have symmetric, ferroelectric shapes (Figure 6.4 (a)). The similarity of the hysteresis loop shapes and P_r values reveal that all ceramics are poled in an equivalent manner. $BC_{15}Z_{10}T$ and $BC_{10}Z_{10}T$ have the highest and lowest E_c, respectively.

Table 6.2: Initial remanent polarisation, coercive field, minimum and maximum strain, remanent relative permittivity, and remanent piezoelectric coefficient values for $BC_{15}Z_{10}T$, $BC_{14}Z_{10}T$, $BC_{12}Z_{10}T$, and $BC_{10}Z_{10}T$.

BCZT	**Ave. P_r ($\mu C/cm^2$)**	**Ave. E_c (kV/cm)**	**$S_{min.}$ (%)**	**$S_{max.}$ (%)**	**ε_r**	**Ave. d_{33r} (pC/N)**
$BC_{15}Z_{10}T$	8.80	1.72	-0.012	0.090	2524	284
$BC_{14}Z_{10}T$	8.63	1.61	-0.010	0.082	2684	283
$BC_{12}Z_{10}T$	8.51	1.55	-0.007	0.086	2621	217
$BC_{10}Z_{10}T$	7.80	1.18	-0.008	0.079	2211	261

The strain loops displayed in Figure 6.4 (b) appear to be well-developed with some asymmetry, which is particularly prominent for $BC_{14}Z_{10}T$. The largest difference between the $S_{min.}$ and $S_{max.}$ values under positive electric field is 0.102 % for $BC_{15}Z_{10}T$.

The relative permittivity hysteresis loops (Figure 6.4 (c)) reflect the same shapes as those presented in Chapter 4 (Figure 4.4 (c)), however, because of the higher signal to noise ratio due to the lower voltage amplitude selection (1 V as opposed to 20 V), only the hysteresis loop for $BC_{15}Z_{10}T$ is displayed for clarity. The relative permittivity loops of $BC_{15}Z_{10}T$, $BC_{14}Z_{10}T$, and $BC_{12}Z_{10}T$ have two maxima under positive applied field, and $BC_{10}Z_{10}T$ displays one maximum. This shows that the first three compositions are primarily tetragonal in composition, while $BC_{10}Z_{10}T$ is mainly rhombohedral. This is in agreement with the phase compositions determined by XRD analysis. The highest ε_r is shown by $BC_{15}Z_{10}T$.

The change in the d_{33r} after mechanical loading indicates the stability of the piezoelectric response as a function of applied load, and ultimately reveals insight into the functional lifetime of a piezoelectric ceramic if it is implanted as a load-bearing material in the body. The piezoelectric coefficient hysteresis loops in Figure 6.4 (d) are slightly asymmetric about the y-axis, with higher values in the positive d_{33} direction. $BC_{15}Z_{10}T$ has the highest d_{33r}, followed by $BC_{14}Z_{10}T$, $BC_{12}Z_{10}T$, and $BC_{10}Z_{10}T$.

6.1.1.4. Piezoelectric Properties After Mechanical Loading

This section presents the piezoelectric properties, including polarisation, strain, and piezoelectric coefficients of the BCZT ceramics during and after uniaxial mechanical loading at -15 MPa for 60 min. The d_{33r} were measured using the set-up as was used during initial characterisation, but the values were obtained for a voltage bias of 0 V. A Berlincourt meter was not utilised in order to avoid influences from the mechanical loads applied using that technique.

The results acquired at mechanical loading intervals of 0, 1, 5, 10, 20, 30, and 60 min are presented in Figure 6.5 (a). A decrease in the d_{33r} is seen for all samples during the loading period. Figure 6.5 (b) shows that $BC_{10}Z_{10}T$ displayed the most prominent reduction in piezoelectric response (≈ 54 %) compared to $BC_{14}Z_{10}T$ (≈ 11 %), which showed the least change (Table 6.3) after the total loading period of 60 min.

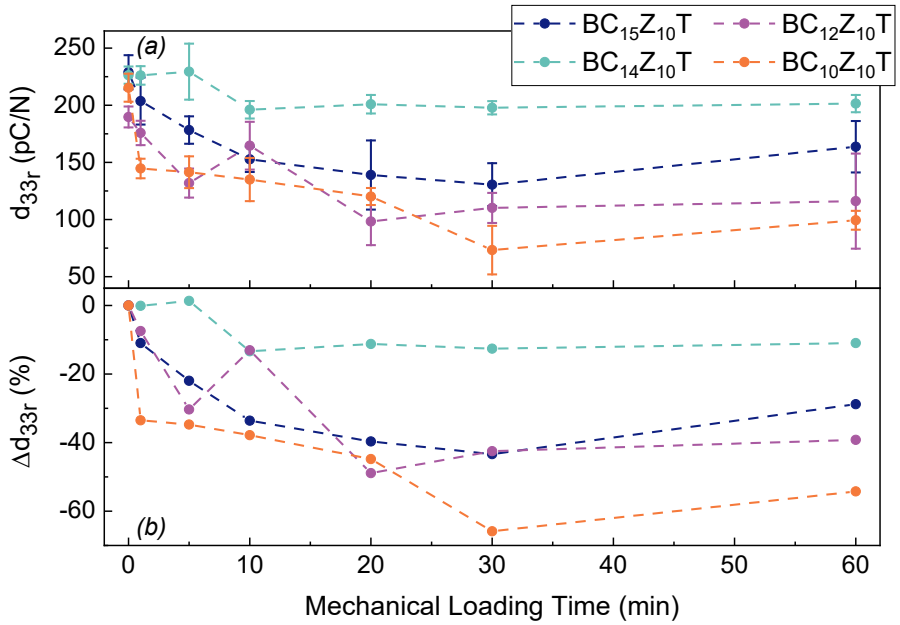

Figure 6.5: Remanent piezoelectric coefficients after compressive static mechanical loading at -15 MPa for 1, 5, 10, 20, 30, and 60 min, and (b) reduction of d_{33r} relative to the initial measured values over the same duration.

Table 6.3: Remanent piezoelectric coefficients at 0 and 60 min of mechanical loading, and the reduction of d_{33r} after 60 min relative to the initial values.

BCZT	d_{33r} **(pC/N)**		Δd_{33r} **(%)**
	0 min	**60 min**	
$BC_{15}Z_{10}T$	229	164	-29
$BC_{14}Z_{10}T$	226	201	-11
$BC_{12}Z_{10}T$	190	116	-39
$BC_{10}Z_{10}T$	215	99	-54

The hysteresis loops for the polarisation, strain, and piezoelectric coefficient were measured after 60 min of mechanical loading at -15 MPa using the same conditions as the initial characterisation measurements to determine the effect of mechanical loading on the piezoelectric response (Figure 6.6, Figure 6.7, and Figure 6.8). The remanent polarisation, minimum and maximum strain, and remanent piezoelectric coefficients after mechanical loading are presented in Table 6.4. The percentage reduction from the initial P_r, S, and d_{33r} are presented in Table 6.5.

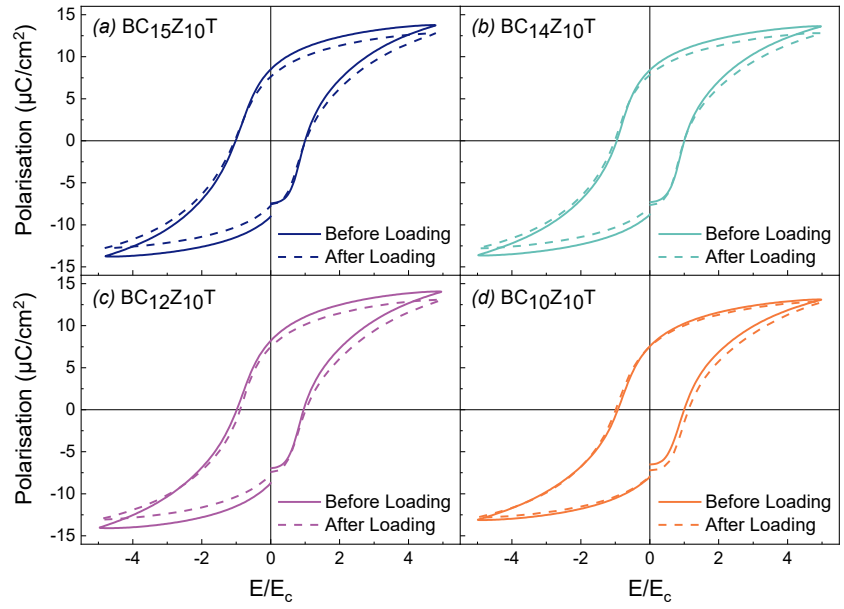

Figure 6.6: Polarisation hysteresis loops of (a) $BC_{15}Z_{10}T$, (b) $BC_{14}Z_{10}T$, (c) $BC_{12}Z_{10}T$, and (d) $BC_{10}Z_{10}T$. Solid lines: initial loops after poling at 5 x E_c. Dashed lines: final loops after compressive static mechanical loading (-15 MPa, 60 min).

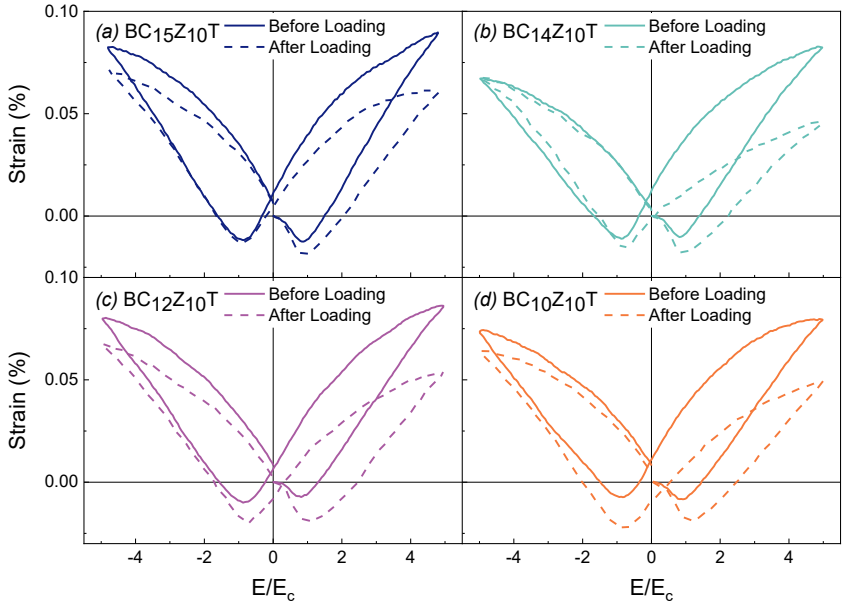

Figure 6.7: Strain hysteresis loops of (a) $BC_{15}Z_{10}T$, (b) $BC_{14}Z_{10}T$, (c) $BC_{12}Z_{10}T$, and (d) $BC_{10}Z_{10}T$. Solid lines: initial loops after poling at 5 x E_c. Dashed lines: final loops after compressive static mechanical loading (-15 MPa, 60 min).

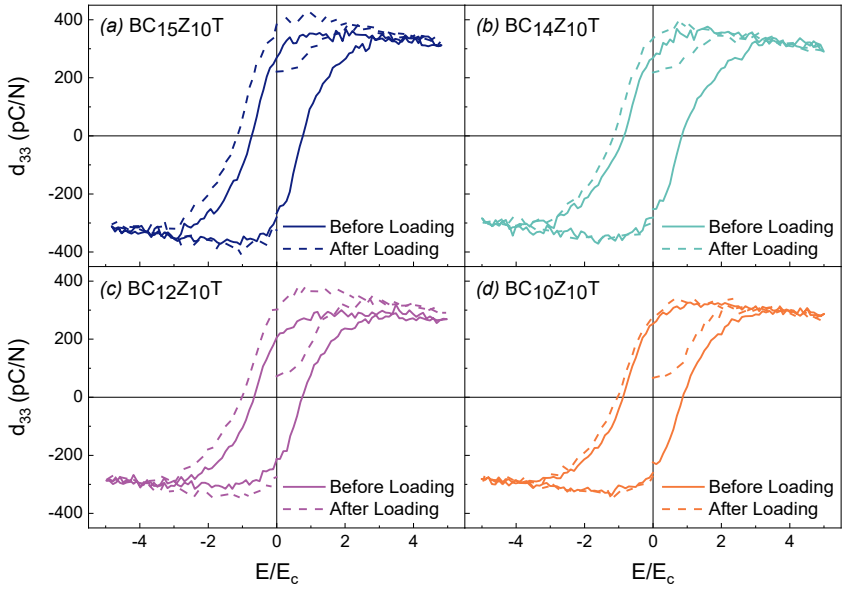

Figure 6.8: Piezoelectric coefficient hysteresis loops of (a) $BC_{15}Z_{10}T$, (b) $BC_{14}Z_{10}T$, (c) $BC_{12}Z_{10}T$, and (d) $BC_{10}Z_{10}T$. Solid lines: initial loops after poling at 5 x E_c. Dashed lines: final loops after compressive static mechanical loading (-15 MPa, 60 min).

Table 6.4: Final remanent polarisation, minimum and maximum strain, and remanent piezoelectric coefficients for $BC_{15}Z_{10}T$, $BC_{14}Z_{10}T$, $BC_{12}Z_{10}T$, and $BC_{10}Z_{10}T$, after compressive static mechanical loading (-15 MPa, 60 min).

BCZT	**Ave. P_r ($\mu C/cm^2$)**	**$S_{min.}$ (%)**	**$S_{max.}$ (%)**	**Ave. d_{33r} (pC/N)**
$BC_{15}Z_{10}T$	7.54	-0.019	0.061	221
$BC_{14}Z_{10}T$	7.63	-0.018	0.046	218
$BC_{12}Z_{10}T$	7.41	-0.019	0.053	72
$BC_{10}Z_{10}T$	7.21	-0.019	0.049	67

Table 6.5: Reduction of the remanent polarisation, total strain, remanent relative permittivity, and remanent piezoelectric coefficient for the four compositions after compressive static mechanical loading (-15 MPa, 60 min).

BCZT	ΔP_r (%)	ΔTotal S (%)	Δd_{33r} (%)
$BC_{15}Z_{10}T$	-14	-22	-22
$BC_{14}Z_{10}T$	-12	-31	-23
$BC_{12}Z_{10}T$	-13	-23	-67
$BC_{10}Z_{10}T$	-8	-23	-74

The shapes of the polarisation hysteresis loops before and after mechanical loading appear similar (Figure 6.6). However, there is a slight reduction of the P_r and P_s values for all materials after mechanical loading. $BC_{15}Z_{10}T$ shows the largest P_r reduction of ≈ 14 % (Table 6.5).

The strain hysteresis loops become more asymmetric after mechanical loading (Figure 6.7). The reduction in total strain is highest for $BC_{14}Z_{10}T$, while all other materials show a similar reduction of the total strain (Table 6.5).

The piezoelectric hysteresis loops of the four materials before and after mechanical loading for 60 min are shown in Figure 6.8. The final d_{33r} is extracted from the 60 min mechanical loading hysteresis loop as the first value upon application of electric field. $BC_{15}Z_{10}T$ has the highest d_{33r} after mechanical loading, followed by $BC_{14}Z_{10}T$, $BC_{12}Z_{10}T$, and $BC_{10}Z_{10}T$. All samples show a reduction in the d_{33r} compared to the original values prior to mechanical loading. $BC_{15}Z_{10}T$ and $BC_{14}Z_{10}T$ show the least change in the d_{33r}, of ≈ 23 % (Table 6.5).

6.1.2. Piezoelectric Stability as a Function of Grain Size

6.1.2.1. Phase Purity and Composition

The XRD patterns of the calcined and sintered $BC_{10}Z_{10}T$ samples are displayed in Figure 6.9. After calcination, the powders appear to be phase pure. Increased crystallinity is observed after sintering, as evidenced by the reduced FWHM. A small amount of a secondary phase is shown by the asterisk (*), described in Chapter 4.

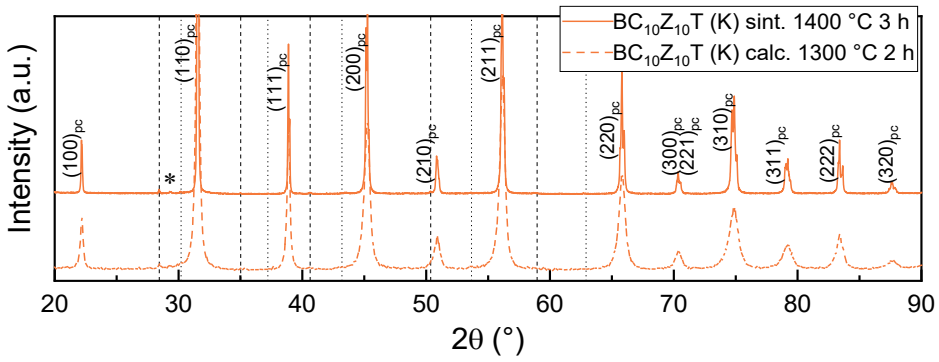

Figure 6.9: XRD patterns of calcined and sintered $BC_{10}Z_{10}T$. Letter (K) represents the synthesis batch. Dashed and dotted black lines: Cu $K\beta_1$ and W $L\alpha_1$ peaks, respectively. Asterisk (*): secondary phases.

Figure 6.10 shows the XRD pattern of sintered $BC_{10}Z_{10}T$ for the 2Θ ranges 44.8–45.8°, 65.4–66.4°, and 82.5–84.5°, which correspond to the pseudo-cubic $(200)_{pc}$, $(220)_{pc}$, and $(222)_{pc}$ reflections, respectively. The $BC_{10}Z_{10}T$ powders are identical to those used in Section 6.1.1.1., which were identified as being mixed-phase (tetragonal, orthorhombic, and rhombohedral) with primary contributions from the rhombohedral structure.

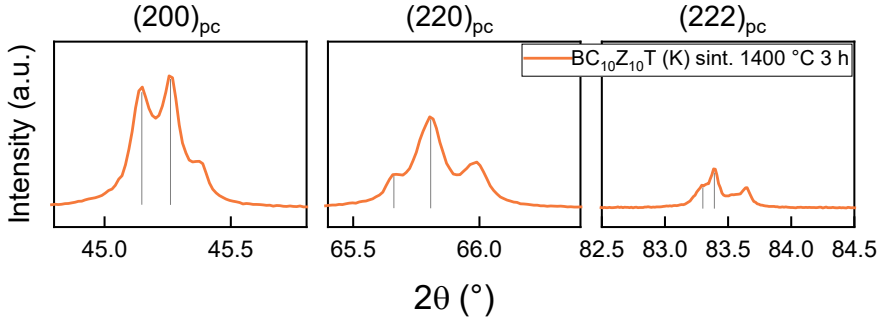

Figure 6.10: XRD pattern of sintered $BC_{10}Z_{10}T$. Ranges 44.8–45.8°, 65.4–66.4°, and 82.5–84.5°, correlate with $(200)_{pc}$, $(220)_{pc}$, and $(222)_{pc}$ reflections, respectively. Grey lines: peak splitting. Unmarked peaks to the right of the grey lines: Cu $K\alpha_2$ contributions.

6.1.2.2. Microstructure

All bulk $BC_{10}Z_{10}T$ ceramics in this section were synthesised using the same calcined powder batch. The calcined and milled powders are displayed in Figure 6.11. The particles show a large size distribution, are irregularly shaped, and are < 1 µm in diameter. The largest particles are on average ≈ 0.9 µm and the smallest are ≈ 0.4 µm.

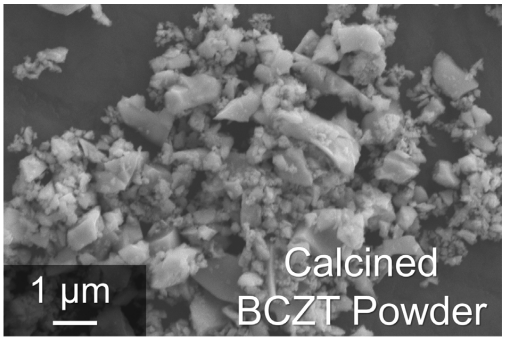

Figure 6.11: SEM micrograph of calcined $BC_{10}Z_{10}T$ (K) powders after 24 h ball-milling and sieving. These powders were used for the synthesis of $BC_{10}Z_{10}T$ bulk ceramics.

Grain size samples of 60, 50, 35, and 2 µm were synthesised using the same $BC_{10}Z_{10}T$ calcined powders by altering sintering regimes. Table 6.6 presents the average grain size, density, and relative density of the materials, as determined from the SEM micrographs displayed in Figure 6.12. In general, all samples have irregularly shaped grains. The 35 µm grain size sample is the densest with a relative density of 98 %, and the 2 µm grain size sample has the lowest density of 91 % (Table 6.6). The relative densities show that the samples were densified, confirmed by the presence of some intergranular porosity at energetically favourable triple points [116]. The standard deviation of the 1–2 µm grain size sample is not given, as the average grain size was determined via visual inspection and not the linear intercept method, as was performed for all other grain sizes.

Table 6.6: Average grain sizes and densities of the $BC_{10}Z_{10}T$ samples with average grain sizes of 60, 50, 35, and 2 µm.

Sample ID	Ave. Grain Size (µm)	Sintering Regime	Ave. Density (g/cm^3)	Relative Density (%)
60 µm	59 ± 11	1400 °C 3 h	5.5 ± (0.07)	95
50 µm	52 ± 11	1400 °C 3 h	5.6 ± (0.16)	97
35 µm	35 ± 14	1400 °C 1 h	5.7 ± (0.09)	98
2 µm	1–2	1100 °C 1 h	5.3 ± (0.17)	91

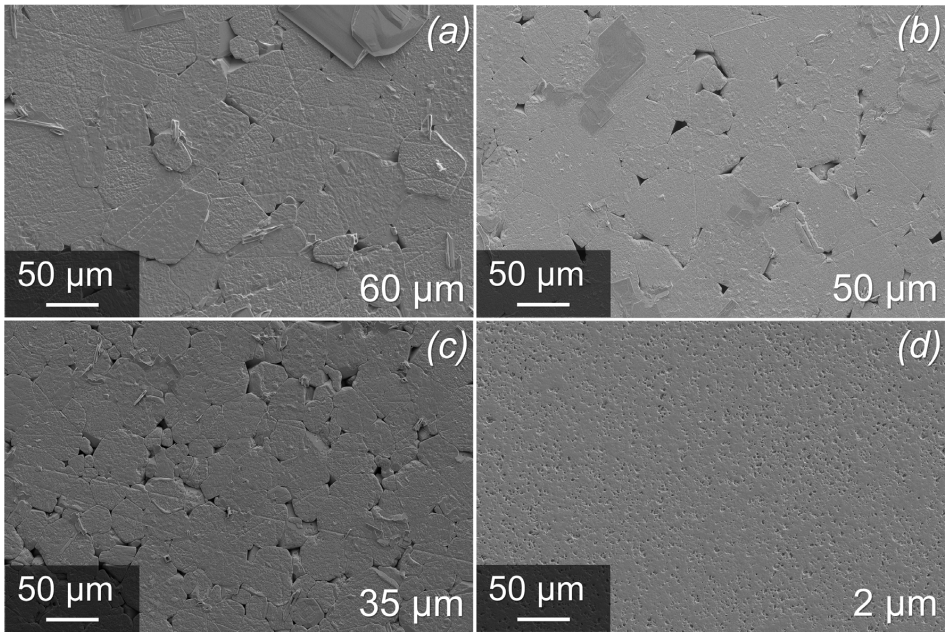

Figure 6.12: SEM micrographs of polished and etched $BC_{10}Z_{10}T$ bulk sintered ceramics with average grain sizes of (a) 60, (b) 50, (c) 35, and (d) 2 µm.

6.1.2.3. Piezoelectric Properties Before Mechanical Loading

Figure 6.13 displays the initial polarisation, strain, relative permittivity, and piezoelectric coefficient hysteresis loops of the grain size sets of $BC_{10}Z_{10}T$ (60, 50, 35, and 2 µm). The ceramic samples were poled at five times their coercive field (5 x E_c) to ensure similar poling conditions for all samples prior to mechanical loading. The exception to this is the 2 µm set, which was poled at 3.5 x E_c, due to hardware constraints that limited the applied field to 1000 V. The remanent polarisation, coercive field, minimum and maximum strain, remanent relative permittivity, and remanent piezoelectric coefficient values are displayed in Table 6.7.

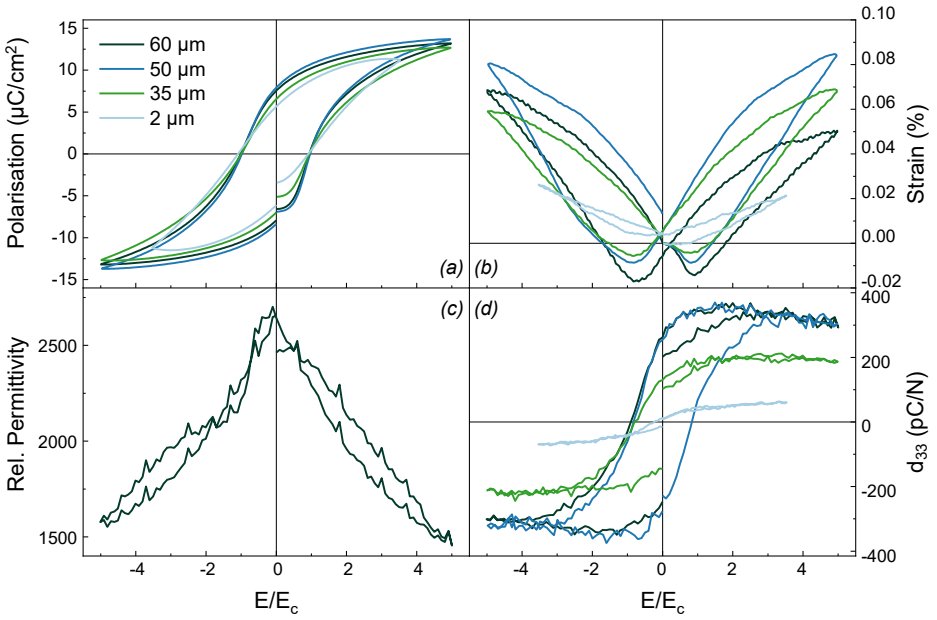

Figure 6.13: (a) Polarisation, (b) strain, (c) relative permittivity, and (d) piezoelectric coefficient hysteresis loops of $BC_{10}Z_{10}T$ ceramics of the following grain sizes – 60, 50, 35, and 2 µm. Only the relative permittivity loop of the 60 µm grain size set is displayed.

The polarisation hysteresis loops of the grain size samples are well-developed and show a ferroelectric shape (Figure 6.13 (a)). The loops for 60, 50, and 35 µm are more saturated than for the 2 µm set due to the higher poling conditions. The ceramics appear to be poled in an equivalent manner, shown by their similar hysteresis loop shapes. The P_r values are between 5.90 and 8.17 µC/cm^2 (Table 6.7). The 60, 50, and 35 µm samples have similar $E_c \approx 1.30$ kV/cm, while the 2 µm set has an $E_c \approx 3.00$ kV/cm.

Table 6.7: Initial remanent polarisation, coercive field, minimum and maximum strain, remanent relative permittivity, and remanent piezoelectric coefficient values for $BC_{10}Z_{10}T$ ceramics of the following average grain sizes – 60, 50, 35, and 2 µm.

Grain Size (µm)	Ave. P_r (µC/cm^2)	Ave. E_c (kV/cm)	$S_{min.}$ (%)	$S_{max.}$ (%)	ε_r	Ave. d_{33r} (pC/N)
60	7.77	1.27	-0.014	0.050	2655	270
50	8.17	1.33	-0.009	0.084	2622	271
35	6.79	1.32	-0.004	0.069	2313	143
2	5.90	3.00	-0.001	0.021	2426	15

The strain hysteresis loops are well-developed for the 60, 50, and 35 µm loops, and is less open for the 2 µm set (Figure 6.13 (b)). The largest total strain, calculated as the difference between $S_{max.}$ and $S_{min.}$ on positive field application, was experienced by the 50 µm sample at 0.093 %. The 2 µm sample showed the least total strain.

Only the hysteresis loop for the 60 µm sample is displayed in Figure 6.13 (c), due to the high signal to noise ratio of all relative permittivity hysteresis loops caused by the low voltage amplitude selection. There is one maximum on positive electric field application, and one to two maxima on negative field application, indicating that the samples are primarily rhombohedral, with some contribution from an orthorhombic or tetragonal phase. This is in agreement with the XRD phase analysis (Section 6.1.2.1). The ε_r was highest for the 60 µm sample, and lowest for the 35 µm sample (Table 6.7)

In this section, the change of the d_{33r} after mechanical loading is of interest as it provides insight into the prospective lifetime of these materials as cell stimulators when used in load-bearing applications. The d_{33} hysteresis loops are presented in Figure 6.13 (d), and the d_{33r} values extracted from these loops are given in Table 6.7. The hysteresis loops for all samples are well-developed, and the 2 µm sample shows a narrow d_{33r} range. The highest d_{33r} were obtained for 60 and 50 µm and were of similar value. The 35 and 2 µm samples showed lower d_{33r}.

6.1.2.4. Piezoelectric Performance After Mechanical Loading

The piezoelectric properties, including polarisation, strain, and piezoelectric coefficients, obtained during and after 60 min of mechanical loading at -15 MPa are presented in this section. The d_{33r} were acquired at 0, 1, 5, 10, 20, 30, and 60 min of mechanical loading. The same set-up as was used for the initial characterisation of the properties was utilised but under a voltage bias of 0 V. The values are presented in Figure 6.14 and Table 6.8.

All grain size samples show a decrease in their d_{33r} values after the 60 min period, with the most significant decrease observed after 1 min of mechanical loading. The 60 µm grain size set is the least stable over the entire period, with the greatest reduction in the d_{33r} of ≈ 92 % after 60 min. The 50 and 35 µm grain size samples have similar reductions in the d_{33r} after 60 min loading. The 2 µm grain size sample is the most stable throughout the mechanical loading period and only has a decrease of ≈ 38 %.

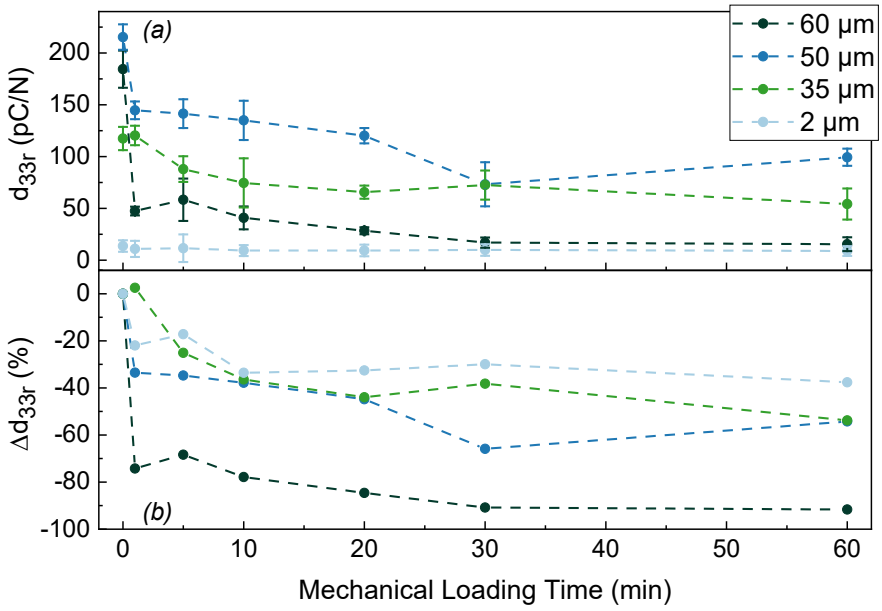

Figure 6.14: Remanent piezoelectric coefficient after uniaxial mechanical loading at -15 MPa for 1, 5, 10, 20, 30, and 60 min, and (b) reduction of d_{33r} relative to the initial measured values over the same duration.

Table 6.8: Remanent piezoelectric coefficients at 0 and 60 min of mechanical loading, and the reduction of d_{33r} after 60 min relative to the initial values.

Grain Size (µm)	**d_{33r} (pC/N)**		**Δd_{33r} (%)**
	0 min	**60 min**	
60	184	15	-92
50	215	99	-54
35	117	54	-54
2	14	9	-38

After mechanical loading for 60 min, the polarisation, strain, and piezoelectric coefficient hysteresis loops were acquired using the same parameters as were used during the initial characterisation of the electric properties, and are presented in Figure 6.15, Figure 6.16, and Figure 6.17. The P_r, total strain, and d_{33r} extracted from these loops are presented in Table 6.9. The change with respect to the initial values are given in Table 6.10.

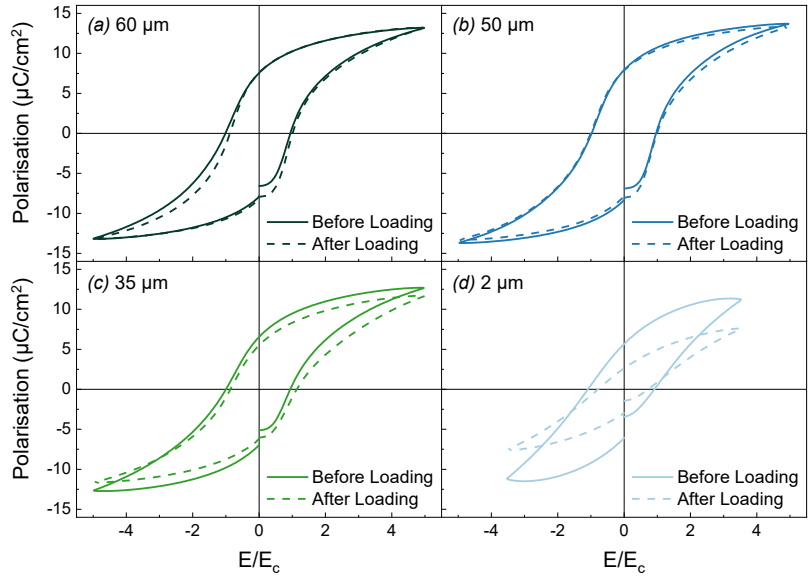

Figure 6.15: Polarisation hysteresis loops of $BC_{10}Z_{10}T$ with (a) 60, (b) 50, (c) 35, and (d) 2 µm grain sizes. Solid lines: initial loops after poling 5 x E_c (60, 50, 35 µm), 3.5 x E_c (2 µm). Dashed lines: final loops after compressive static mechanical loading (-15 MPa, 60 min).

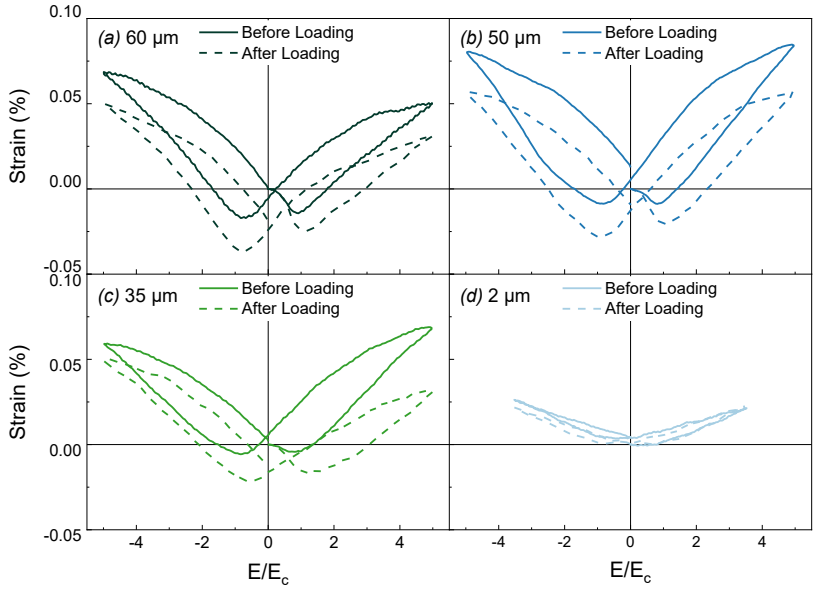

Figure 6.16: Strain hysteresis loops of $BC_{10}Z_{10}T$ with grain sizes of (a) 60, (b) 50, (c) 35, and (d) 2 µm. Solid lines: initial loops after poling 5 x E_c (60, 50, 35 µm) and 3.5 x E_c (2 µm). Dashed lines: final loops after compressive static mechanical loading (-15 MPa, 60 min).

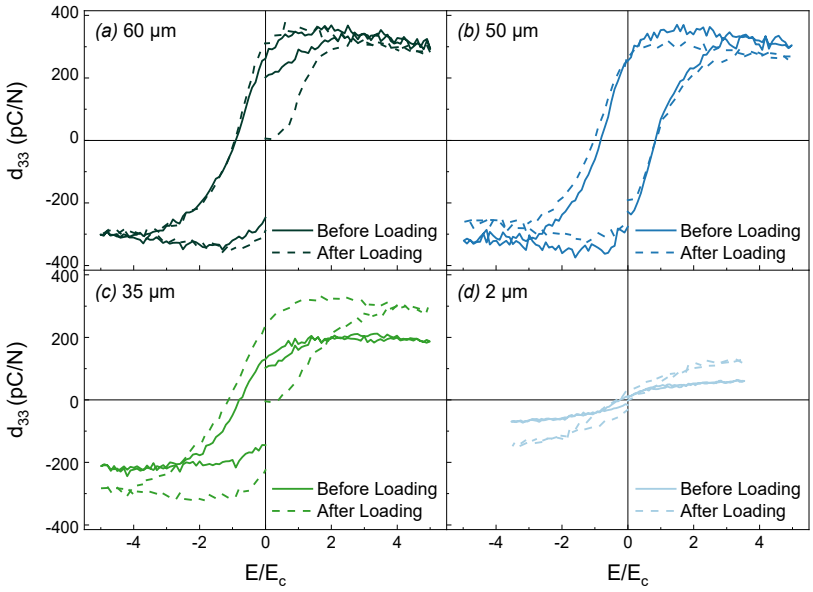

Figure 6.17: Piezoelectric coefficient hysteresis loops of $BC_{10}Z_{10}T$ with grain sizes of (a) 60, (b) 50, (c) 35, and (d) 2 µm. Solid lines: initial loops after poling 5 x E_c (60, 50, 35 µm) and 3.5 x E_c (2 µm). Dashed lines: final loops after compressive static mechanical loading (-15 MPa, 60 min).

Table 6.9: Final remanent polarisation, minimum and maximum strain, and remanent piezoelectric coefficients for $BC_{10}Z_{10}T$ ceramics of the following grain sizes – 60, 50, 35 and 2 µm, after compressive static mechanical loading (-15 MPa, 60 min).

Grain Size (µm)	**Ave. P_r (µC/cm^2)**	**$S_{min.}$ (%)**	**$S_{max.}$ (%)**	**Ave. d_{33r} (pC/N)**
60	7.94	-0.025	0.031	6
50	8.04	-0.018	0.056	191
35	6.05	-0.016	0.031	5
2	1.44	0.000	0.022	2

The polarisation hysteresis loops after mechanical loading appear quite similar to the initial curves for the 60, 50, and 35 µm sets (Figure 6.15). However, the hysteresis loop of the 2 µm sample is significantly narrower and more elongated than its initial loop. The P_r decreases for all samples except for the 60 µm sample. The largest reduction in the P_r is observed for the 2 µm sample (Table 6.10).

Table 6.10: Reduction of the remanent polarisation, total strain, remanent relative permittivity, and remanent piezoelectric coefficient for $BC_{10}Z_{10}T$ ceramics of the following grain sizes – 60, 50, 35, and 2 µm, after compressive static mechanical loading (-15 MPa, 60 min).

Grain Size (µm)	ΔP_r (%)	ΔTotal S (%)	Δd_{33r} (%)
60	2	-13	-98
50	-2	-20	-29
35	-11	-34	-97
2	-76	1	-86

The strain hysteresis loops also appear similar to their original shapes, however, are slightly more asymmetric (Figure 6.16). This is particularly evident for the 35 µm sample. After mechanical loading, the total strain that the ceramics experience in response to an applied field are reduced for the 60, 50, and 35 µm samples, while the 2 µm sample shows a slight increase in the total strain (Table 6.10).

The piezoelectric hysteresis curves for the grain size sets before and after mechanical loading for 60 min are displayed in Figure 6.17. The d_{33r} is extracted from the curves as the first value upon electric field application. The 50 µm set has the highest d_{33r}, followed by the 60, 35, and 2 µm samples. Compared to the initial d_{33r}, the values decrease after 60 min mechanical loading most significantly for the 2, 35, and 60 µm samples (Table 6.10).

6.2. Discussion

In this section of work, the aim was to investigate the effect of static compressive mechanical loading on the stability of the piezoelectric effect, as a function of phase composition and grain size. An understanding of this facilitates the development of BCZT as load-bearing implant materials that can provide sufficient levels of electric stimulation for valuable lengths of time.

6.2.1. Piezoelectric Stability as a Function of BCZT Composition

The MPB composition is known to display the highest remanent polarisation, strain, and remanent piezoelectric coefficients due to the high number of possible domain variants

from both tetragonal and rhombohedral structures that enhance domain reorientation. A higher initial P_r, E_c, $S_{min.}$, $S_{max.}$, and d_{33r} were achieved by $BC_{15}Z_{10}T$ than all other materials (Table 6.2). This is attributed to its more even mixture of tetragonal and rhombohedral phases. From the relative permittivity hysteresis loops, it was clear that the proportion of the tetragonal phase decreased with decreasing Ca content, such that $BC_{10}Z_{10}T$ behaves as a primarily rhombohedral phase material. Since the materials in this chapter are similar to those presented earlier, the reader is referred to Chapter 4 for the discussion of the relationship between electric properties and phase composition.

6.2.1.1. Mechanical Load

In the current work, a compressive static mechanical load of -15 MPa was applied to all ceramic samples. Initially, a load of -25 MPa was chosen for its similarity to loads expected within the knee joint during normal walking [140]. It was anticipated that the ceramic BCZT samples would withstand this load without mechanical failure, as loads up to one order of magnitude higher were successfully applied in other studies [62], [105], [141], [142]. However, initial preliminary experiments were unsuccessful, and some ceramics fractured. Therefore, a lower load of -15 MPa was selected. The failure of the ceramics under -25 MPa may be attributed to their aspect ratio or the planarity of the ceramic faces in contact with the loading set-up. This could create clamping stresses within the material, such that non-uniaxial loads are applied. Further investigation into the experimental set-up is required to enable further testing with more biologically similar mechanical loads. Nonetheless, changes in the piezoelectric properties were observed even with the application of a small load of -15 MPa.

6.2.1.2. Piezoelectric Properties After Mechanical Loading

After 60 min of mechanical loading, the primarily rhombohedral $BC_{10}Z_{10}T$ material shows the largest reduction in the d_{33r} (Table 6.3). This is supported by -50 MPa mechanical loading studies by Ehmke et al. on tetragonal, MPB, and rhombohedral BCZT ceramics [105]. They attribute the large reduction of the d_{33r} after mechanical loading of both MPB and rhombohedral structures to their electrical softness, or the high number of domain variants of these phase compositions (14 and 8, respectively). As the proportion of the tetragonal phase increases from $BC_{10}Z_{10}T$ to $BC_{15}Z_{10}T$, six <100> polarisation directions are possible, thereby providing better mechanical depoling resistance. In

addition, the reduction in d_{33r} observed in the current work is in accordance with literature on soft ferroelectrics that additionally attribute the mechanical depolarisation to extrinsic contributions such as ferroelastic 90° switching, local displacement of non-180° domain walls, and the interaction between domain walls and pinning centres that cause reductions in domain wall density through coalescence of domains into larger ones [62], [104], [105], [141], [143].

Significant mechanical depolarisation was observed after 5 min for most compositions (Figure 6.5), in contrast to the anticipated duration based on the literature. Under static uniaxial compression, depolarisation of PZT was not observed to occur instantaneously but rather over 20 to 30 min due to the slow movement of domain walls with an applied stress [143]. As that work was performed on PZT, it can be assumed that the domain wall mobility is enhanced in BCZT ceramics due to the softer electric nature.

Of all the materials, $BC_{14}Z_{10}T$ appears to stabilise after 10 min of mechanical loading, while the other compositions stabilise after approximately 20 min (Figure 6.5). Furthermore, the d_{33r} decreases only by 11 % after 60 min of mechanical loading, indicating that this phase composition has the ideal combination of high piezoelectric properties ($d_{33rfinal}$ = 201 pC/N) and resistance to mechanical depoling. This would make it suitable for application in the body at load-bearing areas, as the effective charge stimulation to surrounding tissues could be maintained at a more constant value for an extended period of time.

The current mechanical loading experiments were performed using a static mechanical load. In practice, however, a piezoelectric BCZT ceramic would be cyclically loaded when implanted into the body and used as a load-bearing material, due to movements from chewing, walking, and running, for instance. The effect of cyclic loading is important to determine in future studies, as literature on PZT report that the effect of mechanical depoling is significantly increased under cyclic loads compared to static loads [143].

When implanted into the body as for example a joint replacement material, it is anticipated that the piezoelectric ceramic should maintain contact with adjacent bone tissue. If not, the ceramic will not be able to supply charge nor will it form a stable fixation to the surrounding tissue [144]. In the current work, the BCZT ceramics were

mechanically loaded and then completely unloaded before the d_{33r} was measured. Ehmke et al. showed that there is a difference in the observed reduction of the d_{33r} if the ceramic material is completely unloaded prior to d_{33r} measurement, or only unloaded to a pre-stress of -2 MPa [105]. In their work, BCZT ceramics show a greater reduction in the d_{33r} if the maximum load is removed to a pre-stress value of -2 MPa, as the complete removal of load allows the material to relax and restore some of its remanent d_{33}. Since the current work tests the BCZT ceramics when they are completely unloaded, future work should be performed to determine the effect of removing the maximum stress to a pre-stress level that mimics normal contact stresses in the body.

6.2.2. Piezoelectric Stability as a Function of Grain Size

6.2.2.1. Piezoelectric Properties Before Mechanical Loading

Prior to mechanical loading, the 60 and 50 µm samples show the narrowest electric field range where polarisation switching occurs, seen by the perpendicular hysteresis loops in the vicinity of the coercive field (Figure 6.13 (a)). The 2 µm sample shows the broadest range during which switching occurs, or the most sloped curve. Although the domain structures of the current grain sizes are not known, it is proposed that the observed difference in the polarisation loops are due to the different domain structures reported for coarse- and fine-grained ceramics. Fine-grained ceramics have lamellar 90° domain structures, whilst coarse-grained ceramics have twinned (or banded) lamellar 90° and 180° domain structures. As fine grains have one less degree of freedom for domain wall motion, domain switching is restricted and occurs over a broad field range [47]. This is observed by the higher E_c of the 2 µm samples compared to the other grain sizes. In addition, fine-grained ceramics have strong restoring forces from the surrounding grain boundaries acting on the 90° domains, such that much of the polarisation induced upon electric field application is removed through back-switching during field removal, reducing the P_r [60]. A similar effect of the domain structures is observed in the strain hysteresis loops (Figure 6.13 (b)). The 2 µm ceramic has almost no strain response during polarisation switching ($S_{min.}$ -0.01 %), indicating that 90° domain switching is extremely restricted. For future studies, it would be ideal to image the domain structures using transmission electron microscopy (TEM) or piezoelectric force microscopy (PFM) to

confirm the domain structures for each of the produced grain sizes and to definitively correlate the piezoelectric properties to the observed domain structures.

The piezoelectric behaviour is influenced by grain size, however, the effects on BT and BCZT are debated and reports are contradictory. For instance, Huan et al. and Zheng et al. report maximal d_{33} for BT ceramics with 1 µm grain sizes, while Hao et al. and Guo et al. report enhanced d_{33} values for coarse grains ≈ 10 µm for BCZT and BT, respectively [55], [58]–[60]. They assign the enhanced d_{33} in coarse-grained ceramics to improved domain alignment related to the presence of 180° domains, and the reduced clamping effect on 90° domain switching. In the current work, the highest d_{33r} was acquired for the 60 µm sample, and the lowest was for the 2 µm sample (Table 6.7), which is similar to the results that indicate better piezoelectric properties for larger grains. It was also reported that ε_r increases with decreasing grain size as a result of an increase in domain wall density. However, the opposite trend is seen in the current work. The 2 µm samples show lower ε_r than the other grain sizes and this may be due to the slightly lower density of the sample. Porous samples contain less electrically active material and by corollary, a higher proportion of low permittivity pores. Although the difference in relative density between the ceramics is small, other studies have noted that differences of 2 % in the relative density can significantly affect the dielectric properties [59].

6.2.2.2. Piezoelectric Properties After Mechanical Loading

After completion of the loading period, the 60 µm samples showed the most significant degradation of the piezoelectric coefficient of ≈ 92 % (Table 6.8). Although the domain structure of coarse-grained ceramics provides enhanced piezoelectric properties, it conversely causes them to be more susceptible to mechanical depolarisation due to the absence of domain clamping that affects finer grains.

Interestingly, mechanical depolarisation is observed to occur for all grain sizes within 1 min. Currently, the optimal piezoelectric coefficient for osteoblast stimulation is not well-defined. However, it is reported that the bone exhibits a piezoelectric coefficient of 0.7 pC/N [14]. Since the 2 µm samples show the best resistance to mechanical depoling compared to the other grain sizes tested and has stable values within a similar order of magnitude (≈ 10 pC/N) to those observed in bone, it is anticipated that BCZT ceramics of this grain size would be suitable for use as load-bearing materials within the body.

6.3. Summary

Mechanical loading causes depolarisation of BCZT piezoelectric ceramics. This is a critical factor for the implementation of piezoelectric ceramics in load-bearing applications. It is therefore of primary interest to characterise the effect of composition and grain size on the piezoelectric properties and mechanical depoling resistance. In the current work, it has been observed that piezoelectric properties can be enhanced by phase mixtures and domain wall motion. However, these attributes can adversely affect the mechanical depolarisation resistance. By tailoring the composition and grain size of BCZT ceramics, it is possible to optimise the piezoelectric properties and resistance to mechanical depolarisation of these ceramics to suit the requirements of a cell-stimulative implant material.

Chapter 7

Piezoelectric Coatings on Metal Implant Substrates

In this chapter, the optimisation process for the deposition of BCZT powders onto metallic implant materials is presented and discussed. First, the effect of grinding and heat-treatment in argon and air on metallic substrates was investigated (Figure 7.1). Initial trials depositing BCZT ceramic powders directly on stainless steel 316L and Ti-alloy Ti6Al4V showed poor adhesion and densification and led to the investigation of $CaZrO_3$ and $CaTiO_3$ as potential interlayer materials. The effect of heat-treatment temperature, number of heat-treatment steps, argon flow during heat-treatment, as well as thickness of $CaTiO_3$ and BCZT coatings on Ti6Al4V were investigated. An in-depth discussion of the behaviour of the metal/ceramic interface of the optimised coatings follows.

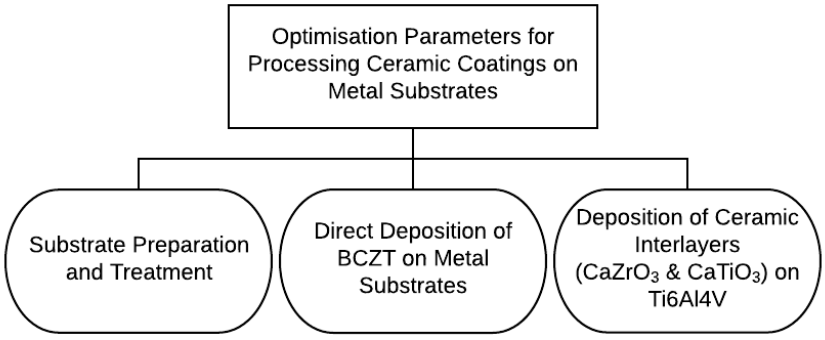

Figure 7.1: Parameters modified during the optimisation process of ceramic coating deposition on metal substrates.

7.1. Results

7.1.1. Substrate Preparation and Treatment

SEM micrographs of the as-received and prepared metal substrates are shown in Figure 7.2. The as-received stainless steel 316L substrate shows a grain-like surface while the as-received Ti6Al4V substrate displays a cratered surface morphology. In order to ensure that both substrates had even surface roughness prior to ceramic slurry deposition, the substrates were grinded using 1200 grit SiC paper, degreased, and cleaned.

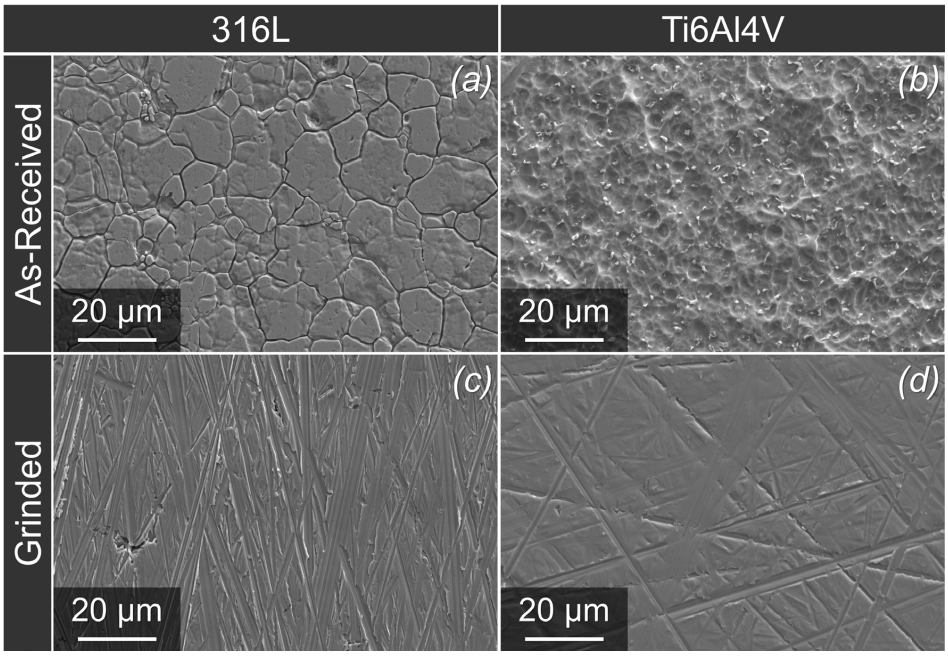

Figure 7.2: Top view SEM micrographs of (a,c) stainless steel 316L and (b,d) Ti6Al4V metal substrate surfaces, as-received and grinded.

Slurries of ceramic powders were spray-coated onto prepared substrate surfaces. Figure 7.3 illustrates the particle size of the two main ceramic powders used: $BC_{10}Z_{10}T$ (BCZT) and $CaTiO_3$. The as-received $CaTiO_3$ powders show a narrow size distribution, with the larger particles having a size of ≈ 0.4 µm. The as-prepared BCZT powders show a wider size distribution with a mixture of fine and coarse particles. The size of the larger BCZT particles is ≈ 0.8 µm.

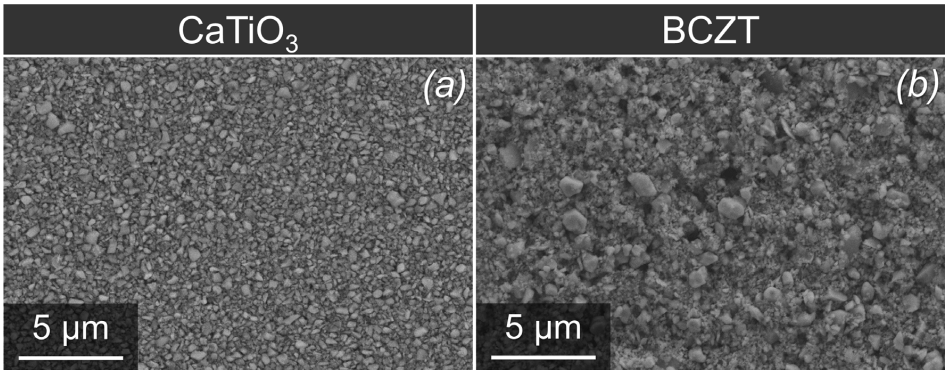

Figure 7.3: SEM micrographs of (a) as-received $CaTiO_3$ and (b) as-prepared $BC_{10}Z_{10}T$ powders.

Metal substrates annealed at high temperature under air atmosphere form a weakly adhered oxidation layer on the surface. This behaviour on Ti6Al4V, heat-treated at 900 °C in air, is displayed in the SEM micrograph in Figure 7.4. To avoid formation of the oxidation layer, a well-sealed tube furnace was used for the heat-treatments, and the furnace was evacuated and purged at least three times with Ar gas prior to each experiment.

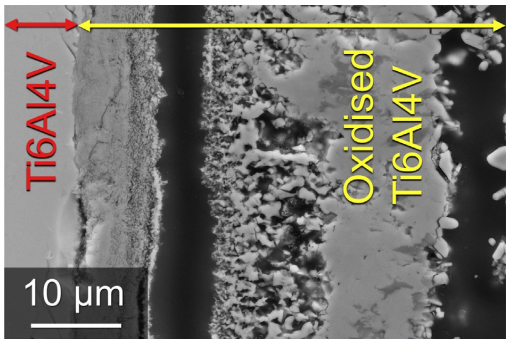

Figure 7.4: Cross-sectional SEM micrograph of grinded Ti6Al4V after heat-treatment at 900 °C in air. The formation of an oxidised surface layer is clearly observed. The arrows indicate the thickness of the Ti6Al4V and the oxidised layer.

7.1.2. Direct Deposition of BCZT on Stainless Steel and Ti-Alloy

As-prepared BCZT ceramic slurries were spray-coated onto prepared stainless steel 316L and Ti6Al4V substrates. The SEM top view and cross-sectional images of the samples after heat-treatment up to 1100 °C in Ar atmosphere are displayed in Figure 7.5.

When deposited directly onto stainless steel 316L, BCZT displayed densification and coarsening (Figure 7.5 (a,b)). However, significant delamination of the BCZT coating from the substrate was observed, as shown in Figure 7.5 (c).

Figure 7.5 (d,e) show the top view and cross-sectional SEM micrographs of BCZT deposited on Ti6Al4V. In contrast to BCZT on stainless steel 316L, direct deposition of BCZT onto Ti6Al4V showed poor densification behaviour of the BCZT particles, as evidenced by the similarity to the particle sizes of the as-synthesised powders displayed in Figure 7.3. Delamination from the Ti6Al4V substrate was also observed, albeit to a lesser degree than observed on stainless steel 316L. Due to the enhanced adhesion and stability of the BCZT coating on Ti6Al4V, this metal substrate was chosen for subsequent experiments.

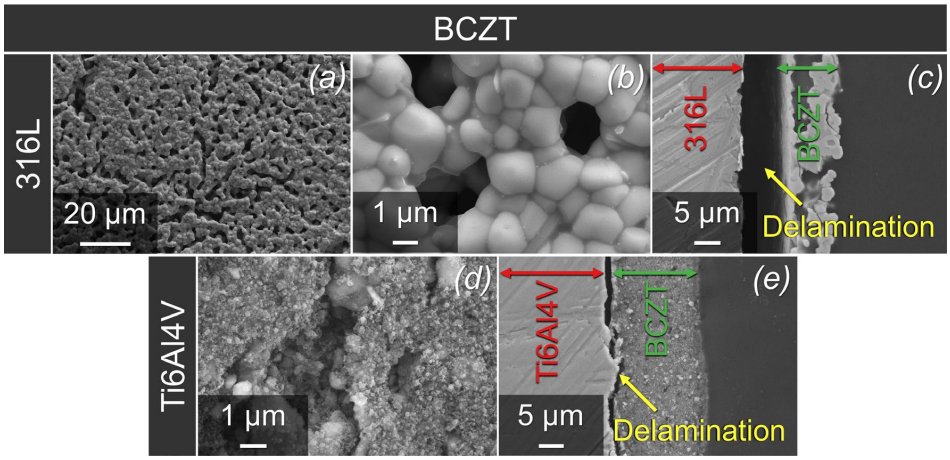

Figure 7.5: SEM top view and cross-sectional micrographs of BCZT deposited on (a-c) stainless steel 316L and (d,e) Ti6Al4V, after heat-treatment in Ar atmosphere between 900–1100 °C.

7.1.3. Deposition of Ceramic Interlayer Materials on Ti-Alloy

To enhance the adhesion between BCZT and the Ti6Al4V substrates, interlayers of $CaZrO_3$ and $CaTiO_3$ were investigated. $CaZrO_3$ was chosen for the high melting point of 2368 °C, high chemical inertness, and suitability for high temperature applications as ceramic refractory materials for titanium melting [108], [145], [146]. In addition, $CaTiO_3$ thin films on Ti6Al4V have been studied for dental implants as a means to encourage hydroxyapatite formation on the alloy surface in simulated body fluid [147]. Hence,

slurries of $CaZrO_3$ and $CaTiO_3$ ceramic powders were spray-coated onto prepared Ti6Al4V substrates and heat-treated at 1100 °C for 1 h in Ar atmosphere. Photographs, top view and cross-sectional SEM micrographs of the samples are shown in Figure 7.6.

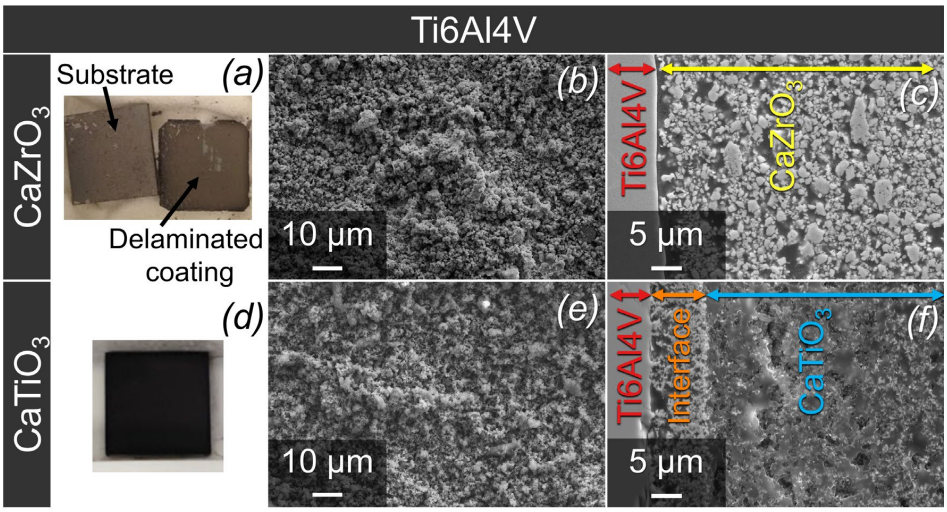

Figure 7.6: Photographs, SEM top view and cross-sectional images of (a-c) $CaZrO_3$ and (d-f) $CaTiO_3$ on Ti6Al4V after heat-treatment in Ar atmosphere at 1100 °C for 1 h.

$CaZrO_3$ on Ti-Alloy Ti6Al4V

Figure 7.6 (b,c) show that $CaZrO_3$ appears well-packed. However, $CaZrO_3$ does not appear to interact with the Ti6Al4V substrate (Figure 7.6 (c)). In addition, the $CaZrO_3$ coatings were not stable over time as they delaminated after ageing for 4 months in an environment with constant temperature and relative humidity (23 °C and 23 %) (Figure 7.6 (a)).

$CaTiO_3$ on Ti-Alloy Ti6Al4V

The $CaTiO_3$ coating on Ti6Al4V also appears well-packed (Figure 7.6 (e,f)). In addition, $CaTiO_3$ interacted with the substrate material as evidenced by the porous interface reaction region between the Ti6Al4V and $CaTiO_3$ (Figure 7.6 (f)). Over the same ageing period at ambient conditions, $CaTiO_3$ appeared to be more stable and more well-adhered to the Ti6Al4V substrate, as shown in Figure 7.6 (d). Complete delamination of the ceramic coating was not observed.

Subsequent experiments focused on the use of $CaTiO_3$ as the ceramic interlayer material due to the better stability observed during ageing, and the formation of the interface reaction region between the metal substrate and ceramic coating. The interface reaction region is desirable as it suggests a chemical interaction occurs that may enhance the interconnection, stability, and strength between the metal substrate and the ceramic coating.

The interface reaction region shown in Figure 7.6 (f) was frequently observed at the Ti6Al4V/$CaTiO_3$ interface when certain processing conditions were met. These included:

- Good metal substrate/ceramic particle contact prior to heat-treatment.
- Thin ceramic coating.

The effect of the metal substrate/ceramic particle contact prior to heat-treatment is shown in Figure 7.7 (a). Inhomogeneous colouring of the spray-coated $CaTiO_3$ on Ti6Al4V is observed after heat-treatment. The dark regions indicate that a reaction occurred between the ceramic coating and metal substrate during heat-treatment, while white regions indicate no reaction. Subsequent heat-treatment did not affect the appearance of the coatings, suggesting that the $CaTiO_3$ powders were not homogeneously in contact with the Ti6Al4V substrate. When $CaTiO_3$ powders were uniaxially pressed (-10 MPa) onto a Ti6Al4V substrate and heat-treated, areas of better contact with the substrate material were apparent as observed by the dark regions in Figure 7.7 (b).

Additionally, the reaction at the metal/ceramic interface was observed when the $CaTiO_3$ ceramic coating was thin. This is depicted in Figure 7.7 (c,d), which show spray-coated $CaTiO_3$ on Ti6Al4V with coatings of $\approx$ 90 and $\approx$ 15 µm in thickness. The interface reaction region was only observed in the sample with a ceramic coating thickness of < 20 µm.

For samples with the interface reaction region, two microstructurally distinct $CaTiO_3$ regions are apparent. The first region, $CaTiO_3(1)$, that interfaces with the porous reaction region appears to be denser, while the second region, $CaTiO_3(2)$, is coarser (Figure 7.7 (d)). In addition, cracks parallel to the substrate were observed in the $CaTiO_3(1)$ region.

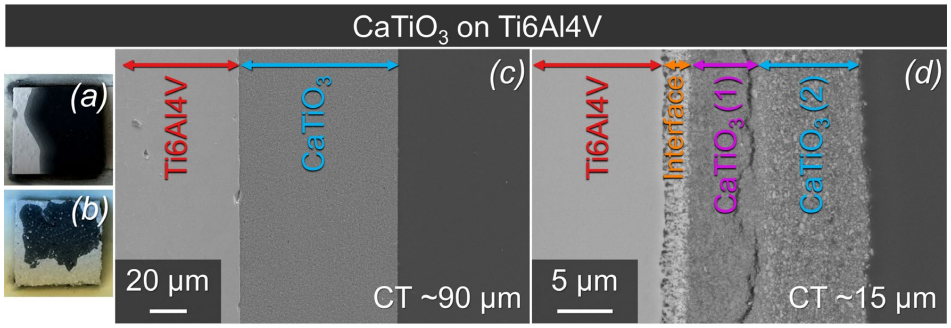

Figure 7.7: Photographs of (a) spray-coated and (b) uniaxially pressed $CaTiO_3$ on Ti6Al4V after heat-treatment in Ar atmosphere. Cross-sectional SEM micrographs of spray-coated $CaTiO_3$ on Ti6Al4V, heat-treated in Ar atmosphere for 1 h at 900 °C, where the $CaTiO_3$ coating thicknesses are (c) ≈ 90 and (d) ≈ 15 µm.

7.1.4. Deposition of Bi-Layer $CaTiO_3$ and BCZT Coatings on Ti-Alloy

$CaTiO_3$ and BCZT ceramics were spray-coated onto grinded Ti6Al4V substrates, and various parameters were adjusted to optimise the adhesion of the ceramics to the Ti6Al4V substrate (Figure 7.8). The effect of heat-treatment temperatures, one- vs. two-step heat-treatment, argon gas flow, and ceramic coating thickness were observed to be the most influential factors affecting the quality of the coatings.

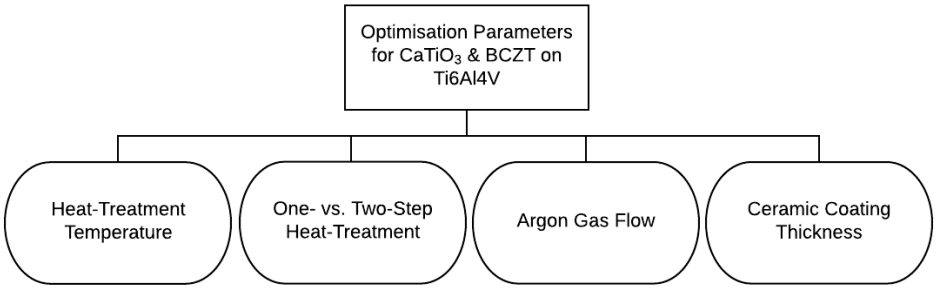

Figure 7.8: Investigated optimisation parameters for the deposition of bi-layer $CaTiO_3$ and BCZT coatings on Ti6Al4V.

7.1.4.1. Effect of Heat-Treatment Temperature

Cross-sectional SEM micrographs of spray-coated $CaTiO_3$ on Ti6Al4V substrates after heat-treatment in Ar atmosphere for 1 h at 900 and 1000 °C are displayed in Figure 7.9. The porous interface region was formed at both temperatures. Consequently, 900 °C was

chosen as the gentler temperature at which an interface reaction region could be achieved, and at which the effect of high temperature annealing could be minimised.

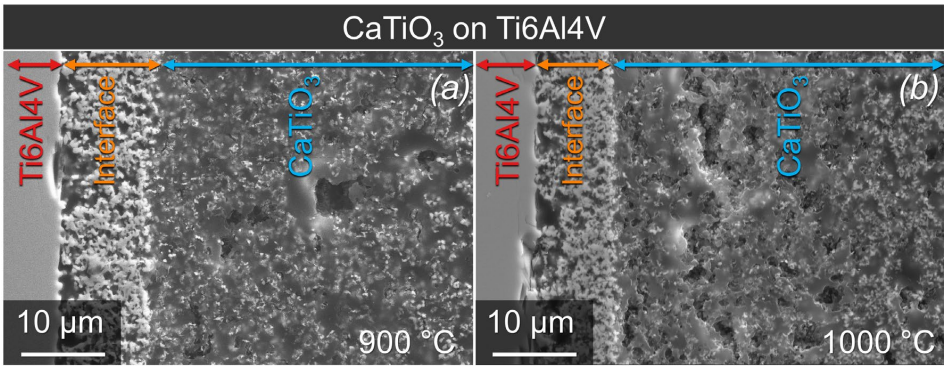

Figure 7.9: Cross-sectional SEM micrographs of spray-coated $CaTiO_3$ on Ti6Al4V after heat-treatment in Ar atmosphere for 1 h at (a) 900 and (b) 1000 °C.

7.1.4.2. Effect of One- vs. Two-Step Heat-Treatment

Cross-sectional SEM micrographs of $CaTiO_3$ and BCZT coatings deposited onto Ti6Al4V substrates and heat-treated in Ar atmosphere for 1 h at 900 °C in one or two heat treatment steps are presented in Figure 7.10. Three distinct regions are observed in all samples: the Ti6Al4V substrate, $CaTiO_3$ ceramic interlayer material, and the upper coating of BCZT.

The one-step heat-treated sample in Figure 7.10 (a) shows good adherence of the $CaTiO_3$ coating to the Ti6Al4V substrate, and good attachment between the $CaTiO_3$ and BCZT ceramic coatings. No porous interface reaction region is apparent at the Ti6Al4V/$CaTiO_3$ interface.

The two-step heat-treated samples in Figure 7.10 (b,c) similarly show good adherence between the Ti6Al4V substrate and the $CaTiO_3$ interlayer material, as well as attachment between the $CaTiO_3$ and BCZT coatings. In contrast to the sample heat-treated in one step, the two-step heated samples show the formation of a porous interface reaction region at the Ti6Al4V/$CaTiO_3$ interface, as well as the formation of two microstructurally distinct $CaTiO_3$ regions (Figure 7.10 (b)), similar to the behaviour observed for Ti6Al4V substrates that were coated only with $CaTiO_3$ (Figure 7.6 (f) & Figure 7.7 (d)). The same behaviour was also apparent in other two-step heat-treated samples when the second step

was performed at 900, 950 or 970 °C (Appendix 16–Appendix 18). Interestingly, when the second heat-treatment was performed at 1000 °C, the positions of the two $CaTiO_3$ microstructural regions contrast with what was previously observed. The dense region interfaced instead with the BCZT ceramic coating, as shown in Figure 7.10 (c).

$CaTiO_3$-coated Ti6Al4V samples containing the interface reaction region often showed cracks lying parallel to the substrate (Figure 7.7 (d)). The same behaviour was observed in samples coated with $CaTiO_3$ and BCZT, as displayed in Figure 7.10 (b,c).

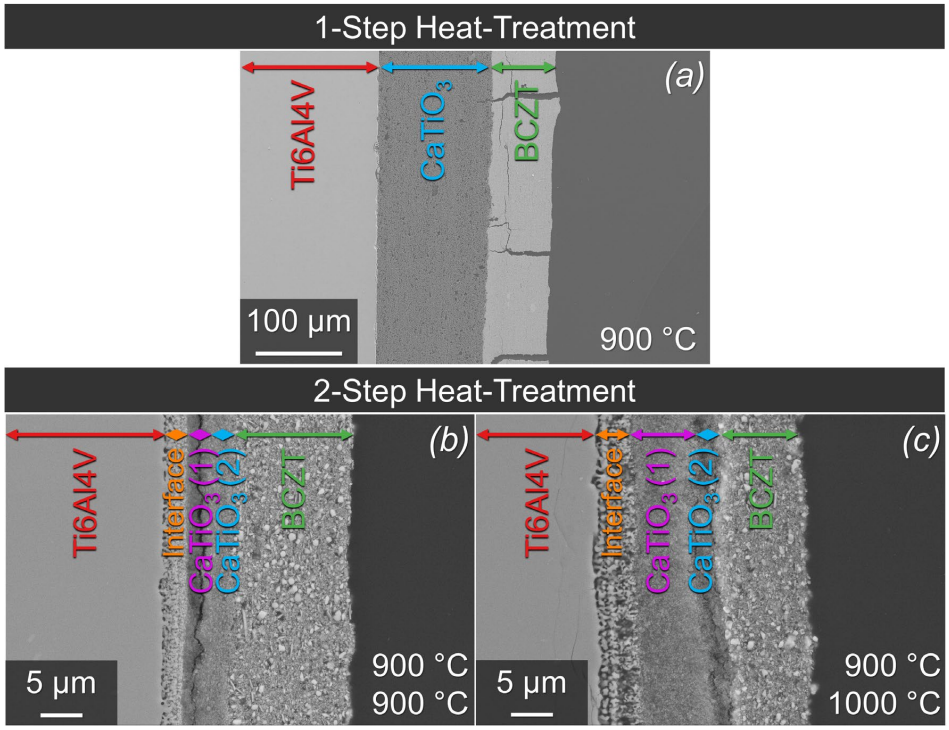

Figure 7.10: Cross-sectional SEM micrographs of $CaTiO_3$ and BCZT coatings on Ti6Al4V, heat-treated in (a) one or (b,c) two steps in Ar atmosphere. The first step was performed at 900 °C and the second step at (b) 900 and (c) 1000 °C.

7.1.4.3. Effect of Argon Flow

During synthesis, only some samples that were placed in a crucible and covered with disc lids showed an inhomogeneous reaction of the coatings, indicating an influence of the Ar gas flow. Figure 7.11 (a) shows a $CaTiO_3$ coating on Ti6Al4V after heat-treatment at

900 °C, and (b) after the subsequent deposition and heat-treatment of BCZT at 900 °C when lids were used. A schematic of the experimental set-up is presented in Figure 7.12.

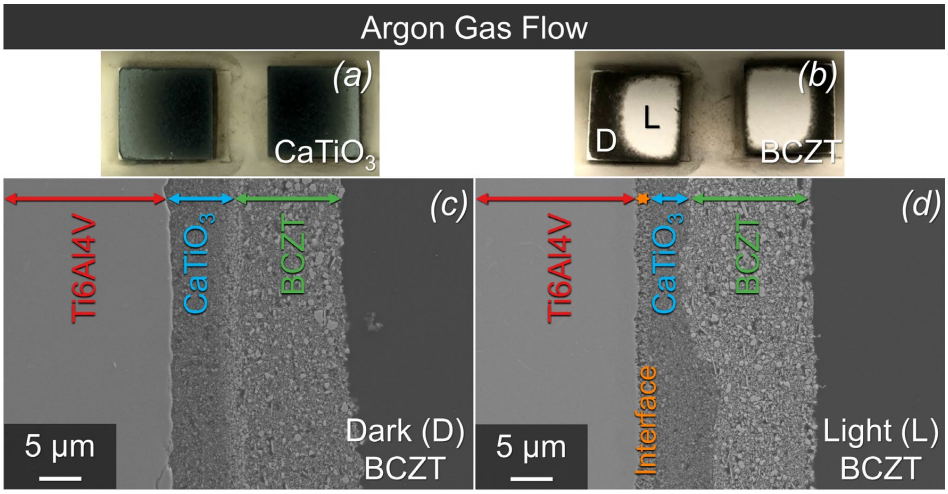

Figure 7.11: Photographs of (a) $CaTiO_3$ and (b) $CaTiO_3$/BCZT coatings on Ti6Al4V after two-step heat-treatment at 900 °C showing a round central reaction region. The SEM cross-sectional micrographs taken at the dark- and light-coloured BCZT regions, labelled as D and L in the photographs are displayed in (c) and (d), respectively.

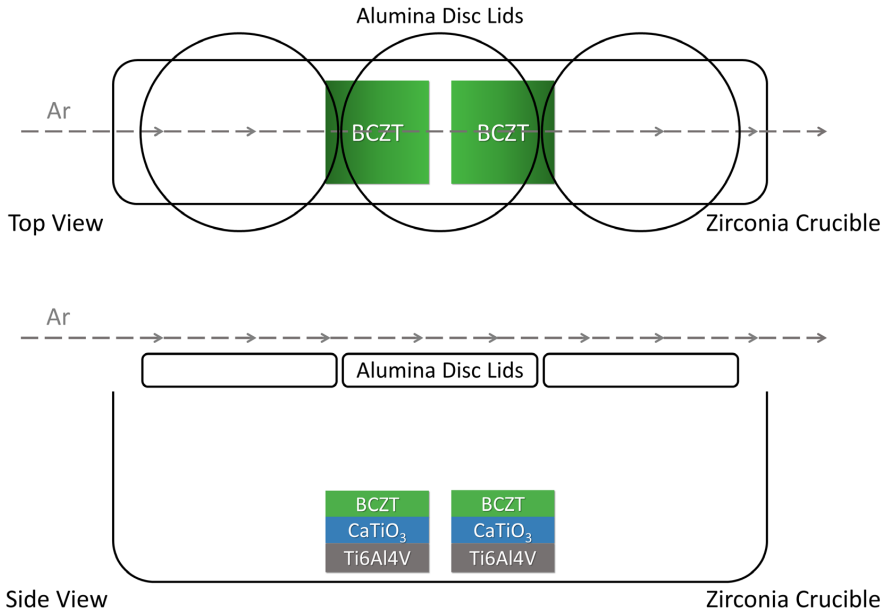

Figure 7.12: Schematic of the Ar gas flow over the ceramic-coated Ti6Al4V samples during heat-treatment with disc lids.

After heat-treatment with the lids, regions of light and dark areas were apparent in both the $CaTiO_3$ and BCZT coatings. The reaction region appears to be localised within a central circular area. After the first heat-treatment step, the $CaTiO_3$ ceramic coating is darker in the central circular area (Figure 7.11 (a)), while the subsequent BCZT coatings deposited on top and heat-treated appear darker at the edge of the circular region (Figure 7.11 (b)). The area where the $CaTiO_3$ appears light and BCZT appears dark shows no reaction region at the Ti6Al4V/$CaTiO_3$ interface and a microstructurally distinct region at the $CaTiO_3$/BCZT interface (Figure 7.11 (c)). Conversely, the area where the $CaTiO_3$ appears dark and BCZT appears light shows an interface reaction region at the Ti6Al4V/$CaTiO_3$ interface and no distinctly different region at the $CaTiO_3$/BCZT interface (Figure 7.11 (d)). A schematic is presented for clarity in Figure 7.13.

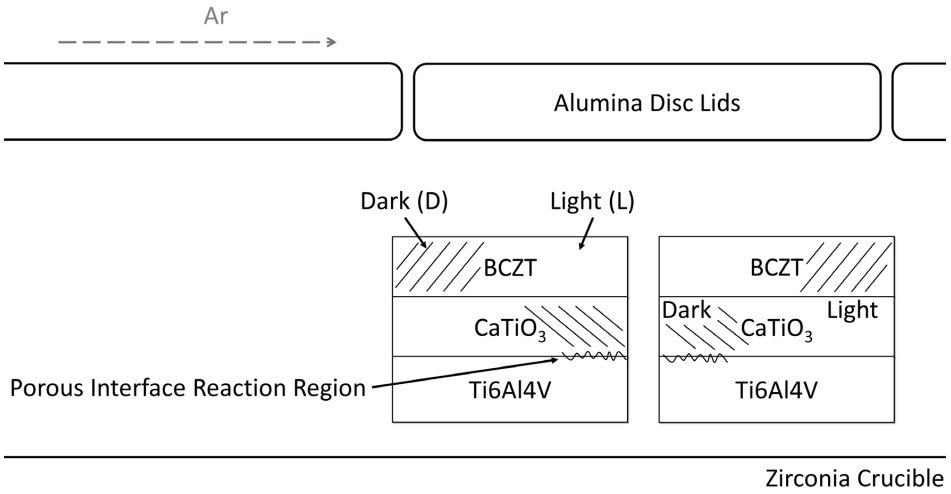

Figure 7.13: Schematic of the colour inhomogeneity of ceramic-coated Ti6Al4V samples after heat-treatment with disc lids. Dark- and light-coloured BCZT regions are labelled as D and L, respectively, as in Figure 7.11.

The same experiment was repeated but without the disc lids during heat-treatment. Homogeneous reaction of the coating was observed, with coatings having an even and dark appearance. Subsequent reoxidation of the samples was performed at 600 °C for 24 h in air and the results are shown in Figure 7.14. The top view photographs displayed in Figure 7.14 (a) show that the coatings become white after reoxidation, and the cross-sectional image in Figure 7.14 (b) reveals an extended reaction region at the Ti6Al4V/$CaTiO_3$ interface.

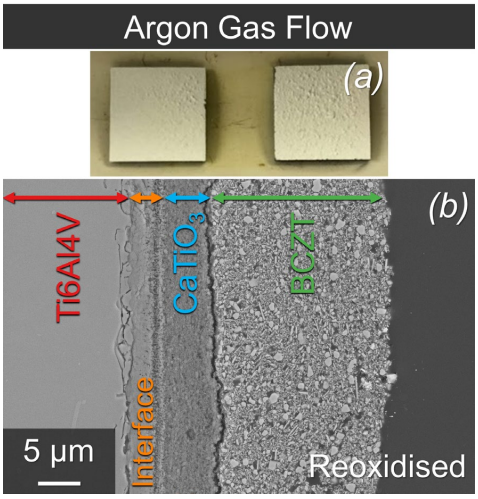

Figure 7.14: (a) Photograph and (b) SEM cross-sectional image of $CaTiO_3$ and BCZT coatings on Ti6Al4V after heat-treatment in Ar atmosphere without disc lids and after reoxidation in air at 600 °C for 24 h.

7.1.4.4. Effect of Coating Thickness

For bi-layer coatings of $CaTiO_3$ and BCZT, the effect of coating thickness was investigated by varying the combination of thin (20 deposition layers) and thick (40 deposition layers) coatings of the two ceramic materials (Figure 7.15). Based on the behaviour observed from previous trials of $CaTiO_3$ coatings of < 20 µm, it was expected that a reaction region at the Ti6Al4V/$CaTiO_3$ interface should form when $CaTiO_3$ and BCZT coatings are thin, and no reaction should occur if both ceramics are deposited in thick coatings. The other two scenarios (thin/thick, thick/thin) could potentially form a reaction region. Ceramic slurries were spray-deposited onto prepared Ti6Al4V substrates and heat-treated in one-step in Ar atmosphere for 1 h at 900 °C.

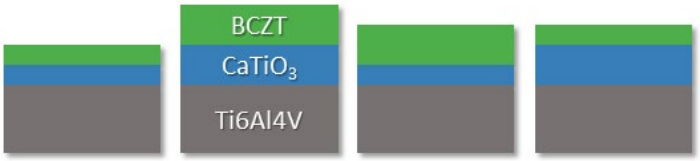

Figure 7.15: Schematic of the bi-layer ceramic coating thicknesses on Ti6Al4V. Combinations of thin and thick ceramic coatings were achieved by deposition of 20 or 40 layers of $CaTiO_3$ and BCZT slurries.

A visual inspection of the coatings prior to heat-treatment revealed that drying cracks formed depending on coating thickness. Thinner coatings maintained their structural integrity (Figure 7.16 (a,b)), whilst thicker coatings tended to crack with advanced deposition steps. The cracks were more obvious after heat-treatment (Figure 7.16 (c,d)). The appearance of white regions of the ceramic coating after heat-treatment confirmed that the coating was detached from the substrate prior to heat-treatment.

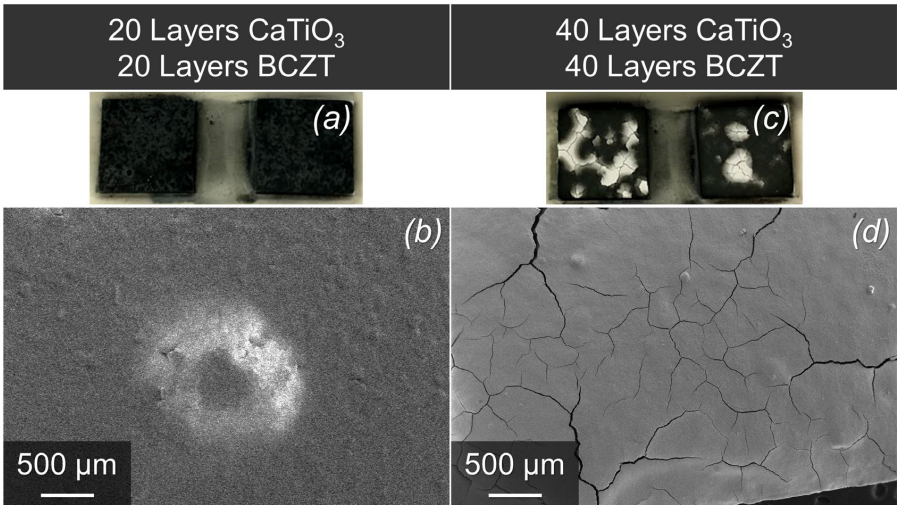

Figure 7.16: Photographs and SEM top view micrographs of (a,b) 20 layers of $CaTiO_3$ and 20 layers of BCZT, and (c,d) 40 layers of $CaTiO_3$ and 40 layers of BCZT on Ti6Al4V after heat-treatment in Ar atmosphere at 900 °C for 1 h.

SEM cross-sectional images of the four ceramic coating arrangements on Ti6Al4V are shown in Figure 7.17 & Figure 7.18. The average thickness of each region and ceramic coating is presented in Table 7.1. All bi-layer $CaTiO_3$/BCZT-coated Ti6Al4V samples clearly show the Ti6Al4V substrate, $CaTiO_3$ ceramic interlayer, and the BCZT upper coating. A porous interface reaction region at the Ti6Al4V/$CaTiO_3$ interface (~2 µm in thickness) is observed for samples with thin $CaTiO_3$ and BCZT coatings (Figure 7.17 (a)). This region is also observed in samples with a combination of thin and thick $CaTiO_3$ and BCZT coatings (Figure 7.17 (b) & Figure 7.18 (a)). For samples that had thick $CaTiO_3$ and BCZT coatings, the region is observed in some areas (Figure 7.18 (b)) but not in others (Figure 7.18 (c)). Two microstructurally distinct $CaTiO_3$ regions were evident in the samples where the porous interface reaction region formed, as seen in previous experiments.

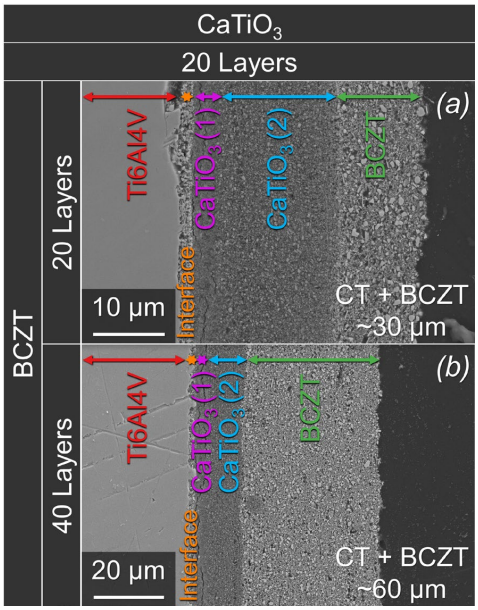

Figure 7.17: Cross-sectional SEM micrographs of 20 deposition layers of $CaTiO_3$, and (a) 20 and (b) 40 deposition layers of BCZT on Ti6Al4V. The bi-layer coatings have total thicknesses of ≈ 30 and ≈ 60 µm, respectively.

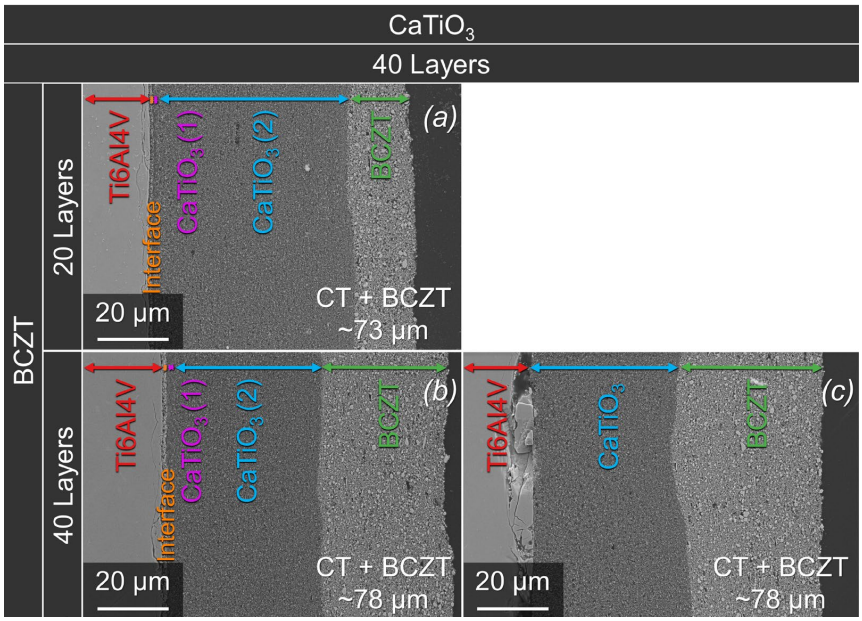

Figure 7.18: Cross-sectional SEM micrographs of 40 deposition layers of $CaTiO_3$, and (a) 20 and (b,c) 40 deposition layers of BCZT on Ti6Al4V. The bi-layer coatings have total thicknesses of ≈ 73 and ≈ 78 µm, respectively.

Table 7.1: Average measured thicknesses of the interface reaction region, $CaTiO_3$, and BCZT coatings on Ti6Al4V for ceramic slurry deposition of 20 and 40 layers.

# Deposited Layers – Material	Average Thickness (µm)				
	Porous Interface Reaction Region	$CaTiO_3$		BCZT	Total (Porous Interface + Ceramic)
		Region 1	Region 2		
20 L $CaTiO_3$ 20 L BCZT	2.0	4.6	11.1	12.3	30.0
40 L $CaTiO_3$ 40 L BCZT	1.7	41.4	–	35.3	78.4
40 L $CaTiO_3$ 40 L BCZT	–	39.5	–	38.0	77.5
20 L $CaTiO_3$ 40 L BCZT	1.8	3.8	12.6	41.6	59.7
40 L $CaTiO_3$ 20 L BCZT	1.3	54.1	–	17.8	73.1
40 L $CaTiO_3$ 20 L BCZT	–	58.0	–	14.0	72.0

SEM EDS mapping was performed to characterise the element distributions through the cross-sectional areas without (Figure 7.19 (a)) and with (Figure 7.19 (b)) the porous interface reaction region. Without the porous interface reaction region, no significant diffusion of the different elements over the Ti6Al4V/$CaTiO_3$ and $CaTiO_3$/BCZT interfaces was apparent (Figure 7.19 (a)). Each material is distinctly delineated from the next as shown by the abrupt change in element concentration correlating with the interface shown in the back-scattered electron (BSE) image. In contrast, the cross-sectional area with a porous interface reaction region shows a more gradual change of the element concentrations at the interfaces, as displayed in Figure 7.19 (b). EPMA WDS mapping confirms these results (Figure 7.20). The porous interface reaction region is slightly O-enriched adjacent to the $CaTiO_3$ coating. Compared to the Ti6Al4V substrate, the porous interface region appears to be Ca-enriched and deficient in Ti, Al, and V.

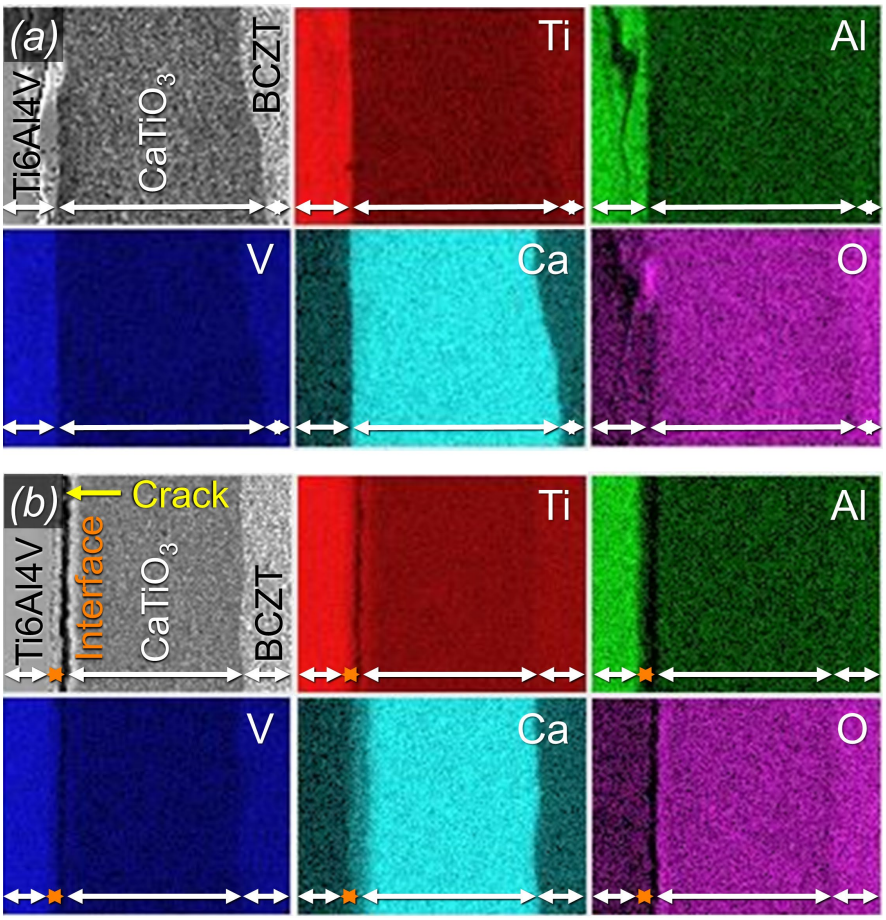

Figure 7.19: SEM EDS mapping of $CaTiO_3$ and BCZT coatings (40 + 40 ceramic slurry deposition layers) on Ti6Al4V (a) without, and (b) with a porous interface reaction region at the Ti6Al4V/$CaTiO_3$ coating. A distinct crack is visible in (b), as well as diffusion of Ti, V, Ca, and O at the Ti6Al4V/$CaTiO_3$ interface.

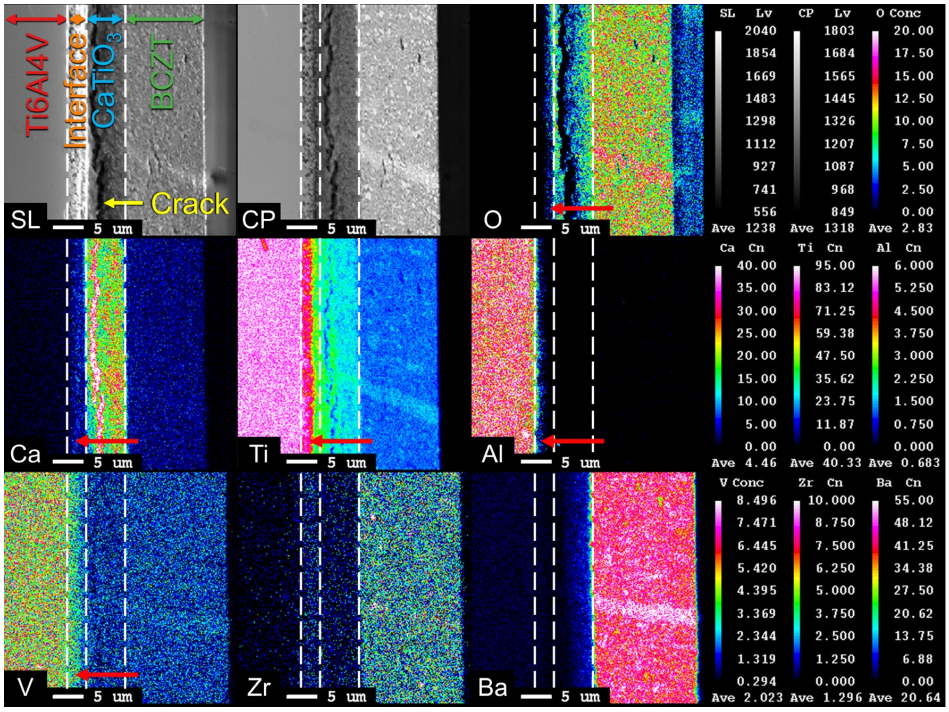

Figure 7.20: EPMA WDS mapping of the Ti6Al4V, $CaTiO_3$ and BCZT cross-section containing the porous interface region. The red arrows indicate regions of interest. Explanation of abbreviations: SL secondary electron image (SEI), CP composition image/backscattered electron image (BEI), Lv grey level intensities of SEI and BEI, Conc/Cn semiquantitative concentrations in mass % (not ZAF corrected; atomic number (Z), absorption of X-rays (A), X-ray fluorescence (F)).

Crack evolution was observed in some samples after ageing for several weeks in ambient conditions with constant temperature and relative humidity (23 °C and 23 %). Figure 7.21 (a) displays the SEM micrograph of a $CaTiO_3$- and BCZT-coated Ti6Al4V sample imaged within one week of being embedded into epoxy. Good adherence and attachment are observed at the Ti6Al4V/$CaTiO_3$ and $CaTiO_3$/BCZT interfaces. Samples were then aged for several weeks and re-imaged (Figure 7.21 (b)). A distinct crack is apparent in the $CaTiO_3$ coating and appears to have formed during ageing. In other samples, the crack is sometimes observed at the $CaTiO_3$/BCZT interface, but it is most often observed within the $CaTiO_3$ coating.

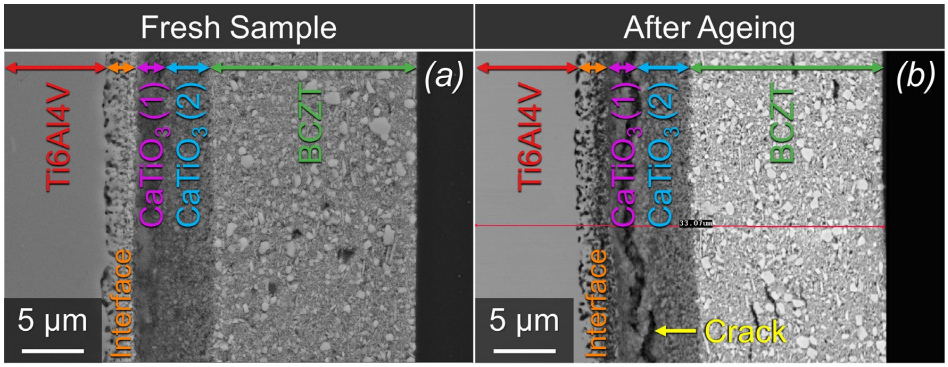

Figure 7.21: Cross-sectional SEM micrographs of a (a) freshly epoxy-embedded $CaTiO_3$- and BCZT-coated Ti6Al4V sample, and (b) the same sample after ageing for several weeks in an environment with constant temperature and relative humidity (23 °C and 23 %). Cracks evolve within the $CaTiO_3$ coatings during ageing.

Some samples that were not embedded in epoxy also displayed signs of instability during ageing. Figure 7.22 shows photographs of a $CaTiO_3$- and BCZT-coated Ti6Al4V sample. The fresh sample displays a well-attached coating (Figure 7.22 (a)). After several weeks of ageing at constant temperature and relative humidity (23 °C and 23 %), the coating detached from the substrate. Peeling and delamination of the coating is obvious at the central left side of the sample, where a dark underlayer is revealed (Figure 7.22 (b)).

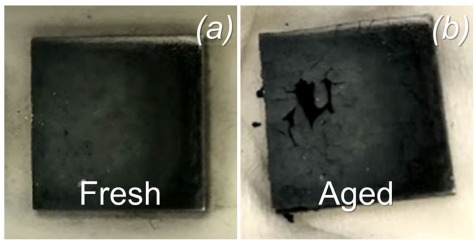

Figure 7.22: Photographs of a $CaTiO_3$- and BCZT-coated Ti6Al4V sample (a) immediately after heat-treatment and (b) after ageing for several weeks at constant temperature and relative humidity (23 °C and 23 %). The aged sample shows delamination and peeling of the ceramic coating from the metal substrate.

7.2. Discussion

The aim of this section of work was to develop robust BCZT coatings on metal implant materials through the optimisation of the spray-coating technique. Several parameters were adjusted to obtain well-adhered and dense ceramic coatings without compromising

the structural integrity of the substrate. The processing details are presented in Section 3.2.4.

7.2.1. Substrate Treatment

One challenge associated with the production of a ceramic coating on a metal substrate is the processing temperature. Bulk BCZT ceramics produced via the solid-state synthesis method require heat-treatment in air at temperatures between 1300 to 1525 °C to produce dense ceramics [119], [148]. In the current work, the optimal processing temperature for the synthesis of dense, bulk BCZT ceramics was determined to be at least 1400 °C based on dilatometry testing (Appendix 1). Metals such as stainless steel 316L and Ti6Al4V cannot withstand these high temperatures in air. Thermal oxidation studies conducted on Ti6Al4V at temperatures as low as 500 °C show that the metal forms a surface oxidation layer which increases in thickness with time and temperature. At temperatures above 800 °C, the oxide layer becomes weakly adhered and spalls off the bulk material [149]. Stainless steels additionally experience a reduction in strength due to metal loss during the oxide formation from 450 °C [150], [151]. In the current work, the formation and spalling of an oxide layer on Ti6Al4V was observed after heat-treatment at 900 °C in air (Figure 7.4). Due to the risk of high temperature oxidation, the BCZT ceramic coatings on metal substrates in this work were heat-treated in a tube furnace in Ar atmosphere. The temperatures were limited to 900 °C. Although heat-treatment in Ar atmosphere protects the mechanical integrity of the metals, reduction of Ti^{4+} to Ti^{3+} occurred shown from the black colour of the samples. As such, a subsequent reoxidation step is required. Figure 7.14 shows a $CaTiO_3$- and BCZT-coated sample after reoxidation in air at 600 °C for 24 h. Successful reoxidation was evidenced by the colour change of the coating from dark black to white [152].

7.2.2. BCZT on Stainless Steel and Ti-Alloy

The direct deposition of BCZT showed that these coatings on stainless steel 316L were not stable. This was observed by the poor adhesion and more pronounced delamination of the coatings from the stainless steel 316L substrate, as compared to the Ti6Al4V substrate (Figure 7.5 (c,e)).

One factor that could influence the delamination behaviour is the thermal expansion mismatch between the metal substrate and coating. BCZT has a lower TEC than stainless steel 316L (Table 2.2). Therefore, the BCZT coatings would be under compressive stress during cooling, which would constrain crack formation and enhance the adhesive strength of the coating to the substrate. In contrast, BCZT has a higher TEC than Ti6Al4V and would be under tensile stress during cooling, which can promote the formation of cracks perpendicular to the interface. However, this is not observed, and the delamination behaviour of the coatings does not appear to be directly related to the thermal expansion mismatch.

The delamination behaviour may instead be more strongly influenced by the densification behaviour of BCZT on the substrates. The BCZT ceramics show larger grains on stainless steel 316L (Figure 7.5 (b,c)) than on Ti6Al4V at similar temperatures (Figure 7.5 (d,e)). The grain growth progression on both substrates from 900 to 1000 °C is presented in Appendix 6 & Appendix 7. It is therefore likely that the dense, coarse-grained BCZT coatings on stainless steel 316L were more strained than the fine BCZT particles on Ti6Al4V, thus causing the delamination observed on stainless steel 316L.

7.2.3. $CaZrO_3$ and $CaTiO_3$ Interlayer Materials

$CaZrO_3$ and $CaTiO_3$ were investigated as interlayer materials to promote the bonding between the BCZT coatings and Ti6Al4V substrates. The TECs for these materials are more similar to the TEC of Ti6Al4V than BT-based ceramics, which should reduce the thermal expansion mismatch between the BCZT coating and Ti6Al4V substrate (Table 2.2). The slightly higher TEC of $CaTiO_3$ compared to $CaZrO_3$ recommends it as a more suitable interlayer material to reduce the strain between the BCZT coating and Ti6Al4V substrate. Furthermore, the deposition and heat-treatment of $CaZrO_3$ and $CaTiO_3$ coatings on Ti6Al4V showed an interface reaction region at the Ti6Al4V/$CaTiO_3$ interface only, indicating better bonding between $CaTiO_3$ and Ti6Al4V (Figure 7.6).

7.2.4. Cracking

Three main types of cracking were observed during the synthesis of $CaTiO_3$ and BCZT coatings on Ti6Al4V. For clarity, the cracking types are presented in Figure 7.23. Figure 7.23 (a) shows cracking in the ceramic surface, reflecting the behaviour observed in the

coating in Figure 7.16 (d). Cracks perpendicular to the metal substrate were also seen in the BCZT coating (Figure 7.10 (a)), as described in Figure 7.23 (b). Cracks parallel to the substrate surface were also evident, mostly within the $CaTiO_3$ coating (Figure 7.23 (c)), and sometimes at the $CaTiO_3$/BCZT interface (Figure 7.7 (d), Figure 7.10 (b,c), Figure 7.14 (b), & Figure 7.21 (b)). In addition, the cracks shown in Figure 7.21 (b) were detected after several weeks of ageing.

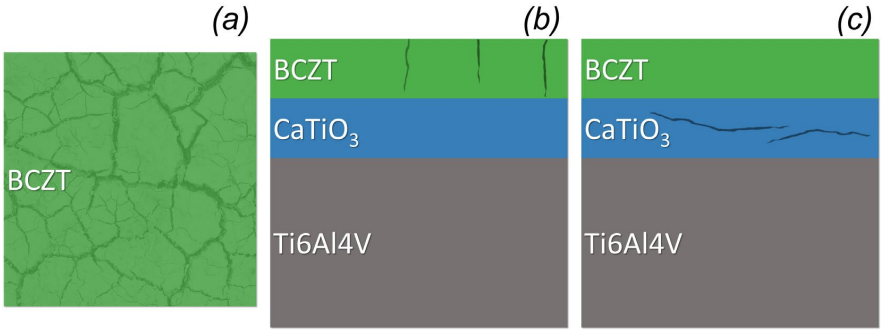

Figure 7.23: Different types of cracking observed during the development of $CaTiO_3$ and BCZT coatings on Ti6Al4V by spray-deposition. (a) Top view of the cracking in the ceramic coating, (b) cross-sectional view of the cracking in the BCZT coating, and (c) cross-sectional view of the cracking in the $CaTiO_3$ coating.

The observed cracking has several origins: drying cracks, densification during heat-treatment, epoxy shrinkage, the reaction between the Ti6Al4V metal substrate and the $CaTiO_3$ ceramic coating, and the subsequent formation of the reaction products of this interface reaction. During spray-deposition, drying cracks (Figure 7.23 (a)) were observed when increasing the number of deposition layers from 40 (20 + 20) to 80 (40 + 40) (Figure 7.16). These features were noticed during spray-deposition and were more visible after heat-treatment due to the variation in the colour of the coating (Figure 7.7 (a,b), Figure 7.16 (c)).

The perpendicular cracks observed in the BCZT coatings (Figure 7.10 (a) and Figure 7.23 (b)) likely originate from the difference in shrinkage between the $CaTiO_3$ and BCZT ceramics during heat-treatment as they do not extend into the $CaTiO_3$ coating, which would otherwise suggest they are drying cracks. The as-received $CaTiO_3$ powders have a narrow size-distribution with particles ≈ 0.4 µm, while the as-prepared BCZT powders have a wider size distribution and larger particles of ≈ 0.8 µm (Figure 7.3). The more

even distribution and smaller particle size of the $CaTiO_3$ powders aided densification during heat-treatment, resulting in strain formation in the BCZT coating and the eventual cracking of the BCZT coating to relieve the strain [153].

Some of the crack formation observed in the ceramic coatings (Figure 7.23 (c)) can be attributed to the shrinkage of the epoxy in which samples were mounted. Samples were cold-mounted in epoxy and polished in preparation for SEM imaging. Imaging of the sample cross-sections was performed within 2–3 days of the completion of the embedding procedure, and again several weeks or months afterwards. Figure 7.21 (a) shows the cross-section of a fresh sample. After several weeks of ageing, cracks can be seen in the same imaging region through the $CaTiO_3$ coating in Figure 7.21 (b). Inspection of the epoxy surrounding the samples shows that the epoxy contracts from the outer edges of the sample surface (Figure 7.24), suggesting that the cracks in the ceramic coatings originate partially from the contraction of the epoxy.

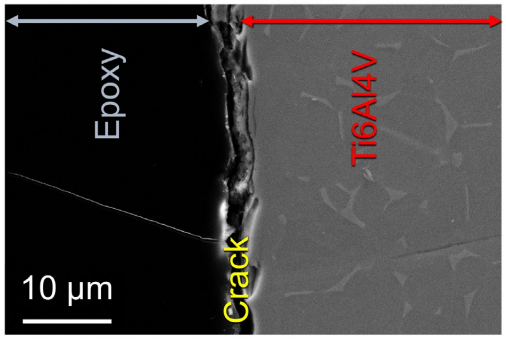

Figure 7.24: Cross-sectional SEM micrograph showing the shrinkage of the epoxy from the mounted ceramic-coated Ti6Al4V samples.

The crack formation observed through the $CaTiO_3$ coating in aged samples (Figure 7.23 (c)) may also be attributed to the porous interface reaction region at the Ti6Al4V/$CaTiO_3$ interface. Figure 7.25 shows a $CaTiO_3$- and BCZT-coated Ti6Al4V sample of ~200 µm in thickness, heat-treated in one step. This sample does not contain the porous interface region. Two areas of the coating were imaged immediately after heat-treatment (Figure 7.25 (a,b)), and again after one year of ageing at constant temperature and relative (23 °C and 23 %) (Figure 7.25 (c,d)). The coatings appear to be stable. No crack formation was observed in the cross-sectional images of the epoxy-mounted sample nor was any peeling or flaking of the sample coating observed in the unmounted sample (Figure 7.25 (e,f)).

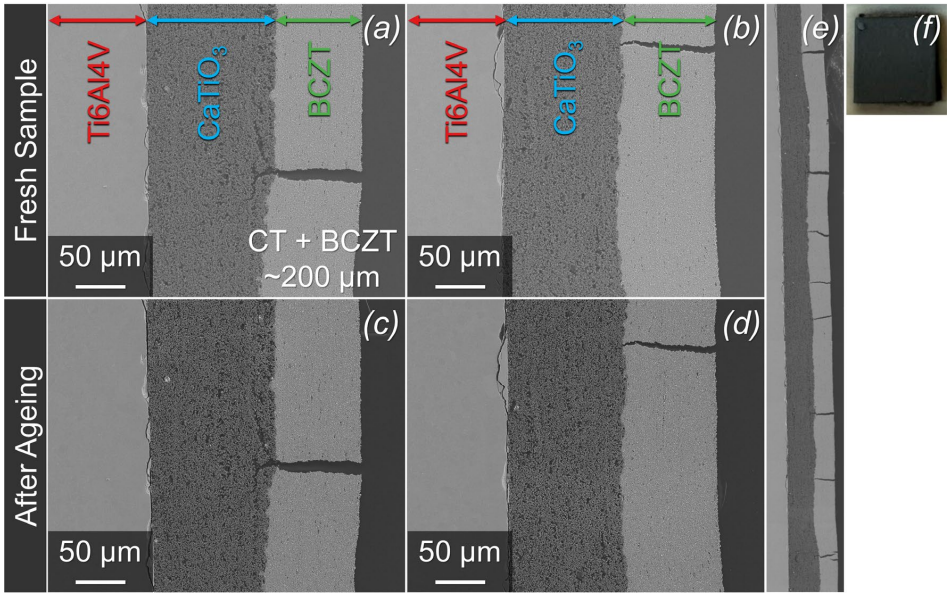

Figure 7.25: (a-d) Cross-sectional SEM micrographs of $CaTiO_3$ and BCZT coatings deposited onto Ti6Al4V metal substrates (a,b) immediately after heat-treatment and (c,d) after ageing for 1 year. The full coating after 1 year of ageing is shown in (e) and (f).

In contrast, some samples showed detachment of the ceramic coating after being aged under the same conditions with a constant humidity and temperature. The cracking shown in Figure 7.21 (b) is likely to have two origins: the epoxy shrinkage as explained above, and the presence of the porous interface reaction region. The cracks in this sample are observed in the $CaTiO_3$ coating in the region adjacent to the porous interface reaction region. The location of these cracks was noticed frequently in other samples where the interface reaction region was present (Figure 7.10 (b,c)). Although the interface reaction region originally appeared to improve the interconnection and bonding between the metal substrate and the ceramic coating, longer term studies showed that the interface region may be unstable with time.

7.2.5. Interface Reaction Region

The porous interface reaction region seen at the Ti6Al4V/$CaTiO_3$ interface may contribute significantly to the crack formation observed through the $CaTiO_3$ coating in aged samples. To formulate a thorough understanding of the interface reaction region,

characterisation of the $CaTiO_3$ coatings on Ti6Al4V, and bi-layer coatings of $CaTiO_3$ and BCZT on Ti6Al4V were analysed for their microstructure and element distributions.

Investigation of the bi-layer coatings deposited on Ti6Al4V showed that there is a relationship between the formation of the porous interface reaction region and the ceramic coating thickness. From previous trials of ceramic coatings of < 20 µm and > 200 µm thickness, it was expected that a Ti6Al4V/$CaTiO_3$ interface reaction region should form when both coatings are thin, and no reaction for when the coatings are both thick. Combinations of thin/thick coatings were expected to potentially form the interface reaction region.

As expected, a reaction region formed at the Ti6Al4V/$CaTiO_3$ interface for samples with thin $CaTiO_3$ and BCZT coatings (Figure 7.17 (a)). Although no reaction region was expected for samples with thick $CaTiO_3$ and BCZT coatings, a reaction was observed in some areas of the sample and not in others (Figure 7.18 (b,c)). The total thickness of the two ceramics coatings for this sample was on average ~78 µm. This is significantly thinner than the stable sample presented in Figure 7.25, which had a total ceramic coating thickness of ~200 µm. Therefore, a ceramic coating thickness of ~80 µm may be the threshold value at which an interface reaction region can be formed.

Figure 7.26 and Figure 7.27 show the EDS point and line scans of $CaTiO_3$- and BCZT-coated Ti6Al4V samples that do and do not contain the porous interface reaction region at the Ti6Al4V/$CaTiO_3$ interface. These corroborate the mapping results shown in Figure 7.19, and provide further information on the element distributions through the interfaces. Without the porous interface, limited diffusion through the interfaces is observed, especially around the point scan areas 2–3 in Figure 7.26 (a) and line scans in Figure 7.27 (a). In contrast, the cross-sectional region containing the porous interface reaction region shows diffusion across the Ti6Al4V/$CaTiO_3$ interface (Figure 7.26 (b) and Figure 7.27 (b)). In the point scan, a more gradual change in the element distributions is seen from points 2–4 (Figure 7.26 (b)) compared to the cross-section without the interface reaction region. From the line scans, the porous interface reaction region shows the presence of Ti, Al, V, Ca, and O (Figure 7.27 (b)). The $CaTiO_3$ region adjacent to the porous interface reaction region is Ca-deficient compared to the bulk $CaTiO_3$ coating. Some interdiffusion of Ca and Ba is observed at the $CaTiO_3$/BCZT interface.

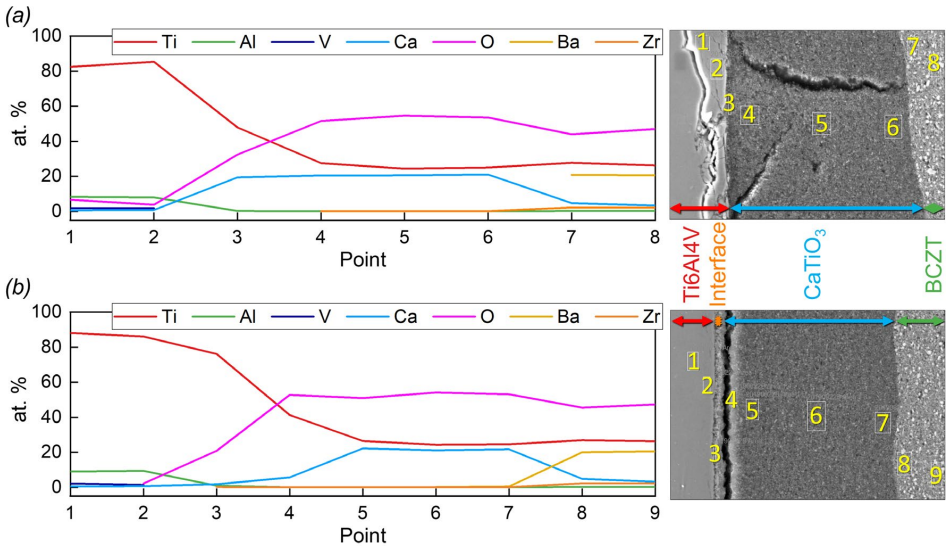

Figure 7.26: EDS point scan plots showing element distributions and the related SEM micrographs of $CaTiO_3$- and BCZT-coated Ti6Al4V samples (a) not containing and (b) containing the porous interface reaction region. Eight and nine EDS point scans were performed across the Ti6Al4V/$CaTiO_3$/BCZT samples in (a) and (b), respectively. The Ti6Al4V/$CaTiO_3$ and $CaTiO_3$/BCZT interfaces lie either side of points 2,3,6,7 (a) and 2,4,7,8 (b).

Precise detection of Ba, Ti, and V with SEM EDS is difficult as their characteristic X-ray energies overlap (Ba Lα 4.465 eV and Ti Kα 4.508 eV, Ti Kβ 4.931 eV and V Kα 4.949 eV), and it is impossible to reliably deconvolute their peaks. This is evident by the identical shape of the Ba and Ti line scans (Figure 7.26 & Figure 7.27), and the incorrect detection of Ba within Ti6Al4V. Using the deconvoluted lower energies is not a reliable alternative as it results in exacerbated ZAF correction errors (atomic number (Z), absorption of X-rays (A), and X-ray fluorescence (F)). To confirm and elaborate on the results observed from EDS analysis, WDS was utilised to eliminate the issue with energy peak overlap. However, like the EDS technique, WDS requires the sample surface to be completely flat as topographical features and porosities can affect the X-ray scattering behaviour. This is shown by the anomaly in the Ca concentration at the crack observed in Figure 7.28. As such, the composition of each of the different regions across the cross-section cannot be precisely determined quantitatively, however, a better impression of the element distributions through the metal substrate/ceramic coatings cross-section can be formed.

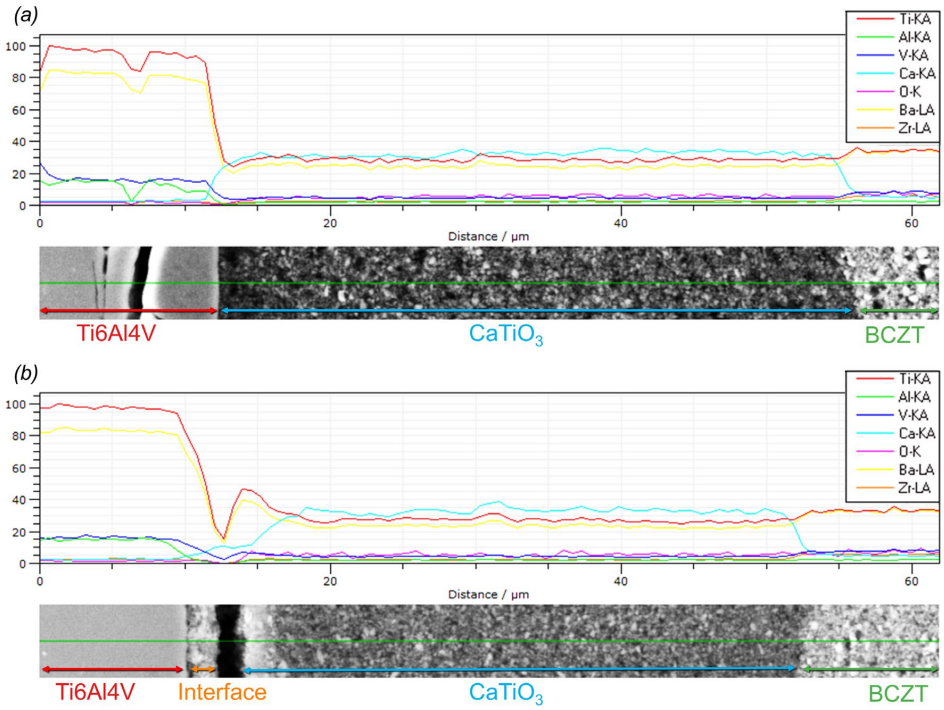

Figure 7.27: SEM EDS line scans of $CaTiO_3$- and BCZT-coated Ti6Al4V samples showing the element distributions over the metal/ceramics cross-sectional area for samples (a) not containing and (b) containing a porous interface reaction region at the Ti6Al4V/$CaTiO_3$ interface.

Comparing the WDS and EDS line scans, similar element distributions are observed confirming the EDS results (Figure 7.27 & Figure 7.28). Oxygen is present at the porous interface reaction region and its concentration increases with proximity to the surface. The interface reaction region is Ca-deficient compared to the bulk $CaTiO_3$ region. The $CaTiO_3$ coating has two distinct microstructural regions, with the first region adjacent to the porous interface having a lower concentration of Ca than the second region closer to the BCZT. Vanadium appears to diffuse from the Ti6Al4V substrate into the interface region from a greater depth in the Ti6Al4V than Al, and V has a slightly higher concentration within the interface region than Al. The signal for Ti decreases from the interface region and onwards into the $CaTiO_3$ and BCZT coatings. Zirconium and Ba are both detected within the BCZT coating, as expected. Also, some interdiffusion of Ca and Ba is observed at the $CaTiO_3$/BCZT interface.

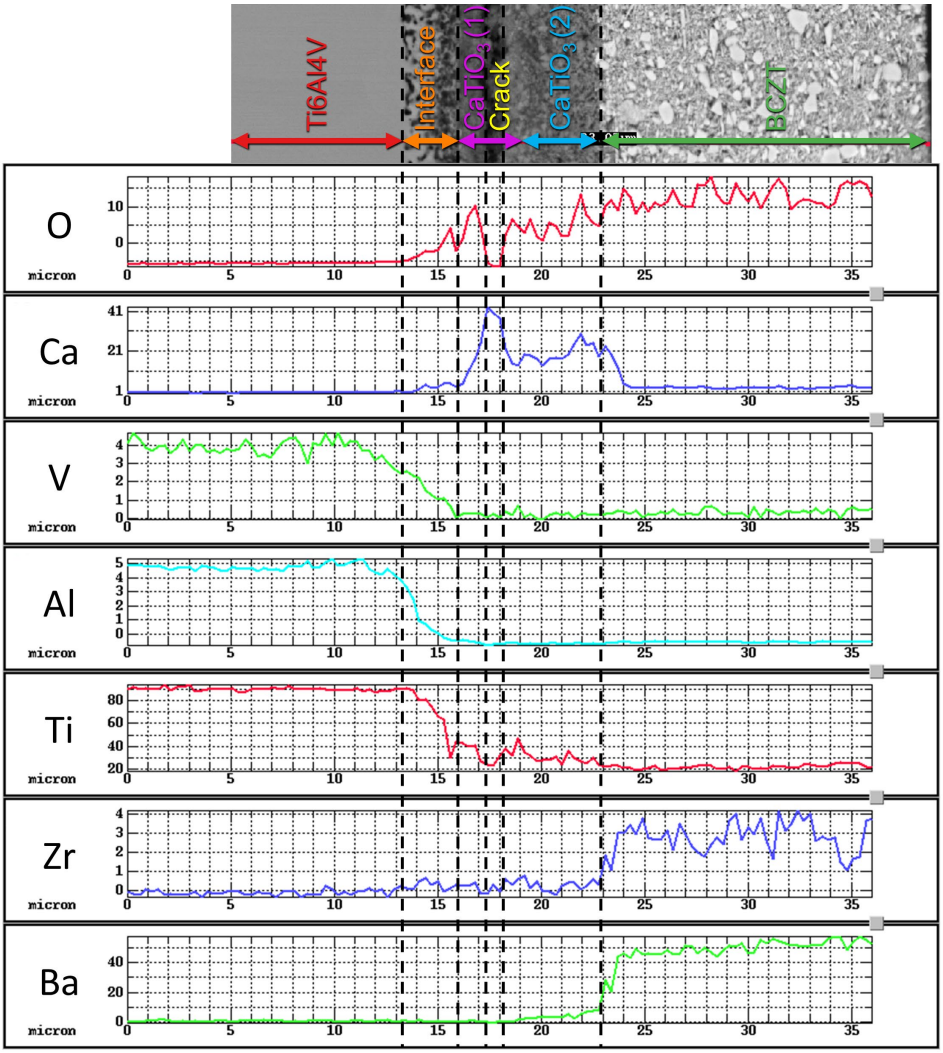

Figure 7.28: EPMA WDS line scans of the cross-section of a $CaTiO_3$ and BCZT coating on Ti6Al4V where a porous interface region between Ti6Al4V and $CaTiO_3$ exists. Semiquantitative concentrations in mass %.

An XRD diffractogram of a $CaTiO_3$- and BCZT-coated Ti6Al4V sample that displayed the porous interface reaction region, and which showed delamination of the ceramic coating during ageing is shown in Figure 7.29. At the delaminated interface, depicted schematically in the inset figure, BCZT and $CaTiO_3$ were detected as expected. In addition, $TiO_{0.84}$ and $Ca(OH)_2$ were observed.

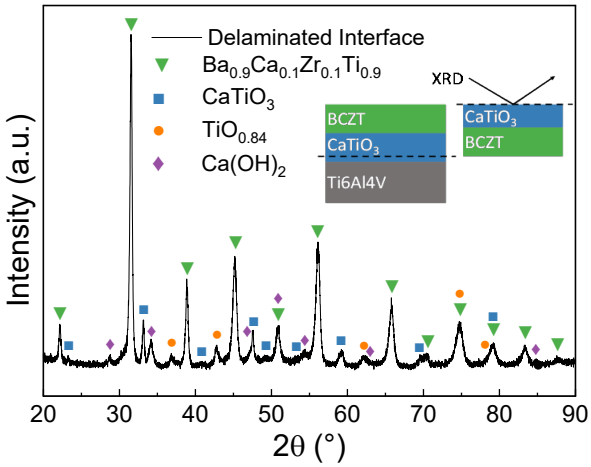

Figure 7.29: XRD diffractogram of the delaminated ceramic coating interface, as described in the inset schematic. The $CaTiO_3$- and BCZT-coated Ti6Al4V sample was heat-treated in two steps at 900 and 950 °C for 1 h in Ar atmosphere and showed a porous interface reaction region at the Ti6Al4V/$CaTiO_3$ interface. The diffractogram is matched with PDF 04-020-5213 $Ba_{0.9}Ca_{0.1}Zr_{0.1}Ti_{0.9}O_3$ barium calcium titanium zirconium oxide, PDF 00-022-0153 $CaTiO_3$ perovskite, PDF 04-006-1902 $TiO_{0.84}$ titanium oxide, and PDF 01-070-5492 $Ca(OH)_2$ portlandite.

7.2.6. Mechanism of the Interface Region Formation

In the following section, a proposed mechanism for the reactions at the Ti6Al4V/$CaTiO_3$ interface during heat-treatment, and the formation of the porous interface reaction region and the unstable $CaTiO_3$ region adjacent to it are presented. A schematic of the mechanism is displayed in Figure 7.30.

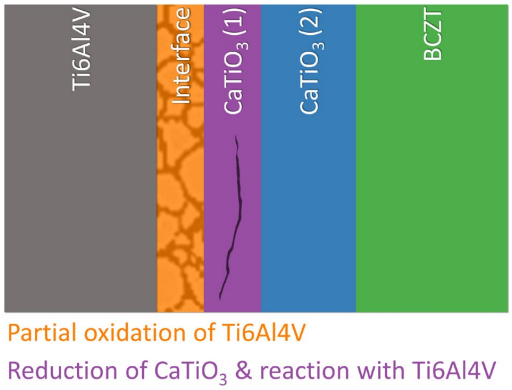

Figure 7.30: Schematic of the proposed mechanism for the formation of the porous interface reaction region between Ti6Al4V and $CaTiO_3$.

The porous interface reaction region arises from oxidation of the Ti6Al4V metal substrate exemplified by:

$$Ti(s) + \frac{x}{2}O_2(g) \rightarrow TiO_x(s) \quad (14)$$

$$V(s) + \frac{x}{2}O_2(g) \rightarrow VO_x(s) \quad (15)$$

with oxygen coming from two main sources. The first source is impurities in the Ar gas, evidenced by the effect of coating thickness on the formation of the interface reaction region. The second source of oxygen is from the reduction of Ti in $CaTiO_3$. During heat-treatment, the $CaTiO_3$ coating reduces because of the low oxygen partial pressure (pO_2) due to the inert atmosphere (Ar). This is described in the following equation:

$$CaTiO_3(s) \rightarrow CaTiO_{3-\delta}(s) + \frac{\delta}{2}O_2(g) \quad (16)$$

Since the partial pressure of oxygen is not known at the Ti6Al4V interface, the oxidation numbers of Ti and V in equations (14) and (15) are not known [154]. The EDS and WDS data showed the presence of Ti and O at the porous interface reaction region (Section 7.2.5), and $TiO_{0.84}$ was observed in the XRD measurements pattern (Figure 7.29). Furthermore, oxidation of the Ti6Al4V substrate facilitates the formation of the porous microstructure of the interface reaction region. This is reminiscent of the Kirkendall effect, or creation of voids, which is observed at the interface between two different metals, as a result of unbalanced ion diffusion rates. A similar microstructure has been presented by Mo et al. at the diffusion bonded interface between stainless steel 316L and Ti6Al4V [155], and at metal/metal oxide interfaces after oxidation of core/shell nanostructures [156].

The further reduction of $CaTiO_{3-\delta}$ when in contact with the Ti6Al4V substrate causes instability of the material and its decomposition, such that $TiO_{1-\delta/2}$ and CaO form. Titanium will have too low of an oxidation state to stabilise the perovskite phase with oxidation states Ti^{4+} or Ti^{3+}.

$$Ti(s) + CaTiO_{3-\delta}(s) \rightarrow 2TiO_{1-\delta/2}(s) + CaO(s) \quad (17)$$

Calcium oxide is highly hygroscopic [157], reacting with moisture in the air and forming $Ca(OH)_2$. This causes expansion, inducing the formation of the observed cracks after ageing in ambient atmosphere. The XRD analysis (Figure 7.29) also confirmed the

presence of $Ca(OH)_2$ at the delaminated interface of a coating containing the porous interface reaction region.

From the WDS line scans (Figure 7.28), Ca^{2+} is observed at the porous interface reaction region. This suggests a possible time-dependent effect. At a certain thickness, the formation of the porous interface reaction region becomes a protective layer between Ti6Al4V and $CaTiO_3$. This decreases the effect of the reduction reaction (17), enabling Ca^{2+} to react with $TiO_{1-\delta/2}$ to form stable $CaTiO_{3-\delta}$ at the interface reaction region.

The bulk $CaTiO_3$ material and the reduced $CaTiO_{3-\delta}$ will have different sintering properties, hence the two microstructurally distinct microstructures observed in the SEM micrographs. The $CaTiO_3$ adjacent to the porous interface reaction region, $CaTiO_3(1)$, is Ca-deficient compared to the bulk $CaTiO_3$ coating, $CaTiO_3(2)$, and both appear microstructurally distinct.

Suggestions for Improving the Synthesis Process

Although the interface reaction region appeared to improve bonding between Ti6Al4V and $CaTiO_3$, the formation of CaO and the subsequent formation of $Ca(OH)_2$ in ambient conditions proves this reaction region to be undesirable. Therefore, measures must be enforced to prevent the reactions described above during heat-treatment. Possible solutions include pre-oxidation of the Ti6Al4V substrate prior to coating deposition, oxygen-depletion of the heat-treatment environment, or kinetically hindering oxygen diffusion through the coating by modifying the microstructure of the ceramics.

Pre-oxidation of the Ti6Al4V substrate prior to coating deposition will create a passive layer of TiO_2 [158]. The TiO_2 layer can act as a separation layer between Ti6Al4V and $CaTiO_3$, preventing their interaction and the reduction of $CaTiO_3$ and formation of oxygen at the interface during heat-treatment. However, the type of oxidation treatment should be carefully considered. As mentioned earlier, studies have shown that thermal oxidation of Ti6Al4V occurs from 500 °C. At temperatures above 800 °C, the oxide layer becomes weakly adhered [149]. Therefore, to ensure that the adhesion of a ceramic coating to the oxidised Ti6Al4V substrate remains strong, pre-oxidation of the Ti6Al4V substrate must be performed at temperatures below 800 °C.

Another method to minimise the thermal oxidation of Ti6Al4V is to limit the amount of available oxygen in the gaseous heat-treatment environment to prevent oxygen diffusion through the ceramic coatings to the Ti6Al4V/$CaTiO_3$ interface. In the current work, an inert atmosphere (99.999 % pure Ar gas) was used in combination with several evacuation and purge cycles to prepare the furnace before heat-treatment. Additionally, pure Ti was used as an oxygen-getter to remove excess oxygen in the Ar flow prior to reaching the ceramic/metal samples due to the lower oxidation resistance compared to Ti6Al4V [159]. Despite these practices, oxidation of Ti6Al4V was still observed as full removal of oxygen from the environment was not achievable. In addition, depleting the heat treatment environment of oxygen only serves to drive the reduction of $CaTiO_3$ and the formation of oxygen at the Ti6Al4V/$CaTiO_3$ interface. Therefore, this method is not considered as effective as pre-oxidising the Ti6Al4V substrates prior to ceramic coating deposition.

Modifying the properties of the ceramic coating may help to limit the oxidation of the Ti6Al4V substrates during heat-treatment. Taking inspiration form Darcy's law, which describes fluid and gas flow through porous media, the green body density of the ceramic coatings can be increased to kinetically hinder the diffusion of oxygen from the environment to the Ti6Al4V surface. In addition, the coating thickness can be increased. In this work, it was seen that increasing the coating thickness to > 80 µm minimised the formation of the porous interface region in bi-layer coatings of $CaTiO_3$ and BCZT on Ti6Al4V. However, the coating thickness must be carefully considered as very thick coatings can induce residual stresses that can form drying cracks.

7.3. Summary

BCZT ceramic coatings were spray-deposited onto common bone implant metals: stainless steel 316L and Ti-alloy Ti6Al4V. BCZT ceramics attach better to Ti6Al4V than stainless steel 316L due to the lower densification of BCZT on Ti6Al4V than on stainless steel 316L. To reduce the thermal expansion mismatch between Ti6Al4V and BCZT, $CaTiO_3$ interlayer materials were determined to be useful. However, certain processing parameters can cause an intensive reaction between Ti6Al4V and $CaTiO_3$ during heat-treatment, and the formation of an interface reaction region that proves to be unstable during ageing in ambient conditions. Analysis of the element distributions through the

Ti6Al4V/$CaTiO_3$ interface showed the presence of Ti, Al, V, Ca, and O at the interface reaction region. The reaction between Ti6Al4V and $CaTiO_3$ enabled the formation of CaO at the interface region, which can subsequently become unstable, hygroscopic $Ca(OH)_2$ in humid ambient conditions and cause delamination of the coating. Therefore, processing parameters must be optimised to prevent the formation of CaO to obtain stable, well-adherent BCZT coatings on Ti6Al4V. To improve the coating stability, pre-oxidation of Ti6Al4V substrates, and the application of thicker, denser ceramic coatings are recommended.

Chapter 8

Conclusions

The replacement of damaged or diseased bone tissue with synthetic biomaterials for repair and regeneration is a common practice, involving the use of materials such as metals and ceramics. However, conventional implant designs are not electroactive, despite the knowledge that bone itself displays a piezoelectric effect, and that bone cell attachment and proliferation are stimulated by the application of electric charge. BCZT piezoelectric ceramics are one of the best lead-free alternatives that exhibit exceptional piezoelectric responses. Although these materials are often utilised in electrical applications, they have yet to be applied as biomedical implant materials.

In this thesis, several aspects of the potential of BCZT piezoelectric ceramics as bone replacement materials were investigated. These included the ability to modify the piezoelectric response and the resistance to mechanical depolarisation without toxic elemental additives, the compatibility with biological cells in terms of cell proliferation and viability, the influence of soaking in liquid environments, and how to deposit mechanically robust coatings of BCZT onto metal substrates. These aspects were addressed as a preliminary study into the functionalisation of current metal implant materials for accelerated healing through autonomous and localised delivery of electrical stimuli at an implant site. Several conclusions were drawn from these experiments.

First, prediction of the piezoelectric properties for a given BCZT chemical composition is challenging due to the complex nature of the BCZT system. The ongoing debate surrounding the MPB region in literature, combined with the observation of a mixed-phase structural transition region from primarily tetragonal ($BC_{15}Z_{10}T$) to primarily rhombohedral ($BC_{10}Z_{10}T$) compositions in the current work highlight this. However, it was determined that the phase mixture, and especially phase fractions affect the piezoelectric response and depolarisation resistance to static compressive mechanical loads. In addition, microstructure was observed to have a significant influence. Thus, new

avenues for the tailoring of the piezoelectric response and mechanical depolarisation resistance of BCZT ceramics for specific physiological environments without the need for toxic elemental dopants have been revealed.

To determine the compatibility of BCZT ceramics with the biological environment, *in vitro* cell viability and proliferation studies of bulk BCZT ceramics with human osteoblast and endothelial cells were conducted over a 10-day period. The experiments showed that BCZT ceramics are not cytotoxic, indicating the potential implementation of these ceramics as biomaterials. Additionally, 90-day soaking studies in deionised water and 0.154 M NaCl solution showed that although BCZT ceramics exhibit ion loss during soaking, the nature of the ion release suggests the possibility of a pre-conditioning procedure for BCZT implant materials. Significant release of A-site ions, particularly Ba^{2+}, was observed within the first 10 days of soaking followed by a possible formation of stable non-toxic B-site terminated BCZT surfaces. As such, it is proposed that BCZT implant materials could feasibly be soaked for at least 10 days and thoroughly washed prior to implantation to remove toxic mobile Ba ions.

Finally, the formation of mechanically robust BCZT coatings on metal substrates via spray-deposition and heat-treatment is challenging. Direct deposition of BCZT onto stainless steel 316L and Ti-alloy Ti6Al4V metal substrates showed slightly better adhesion of the ceramic to Ti6Al4V. However, to reduce thermal expansion mismatch between the Ti6Al4V and BCZT, $CaZrO_3$ and $CaTiO_3$ interlayer ceramics were investigated. Although $CaTiO_3$ has a more suitable thermal expansion coefficient than $CaZrO_3$, it reacts intensely with Ti6Al4V during heat-treatment under certain processing conditions. The reduction of $CaTiO_3$ in the presence of Ti at the Ti6Al4V/$CaTiO_3$ interface causes the formation of CaO. This compound becomes $Ca(OH)_2$ in humid ambient conditions and causes delamination of the ceramic coating. Therefore, processing parameters such as the heat-treatment temperature, gas type and flow, ceramic coating density and thickness must be carefully monitored and optimised to obtain stable BCZT coatings on Ti6Al4V. Pre-oxidation of the Ti6Al4V metal substrates prior to ceramic coating deposition is proposed as the most effective solution for avoiding the adverse reactions at the Ti6Al4V/$CaTiO_3$ interface.

Chapter 9

Outlook

The work presented in this thesis demonstrates the promising nature of BCZT as an electroactive bone replacement material. Further work on the system is however necessary for the implementation of these materials in the biomedical field.

Good piezoelectric properties were shown for all BCZT materials, and routes for modifying the piezoelectric response and resistance to mechanical depolarisation were highlighted through grain size and compositional tailoring. This enables BCZT to be optimised to the specific stimulation requirements of the implant site. Further work is suggested to determine the effect of cyclic mechanical loading on mechanical depolarisation. As a component part of a dental or joint implant, BCZT will be subjected to cyclic mechanical loads, which may affect the functional lifetime of BCZT as an electrically stimulative material.

Unpoled BCZT was shown to be biocompatible in this work. It is suggested that continued work on the biological effect of BCZT be focused on how cells respond to electrical stimuli generated by the material. It would be of particular interest to investigate the effect of poled BCZT surfaces and how local piezoelectric effects can affect cell responses such as attachment, migration and proliferation. A pre-conditioning treatment was proposed based on the results from the soaking studies. Further studies should therefore investigate the potential and efficacy of this treatment for Ba^{2+} removal from the material surface.

The functionalisation of current metal implant materials with BCZT is a primary goal for the implementation of this material class in the biomedical field. However, spray-deposition proved to be challenging. Moreover, enhanced integration of the implant to the bone tissue is achievable with porous implant surfaces. Therefore, it is recommended that further work on BCZT ceramic coatings on porous Ti6Al4V substrates be pursued, perhaps with deposition techniques such as plasma electrolytic oxidation, that is currently utilised for hydroxyapatite implant coatings.

References

[1] M. Saini, Y. Singh, P. Arora, V. Arora, and K. Jain, "Implant biomaterials: A comprehensive review," *World J. Clin. Cases*, vol. 3, pp. 52–7, 2015, doi: 10.12998/wjcc.v3.i1.52.

[2] A. Butscher, M. Bohner, S. Hofmann, L. Gauckler, and R. Müller, "Structural and material approaches to bone tissue engineering in powder-based three-dimensional printing," *Acta Biomater.*, vol. 7, pp. 907–920, 2011, doi: 10.1016/j.actbio.2010.09.039.

[3] B. J. McEntire, B. S. Bal, M. N. Rahaman, J. Chevalier, and G. Pezzotti, "Ceramics and ceramic coatings in orthopaedics," *J. Eur. Ceram. Soc.*, vol. 35, pp. 4327–4369, 2015, doi: 10.1016/j.jeurceramsoc.2015.07.034.

[4] J. M. Anderson, "Inflammation, wound healing, and the foreign-body response," in *Biomaterials Science: An Introduction to Materials in Medicine*, 3rd ed., B. D. Ratner, A. S. Hoffman, F. J. Schoen, and J. E. Lemons, Eds. Academic Press, 2013, pp. 503–512.

[5] M. Sundfeldt, L. V Carlsson, C. B. Johansson, P. Thomsen, and C. Gretzer, "Aseptic loosening, not only a question of wear: A review of different theories," *Acta Orthop.*, vol. 77, pp. 177–197, 2006, doi: 10.1080/17453670610045902.

[6] Norwegian National Advisory Unit on Arthroplasty and Hip Fracture, "Annual Report 2019."

[7] M. Vandrovcová and L. Bačáková, "Adhesion, growth and differentiation of osteoblasts on surface-modified materials developed for bone implants," *Physiol. Res*, vol. 60, pp. 403–417, 2011.

[8] S. Bodhak, S. Bose, and A. Bandyopadhyay, "Role of surface charge and wettability on early stage mineralization and bone cell–materials interactions of polarized hydroxyapatite," *Acta Biomater.*, vol. 5, pp. 2178–2188, 2009, doi: 10.1016/J.ACTBIO.2009.02.023.

[9] C. M. Murphy, M. G. Haugh, and F. J. O'Brien, "The effect of mean pore size on cell attachment, proliferation and migration in collagen-glycosaminoglycan scaffolds for bone tissue engineering," *Biomaterials*, vol. 31, pp. 461–466, 2010, doi: 10.1016/j.biomaterials.2009.09.063.

[10] S. K. Nishimoto *et al.*, "The effect of titanium surface roughening on protein absorption, cell attachment, and cell spreading," *Int. J. Oral Maxillofac. Implants*, vol. 23, pp. 675–680, 2008.

[11] J. Henkel *et al.*, "Bone regeneration based on tissue engineering conceptions — A 21st century perspective," *Bone Res.*, vol. 1, pp. 216–248, 2013, doi: 10.4248/BR201303002.

[12] E. García-Gareta, M. J. Coathup, and G. W. Blunn, "Osteoinduction of bone

grafting materials for bone repair and regeneration," *Bone*, vol. 81, pp. 112–121, 2015, doi: 10.1016/J.BONE.2015.07.007.

[13] E. Fukada and I. Yasuda, "On the piezoelectric effect of bone," *J. Phys.*, vol. 12, pp. 1158–1162, 1957.

[14] M. Minary-Jolandan and M.-F. Yu, "Nanoscale characterization of isolated individual type I collagen fibrils: Polarization and piezoelectricity," *Nanotechnology*, vol. 20, p. 085706, 2009, doi: 10.1088/0957-4484/20/8/085706.

[15] H.-P. Wiesmann, M. Hartig, U. Stratmann, U. Meyer, and U. Joos, "Electrical stimulation influences mineral formation of osteoblast-like cells *in vitro*," *Biochim. Biophys. Acta*, vol. 1538, pp. 28–37, 2001, doi: 10.1016/S0167-4889(00)00135-X.

[16] M. Hartig, U. Joos, and H.-P. Wiesmann, "Capacitively coupled electric fields accelerate proliferation of osteoblast-like primary cells and increase bone extracellular matrix formation *in vitro*," *Eur. Biophys. J.*, vol. 29, pp. 499–506, 2000, doi: 10.1007/s002490000100.

[17] R. Balint, N. J. Cassidy, and S. H. Cartmell, "Electrical stimulation: A novel tool for tissue engineering," *Tissue Eng. - Part B Rev.*, vol. 19, pp. 48–57, 2013, doi: 10.1089/ten.teb.2012.0183.

[18] P. R. Kuzyk and E. H. Schemitsch, "The science of electrical stimulation therapy for fracture healing.," *Indian J. Orthop.*, vol. 43, pp. 127–31, 2009, doi: 10.4103/0019-5413.50846.

[19] I. S. Aleem *et al.*, "Efficacy of electrical stimulators for bone healing: A meta-analysis of randomized sham-controlled trials," *Sci. Rep.*, vol. 6, p. 31724, 2016, doi: 10.1038/srep31724.

[20] M. Griffin and A. Bayat, "Electrical stimulation in bone healing: Critical analysis by evaluating levels of evidence.," *Eplasty*, vol. 11, pp. 303–353, 2011.

[21] M. Fiebig, T. Lottermoser, D. Meier, and M. Trassin, "The evolution of multiferroics," *Nat. Rev. Mater.*, vol. 1, pp. 1–14, 2016, doi: 10.1038/natrevmats.2016.46.

[22] F.-C. Kao, P.-Y. Chiu, T.-T. Tsai, and Z.-H. Lin, "The application of nanogenerators and piezoelectricity in osteogenesis," *Sci. Technol. Adv. Mater.*, vol. 20, pp. 1103–1117, 2019, doi: 10.1080/14686996.2019.1693880.

[23] P. M. Vilarinho, N. Barroca, S. Zlotnik, P. Félix, and M. H. Fernandes, "Are lithium niobate ($LiNbO_3$) and lithium tantalate ($LiTaO_3$) ferroelectrics bioactive?," *Mater. Sci. Eng. C*, vol. 39, pp. 395–402, 2014, doi: 10.1016/J.MSEC.2014.03.026.

[24] P. Vaněk *et al.*, "Electrical activity of ferroelectric biomaterials and its effects on the adhesion, growth and enzymatic activity of human osteoblast-like cells," *J. Phys. D. Appl. Phys.*, vol. 49, p. 175403, 2016, doi: 10.1088/0022-3727/49/17/175403.

[25] S. A. M. Tofail and J. Bauer, "Electrically polarized biomaterials," *Adv. Mater.*, vol. 28, pp. 5470–5484, 2016, doi: 10.1002/adma.201505403.

[26] T. Zheng, J. Wu, D. Xiao, and J. Zhu, “Recent development in lead-free perovskite piezoelectric bulk materials,” *Progress in Materials Science*. pp. 552–624, 2018, doi: 10.1016/j.pmatsci.2018.06.002.

[27] W. Liu and X. Ren, “Large piezoelectric effect in Pb-free ceramics,” *Phys. Rev. Lett.*, vol. 103, pp. 1–4, 2009, doi: 10.1103/PhysRevLett.103.257602.

[28] J. P. Ball, B. A. Mound, J. C. Nino, and J. B. Allen, “Biocompatible evaluation of barium titanate foamed ceramic structures for orthopedic applications,” *J. Biomed. Mater. Res. Part A*, vol. 102, pp. 2089–2095, 2014, doi: 10.1002/jbm.a.34879.

[29] Y. Mao *et al.*, “Formation and properties of bioactive barium titanate coatings produced by plasma electrolytic oxidation,” *Ceram. Int.*, vol. 44, pp. 12978–12986, Aug. 2018, doi: 10.1016/J.CERAMINT.2018.04.115.

[30] Y. Tang, C. Wu, Z. Wu, L. Hu, W. Zhang, and K. Zhao, “Fabrication and *in vitro* biological properties of piezoelectric bioceramics for bone regeneration,” *Sci. Rep.*, vol. 7, pp. 1–12, 2017, doi: 10.1038/srep43360.

[31] B. S. Bhoelan, C. H. Stevering, A. T. J. van der Boog, and M. A. G. van der Heyden, “Barium toxicity and the role of the potassium inward rectifier current,” *Clin. Toxicol.*, vol. 52, pp. 584–593, 2014, doi: 10.3109/15563650.2014.923903.

[32] N. Pisitpipathsin *et al.*, “Effect of BCZT on electrical properties and bioactivity of 45S5 bioglass,” *Integr. Ferroelectr.*, vol. 142, pp. 144–153, 2013, doi: 10.1080/10584587.2013.780574.

[33] N. D. Scarisoreanu *et al.*, “Lead-free piezoelectric (Ba,Ca)(Zr,Ti)O_3 thin films for biocompatible and flexible devices,” *ACS Appl. Mater. Interfaces*, vol. 9, pp. 266–278, 2017, doi: 10.1021/acsami.6b14774.

[34] C. S. Manohar *et al.*, “Novel lead-free biocompatible piezoelectric hydroxyapatite (HA)-BCZT ($Ba_{0.85}Ca_{0.15}Zr_{0.1}Ti_{0.9}O_3$) nanocrystal composites for bone regeneration,” *Nanotechnol. Rev.*, vol. 8, pp. 61–78, 2019, doi: 10.1515/ntrev-2019-0006.

[35] K. K. Poon, M. C. Wurm, D. M. Evans, M. A. Einarsrud, R. Lutz, and J. Glaum, “Biocompatibility of (Ba,Ca)(Zr,Ti)O_3 piezoelectric ceramics for bone replacement materials,” *J. Biomed. Mater. Res. - Part B Appl. Biomater.*, vol. 108, pp. 1295–1303, 2020, doi: 10.1002/jbm.b.34477.

[36] W. D. Callister and D. G. Rethwisch, *Materials Science and Engineering*, 8th ed. John Wiley & Sons, 2011.

[37] C. Kittel, *Introduction to Solid State Physics*, 8th ed. John Wiley & Sons, Inc., 2005.

[38] D. W. Richerson, *Modern Ceramic Engineering: Properties, Processing, and Use in Design*, 3rd ed. Boca Raton, FL: CRC Press Taylor & Francis Group, 2006.

[39] A. J. Moulson and J. M. Herbert, *Electroceramics*, 2nd ed. Chichester: John Wiley & Sons Inc., 2003.

[40] D. Damjanovic, “Ferroelectric, dielectric and piezoelectric properties of

ferroelectric thin films and ceramics," *Reports Prog. Phys.*, vol. 61, pp. 1267–1324, 1998.

[41] P. Potnis, N.-T. Tsou, and J. Huber, "A review of domain modelling and domain imaging techniques in ferroelectric crystals," *Materials (Basel).*, vol. 4, pp. 417–447, 2011, doi: 10.3390/ma4020417.

[42] C. N. R. Rao and J. Gopalakrishnan, *New Directions in Solid State Chemistry*, 2nd ed. Cambridge: Cambridge University Press, 1997.

[43] G. H. Kwei, A. C. Lawson, S. J. L. Billinge, and S. W. Cheong, "Structures of the ferroelectric phases of barium titanate," *J. Phys. Chem.*, vol. 97, pp. 2368–2377, 1993, doi: 10.1021/j100112a043.

[44] Y. C. Shu and K. Bhattacharya, "Domain patterns and macroscopic behaviour of ferroelectric materials," *Philos. Mag. B*, vol. 81, pp. 2021–2054, 2001, doi: 10.1080/13642810108208556.

[45] C. A. Randall, N. Kim, J.-P. Kucera, W. Cao, and T. R. Shrout, "Intrinsic and extrinsic size effects in fine-grained morphotropic-phase-boundary lead zirconate titanate ceramics," *J. Am. Ceram. Soc.*, vol. 81, pp. 677–688, 1998, doi: 10.1111/j.1151-2916.1998.tb02389.x.

[46] W. Heywang, K. Lubitz, and W. Wersing, Eds., *Piezoelectricity: Evolution and Future of a Technology*. Springer-Verlag Berlin Heidelberg, 2008.

[47] G. Arlt, "The influence of microstructure on the properties of ferroelectric ceramics," *Ferroelectrics*, vol. 104, pp. 217–227, 1990, doi: 10.1080/00150199008223825.

[48] L. Jin, F. Li, and S. Zhang, "Decoding the fingerprint of ferroelectric loops: Comprehension of the material properties and structures," *J. Am. Ceram. Soc.*, vol. 97, pp. 1–27, 2014, doi: 10.1111/jace.12773.

[49] M. Morozov, "Softening and hardening transitions in ferroelectric $Pb(Zr,Ti)O_3$ ceramics," PhD Thesis: École Polytechnique Fédérale de Lausanne.

[50] N. Bar-Chaim, M. Brunstein, J. Grünberg, and A. Seidman, "Electric field dependence of the dielectric constant of PZT ferroelectric ceramics," *J. Appl. Phys.*, vol. 45, pp. 2398–2405, 1974.

[51] M. C. Ehmke, J. Glaum, M. Hoffman, J. E. Blendell, and K. J. Bowman, "*In situ* X-ray diffraction of biased ferroelastic switching in tetragonal lead-free (1-x)$Ba(Zr_{0.2}Ti_{0.8})O_3$-x$(Ba_{0.}Ca_{0.3})TiO_3$ piezoelectrics," *J. Am. Ceram. Soc.*, vol. 96, pp. 2913–2920, 2013, doi: 10.1111/jace.12424.

[52] M. C. Ehmke, J. Glaum, M. Hoffman, J. E. Blendell, and K. J. Bowman, "The effect of electric poling on the performance of lead-free (1-x)$Ba(Zr_{0.2}Ti_{0.8})O_3$–x$(Ba_{0.7}Ca_{0.3})TiO_3$ piezoceramics," *J. Am. Ceram. Soc.*, vol. 96, pp. 3805–3811, 2013, doi: 10.1111/jace.12586.

[53] Y. Tan *et al.*, "Unfolding grain size effects in barium titanate ferroelectric ceramics," *Sci. Rep.*, vol. 5, pp. 1–9, 2015, doi: 10.1038/srep09953.

[54] H. Ghayour and M. Abdellahi, “A brief review of the effect of grain size variation on the electrical properties of $BaTiO_3$-based ceramics,” *Powder Technol.*, vol. 292, pp. 84–93, 2016, doi: 10.1016/J.POWTEC.2016.01.030.

[55] J. Hao, W. Bai, W. Li, and J. Zhai, “Correlation between the microstructure and electrical properties in high-performance $(Ba_{0.85}Ca_{0.15})(Zr_{0.1}Ti_{0.9})O_3$ lead-free piezoelectric ceramics,” *J. Am. Ceram. Soc.*, vol. 95, pp. 1998–2006, 2012, doi: 10.1111/j.1551-2916.2012.05146.x.

[56] G. Arlt, D. Hennings, and G. de With, “Dielectric properties of fine-grained barium titanate ceramics,” *J. Appl. Phys.*, vol. 58, pp. 1619–1625, 1985, doi: 10.1063/1.336051.

[57] D. Ghosh *et al.*, “Domain wall displacement is the origin of superior permittivity and piezoelectricity in $BaTiO_3$ at intermediate grain sizes,” *Adv. Funct. Mater.*, vol. 24, pp. 885–896, 2014, doi: 10.1002/adfm.201301913.

[58] Y. Huan, X. Wang, J. Fang, and L. Li, “Grain size effects on piezoelectric properties and domain structure of $BaTiO_3$ ceramics prepared by two-step sintering,” *J. Am. Ceram. Soc.*, vol. 96, pp. 3369–3371, 2013, doi: 10.1111/jace.12601.

[59] P. Zheng, J. L. Zhang, Y. Q. Tan, and C. L. Wang, “Grain-size effects on dielectric and piezoelectric properties of poled $BaTiO_3$ ceramics,” *Acta Mater.*, vol. 60, pp. 5022–5030, 2012, doi: 10.1016/j.actamat.2012.06.015.

[60] F. Q. Guo *et al.*, “Grain size effects on piezoelectric properties of $BaTiO_3$ ceramics prepared by spark plasma sintering,” *J. Mater. Sci. Mater. Electron.*, vol. 27, pp. 5967–5971, 2016, doi: 10.1007/s10854-016-4518-1.

[61] J. Rödel, W. Jo, K. T. P. Seifert, E. M. Anton, T. Granzow, and D. Damjanovic, “Perspective on the development of lead-free piezoceramics,” *J. Am. Ceram. Soc.*, vol. 92, pp. 1153–1177, 2009, doi: 10.1111/j.1551-2916.2009.03061.x.

[62] K. G. Webber, M. Vögler, N. H. Khansur, B. Kaeswurm, J. E. Daniels, and F. H. Schader, “Review of the mechanical and fracture behavior of perovskite lead-free ferroelectrics for actuator applications,” *Smart Mater. Struct.*, vol. 26, p. 63001, 2017, doi: 10.1088/1361-665X/aa590c.

[63] Y. Saito *et al.*, “Lead-free piezoceramics,” *Lett. to Nat.*, vol. 432, pp. 84–87, 2004, doi: 10.1038/nature03008.1.

[64] B. Jaffe, W. R. Cook, and H. Jaffe, *Piezoelectric Ceramics*. London: Academic Press, 1971.

[65] C. Galassi, E. Roncari, C. Capiani, and A. Costa, “Influence of processing parameters on the properties of PZT materials,” in *Piezoelectric Materials: Advances in Science, Technology and Applications*, C. Galassi, M. Dinescu, K. Uchino, and M. Sayer, Eds. Dordrecht: Springer Science & Business Media, 2000, pp. 75–86.

[66] R. Whatmore, “Ferroelectric Materials,” in *Springer Handbook of Electronic and Photonic Materials*, S. Kasap and P. Capper, Eds. Springer, 2017.

[67] H. Jaffe, “Piezoelectric Ceramics,” in *Sixtieth Annual Meeting, The American Ceramic Society*, 1958, pp. 494–498.

[68] T. R. Shrout and S. J. Zhang, “Lead-free piezoelectric ceramics: Alternatives for PZT?,” *J. Electroceramics*, vol. 19, pp. 111–124, 2007, doi: 10.1007/s10832-007-9047-0.

[69] M. McQuarrie and F. W. Behnke, “Structural and dielectric studies in the system (Ba,Ca)(Ti,Zr)O_3,” *J. Am. Ceram. Soc.*, vol. 37, pp. 539–543, 1954, doi: 10.1111/j.1151-2916.1954.tb13986.x.

[70] Y. Tian, L. Wei, X. Chao, Z. Liu, and Z. Yang, “Phase transition behavior and large piezoelectricity near the morphotropic phase boundary of lead-free $(Ba_{0.85}Ca_{0.15})(Zr_{0.1}Ti_{0.9})O_3$ ceramics,” *J. Am. Ceram. Soc.*, vol. 96, pp. 496–502, 2013, doi: 10.1111/jace.12049.

[71] D. S. Keeble, F. Benabdallah, P. A. Thomas, M. Maglione, and J. Kreisel, “Revised structural phase diagram of $(Ba_{0.7}Ca_{0.3}TiO_3)$-$(BaZr_{0.2}Ti_{0.8}O_3)$,” *Appl. Phys. Lett*, vol. 102, p. 92903, 2013, doi: 10.1063/1.4793400.

[72] A. Bjørnetun Haugen, J. S. Forrester, D. Damjanovic, B. Li, K. J. Bowman, and J. L. Jones, “Structure and phase transitions in $0.5(Ba_{0.7}Ca_{0.3}TiO_3)$-$0.5(BaZr_{0.2}Ti_{0.8}O_3)$ from −100 °C to 150 °C,” *J. Appl. Phys.*, vol. 113, p. 014103, 2013, doi: 10.1063/1.4772741.

[73] J. Gao, D. Xue, W. Liu, C. Zhou, and X. Ren, “Recent progress on $BaTiO_3$-based piezoelectric ceramics for actuator applications,” *Actuators*, vol. 6, p. 24, 2017, doi: 10.3390/act6030024.

[74] D. J. Hadjidakis and I. I. Androulakis, “Bone Remodeling,” *Ann. N. Y. Acad. Sci.*, vol. 1092, pp. 385–396, 2006, doi: 10.1196/annals.1365.035.

[75] U. G. K. Wegst, H. Bai, E. Saiz, A. P. Tomsia, and R. O. Ritchie, “Bioinspired structural materials,” *Nat. Mater.*, vol. 14, pp. 23–36, 2015, doi: 10.1038/nmat4089.

[76] C. R. Jacobs, S. Temiyasathit, and A. B. Castillo, “Osteocyte mechanobiology and pericellular mechanics,” *Annu. Rev. Biomed. Eng.*, vol. 12, pp. 369–400, 2010, doi: 10.1146/annurev-bioeng-070909-105302.

[77] J. C. Crockett, M. J. Rogers, F. P. Coxon, L. J. Hocking, and M. H. Helfrich, “Bone remodelling at a glance,” *J. Cell Sci.*, vol. 124, 2011.

[78] H. M. Frost, “Wolff’s Law and bone’s structural adaptations to mechanical usage: An overview for clinicians,” *Angle Orthodontist*, vol. 64. pp. 175–188, 1994, doi: 10.1043/0003-3219(1994)064<0175:WLABSA>2.0.CO;2.

[79] R. Marsell and T. A. Einhorn, “The biology of fracture healing,” *Injury*, vol. 42, pp. 551–555, 2011.

[80] F. Loi, L. A. Córdova, J. Pajarinen, T. Lin, Z. Yao, and S. B. Goodman, “Inflammation, fracture and bone repair,” *Bone*, vol. 86, pp. 119–130, 2016, doi: 10.1016/j.bone.2016.02.020.

[81] A. H. Rajabi, M. Jaffe, and T. L. Arinzeh, “Piezoelectric materials for tissue regeneration: A review,” *Acta Biomater.*, vol. 24, pp. 12–23, 2015, doi: 10.1016/j.actbio.2015.07.010.

[82] *FDA ISO10993: Biological Evaluation of Medical Devices*. USA.

[83] M. M. Stevens, “Biomaterials for bone tissue engineering,” *Mater. Today*, vol. 11, pp. 18–25, 2008, doi: 10.1016/S1369-7021(08)70086-5.

[84] L. L. Hench, “Biomaterials,” *Science*, vol. 208, pp. 826–831, 1980, doi: 10.1126/science.6246576.

[85] Y. Abu-Amer, I. Darwech, and J. C. Clohisy, “Aseptic loosening of total joint replacements: Mechanisms underlying osteolysis and potential therapies,” *Arthritis Res. Ther.*, vol. 9, pp. 1–7, 2007, doi: 10.1186/ar2170.

[86] B. L. Cheng, M. Gabbay, W. Duffy, and G. Fantozzi, “Mechanical loss and Young’s modulus associated with phase transitions in barium titanate based ceramics,” *J. Mater. Sci.*, vol. 31, pp. 4951–4955, 1996, doi: 10.1007/BF00355886.

[87] R. C. Bradt, D. Munz, M. Sakai, and K. W. White, *Fracture Mechanics of Ceramics - Active Materials, Nanoscale Materials, Composites, Glass and Fundamentals*. Springer Science and Business Media, Inc., 2005.

[88] A. Srinivas, R. V. Krishnaiah, V. L. Niranjani, S. V. Kamat, T. Karthik, and S. Asthana, “Ferroelectric, piezoelectric and mechanical properties in lead free $(0.5)Ba(Zr_{0.2}Ti_{0.8})O_3–(0.5)(Ba_{0.7}Ca_{0.3})TiO_3$ electroceramics,” *Ceram. Int.*, vol. 41, pp. 1980–1985, 2015, doi: 10.1016/j.ceramint.2014.08.127.

[89] M. Vögler, M. Acosta, D. R. J. Brandt, L. Molina-Luna, and K. G. Webber, “Temperature-dependent R-curve behavior of the lead-free ferroelectric $0.615Ba(Zr_{0.2}Ti_{0.8})O_3$-$0.385(Ba_{0.7}Ca_{0.3})TiO_3$ ceramic,” *Eng. Fract. Mech.*, vol. 144, pp. 68–77, 2015, doi: 10.1016/j.engfracmech.2015.06.069.

[90] P. Sailaja *et al.*, “Investigation of ferroelectric, piezoelectric and mechanically coupled properties of lead-free $(Ba_{0.85}Ca_{0.15})(Zr_{0.1}Ti_{0.9})O_3$ ceramics,” *Adv. Appl. Ceram.*, vol. 118, pp. 300–307, 2019, doi: 10.1080/17436753.2019.1573565.

[91] M. Navarro, A. Michiardi, O. Castaño, and J. A. Planell, “Biomaterials in orthopaedics,” *J. R. Soc. Interface*, vol. 5, pp. 1137–58, 2008, doi: 10.1098/rsif.2008.0151.

[92] J. Yan, K. B. Clifton, J. J. Mecholsky, and R. L. Reep, “Fracture toughness of manatee rib and bovine femur using a chevron-notched beam test,” *J. Biomech.*, vol. 39, pp. 1066–1074, 2006, doi: 10.1016/j.jbiomech.2005.02.016.

[93] H. Maeda, K. Tsuda, and E. Fukada, “The dependence on temperature and hydration of piezoelectric, dielectric and elastic constants of bone,” *Jpn. J. Appl. Phys.*, vol. 15, pp. 2333–2336, 1976.

[94] AZoM, “Stainless Steel - Grade 316 (UNS S31600),” *AZoM - Atlas Steels Australia*, 2001. [Online]. Available: https://www.azom.com/article.aspx?ArticleID=863.

[95] AZoM, “Titanium Alloys - Ti6Al4V Grade 5,” *AZoM - Titanium Information Group*, 2002. [Online]. Available: http://www.azom.com/properties.aspx?ArticleID=1547.

[96] G. Dergin, M. Akta, B. Gürsoy, Y. Devecioglu, M. Kürkçü, and E. Benlidayi, “Direct current electric stimulation in implant osseointegration: An experimental animal study with sheep,” *J. Oral Implantol.*, vol. 39, pp. 671–679, 2013, doi: 10.1563/AAID-JOI-D-10-00172.

[97] B. M. Isaacson, L. B. Brunker, A. A. Brown, J. P. Beck, G. L. Burns, and R. D. Bloebaum, “An evaluation of electrical stimulation for improving periprosthetic attachment,” *J. Biomed. Mater. Res. - Part B Appl. Biomater.*, vol. 97 B, pp. 190–200, 2011, doi: 10.1002/jbm.b.31803.

[98] N. N. Salman and J. B. Park, “The effect of direct electrical current stimulation on the bone/porous metallic implant interface,” *Biomaterials*, vol. 1, pp. 209–213, 1980, doi: 10.1016/0142-9612(80)90019-8.

[99] J. B. Park, G. H. Kenner, S. D. Brown, and J. K. Scott, “Mechanical property changes of barium titanate (ceramic) after *in vivo* and *in vitro* aging,” *Biomater. Med. Devices. Artif. Organs*, vol. 5, pp. 267–276, 1977.

[100] J. B. Park, A. F. von Recum, G. H. Kenner, B. J. Kelly, W. W. Coffeen, and M. F. Grether, “Piezoelectric ceramic implants: A feasibility study,” *J. Biomed. Mater. Res.*, vol. 14, pp. 269–77, 1980, doi: 10.1002/jbm.820140308.

[101] ATSDR, “Toxicological Profile for Barium and Barium Compounds,” 2014.

[102] G. Geneste and B. Dkhil, “Adsorption and dissociation of H_2O on in-plane-polarized $BaTiO_3$ (001) surfaces and their relation to ferroelectricity,” *Phys. Rev. B - Condens. Matter Mater. Phys.*, vol. 79, pp. 1–11, 2009, doi: 10.1103/PhysRevB.79.235420.

[103] H. Lee *et al.*, “Imprint control of $BaTiO_3$ thin films via chemically induced surface polarization pinning,” *Nano Lett.*, vol. 16, pp. 2400–2406, 2016, doi: 10.1021/acs.nanolett.5b05188.

[104] C. S. Lynch, “The effect of uniaxial stress on the electro-mechanical response of 8/65/35 PLZT,” *Acta Mater.*, vol. 44, pp. 4137–4148, 1996, doi: 10.1016/S1359-6454(96)00062-6.

[105] M. C. Ehmke, J. Daniels, J. Glaum, M. Hoffman, J. E. Blendell, and K. J. Bowman, “Reduction of the piezoelectric performance in lead-free $(1-x)Ba(Zr_{0.2}Ti_{0.8})O_3$-$x(Ba_{0.7}Ca_{0.3})TiO_3$ piezoceramics under uniaxial compressive stress,” *J. Appl. Phys.*, vol. 112, pp. 0–5, 2012, doi: 10.1063/1.4768273.

[106] M. Wei, A. J. Ruys, B. K. Milthorpe, C. C. Sorrell, and J. H. Evans, “Electrophoretic deposition of hydroxyapatite coatings on metal substrates: A nanoparticulate dual-coating approach,” *J. Sol-Gel Sci. Technol.*, vol. 21, pp. 39–48, 2001, doi: 10.1023/A:1011201414651.

[107] J. A. Bland, “The thermal expansion of cubic barium titanate ($BaTiO_3$) from 350 °C to 1050 °C,” *Can. J. Phys.*, vol. 37, pp. 417–421, 1959.

[108] S. Schafföner, C. G. Aneziris, H. Berek, B. Rotmann, and B. Friedrich, "Investigating the corrosion resistance of calcium zirconate in contact with titanium alloy melts," *J. Eur. Ceram. Soc.*, vol. 35, pp. 259–266, 2015, doi: 10.1016/j.jeurceramsoc.2014.08.031.

[109] Y. Jiang, R. Guo, and A. S. Bhalla, "Growth and properties of $CaTiO_3$ single crystal fibers," *J. Electroceramics*, vol. 2, pp. 199–203, 1998, doi: 10.1023/A:1009978901009.

[110] M. C. Wurm *et al.*, "*In vitro* evaluation of polylactic acid (PLA) manufactured by fused deposition modeling," *J. Biol. Eng.*, vol. 11, p. 29, 2017, doi: 10.1186/s13036-017-0073-4.

[111] J. H. McDonald, *Handbook of Biological Statistics*. Baltimore, Maryland: Sparky House Publishing, 2014.

[112] D. C. Montgomery, G. C. Runger, and N. F. Hubele, *Engineering Statistics*, Fifth. John Wiley & Son (Asia) Pte. Ltd., 2012.

[113] E. Khomyakova, S. Wenner, K. Bakken, T. Grande, J. Glaum, and M.-A. Einarsrud, "On the formation mechanism of BCZT thin films by aqueous chemical solution deposition," Manuscript Submitted for Publication: Norwegian University of Science and Technology.

[114] R. D. Shannon, "Revised effective ionic radii and systematic studies of interatomic distances in halides and chalcogenides," *Acta Crystallogr.*, vol. 32, p. 751, 1976.

[115] H. Kaddoussi *et al.*, "Sequence of structural transitions and electrocaloric properties in $(Ba_{1-x}Ca_x)(Zr_{0.1}Ti_{0.9})O_3$ ceramics," *J. Alloys Compd.*, vol. 713, pp. 164–179, 2017, doi: 10.1016/j.jallcom.2017.04.148.

[116] T. A. Ring, *Fundamentals of Ceramic Powder Processing and Synthesis*. San Diego: Academic Press, 1996.

[117] M. C. Ehmke, S. N. Ehrlich, J. E. Blendell, and K. J. Bowman, "Phase coexistence and ferroelastic texture in high strain $(1-x)Ba(Zr_{0.2}Ti_{0.8})O_3$-$x(Ba_{0.7}Ca_{0.3})TiO_3$ piezoceramics," *J. Appl. Phys*, vol. 111, p. 124110, 2012, doi: 10.1063/1.4730342.

[118] D. Damjanovic, A. Biancoli, L. Batooli, A. Vahabzadeh, and J. Trodahl, "Elastic, dielectric, and piezoelectric anomalies and Raman spectroscopy of $0.5Ba(Ti_{0.8}Zr_{0.2})O_3$-$0.5(Ba_{0.7}Ca_{0.3})TiO_3$," *Appl. Phys. Lett*, vol. 100, p. 192907, 2012, doi: 10.1063/1.4714703.

[119] Y. Zhang *et al.*, "Correlation between piezoelectric properties and phase coexistence in $(Ba,Ca)(Ti,Zr)O_3$ ceramics," *J. Am. Ceram. Soc.*, vol. 97, pp. 2885–2891, 2014, doi: 10.1111/jace.13047.

[120] G. Singh, V. S. Tiwari, and P. K. Gupta, "Evaluating the polymorphic phase transition in calcium-doped $Ba(Zr_{0.05}Ti_{0.95})O_3$: A lead-free piezoelectric ceramic," *J. Appl. Crystallogr.*, vol. 46, pp. 324–331, 2013, doi: 10.1107/S0021889813000666.

[121] L. Qin *et al.*, "Temperature-driven phase transitions and enhanced piezoelectric responses in $Ba(Ti_{0.92}Sn_{0.08})O_3$ lead-free ceramic," *Ceram. Int.*, vol. 45, pp. 4461–

4466, 2019, doi: 10.1016/j.ceramint.2018.11.125.

[122] D. Damjanovic, "A morphotropic phase boundary system based on polarization rotation and polarization extension," *Appl. Phys. Lett.*, vol. 97, p. 062906, 2010, doi: 10.1063/1.3479479.

[123] S. M. Selbach *et al.*, "PbO-deficient $PbTiO_3$: Mass transport, structural effects and possibility for intrinsic screening of the ferroelectric polarization," *Appl. Phys. Lett.*, vol. 98, pp. 0–3, 2011, doi: 10.1063/1.3555336.

[124] S. Lavenus, P. Pilet, J. Guicheux, P. Weiss, G. Louarn, and P. Layrolle, "Behaviour of mesenchymal stem cells, fibroblasts and osteoblasts on smooth surfaces," *Acta Biomater.*, vol. 7, pp. 1525–1534, 2011, doi: 10.1016/j.actbio.2010.12.033.

[125] O. Andrukhov *et al.*, "Proliferation, behavior, and differentiation of osteoblasts on surfaces of different microroughness," *Dent. Mater.*, vol. 32, pp. 1374–1384, 2016, doi: 10.1016/J.DENTAL.2016.08.217.

[126] R. A. Gittens *et al.*, "The roles of titanium surface micro/nanotopography and wettability on the differential response of human osteoblast lineage cells," *Acta Biomater.*, vol. 9, pp. 6268–6277, 2013, doi: 10.1016/j.actbio.2012.12.002.

[127] S. Samavedi, A. R. Whittington, and A. S. Goldstein, "Calcium phosphate ceramics in bone tissue engineering: A review of properties and their influence on cell behavior," *Acta Biomater.*, vol. 9, pp. 8037–8045, 2013, doi: 10.1016/J.ACTBIO.2013.06.014.

[128] D. M. Mattox, "Substrate ('real') surfaces and surface modification," in *Handbook of Physical Vapor Deposition (PVD) Processing*, 2nd ed., Elsevier Inc., 2010, p. 55.

[129] D. Y. He, L. J. Qiao, A. A. Volinsky, Y. Bai, M. Wu, and W. Y. Chu, "Humidity effects on (001) $BaTiO_3$ single crystal surface water adsorption," *Appl. Phys. Lett.*, vol. 98, pp. 98–101, 2011, doi: 10.1063/1.3544586.

[130] A. Kaushal, S. M. Olhero, and J. M. F. Ferreira, "Lead-free $0.5Ba(Zr_{0.2}Ti_{0.8})O_3$-$0.5(Ba_{0.7}Ca_{0.3})TiO_3$ powder surface treated against hydrolysis - A key for a successful aqueous processing," *J. Mater. Chem. C*, vol. 1, pp. 4846–4853, 2013, doi: 10.1039/c3tc30741g.

[131] O. Ozmen, C. Ozsoy-Keskinbora, and E. Suvaci, "Chemical stability of $KNbO_3$, $NaNbO_3$, and $K_{0.5}Na_{0.5}NbO_3$ in aqueous medium," *J. Am. Ceram. Soc.*, vol. 101, pp. 1074–1086, 2018, doi: 10.1111/jace.15291.

[132] Y.-R. Luo, "Bond Dissociation Energies," in *CRC Handbook of Chemistry and Physics*, 89th ed., D. R. Lide, Ed. Boca Raton: CRC Press Taylor & Francis Group, 2009, pp. 65–98.

[133] D. Yoon, B. I. Lee, P. Badheka, and X. Wang, "Barium ion leaching from barium titanate powder in water," vol. 4, pp. 165–169, 2003.

[134] R. C. Weast, Ed., *CRC Handbook of Chemistry and Physics*, 60th ed. CRC Press, 1980.

[135] H. W. Nesbitt, G. M. Bancroft, W. S. Fyfe, S. N. Karkhanis, and A. Nishijima, "Thermodynamic stability and kinetics of perovskite dissolution," *Nature*, vol. 289, pp. 358–362, 1981.

[136] R. A. Kimel and J. H. Adair, "Aqueous degradation and chemical passivation of yttria-tetragonally-stabilized zirconia at 25 °C," *J. Am. Ceram. Soc.*, vol. 85, pp. 1403–1408, 2002, doi: 10.1111/j.1151-2916.2002.tb00288.x.

[137] A. Yamamoto, R. Honma, and M. Sumita, "Cytotoxicity evaluation of 43 metal salts using murine fibroblasts and osteoblastic cells," *J. Biomed. Mater. Res.*, vol. 39, pp. 331–340, 1998.

[138] E. Salahinejad *et al.*, "Surface modification of stainless steel orthopedic implants by sol-gel $ZrTiO_4$ and $ZrTiO_4$-PMMA coatings," *J. Biomed. Nanotechnol.*, vol. 9, pp. 1327–1335, 2013, doi: https://doi.org/10.1166/jbn.2013.1619.

[139] J. Shin *et al.*, "Atomistic screening mechanism of ferroelectric surfaces: An *in situ* study of the polar phase in ultrathin $BaTiO_3$ films exposed to H_2O," *Nano Lett.*, vol. 9, pp. 3720–3725, 2009, doi: 10.1021/nl901824x.

[140] D. D. D'Lima, N. Steklov, B. J. Fregly, S. A. Banks, and C. W. Colwell, "*In vivo* contact stresses during activities of daily living after knee arthroplasty," *J. Orthop. Res.*, vol. 26, pp. 1549–1555, 2008, doi: 10.1002/jor.20670.

[141] D. R. J. Brandt, M. Acosta, J. Koruza, and K. G. Webber, "Mechanical constitutive behavior and exceptional blocking force of lead-free BZT-xBCT piezoceramics," *J. Appl. Phys.*, vol. 115, p. 204107, 2014.

[142] M. C. Ehmke, F. H. Schader, K. G. Webber, J. Rödel, J. E. Blendell, and K. J. Bowman, "Stress, temperature and electric field effects in the lead-free $(Ba,Ca)(Ti,Zr)O_3$ piezoelectric system," *Acta Mater.*, vol. 78, pp. 37–45, 2014, doi: 10.1016/j.actamat.2014.06.005.

[143] M. Algueró, B. L. Cheng, F. Guiu, M. J. Reece, M. Poole, and N. Alford, "Degradation of the d_{33} piezoelectric coefficient for PZT ceramics under static and cyclic compressive loading," *J. Eur. Ceram. Soc.*, vol. 21, pp. 1437–1440, 2001, doi: 10.1016/S0955-2219(01)00036-X.

[144] J. B. Park, B. J. Kelly, G. H. Kenner, and A. F. Von Recum, "Piezoelectric ceramic implants: *In vivo* results," *Biomed. Mater.*, vol. 15, pp. 103–110, 1981, doi: 10.1002/jbm.820150114.

[145] Y. Du, Z. Jin, and P. Huang, "Thermodynamic calculation of the zirconia-calcia system," *J. Am. Ceram. Soc.*, vol. 75, pp. 3040–3048, 1992.

[146] L. Freitag, S. Schafföner, C. Faßauer, and C. G. Aneziris, "Functional coatings for titanium casting molds using the replica technique," *J. Eur. Ceram. Soc.*, vol. 38, pp. 4560–4567, 2018, doi: 10.1016/J.JEURCERAMSOC.2018.05.020.

[147] H. Katsui and T. Goto, "Bio-ceramic coating of Ca–Ti–O system compound by laser chemical vapor deposition," *Interface Oral Heal. Sci. 2016*, pp. 47–62, 2017, doi: 10.1007/978-981-10-1560-1_4.

[148] Y. Bai *et al.*, "$(Ba,Ca)(Zr,Ti)O_3$ lead-free piezoelectric ceramics—The critical role

of processing on properties," *J. Eur. Ceram. Soc.*, vol. 35, pp. 3445–3456, 2015, doi: 10.1016/j.jeurceramsoc.2015.05.010.

[149] S. Kumar, T. S. N. Sankara Narayanan, S. Ganesh Sundara Raman, and S. K. Seshadri, "Thermal oxidation of Ti6Al4V alloy: Microstructural and electrochemical characterization," *Mater. Chem. Phys.*, vol. 119, pp. 337–346, 2010, doi: 10.1016/j.matchemphys.2009.09.007.

[150] "North American Stainless Brochure." [Online]. Available: https://www.northamericanstainless.com/flat-products/steel-grades/.

[151] A. Kosmač, *Stainless Steels at High Temperatures - Materials and Applications Series*, vol. 18. Brussels: Euro Inox, 2012.

[152] R. Waser, T. Baiatu, and K.-H. Hardtl, "dc Electrical degradation of perovskite-type titanates: II, single crystals," *J. Am. Ceram. Soc.*, vol. 73, pp. 1654–1662, 1990, doi: 10.1111/j.1151-2916.1990.tb09810.x.

[153] R. K. Bordia and R. Raj, "Sintering behavior of ceramic films constrained by a rigid substrate," *J. Am. Ceram. Soc.*, vol. 68, pp. 287–292, 1985, doi: 10.1111/j.1151-2916.1985.tb15227.x.

[154] M. Serratos and A. Bronson, "The effect of oxygen partial pressure on the stability of Magneli phases in high temperature corrosive wear," *Wear*, vol. 198, pp. 267–270, 1996, doi: 10.1016/0043-1648(96)06986-4.

[155] D. Mo *et al.*, "A review on diffusion bonding between titanium alloys and stainless steels," *Adv. Mater. Sci. Eng.*, p. 15, 2018.

[156] A.-A. El Mel, R. Nakamura, and C. Bittencourt, "The Kirkendall effect and nanoscience: Hollow nanospheres and nanotubes," *Beilstein J. Nanotechnol.*, vol. 6, pp. 1348–1361, 2015, doi: 10.3762/bjnano.6.139.

[157] "Calcium oxide, CID=14778," *National Center for Biotechnology Information. PubChem Database.* [Online]. Available: https://pubchem.ncbi.nlm.nih.gov/compound/Calcium-oxide.

[158] J. Dai, J. Zhu, C. Chen, and F. Weng, "High temperature oxidation behavior and research status of modifications on improving high temperature oxidation resistance of titanium alloys and titanium aluminides: A review," *Journal of Alloys and Compounds*, vol. 685. Elsevier Ltd., pp. 784–798, 2016, doi: 10.1016/j.jallcom.2016.06.212.

[159] D. M. Mattox, "Adhesion and Deadhesion," in *Handbook of Physical Vapor Deposition (PVD) Processing*, 2nd ed., 2010, pp. 439–474.

Appendix

Appendix 1: (a) Shrinkage and (b) sintering rate curves obtained from dilatometry measurements on $BC_{15}Z_{10}T$, $BC_{14}Z_{10}T$, $BC_{12}Z_{10}T$, and $BC_{10}Z_{10}T$.

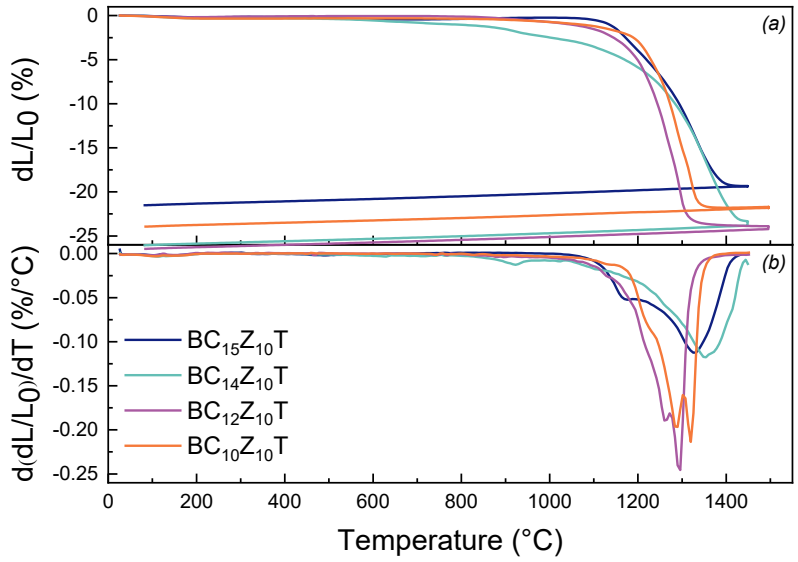

Appendix 2: Details of the $CaCO_3$ and ZrO_2 precursor powders used to synthesise $CaZrO_3$ powders, and details of the as-received $CaTiO_3$ powders utilised as interlayer materials in Chapter 7. $CaZrO_3$ powders were prepared via the solid-state synthesis route. Calcination was performed in two steps at 900 °C 1 h and 1250 °C 6 h, with heating and cooling rates of 200 °C/h. Most $CaTiO_3$ coatings were prepared from Lot #MKBX2321V (2018).

Material	**Chemical Formula**	**Usage**	**Purity (%)**	**Supplier & Identification No.**
Calcium carbonate	$CaCO_3$	Synthesis of $CaZrO_3$	98.500	Roth 6230.1
Zirconium dioxide Monoclinic 5 µm	ZrO_2	Synthesis of $CaZrO_3$	99.970	Imerys Fused Minerals
Calcium titanate < 100 nm	$CaTiO_3$	As-received	99.000	Sigma Aldrich 633801 Lot #MKBQ7945V (2017) Lot #MKBX2321V (2018)

Appendix 3: XRD patterns of $CaTiO_3$ powders: Lot #MKBX2321V (2018) as-received, Lot #MKBQ7945V (2017) as-received, and heat-treated at 900 °C for 1 h in air. The $CaTiO_3$ PDF 01-072-6807 is represented by the dashed lines.

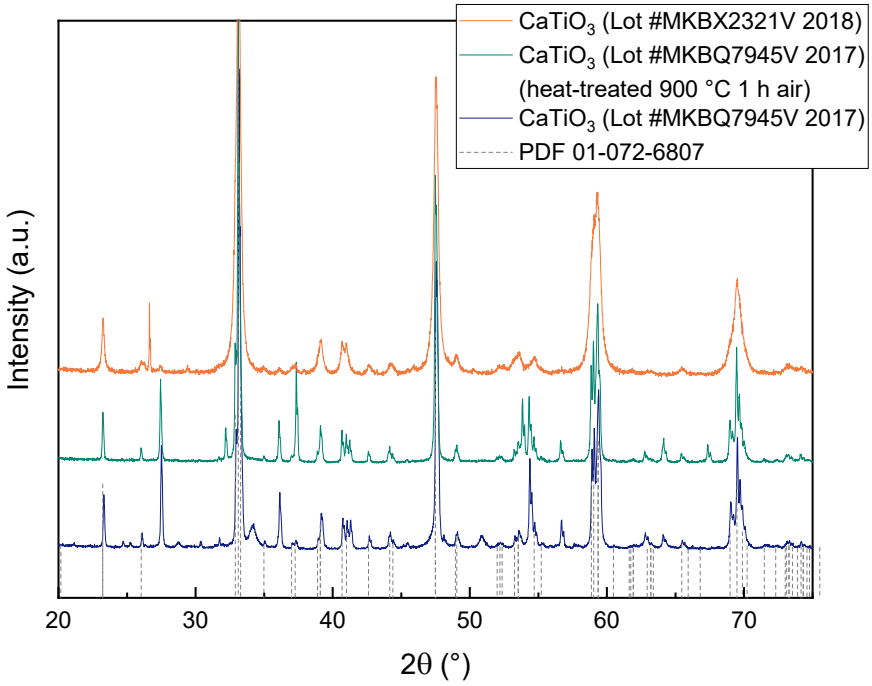

The following pages present the various processing parameters investigated in the optimisation process for the deposition of BCZT ceramics coatings on metal implant materials. The code 20*yymmdd* indicates the synthesis date of each sample. The letter *L* denotes the number of slurry deposition layers.

Appendix 4: Surface-treatment and heat-treatment of stainless steel 316L.

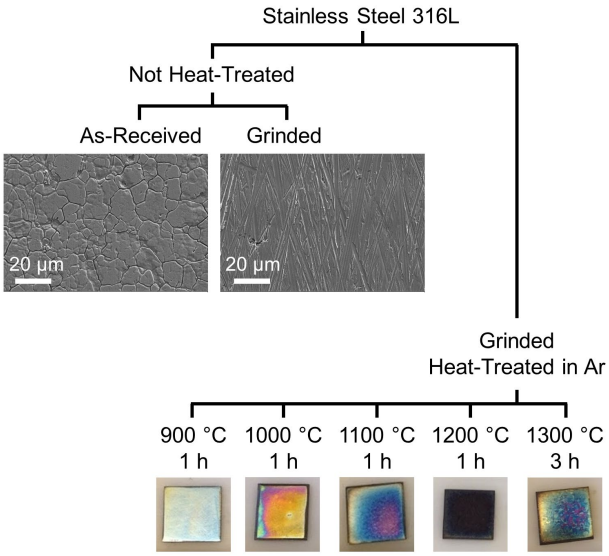

Appendix 5: Surface-treatment and heat-treatment of Ti6Al4V.

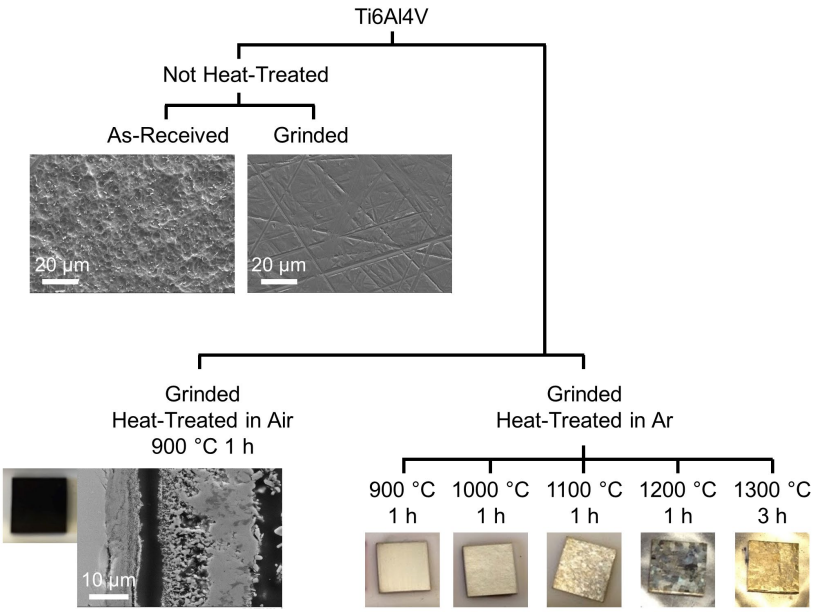

Appendix 6: Heat-treatment of BCZT-coated stainless steel 316L.

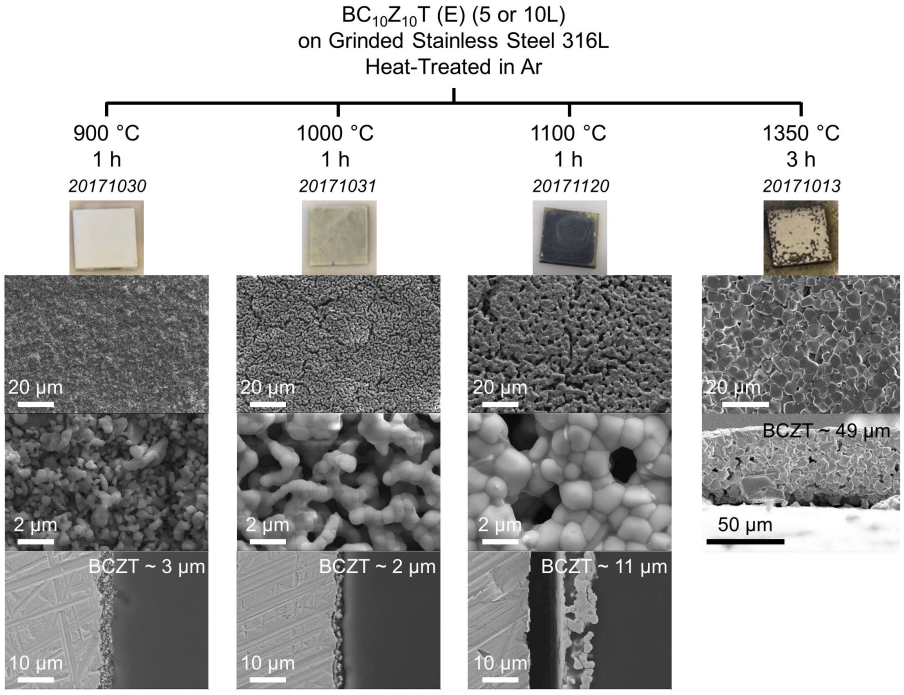

Appendix 7: Heat-treatment of BCZT-coated Ti6Al4V.

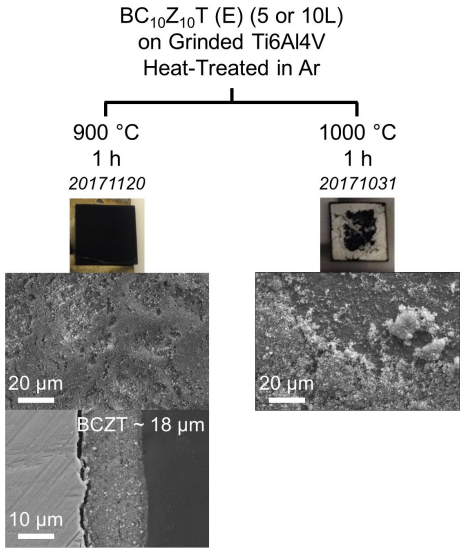

Appendix 8: Heat-treatment of $CaZrO_3$-coated Ti6Al4V.

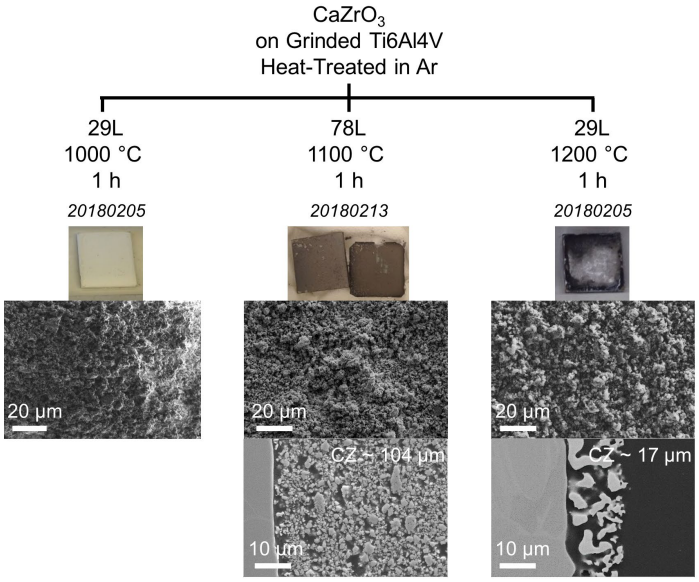

Appendix 9: Heat-treatment of $CaTiO_3$-coated pure Ti.

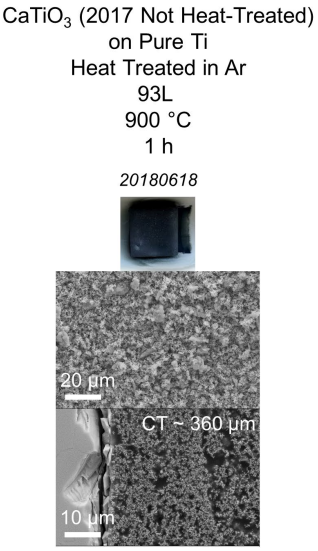

Appendix 10: Heat-treatment of $CaTiO_3$-coated Ti6Al4V.

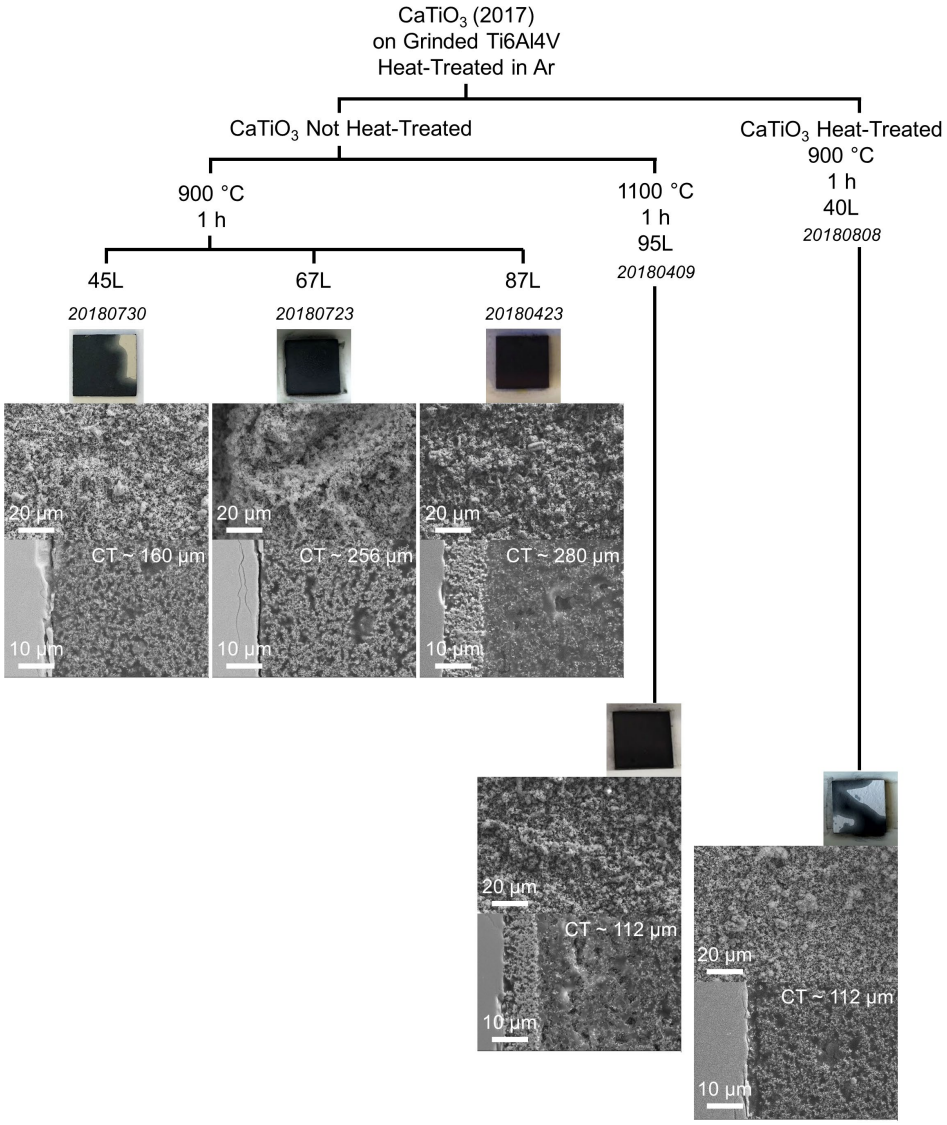

Appendix 11: Heat-treatment of $CaTiO_3$-coated Ti6Al4V.

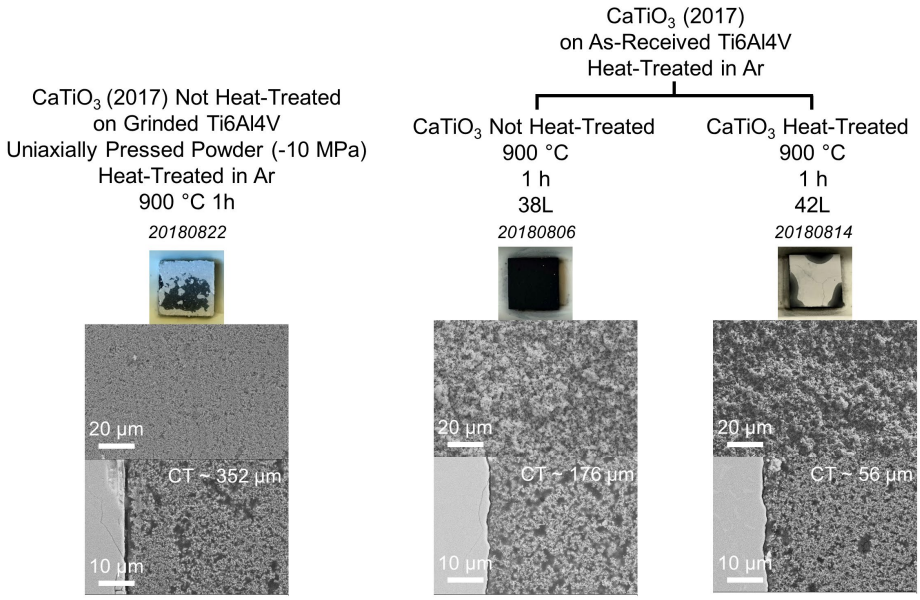

Appendix 12: Heat-treatment of $CaTiO_3$-coated Ti6Al4V.

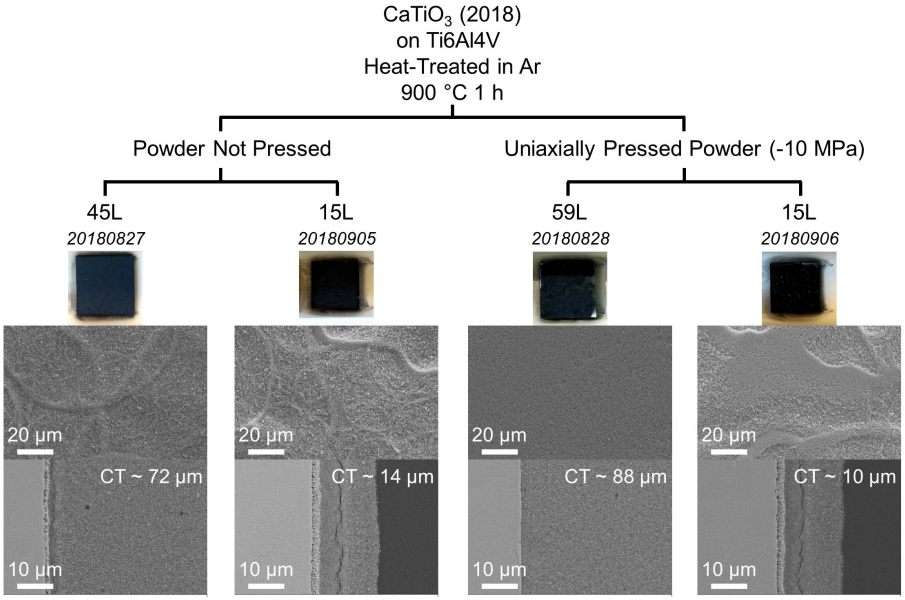

Appendix 13: Heat-treatment of $CaTiO_3$- and BCZT-coated Ti6Al4V.

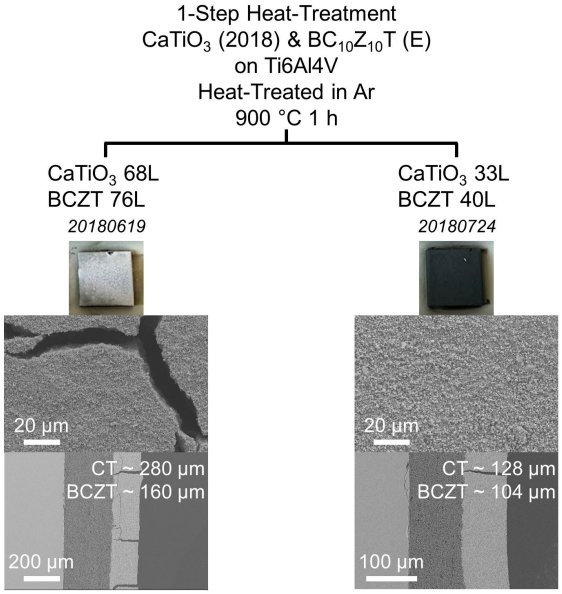

Appendix 14: Heat-treatment of $CaTiO_3$- and BCZT-coated Ti6Al4V.

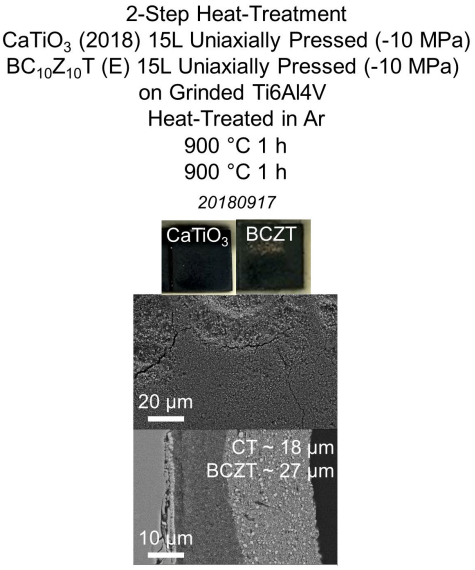

Appendix 15: Heat-treatment $CaTiO_3$- and BCZT-coated Ti6Al4V.

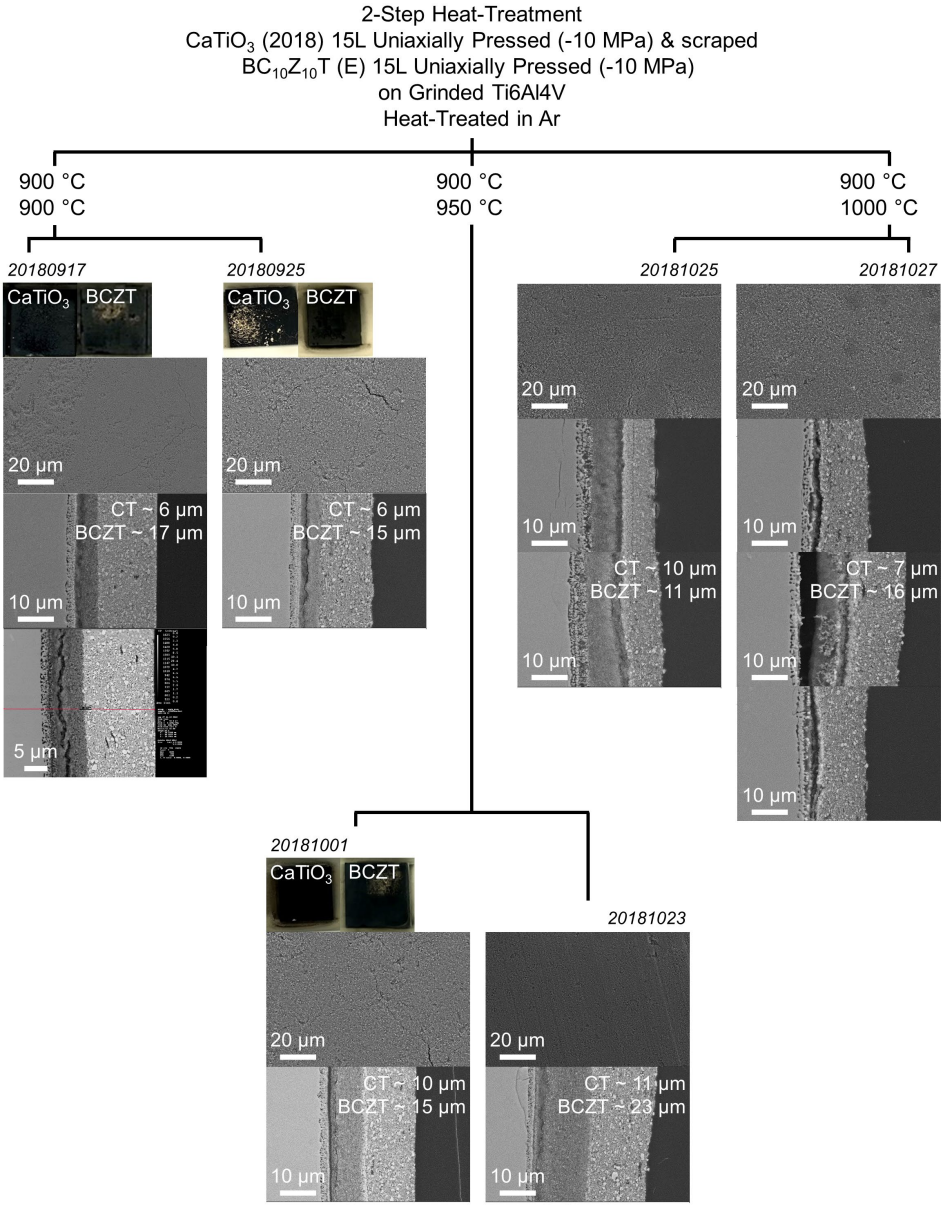

Appendix 16: Heat-treatment of $CaTiO_3$- and BCZT-coated Ti6Al4V.

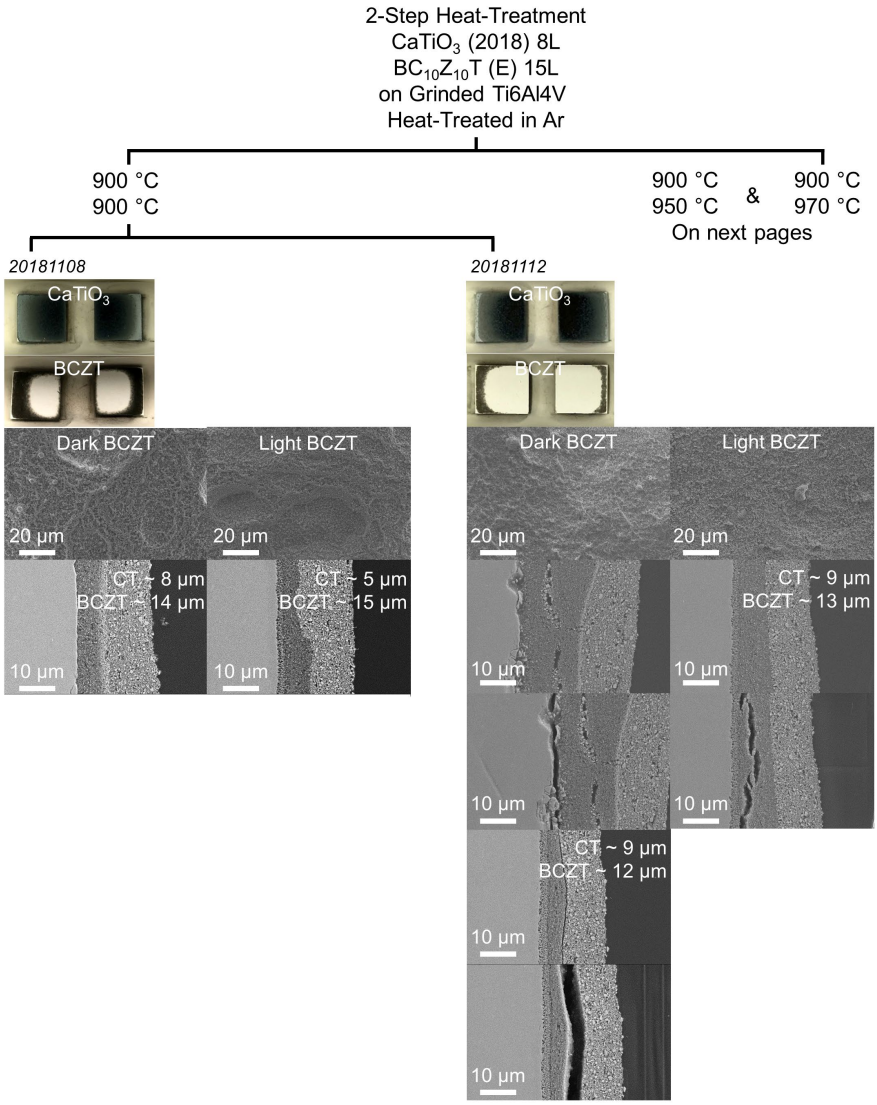

Appendix 17: Heat-treatment of $CaTiO_3$- and BCZT-coated Ti6Al4V.

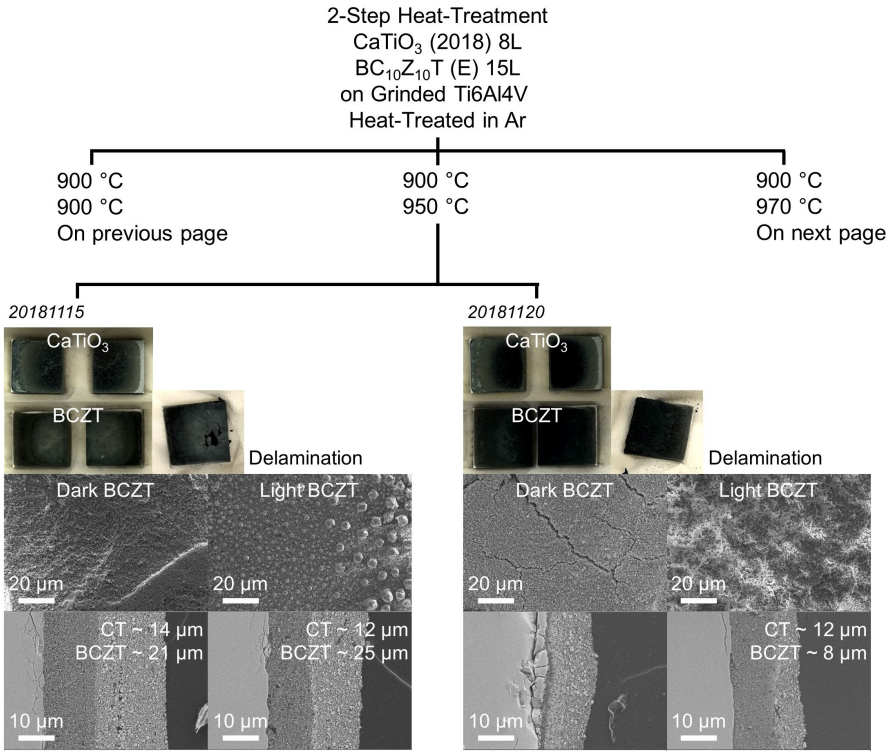

Appendix 18: Heat-treatment of $CaTiO_3$- and BCZT-coated Ti6Al4V.

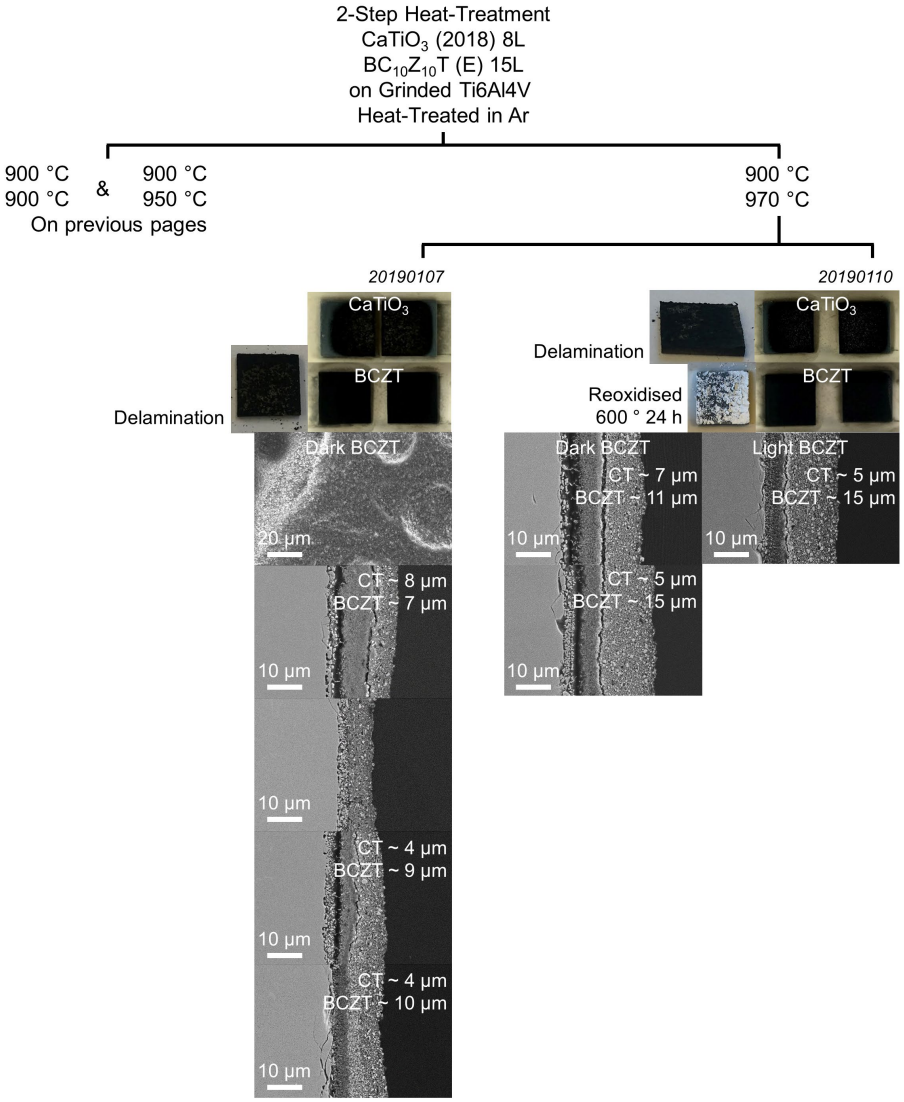

Appendix 19: Heat-treatment of $CaTiO_3$- and BCZT-coated Ti6Al4V.

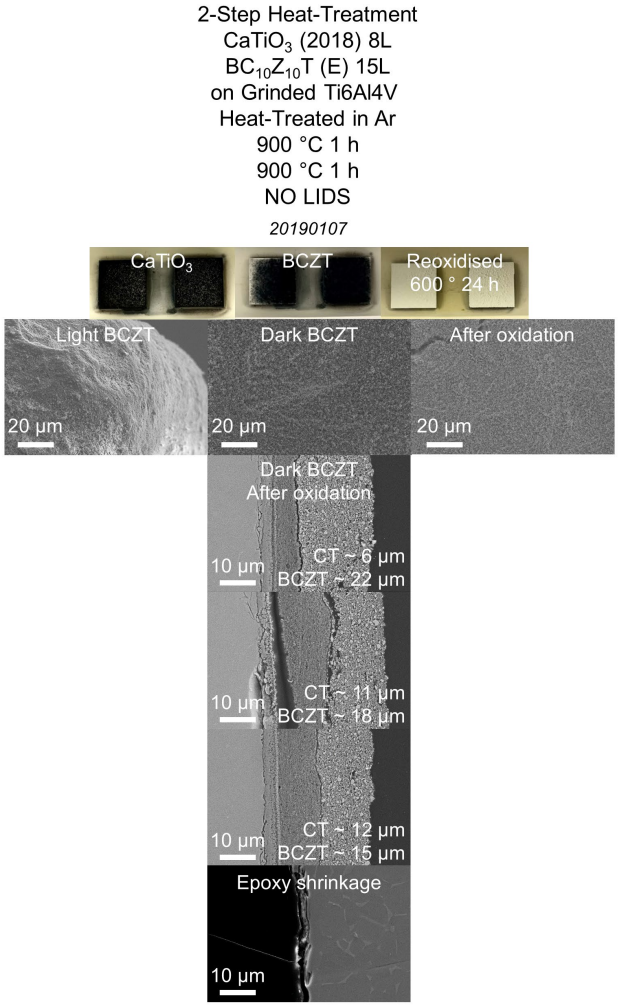

Appendix 20: Heat-treatment of $CaTiO_3$- and BCZT-coated Ti6Al4V.

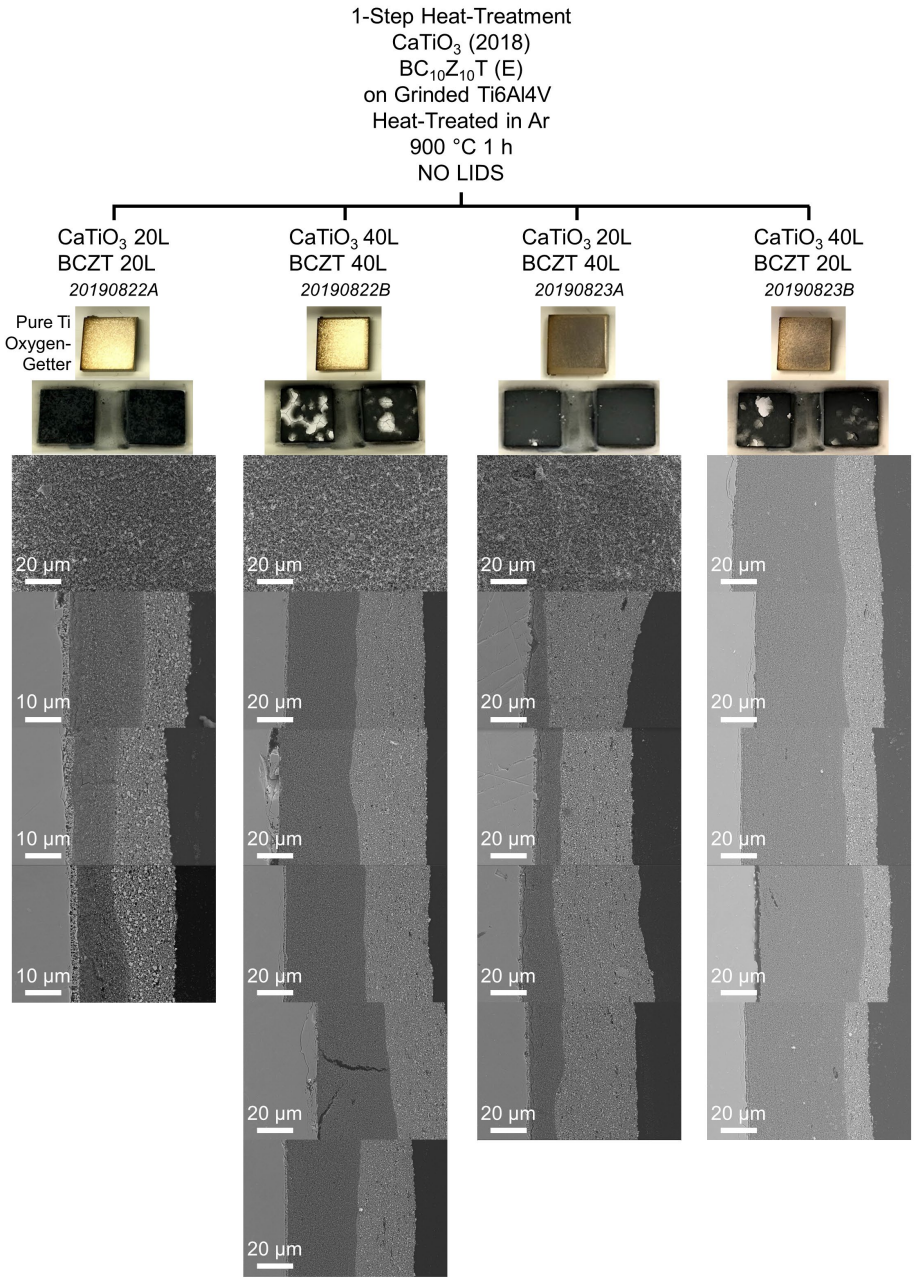

Appendix 21: Heat-treatment of $CaTiO_3$- and BCZT-coated Ti6Al4V.

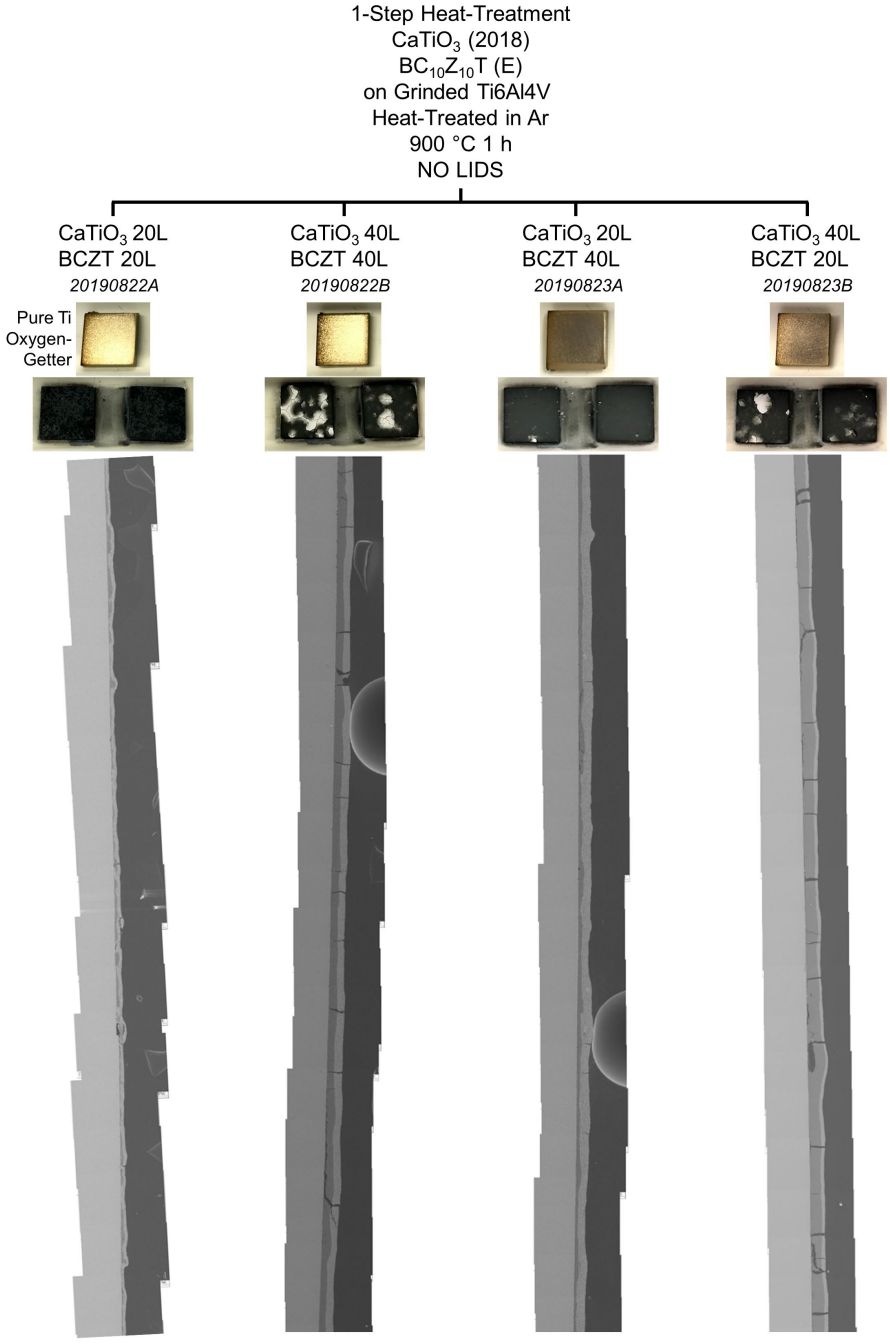

Paper

Received: 31 May 2019 | Revised: 1 August 2019 | Accepted: 6 August 2019

DOI: 10.1002/jbm.b.34477

ORIGINAL RESEARCH REPORT

Biocompatibility of (Ba,Ca)(Zr,Ti)O_3 piezoelectric ceramics for bone replacement materials

Kara K. Poon[1] | Matthias C. Wurm[2] | Donald M. Evans[1] | Mari-Ann Einarsrud[1] | Rainer Lutz[2] | Julia Glaum[1]

[1]Department of Materials Science and Engineering, NTNU Norwegian University of Science and Technology, Trondheim, Norway

[2]Department of Oral and Maxillofacial Surgery, Friedrich-Alexander-Universität Erlangen-Nürnberg, Erlangen, Germany

Correspondence
Kara K. Poon, Kjemi 2-332, Gløshaugen, Sem Sælands vei 12, 7491, Trondheim, Norway.
Email: kara.poon@ntnu.no

Funding information
H2020 Marie Skłodowska-Curie Actions, Grant/Award Number: H2020- MSCA-IF-2014 Grant 655866; Norges Forskningsråd, Grant/Award Number: FRINATEK Project 250098

Abstract

Total joint replacement implants are generally designed to physically mimic the biological environment to ensure compatibility with the host tissue. However, implant instability exposes patients to long recovery periods, high risk for revision surgeries, and high expenses. Introducing electrical stimulation to the implant site to accelerate healing is promising, but the cumbersome nature of wired devices is detrimental to the implant design. We propose a novel strategy to stimulate cells at the implant site by utilizing piezoelectric ceramics as electrical stimulation sources. The inherent ability of these materials to form electric surface potentials under mechanical load allows them to act as internal power sources. This characteristic is commonly exploited in non-biomedical applications such as transducers or sensors. We investigate calcium/zirconium-doped barium titanate (BCZT) ceramics in an *in vitro* environment to determine their potential as implant materials. BCZT exhibits low cytotoxicity with human osteoblast and endothelial cells as well as high piezoelectric responses. Microstructural adaptation was identified as a route for optimizing piezoelectric behavior. Our results show that BCZT is a promising system for biomedical applications. Its characteristic ability to autonomously generate electric surface potentials opens the possibility to functionalize existing bone replacement implant designs to improve implant ingrowth and long-term stability.

KEYWORDS
BCZT, cell proliferation and cytotoxicity, endothelial cells, osteoblasts, piezoelectric ceramics

1 | INTRODUCTION

Bone regenerative therapies involving the replacement or augmentation of diseased, or injured, bone tissue with implants are a standard procedure in current clinical practice. Today, synthetic bone replacement materials such as ceramics, metals, polymers, and glasses physically mimic the biological environment to ensure compatibility between the living tissue and the implant (Saini, Singh, Arora, Arora, & Jain, 2015). Strength, stiffness, topography, and toughness are the most carefully considered properties in implant design (Mandracci, Mussano, Rivolo, & Carossa, 2016; Smeets et al., 2016; Vandrovcová & Bačáková, 2011). Recent advancements in tissue engineering have focused on the use of biochemical and physicochemical cues to trigger specific cell responses to encourage better biological interaction between the implant and the living tissue.

A novel approach to improve the interface between synthetic materials and living bone tissue is to elicit particular cell behaviors with mechanical and electrical stimulation. The cell response to mechanical stimulation is well described by Wolff's law (Wolff, 1892), which states that the inner architecture of bone will adapt and restructure itself to withstand the mechanical forces acting upon it. In addition, cells convert mechanical stimuli into electrochemical activity via a number of mechanisms classified under the general term of "mechanotransduction" (Orr, Helmke, Blackman, & Schwartz, 2006). One of these mechanisms is the formation of electric potentials in load-bearing bone upon application of mechanical stress (Rajabi, Jaffe, & Arinzeh, 2015; Riddle & Donahue, 2009). *In vivo* studies indicate that direct current electrical stimulation applied to an implant site enhances initial-stage implant osseointegration, improves interfacial strength, and increases bone formation (Dergin et al., 2013; Isaacson et al., 2011; Salman & Park, 1980). In current clinical practice, electrical stimulation is used to treat non-union fractures via direct current, inductive, and capacitive coupling procedures (Aleem et al., 2016; Griffin & Bayat, 2011; Kuzyk & Schemitsch, 2009). These procedures rely on an external power source and the electrical stimulation can only be applied infrequently. For constant and power source independent electrical stimulation of the bone tissue, it is thus crucial to develop implant materials that autonomously generate electric charges under mechanical loads as they are generated by the body itself.

Piezoelectric ceramics may be the key to functionalizing current implant designs, as they exhibit mechanically generated electric surface potentials due to their non-centrosymmetric crystal structure. Thus, they can be used to mimic the bone's ability to generate electrical potentials under a mechanical load without the need for an external power source. Piezoelectric ceramics as bone replacement materials are currently not used in implant devices; however, *in vitro* studies indicate improved biocompatibility and bone-inductive ability on piezoelectric ceramic surfaces (Bodhak, Bose, & Bandyopadhyay, 2009; Tofail & Bauer, 2016).

A piezoelectric ceramic to be used as an active bone replacement material should be biocompatible and induce a sufficiently high electric potential to stimulate human cells (Büchter et al., 2005; Foulds & Barker, 1983; Hartig, Joos, & Wiesmann, 2000; Kuzyk & Schemitsch, 2009; Meyer, Büchter, Wiesmann, Joos, & Jones, 2005; Minary-Jolandan & Yu, 2009; Wiesmann, Hartig, Stratmann, Meyer, & Joos, 2001; Zigman et al., 2013). The highest piezoelectric coefficients, which quantify the generation of charge per unit of mechanical load, are currently achieved by lead-based piezoelectric ceramics; however, their high lead content renders them toxic (Shrout & Zhang, 2007). Among the lead-free piezoelectric systems, barium titanate (BT)-based materials are a promising class for bone replacement as indicated by cytotoxicity, cell viability, and proliferation studies (Ball, Mound, Nino, & Allen, 2014; Baxter, Bowen, Turner, & Dent, 2010; Park et al., 1981; Tang et al., 2017; Zhang, Chen, Zeng, Zhou, & Zhang, 2014). Particularly, the BT-derivative $(Ba,Ca)(Zr,Ti)O_3$ (BCZT) is of interest because of exceptionally high piezoelectric values compared to other lead-free piezoelectric materials available today (Liu & Ren, 2009). Additionally, fracture analysis studies of BCZT indicate that the hardness values of BCZT are approximately one to two orders of magnitude larger than human bone tissue, and approximately of the same order of magnitude for fracture toughness (Esguerra-Arce et al., 2015; Lucksanasombool, Higgs, Higgs, & Swain, 2001; Öhman, Zwierzak, Baleani, & Viceconti, 2013; Phelps, Hubbard, Wang, & Agrawal, 2000; Prabahar et al., 2017; Rattanachan, Miyashita, & Mutoh, 2005; Sailaja et al., 2019; Srinivas et al., 2015; Zioupos & Currey, 1998).

In this study, we investigate the piezoelectric properties of $(Ba_{0.85}Ca_{0.15})(Zr_{0.10}Ti_{0.90})O_3$ bulk ceramics and their compatibility with primary human osteoblast cells (HOBs) and primary human umbilical vein endothelial cells (HUVECs). The piezoelectric performance of the BCZT ceramics was determined as two orders of magnitude larger than observed in type I collagen fibrils, which are one of the origins of the stress-induced electric potentials in bone (Minary-Jolandan & Yu, 2009). In addition, the ceramic's piezoelectric response depends on the grain size, highlighting the possibility to tune the piezoelectric characteristics through microstructural modifications. Cytotoxicity, cell proliferation, and cell viability studies were performed using HOB and HUVEC cells. These cell studies demonstrate low cytotoxicity and enhanced cell viability and proliferation on the BCZT ceramics as compared to a polystyrene control group. The combination of good piezoelectric performance and low cytotoxicity highlights the potential of this class of materials to mimic the "piezoelectric effect" observed in natural bone, making it suitable for active, cell stimulating implants.

2 | MATERIALS AND METHODS

$(Ba_{0.85}Ca_{0.15})(Zr_{0.10}Ti_{0.90})O_3$ (BCZT) ceramics were synthesized via a solid-state reaction following the procedure by Zhang et al. (2014). This BCZT composition was chosen as it is located at the morphotropic phase boundary (MPB), where a high piezoelectric coefficient can be expected (Bai et al., 2015; Zhang, Glaum et al., 2014). The synthesis procedures of BCZT Series 1 and Series 2 were identical, only the barium carbonate precursor powder was of different purity (≥ 99% (Sigma Aldrich) for Series 1 and ≥99.98% (Sigma Aldrich) for Series 2). The other precursor powders were calcium carbonate ($CaCO_3$ ≥99%, Sigma Aldrich), zirconium dioxide (ZrO_2 ≥99.978%, Alfa Aesar), and titanium dioxide (TiO_2 ≥99.8%, Sigma Aldrich). The precursor powders were ball-milled in a 250 mL HDPE milling bottle on a long roll jar mill (U.S. Stoneware, East Palestine) for 24 hr with 5 mm diameter yttria-stabilized zirconia milling balls (Tosoh, Amsterdam, Netherlands) in 96% ethanol. The mixed precursor powders were dried using a rotary evaporator (Büchi Labortechnik AG, Flawil, Switzerland) and sieved using a 250 μm mesh. Subsequently, the powders were uniaxially pressed into cylindrical discs (3 g, 25 mm in diameter). The pellets were calcined at 1300°C for 2 hr, with a heating rate of 350°C/hr and a cooling rate of 400°C/hr. After calcination, the pellets were ground using an agate mortar and pestle, sieved with a 250 μm mesh, ball-milled in ethanol for 24 hr, and dried using a rotary evaporator. Calcined powders were sieved with a 250 μm mesh and uniaxially pressed into cylindrical disks (0.5 g, 15 mm in diameter). The green body pellets were sintered at

1450°C for 3 hr, with a heating rate of 350°C/hr and a cooling rate of 400°C/hr. Platinum crucibles were used for both calcination and sintering to avoid chemical reactions between the samples and the crucibles. Sintered pellets were approximately 12 mm in diameter and 1 mm in thickness. In total, 88 pellets of BCZT Series 1 were produced, as well as 23 pellets of BCZT Series 2. The bulk density of the sintered BCZT samples was determined from geometric measurements using a digital caliper and is presented as mean and *SD*.

Plan view images of the grain microstructure and surface topography of the BCZT and polystyrene control group materials used in the cell testing were obtained using a Zeiss Ultra 55 scanning electron microscope (SEM) (Carl Zeiss AG, Oberkochen, Germany). To expose the grain boundaries, BCZT samples were polished to a 3 μm finish, chemically etched using 37% hydrochloric acid and deionized water in a 1:1 ratio for 30 s (≈ 6.1 M), thermally etched at 1350°C for 5 min using a heating and cooling rate of 600°C/hr, and carbon coated prior to imaging. For cell testing, BCZT samples were grinded using 1200 grit silicon carbide (SiC) paper, whereas polystyrene samples (T175 Nunc™ EasYFlask™, Thermo Scientific, Waltham, MA) were used as-received.

Grain size measurements were performed using Lince software (Lince 2.31, Ceramics Group, TU Darmstadt, Germany), following a linear intercept method. At least 50 intersections were measured for each series of BCZT and expressed as mean and *SD*.

The phase purity of the BCZT ceramics was determined by X-ray diffraction (XRD) on sintered samples ground into powders with an agate mortar and pestle. A Bruker D8 A25 DaVinci X-ray diffractometer (Bruker, Billerica, MA) with an accelerating Cu Kα radiation of 1.54 Å was used. Phase purity analysis was performed with respect to PDF 00-065-0109 (International Center for Diffraction Data, Newtown Square, PA, 2016).

In preparation for piezoelectric property measurements, samples were grinded using 1200 grit SiC paper, and gold electrodes were applied by sputter deposition. Piezoelectric coefficient, d_{33}, measurements were performed using a TF Analyzer 2000 (aixACCT Systems GmbH, Aachen, Germany). The piezoelectric coefficient was measured using a small signal frequency and amplitude of 1 kHz and 3 V, respectively. At least five measurements were performed on one sample of each series and are expressed as mean and *SD*.

Surface property measurements were performed on BCZT samples grinded using 1200 grit SiC paper and as-received polystyrene samples, prepared as for the cell tests. The surface roughness was determined using an NT-MDT Ntegra Prima Scanning Probe Microscope (NT-MDT Spectrum Instruments Ltd., Moscow, Russia) with HQ:NSC35/Pt tips in contact mode. The scan size area was 85 × 85 μm^2. The static contact angles of sessile drops of 1 μL deionized water on BCZT and polystyrene samples were measured using the Krüss Drop Shape Analyzer DSA100 (Krüss GmbH, Hamburg, Germany). Deionized water drops were deposited at a speed of 40 mm/min and were allowed to sit on the sample surface for 30 s before the measurement was taken. Ten independent measurements per sample were obtained at 37°C. The contact angles were determined using the Young-Laplace fitting method. They are presented as mean and *SD*.

Cell viability and proliferation tests were performed on BCZT samples, which were grinded using 1200 grit SiC paper, and on as-received polystyrene samples of 12 mm diameter (Wurm et al., 2017). Primary human umbilical vein endothelial cells (HUVEC, PromoCell GmbH, Heidelberg, Germany) and primary human osteoblast cells (HOB, PromoCell GmbH, Heidelberg, Germany) were used for cell testing. The cells were cultured in flasks with cell growth areas of 25, 75, and 175 cm^2 (Greiner Bio-One, Frickenhausen, Germany) with Endothelial Cell Growth Medium (Ready-to use) (PromoCell GmbH, Heidelberg, Germany) at 98% humidity, 37°C, and 5% CO_2 (Heracell 240i CO_2 incubator, Thermo Scientific, Waltham, MA). At 70–90% confluency, splitting was performed until the third passage. A 24-well plate was filled with the corresponding media, and a 12 × 1 mm disc BCZT sample or polystyrene sample (as a control) was inserted. Each sample was seeded with 1×10^4 cells, and the samples were incubated at 37°C and 5% CO_2 for 30 min.

Cytotoxicity and morphology were analyzed with FDA (fluorescein diacetate)/PI (propidium iodide) dual staining (FDA of 10 μg/mL in phosphate-buffered saline [PBS], Invitrogen GmbH, Karlsruhe, Germany; PI of 50 μg/mL in PBS, Invitrogen GmbH, Karlsruhe, Germany). Media were removed after 24 hr and samples were stained for 20 min. After rinsing with PBS, the samples were inspected with an inverse microscope (Axioskop, Carl Zeiss AG, Oberkochen, Germany). Polystyrene and BCZT samples were compared for cell proliferation. Cell proliferation was determined by the number of live cells after 1, 3, 7, and 10 days with Scepter™ 2.0 Cell Counter (Merck KGaA, Darmstadt, Germany). The cells were detached at specific time points with Accutase (Accutase© Innovative Cell Technologies Inc., San Diego, CA), washed with PBS, and counted. Cell viability was determined from the activity of mitochondrial dehydrogenase using the WST-1 Cell Proliferation Assay (Roche Diagnostics GmbH, Mannheim, Germany).

All cell testing measurements were performed at least five times and expressed as mean and *SD*. The BiAs software (BiAs 11.08, epsilon-Verlag, Frankfurt, Germany) was used for analysis. The Kruskal–Wallis test was employed to assess the statistical significance of the data. The probability values of $p < 0.05$ were considered to be statistically significant (McDonald, 2014).

3 | RESULTS

3.1 | Structural analysis

Figure 1 displays the XRD patterns of sintered powder BCZT Series 1 and 2. The absence of secondary phases in the diffractograms shows that both Series 1 and 2 are phase pure. In addition, peak splitting is observed for the (200) and (222) reflections at 45° and 83°, showing that both tetragonal and rhombohedral crystal structures are present. This confirms the composition as being located in the morphotropic phase boundary region.

3.2 | Microstructural analysis

Figure 2 shows the representative SEM images of both series of sintered BCZT samples and the average grain sizes are provided in Table 1

together with the average densities. It can be seen that Series 1 has significantly smaller grains than Series 2 and a higher average density.

3.3 | Characterization of the piezoelectric properties

The piezoelectric coefficient, d_{33}, is the amount of induced charge per unit of applied mechanical stress. For a piezoelectric ceramic to exhibit a macroscopic piezoelectric response, the material must be electrically poled at first. This is because the electric dipoles are aligned with each other within a domain, but each domain is spatially oriented in a random fashion cancelling out the overall piezoelectric characteristic. The application of a sufficiently high electric field will cause the dipoles to align with the direction of the applied electric field and a macroscopic piezoelectric coefficient can be measured. A visual illustration of this process is given in Figure 3, which shows the d_{33} hysteresis loop of BCZT Series 1 ceramics during the initial polarization step. At point A (d_{33} = 0), the piezoelectric material is unpoled and contains randomly oriented domains that form a net zero piezoelectric coefficient. As the electric field is increased up to the coercive field, E_c, there is a sudden increase in d_{33} as the domains align along the direction of the applied electric field. At point B (d_{33s} > 0), a saturation state is reached. As the electric field is reduced again, some domains move out of alignment, but the material does not return to its original state. Instead it maintains a remanent alignment of domains at point C (d_{33r} > 0) upon complete removal of the electric field. This remanent piezoelectric coefficient, d_{33r}, is important as it demonstrates the amount of charge that can be retained without electric field application and therefore be applied to surrounding human cells when used in a biological environment. Upon further application of a negative electric field, domains within the material switch their direction, allowing the material to express a surface charge and with this a piezoelectric coefficient of opposite polarity.

Figure 4 shows the d_{33} hysteresis loops for Series 1 and 2 in comparison. Although Series 1 exhibits significantly higher piezoelectric responses while high electric fields are applied, both series demonstrate similarly high remanent d_{33r} values of ≈ 280 pC/N.

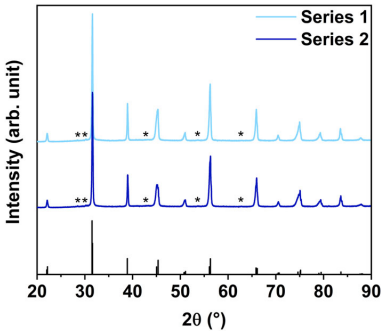

FIGURE 1 XRD patterns of BCZT–Series 1 and 2, synthesized using $BaCO_3$ precursor powders of purity level ≥ 99% and ≥ 99.98%, respectively. The asterisks (*) mark contributions from Cu Kβ1 and W Lα1 radiation from the XRD measurement. The reference diffractogram, PDF 00-065-0109, used for the phase purity analysis is shown

3.4 | Cell studies

The cell viability of primary HOBs and primary HUVECs on BCZT and a polystyrene control group was investigated by FDA/PI dual staining,

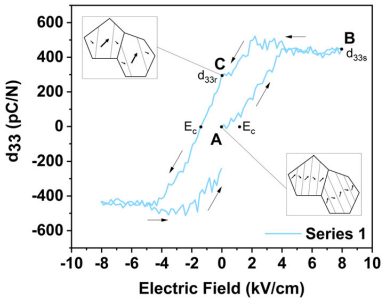

FIGURE 3 d_{33} hysteresis loop of BCZT Series 1, during the initial polarization step. The d_{33} increases from a value of zero with the application of electric field. Arrows denote the direction of electric field application

TABLE 1 Average grain sizes and densities of BCZT Series 1 and 2, synthesized using $BaCO_3$ ≥99% and ≥99.98% precursor powders, respectively

Sample	Number of samples	Average grain size (μm)	Average density (g/cm^3)
Series 1	88	10 ± 2	6.0 ± 0.3
Series 2	23	35 ± 8	5.6 ± 0.3

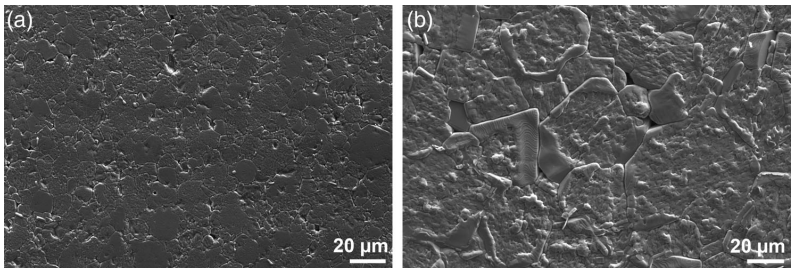

FIGURE 2 SEM micrographs of polished and etched BCZT (a) Series 1, synthesized using $BaCO_3$ precursor powder of purity level ≥ 99%, and (b) Series 2, synthesized using $BaCO_3$ precursor powder of purity level ≥ 99.98%

as displayed in Figure 5. Viable cells are stained green and dead cells are stained red. As shown in Figure 5, vital and adjacent cells with well-spread filopodiae were observed on both BCZT and the polystyrene control group after 24 hr in cell culture. In general, significantly more vital HOBs were observed on both materials than HUVECs and an increased number of viable HOB cells are observed on BCZT than on the polystyrene control group.

Cell proliferation was observed on both BCZT and the polystyrene control group, as shown in Figure 6. A constant proliferation of HUVECs and HOBs on BCZT was observed from Days 1 to 7. On Day 10, the cell count on BCZT decreased to 3.4×10^4 for HUVECs and 3.8×10^4 for HOBs. Constant proliferation of HUVECs and HOBs was observed on the polystyrene control group over the entire 10-day period. The HUVECs cell culture showed better statistically significant proliferation rates on BCZT from Days 1 to 7, as shown in Table 2 and Figure 6. The cell culture of HOBs, however, reveals statistically significant results on Days 7 and 10, as shown in Table 2 and Figure 6.

Cell viability studies performed using a WST assay show that a higher number of living cells were detected on the BCZT ceramics at all time points during the 10-day period as compared to the control group for both cell lines. This is evident in Figure 7, which shows the percentage of viable HUVECs and HOBs on BCZT in comparison to the polystyrene control group over the 10-day period.

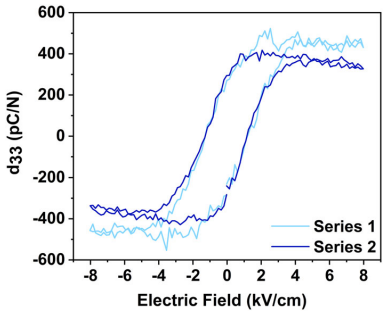

FIGURE 4 d_{33} hysteresis loops of BCZT Series 1 and 2 after polarization

Detailed progressions of the cell viability during the testing period for HUVECs and HOBs on the BCZT ceramics and polystyrene control group are presented in Figure 8, with a higher absorbance indicating a higher activity of mitochondrial dehydrogenase and amount of viable metabolically active cells. A greater proportion of HUVECs were viable on the BCZT ceramics as compared to the polystyrene control group for all days. A similar trend is seen for the HOBs, with the exception on Day 7, which shows a greater proportion of viable cells on the polystyrene samples. This is likely due to cell overcrowding limiting growth.

3.5 | Surface properties

Surface morphologies of BCZT and polystyrene samples as prepared for cell testing are shown in Figure 9. These images show that the BCZT ceramics, prepared by grinding with SiC paper, are rougher than the as-received polystyrene samples. The surface roughness, R_a, for BCZT was determined as 0.840 μm and <0.001 μm for the polystyrene control group. Deionized water contact angle measurements were performed on BCZT and polystyrene. A greater wettability of BCZT than polystyrene was observed, with BCZT surfaces showing

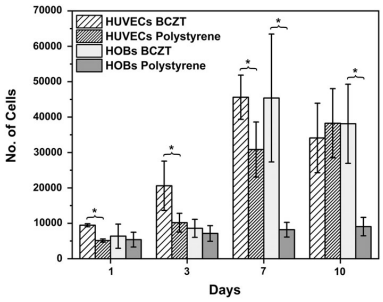

FIGURE 6 Proliferation of HUVECs and HOBs on BCZT and the polystyrene control group during a 10-day period. Statistically significant results ($p < 0.05$) are marked with an asterisk (*). Significantly higher cell numbers were observed on Days 1, 3, and 7 on BCZT as compared to the polystyrene control group for the HUVEC cell line, and on Days 7 and 10 for the HOB cell line

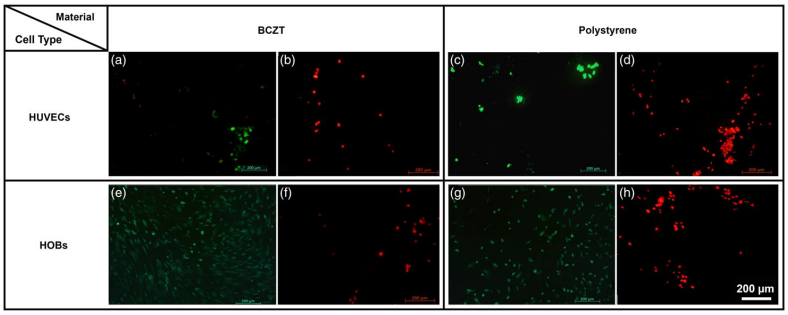

FIGURE 5 FDA/PI-viability staining of HUVECs (a–d) and HOBs (e–h) after 24 hr of cell culture on BCZT (a,b,e,f) and polystyrene (c,d,g,h). Viable cells are stained green and dead cells red

TABLE 2 Counted cell numbers at given time points

HUVECs				
	Day 1	**Day 3**	**Day 7**	**Day 10**
BCZT	9,457 ± 423	20,608 ± 6,963	45,620 ± 6,254	34,110 ± 9,822
Polystyrene	5,126 ± 461	10,175 ± 2,659	30,840 ± 7,786	38,270 ± 9,771
p	0.008*	0.016*	0.032*	0.690
HOBs				
	Day 1	**Day 3**	**Day 7**	**Day 10**
BCZT	6,368 ± 3,414	8,582 ± 2,538	45,400 ± 18,062	38,120 ± 11,179
Polystyrene	5,388 ± 2090	7,138 ± 2,203	8,200 ± 2083	9,072 ± 2,605
p	0.690	0.690	0.008*	0.008*

Note: BCZT showed highest proliferation. Statistically significant differences ($p < 0.05$) in proliferation are marked with an asterisk (*).

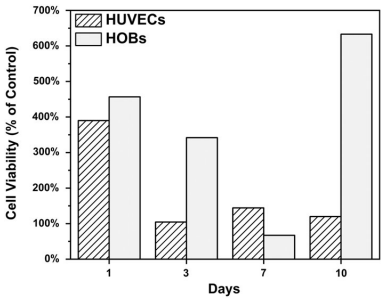

FIGURE 7 The relative amount of viable cells observed on BCZT as compared to polystyrene

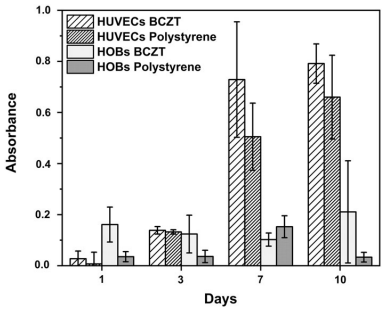

FIGURE 8 Absorbance of mitochondrial dehydrogenase activity on BCZT and polystyrene over a 10-day period

contact angles of 41.2 ± 3.9° as compared to contact angles of 87.6 ± 1.6° for polystyrene surfaces.

4 | DISCUSSION

4.1 | Grain size dependency of the piezoelectric response

The piezoelectric performance of BT-based ceramics is influenced by the microstructure and especially by the size of the grains (Arlt, 1990). Tailoring of the grain size distribution can as such be used as a tool to optimize the piezoelectric response. This is of utmost interest when piezoelectric materials are used *in vivo* as material optimization through chemical doping is restricted to the usage of non-toxic elements.

In the present study, two $BaCO_3$ precursor powders with different levels of purity were used, resulting in significantly different grain sizes of the two BCZT series. It has been reported for the $PbTiO_3$ system that minor cation non-stoichiometry can affect the microstructure due to alterations in defect chemistry and mass transport mechanisms. Although A-site deficiency leads to submicron-sized grains, B-site deficiency causes grain growth and grains become approximately two orders of magnitude larger in size (Selbach, Tybell, Einarsrud, & Grande, 2011). Parallels in behavior to the $PbTiO_3$ system can be observed in the present BCZT composition. Series 1 synthesized using $BaCO_3$ with purity ≥99% exhibits similar behavior as the A-site-deficient $PbTiO_3$, and Series 2 synthesized using $BaCO_3$ with purity ≥99.98% exhibits significantly larger grains consistent with the grain growth behavior observed in B-site deficient $PbTiO_3$ (Selbach et al., 2011). The slight variations in chemical composition introduced this way were sufficient to alter the sintering behavior leading to different grain microstructures.

Figure 4 highlights the influence of the microstructure variations on the piezoelectric performance. The figure of merit in this study is the remanent piezoelectric coefficient, d_{33r}, that is retained without the application of an external electric field. It determines the amount of charge the piezoelectric ceramics are able to supply to surrounding cells when used as a load-bearing implant. High remanent d_{33r} values of approximately 280 pC/N were obtained for both Series 1 and 2. In contrast to the values obtained under electric field application, no influence of the grain size is observed for the remanent state. This can be attributed to the inherent electrical "softness" of $BaTiO_3$-based materials. This is reflected in strong domain switching and development of high piezoelectric response under electric field application, but as well a strong relaxation of the aligned domain structure and a

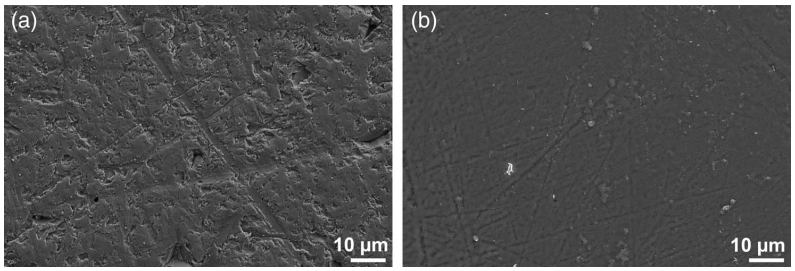

FIGURE 9 SEM micrographs of (a) BCZT surface grinded with 1200 grit SiC paper, and (b) as-received polystyrene surface, reflecting the surface roughness as present during the cell tests

corresponding reduction in response, when the electric field is reduced (Ehmke, Glaum, Hoffman, Blendell, & Bowman, 2013a; Ehmke, Glaum, Hoffman, Blendell, & Bowman, 2013b). Although the exact influence of grain size on the piezoelectric behavior of BCZT is unascertained, there are indications that there is a positive correlation between enhanced piezoelectric performance and the movement of 90° domain walls in larger grains (Arlt, 1990; Ghayour & Abdellahi, 2016). The change in mechanical constraints as imposed by a variation in average grain size does not overrule the electrical "softness" for the composition investigated in the present study. However, the grain size might take a more determining role for single phase compositions, as their piezoelectric response is less sensitive to changes in the electric field. This suggests that the piezoelectric response and, therefore, the amount of charge that can be supplied to surrounding cells may be tuned and optimized by modification of the grain size, thus removing the need for toxic elemental additives.

The density of a ceramic can influence piezoelectric performance. Higher piezoelectric performances are expected of high-density samples due to the absence of lower permittivity pores. However, it is expected that grain size is the dominant factor affecting the piezoelectric performance in this study. Despite a difference in densities for Series 1 and 2 of 6.0 g/cm^3 and 5.6 g/cm^3, it is shown that the density variation is not significant enough to affect the remanent piezoelectric state, as shown in Figure 4.

4.2 | The influence of surface properties on the cell response

It is well understood that the surface properties of an implant can affect the biological response. This has led to developments in implant surface designs, where factors such as surface roughness and wettability are considered. In the present study, the cell responses to the presence of the piezoelectric ceramics were compared to a control group, where polystyrene samples served as the substrates.

Surface wettability is one factor that can affect the biological response with respect to cell adhesion and spreading. Studies suggest that moderate contact angles of approximately 60° enhance osteoblast adhesion (Lavenus et al., 2011; Vandrovcová & Bačáková, 2011). As such, the greater wettability of the present BCZT ceramics compared to the polystyrene samples may have enhanced cell adhesion and spreading, contributing to the larger number of osteoblast cells and endothelial cells measured on the BCZT surfaces at the different time points of the cell proliferation tests, as shown in Figure 6.

Due to the nature of the sample preparation routine used, the present BCZT ceramics exhibited a significantly higher surface roughness than the polystyrene control samples (0.840 μm for the ceramics compared to <0.001 μm for the control). Roughness at the nano-, micro-, and macroscale each can have an influence on cell adhesion, spreading, and proliferation (Andrukhov et al., 2016; Gittens et al., 2013; Lavenus et al., 2011; Nishimoto et al., 2008; Samavedi, Whittington, & Goldstein, 2013; Vandrovcová & Bačáková, 2011). Enhanced cell adhesion of osteoblasts has been observed for surface roughnesses of approximately 1 μm, as compared to smoother surfaces (Andrukhov et al., 2016; Nishimoto et al., 2008; Vandrovcová & Bačáková, 2011). This indicates that the higher surface roughness of the BCZT samples may be one reason for the enhanced cell attachment as compared to the smooth surfaces of the polystyrene control group.

The intrinsic microstructure of ceramics is determined by their grain morphology (Figure 2). The grain size and shape are not expected to be critical factors for the surface properties in the current work, as the surface features exposed to the cells were determined by the grinding process (Figure 9). Furthermore, the BCZT bulk ceramic samples used for cell proliferation and viability testing were not electrically polarized. The domain structure in individual grains was therefore random (Point A in Figure 3), and it can be expected that individual grains were not electrically distinguishable to the osteoblast or endothelial cells.

However, to maximize the stimulating effect of the piezoelectrically generated charges in bone replacement applications, electrically poled materials must be used. As every grain has a different orientation of the crystallographic axis with respect to the surface of the sample, the surface charge developed under mechanical load will vary spatially from grain to grain as well as within one grain from domain to domain. Although grain to grain variations occur on a length scale from about 1–100 μm, variations on the domain scale are expected in the range of 10–500 nm with domain size becoming smaller as the grain size decreases (Tan et al., 2015). This highlights that even though the macroscopic remanent piezoelectric coefficient was found to be independent of the grain size in the present system, grain size and domain size are expected to have profound influence on the local cell responses.

5 | CONCLUSIONS

BCZT ceramics were synthesized via solid-state synthesis, and the piezoelectric performance and compatibility with human osteoblast and endothelial cells were investigated. Cell studies demonstrating elevated

cell proliferation and viability results for BCZT as compared to a polystyrene control group show the possible encouragement of cell activity. Due to good piezoelectric performance and compatibility with human osteoblast and endothelial cells, BCZT demonstrates high potential as an active bone replacement material. Further studies mapping the relationship between microstructure, local piezoelectric response, and cell stimulation are in demand to be able to take advantage of the possibility to optimize the material's functionality without the need for additional doping elements.

ACKNOWLEDGMENTS

The authors acknowledge funding from The Research Council of Norway (FRINATEK Project No. 250098) as well as from the EU call H2020- MSCA-IF-2014 under grant number 655866.

ORCID

Matthias C. Wurm https://orcid.org/0000-0002-4877-0042

REFERENCES

Aleem, I. S., Aleem, I., Evaniew, N., Busse, J. W., Yaszemski, M., Agarwal, A., & Einhorn Tand Bhandari, M. (2016). Efficacy of electrical stimulators for bone healing: A meta-analysis of randomized sham-controlled trials. *Scientific Reports*, *6*, 31724.

Andrukhov, O., Huber, R., Shi, B., Berner, S., Rausch-Fan, X., Moritz, A., … Schedle, A. (2016). Proliferation, behavior, and differentiation of osteoblasts on surfaces of different microroughness. *Dental Materials*, *32*, 1374–1384.

Arlt, G. (1990). The influence of microstructure on the properties of ferroelectric ceramics. *Ferroelectrics*, *104*, 217–227.

Bai, Y., Matousek, A., Tofel, P., Bijalwan, V., Nan, B., Hughes, H., & Button, T. W. (2015). (Ba,Ca)(Zr,Ti)O_3 lead-free piezoelectric ceramics—The critical role of processing on properties. *Journal of the European Ceramic Society*, *35*, 3445–3456.

Ball, J. P., Mound, B. A., Nino, J. C., & Allen, J. B. (2014). Biocompatible evaluation of barium titanate foamed ceramic structures for orthopedic applications. *Journal of Biomedical Materials Research. Part A*, *102*, 2089–2095.

Baxter, F. R., Bowen, C. R., Turner, I. G., & Dent, A. C. E. (2010). Electrically active bioceramics: A review of interfacial responses. *Annals of Biomedical Engineering*, *38*, 2079–2092.

Bodhak, S., Bose, S., & Bandyopadhyay, A. (2009). Role of surface charge and wettability on early stage mineralization and bone cell–materials interactions of polarized hydroxyapatite. *Acta Biomaterialia*, *5*, 2178–2188.

Büchter, A., Wiechmann, D., Koerdt, S., Wiesmann, H. P., Piffko, J., & Meyer, U. (2005). Load-related implant reaction of mini-implants used for orthodontic anchorage. *Clinical Oral Implants Research*, *16*, 473–479.

Dergin, G., Akta, M., Gürsoy, B., Devecioglu, Y., Kürkçü, M., & Benlidayi, E. (2013). Direct current electric stimulation in implant osseointegration: An experimental animal study with sheep. *The Journal of Oral Implantology*, *39*, 671–679.

Ehmke, M. C., Glaum, J., Hoffman, M., Blendell, J. E., & Bowman, K. J. (2013a). The effect of electric poling on the performance of lead-free (1-x)Ba($Zr_{0.2}Ti_{0.8}$)O_3-x($Ba_{0.7}Ca_{0.3}$)TiO_3 piezoceramics. *Journal of the American Ceramic Society*, *96*, 3805–3811.

Ehmke, M. C., Glaum, J., Hoffman, M., Blendell, J. E., & Bowman, K. J. (2013b). In situ X-ray diffraction of biased ferroelastic switching in tetragonal lead-free (1-x)Ba($Zr_{0.2}Ti_{0.8}$)O_3-x($Ba_{0.7}Ca_{0.3}$)TiO_3 piezoelectrics. *Journal of the American Ceramic Society*, *96*, 2913–2920.

Esguerra-Arce, J., Aguilar-Castro, Y., Aperador-Chaparro, W., Ipaz-Cuastumal, L., Bolaños Pantoja, G., & Rincón-López, C. A. (2015). Tribological behavior of bone against calcium titanate coating in simulated body fluid. *Ingeniería, Investigación y Tecnología.*, *16*, 279–286.

Foulds, I. S., & Barker, A. T. (1983). Human skin battery potentials and their possible role in wound healing. *The British Journal of Dermatology*, *109*, 515–522.

Ghayour, H., & Abdellahi, M. (2016). A brief review of the effect of grain size variation on the electrical properties of $BaTiO_3$-based ceramics. *Powder Technology*, *292*, 84–93.

Gittens, R. A., Olivares-Navarrete, R., Cheng, A., Anderson, D. M., McLachlan, T., Stephan, I., … Schwarz, Z. (2013). The roles of titanium surface micro/nanotopography and wettability on the differential response of human osteoblast lineage cells. *Acta Biomaterialia*, *9*, 6268–6277.

Griffin, M., & Bayat, A. (2011). Electrical stimulation in bone healing: Critical analysis by evaluating levels of evidence. *Eplasty*, *11*, 303–353.

Hartig, M., Joos, U., & Wiesmann, H. P. (2000). Capacitively coupled electric fields accelerate proliferation of osteoblast-like primary cells and increase bone extracellular matrix formation in vitro. *European Biophysics Journal*, *29*, 499–506.

Isaacson, B. M., Brunker, L. B., Brown, A. A., Beck, J. P., Burns, G. L., & Bloebaum, R. D. (2011). An evaluation of electrical stimulation for improving periprosthetic attachment. *Journal of Biomedical Materials Research. Part B, Applied Biomaterials*, *97*, 190–200.

Kuzyk, P. R., & Schemitsch, E. H. (2009). The science of electrical stimulation therapy for fracture healing. *Indian J Orthop.*, *43*, 127–131.

Lavenus, S., Pilet, P., Guicheux, J., Weiss, P., Louarn, G., & Layrolle, P. (2011). Behaviour of mesenchymal stem cells, fibroblasts and osteoblasts on smooth surfaces. *Acta Biomaterialia*, *7*, 1525–1534.

Liu, W., & Ren, X. (2009). Large piezoelectric effect in Pb-free ceramics. *Physical Review Letters*, *103*, 1–4.

Lucksanasombool, P., Higgs, W. A. J., Higgs, R. J. E. D., & Swain, M. V. (2001). Fracture toughness of bovine bone: Influence of orientation and storage media. *Biomaterials*, *22*, 3127–3132.

Mandracci, P., Mussano, F., Rivolo, P., & Carossa, S. (2016). Surface treatments and functional coatings for biocompatibility improvement and bacterial adhesion reduction in dental implantology. *Coatings*, *6*, 7.

McDonald, J. H. (2014). *Handbook of biological statistics*. Baltimore, Maryland: Sparky House Publishing.

Meyer, U., Büchter, A., Wiesmann, H. P., Joos, U., & Jones, D. B. (2005). Basic reactions of osteoblasts on structured material surfaces. *European Cells & Materials*, *9*, 39–49.

Minary-Jolandan, M., & Yu, M. F. (2009). Nanoscale characterization of isolated individual type I collagen fibrils: Polarization and piezoelectricity. *Nanotechnology*, *20*, 085706.

Nishimoto, S. K., Nishimoto, M., Park, S. W., Lee, K. M., Kim, H. S., Koh, J. T., … Yang, T. (2008). The effect of titanium surface roughening on protein absorption, cell attachment, and cell spreading. *The International Journal of Oral & Maxillofacial Implants*, *23*, 675–680.

Öhman, C., Zwierzak, I., Baleani, M., & Viceconti, M. (2013). Human bone hardness seems to depend on tissue type but not on anatomical site in the long bones of an old subject. *Proceedings of the Institution of Mechanical Engineers. Part H*, *227*, 200–206.

Orr, A. W., Helmke, B. P., Blackman, B. R., & Schwartz, M. A. (2006). Review mechanisms of mechanotransduction. *Developmental Cell*, *10*, 11–20.

Park, J. B., Kelly, B. J., Kenner, G. H., von Recum, A. F., Grether, M. F., & Coffeen, W. W. (1981). Piezoelectric ceramic implants: in vivo results. *Journal of Biomedical Materials Research*, *15*, 103–110.

Phelps, J. B., Hubbard, G. P., Wang, X., & Agrawal, C. M. (2000). Microstructural heterogeneity and the fracture toughness of bone. *Journal of Biomedical Materials Research*, *51*, 735–741.

Prabahar, K., Ranjith, R., Srinivas, A., Kamat, S. V., Mallesham, B., Niranjani, V. L., … Das, D. (2017). Effect of deposition temperature on the microstructure, ferroelectric and mechanical properties of lead free BCZT ceramic thin films. *Ceramics International*, *43*, 5356–5361.

Rajabi, A. H., Jaffe, M., & Arinzeh, T. L. (2015). Piezoelectric materials for tissue regeneration: A review. *Acta Biomaterialia*, *24*, 12–23.

Rattanachan, S., Miyashita, Y., & Mutoh, Y. (2005). Fracture toughness of $BaTiO_3$ and $BaTiO_3$-Al_2O_3 composite under electric field. In R. C. Bradt, D. Munz, M. Sakai, & K. W. White (Eds.), *Fracture Mechanics of Ceramics* (Vol. 14, pp. 297–305). Boston: Springer.

Riddle, R. C., & Donahue, H. J. (2009). From streaming potentials to shear stress: 25 years of bone cell mechanotransduction. *Journal of Orthopaedic Research*, *27*, 143–149.

Sailaja, P., Kumar, N. P., Sowmya, N. S., James, A. R., Kumar, A., Arockiakumar, R., & Srinivas, A. (2019). Investigation of ferroelectric, piezoelectric and mechanically coupled properties of lead-free $(Ba_{0.85}Ca_{0.15})(Zr_{0.1}Ti_{0.9})O_3$ ceramics. *Advances in Applied Ceramics*, *118*, 300–307.

Saini, M., Singh, Y., Arora, P., Arora, V., & Jain, K. (2015). Implant biomaterials: A comprehensive review. *World Journal of Clinical Cases*, *3*, 52–57.

Salman, N. N., & Park, J. B. (1980). The effect of direct electrical current stimulation on the bone/porous metallic implant interface. *Biomaterials*, *1*, 209–213.

Samavedi, S., Whittington, A. R., & Goldstein, A. S. (2013). Calcium phosphate ceramics in bone tissue engineering: A review of properties and their influence on cell behavior. *Acta Biomaterialia*, *9*, 80337–88045.

Selbach, S. M., Tybell, T., Einarsrud, M. A., & Grande, T. (2011). PbO-deficient $PbTiO_3$: Mass transport, structural effects and possibility for intrinsic screening of the ferroelectric polarization. *Applied Physics Letters*, *98*, 091912.

Shrout, T. R., & Zhang, S. J. (2007). Lead-free piezoelectric ceramics: Alternatives for PZT? *Journal of Electroceramics*, *19*, 111–124.

Smeets, R., Stadlinger, B., Schwarz, F., Beck-Broichsitter, B., Jung, O., Precht, C., … Ebker, T. (2016). Impact of dental implant surface modifications on osseointegration. *BioMed Research International*, *2016*, 1–16.

Srinivas, A., Krishnaiah, R. V., Niranjani, V. L., Kamat, S. V., Karthik, T., & Asthana, S. (2015). Ferroelectric, piezoelectric and mechanical properties in lead free $(0.5)Ba(Zr_{0.2}Ti_{0.8})O_3$-$(0.5)(Ba_{0.7}Ca_{0.3})TiO_3$ electroceramics. *Ceramics International*, *41*, 1980–1985.

Tan, Y., Zhang, J., Wu, Y., Wang, C., Koval, V., Shi, B., … Yan, H. (2015). Unfolding grain size effects in barium titanate ferroelectric ceramics. *Scientific Reports*, *5*, 9953.

Tang, Y., Wu, C., Wu, Z., Hu, L., Zhang, W., & Zhao, K. (2017). Fabrication and in vitro biological properties of piezoelectric bioceramics for bone regeneration. *Scientific Reports*, *7*, 1–12.

Tofail, S. A. M., & Bauer, J. (2016). Electrically polarized biomaterials. *Advanced Materials*, *28*, 5470–5484.

Vandrovcová, M., & Bačáková, L. (2011). Adhesion, growth and differentiation of osteoblasts on surface-modified materials developed for bone implants. *Physiological Research*, *60*, 403–417.

Wiesmann, H. P., Hartig, M., Stratmann, U., Meyer, U., & Joos, U. (2001). Electrical stimulation influences mineral formation of osteoblast-like cells in vitro. *Biochimica et Biophysica Acta*, *1538*, 28–37.

Wolff, J. (1892). *Das Gesetz der Transformation der Knochen*. Berlin: Hirschwald.

Wurm, M. C., Möst, T., Bergauer, B., Rietzel, D., Neukam, F. W., Cifuentes, S. C., & Wilmowsky, C. V. (2017). In-vitro evaluation of polylactic acid (PLA) manufactured by fused deposition modeling. *Journal of Biological Engineering*, *11*, 29.

Zhang, Y., Chen, L., Zeng, J., Zhou, K., & Zhang, D. (2014). Aligned porous barium titanate/hydroxyapatite composites with high piezoelectric coefficients for bone tissue engineering. *Materials Science and Engineering: C*, *39*, 143–149.

Zhang, Y., Glaum, J., Groh, C., Ehmke, M. C., Blendell, J. E., Bowman, K. J., & Hoffman, M. J. (2014). Correlation between piezoelectric properties and phase coexistence in $(Ba,Ca)(Ti,Zr)O_3$ ceramics. *Journal of the American Ceramic Society*, *97*, 2885–2891.

Zigman, T., Davila, S., Dobric, I., Antoljak, T., Augustin, G., Rajacic, D., … Ehrenfreund, T. (2013). Intraoperative measurement of bone electrical potential: A piece in the puzzle of understanding fracture healing. *Injury*, *44*, S16–S19.

Zioupos, P., & Currey, J. D. (1998). Changes in the stiffness, strength, and toughness of human cortical bone with age. *Bone*, *22*, 57–66.

How to cite this article: Poon KK, Matthias C. Wurm, Evans DM, Einarsrud M-A, Lutz R, Glaum J. Biocompatibility of $(Ba,Ca)(Zr,Ti)O_3$ piezoelectric ceramics for bone replacement materials. *J Biomed Mater Res*. 2019;1–9. https://doi.org/10.1002/jbm.b.34477